UNIVERSITY OF TECHNOLOGY, SYDNEY

Numerical Modelling and Condition Assessment of Timber Utility Poles using Stress Wave Techniques

---

by

Ning Yan

A dissertation submitted in partial fulfilment of the requirements for the degree of Doctor of Philosophy

June 2015

Certificate of authorship/originality

I certify that the work in this thesis has not previously been submitted for a degree nor has it been submitted as part of requirements for a degree except as fully acknowledged within the text.

I also certify that the thesis has been written by me. Any help that I have received in my research work and the preparation of the thesis itself has been acknowledged. In addition, I certify that all information sources and literature used are indicated in the thesis.

Signature of Candidate

_____

Ning Yan

Sydney, June 2015

Acknowledgement

I would like to express my deep appreciation to my supervisors Professor Jianchun Li, Professor Bijan Samali and Dr Ulrike Dackermann who were very supportive and motivating throughout my degree. Professor Jianchun Li was an excellent advisor in technical questions and always inspired me in achieving my goals. He allowed me to meet him any time I required to and spent lots of time to explain difficult concepts to me or helped me with some programming work. I believe the dissertation would have never been possible without his guidance and help.

I would also like to give special thanks to Professor Bijan Samali. He provided me this precious opportunity to start my research work at UTS in Australia. I always felt very comfortable to express my opinion regarding the research and discuss my personal issues. The kindness and co-operation of him would always be memorable throughout my life.

I would also like to express my gratitude to my co-supervisor Dr. Ulrike Dackermann who gave me great support in technical as well as academic writing matters. English is not my first language, and, therefore, I sometimes faced problems in academic writing. She always assisted very professionally with my writing and it was a pleasure working with her.

I am also very thankful to Dr. Ali Saleh, Dr. Emre Erkmen, Dr Behzad Fatahi and A./Prof. Hadi Khabbaz because of the time they spent with me for strengthening some of my fundamental concepts on structural analysis, numerical modelling and soil mechanics.

I would also like to thank my fellow students and colleagues, Saad Subhani, Roman Elsener and Bahram Jozi. Working together with you was a great pleasure for me since we were a real team in supporting and helping each other in many aspects of our work.

I cannot thank enough Dr Yang Yu for his patient and cordial support and spending lots of time with me for explaining some complicated concepts of the algorithms used in my research. I was always comfortable to work with him.

My parents and friends have made an invaluable contribution to the completion of my research. Many times during my PhD, I felt depressed when facing some difficult problems; however, I was always motivated and encouraged by them to complete my research work.

Finally, I would like to acknowledge the financial supports provided by the ARC linkage project (LP110200162) in conjunction with industrial partner Ausgrid for conducting my research. Also, the IRS scholarship offered by UTS provided me extensive support to accomplish my PhD goal.

Abstract

Timber utility poles are traditionally used for electricity and telecommunication distribution and represent a significant part of the infrastructure for electricity distribution and communication networks in Australia and New Zealand. Nearly 7 million timber poles are in service and about $40-$50 million is spent annually on their maintenance and asset management. To prevent the ageing poles from collapse, about 300,000 electricity poles are replaced in the Eastern States of Australia every year. However, up to 80% of the replaced poles are still in a very good condition (Nguyen et al., 2004). Therefore, huge natural resources and money is wasted. Accordingly, a reliable non-destructive evaluation technique is essential for the condition assessment of timber poles/piles to ensure public safety, operational efficiency and to reduce the maintenance cost.

Several non-destructive testing (NDT) methods based on stress wave propagation have been used in practice for the condition assessment of timber poles. However, stress wave propagation in timber poles especially with the effect of soil embedment coupled with unknown pole conditions below ground line (such as deterioration, moisture etc.) is complicated, and therefore it hindered the successful application of these NDT methods for damage identification of timber poles. Moreover, some stress wave based NDT methods are often based on over-simplified assumptions and thus fail to deliver reliable results.

In the presented study, in order to gain an in-depth understanding of the propagation of stress waves in damaged poles and to develop an effective damage detection method, a solid numerical study of wave behaviour is undertaken and novel wavelet packet energy (WPE) method is investigated for damage identification. Numerical studies utilises finite element (FE) models to track the wave propagation behaviour characteristics considering different boundary conditions, material properties as well as impact and sensing locations.

WPE is a sensitive indicator for structural damage and has been used for damage detection in various types of structures. This thesis presents a comprehensive investigation on the novel use of WPE for damage identification in timber utility poles

using FE models. The research study comprises several aspects of investigations such as a comparative study between 2D and 3D models, a sensitivity study of mesh density for 2D models, and a study of the novel WPE-based technique for damage classification and detection in timber poles. Support vector machine (SVM) is imported for damage classification and particle swarm optimisation (PSO) is selected to achieve the classification. The results clearly show the effectiveness of the proposed novel WPE based damage identification technique.

Damage prediction based on optimisation procedure is also carried out in this thesis. Several numerical models with different damage conditions are created and the damage size is predicted according to optimisation procedure based on information from sample damaged model. Genetic algorithm and artificial fish swarm algorithm are used as optimisation algorithms and the comparative study is conducted based on the prediction results.

The influence of damage on the strength of timber utility poles is also studied in this thesis. The damage conditions are changes in diameter, length as well as location. Wind is considered as a main reason to cause the collapse of timber utility poles in this research. Wind load is defined based on Australian standards and the Ausgrid manual, and the corresponding stress is calculated through FE analysis. According to this analysis, it can be found that under specific damage conditions, some small damage may cause collapse; however, for certain conditions, the timber poles can still be safe even when large damage exists.

In conclusion, a novel WPE based damage detection method has been successfully developed to address the limitations of existing methods for condition assessment of timber utility poles. The numerical verification has shown the method is effective for identification of the classification and severity of damage.

List of Publications Based on This Research

Refereed Conference Papers

1. N. Yan, J. Li, U. Dackermann and B. Samali, (2012), 'Numerical and Experimental Investigations of Stress Wave Propagation in Utility Poles under Soil Influence', *Proceedings of 22nd Australasian Conference on the Mechanics of Structures and Material,* 11–14 December2012, University of Technology Sydney, Australia.
2. N. Yan, U. Dackermann, J. Li and B. Samali, (2013), 'Numerical Investigations of Stress Wave Behaviour in Timber Utility Poles', *Proceedings of 6st International Conference on Structural Health Monitoring of Intelligent Infrastructure,* 9-11 December 2013, Hongkong, China.
3. N. Yan, J.C. Li, U. Dackermann and B. Samali, (2014), 'A Numerical Investigation on the Damage Identification of Timber Utility Poles Based on Wavelet Packet Energy', *Proceedings of 23rd Australasian Conference on the Mechanics of Structures and Materials,* 9-12 December 2014, Byron Bay, Australia.

Refereed Journal Papers

4. M. Subhani, J. Li, B. Samali and N. Yan (2013), 'Determination of the embedded lengths of electricity timber poles utilising flexural wave generated from impacts', *Australian Journal of Structural Engineering*, vol. 14, no. 1, pp. 85.

Content

List of Figures

List of Tables

Nomenclature

Error! Not a valid link.

β	velocity adjustment factor
ε	elastic strain vector
γ	shear strain vector
σ	stress vector
ν	Poison's ratio
$\{\varepsilon\}$	strain tensor
$\{\sigma\}$	stress tensor
$[C]_{orth}$	orthotropic elastic matrix
u_r	displacement components along radial direction
u_θ	displacement components along tangential direction
u_z	displacement components along longitudinal direction
k	wavenumber
ω	angular frequency
c_0	wave speed
c	phase velocity
$\varphi(t)$	mother wavelet
$x[n]$	original signal
g(k)	group-conjugated orthogonal filters
h(k)	group-conjugated orthogonal filters
$C_{j,k}^i$	wavelet packet coefficients
f_j^i	component signal in a WP tree
2D	two-dimensional
3D	three-dimensional
ASFA	artificial fish swarm algorithm
BEM	boundary element method
BW	Bending Wave method
CWT	continuous wavelet transform
Dav	average diameter of the pole
DEC	difference of each energy component among the sensors
DOF	degree of freedom
DWT	discrete wavelet transform
E	elastic modulus
$E_{f_j^i}$	component energy of the decomposed signal
EF	parameter of the energy feature
E_{Di}	total WP energy under the damaged conditions
E_{Si}	total WP energy under the intact condition
F	measured frequency interval
FDM	finite difference method

FE	finite element
FEA	finite element analysis
FEM	Finite element method
FFT	Fast Fourier Transform
FF	parameter of the frequency feature
FT	tip strength of a pole
f_{Di}	frequency of the corresponding mode under damaged conditions
f_{Si}	frequency of the corresponding mode under intact conditions
FRF	Frequency Response Function
G	shear modulus
GA	genetic algorithm
GW	guided wave
IR	impulse response method
L (for timber material)	longitudinal direction
L	Length of the pole
Ld	length of pole in the dry zone
L_T	length between the location of the sensor and the bottom of a pole or the location of a defect
Lw	length of a pole in the wet zone
LCR	rate of the maximum load capacity
NDT	non-destructive testing
OAO	multi-class classification using SVM: one-against-one
OAR	multi-class classification using SVM: one-against-the rest
PSO	particle swarm optimization
R (for timber material)	radius direction
R	cross-correlation coefficients
SE	sonic echo method
SEM	spectral element method
SVM	support vector machines
T	time difference between the first arrival event and the first reflection event of stress wave
T (for direction)	tangential direction
US	Ultraseismic method
V	velocity of the longitudinal wave
Vd	wave velocity of the dry wood
Vw	wave velocity of the wet wood
WP	wavelet packet
WPT	wavelet packet transform

1 Introduction

This chapter starts with the background of the project and then provides the rationale for the research to be conducted. The research aim and objectives are identified and the organisation of this thesis is demonstrated at the end of this chapter.

1.1 BACKGROUND

Utility poles made of timber are traditionally used all over the world as they are relatively low cost and environmentally friendly. Especially in Australia, timber utility poles represent a significant part of the country's infrastructure for power distribution and communication networks. There are nearly 7 million timber poles in the current network in Australia, and among them, 5 million poles are used for power and communication supplies (Nguyen et al., 2004). The nationwide demand for timber power poles was approximately 62,000 in 2004 and 75,000 in 2006 (Lesley and Jack, 2006).

Failure of timber utility poles can cause serious loss of life and economic cost. A number of fatalities have been reported where poles failed while line workers were performing operations on the poles. It is also reported that some bush fires have been caused by failure of timber poles. Failure of poles also leads to loss of power and possibly other functional facilities supporting daily life (Baraneedaran et al., 2009).

To carry out routine inspection on poles to assess the structural integrity, $40-$50 million is spent annually on maintenance and asset management to prevent utility lines failure. The lack of reliable tools for assessing the condition of in-situ poles seriously

jeopardizes the maintenance and asset management. For example, in the Eastern States of Australia, about 300,000 electricity poles are replaced every year. However, up to 80% of them are still in a very good serviceable condition, causing a large waste of natural resources and money (Nguyen et al., 2004).

To address the needs of the utility pole asset management industry, a cost-effective and reliable non-destructive testing (NDT) method needs to be developed that is able to identify and separate healthy from unhealthy poles. In the last 20 years, various NDT techniques have been developed to evaluate the conditions and integrity of pile/foundation structures. Among those methods/techniques, visual inspection, sounding and stress wave methods remain the most widely used techniques in practice (Tanasoiu et al., 2002). Visual inspection is undoubtedly one of the oldest methods used in practice but suffers a major drawback on reliability and accuracy of its results since the method relies on the experience of the operator and accessibility of the structure. Stress wave methods, on the other hand, can offer simple and cost-effective tools for identifying the in-service condition as well as the embedment length of timber poles/piles. However, due to the lack of understanding of stress wave propagation in pole structures, especially with the effect of soil embedment coupled with unknown pole conditions below ground line (such as deterioration, rot, termite attack), the results rely heavily on experience and interpretations from individual operators. Another issue influencing the testing accuracy is related to the complexity of the timber material with anisotropy, non-homogeneity and many uncertainties on material properties. As a matter of fact, the material properties of timber can be affected heavily by environmental factors such as temperature and moisture changes. As a result, current stress wave NDT methods often fail to produce reliable results, which are vital for the utility pole management industry.

In order to address this pressing and critical issue, an industry supported research project, involving three PhD students and one Master student, started in 2011 with the aim of developing a reliable non-destructive assessment method for timber utility poles based on stress wave techniques. Research students assigned to the project worked in four different areas to tackle the problem: firstly, stress wave theory study for pole structures including wavelet analysis; secondly, finite element analysis to investigate ideal wave propagation behaviour in simulated pole structures; thirdly, data post

processing and data fusion for numerical and experimental results; and fourthly, laboratory and field work to verify stress wave propagation characteristics in timber poles and to determine material properties of timber using static and dynamic testing approaches.

To study wave behaviour in depth, numerical studies needed to be undertaken to understand the wave propagation in timber poles, and this is the main focus of this PhD research, which is numerical investigation of stress wave propagation in timber poles considering effects of soil embedment such as in-situ timber pole conditions. Finite element analysis (FEA) has become commonplace in recent years for the simulation of complex real-life structural interactions. It typically involves the generation of a computer model of a structure that is stressed and analysed for specific results. Much software has been developed to assist engineers, analysts and designers to perform simulations, calculations and design. In this study, the commercial finite element analysis software ANSYS is the main tool used.

1.2 RATIONALE FOR THE RESEARCH STUDY

Based on the literature review (Chapter 2), the following challenges in this research were identified:

- Limited research on numerical simulation of wave propagation in timber utility poles
- Limited research on wave behaviour in utility poles influenced by soil
- Limited research on effective and reliable damage detection methods for timber utility poles utilising wave patterns of utility poles
- Limited research on strength prediction of timber utility poles under different damage scenarios

From the research challenges mentioned above, it can be noticed that the research on stress wave propagation behaviour and damage detection for timber utility poles is seen to be limited. The main contribution of this research includes providing numerical investigations of wave propagation in timber poles as well as proposing a novel theoretical damage detection technique based on wavelet packet energy analysis. The

findings provide a sound platform for development of a practical and cost effective assessment technique for in-situ timber utility poles.

1.3 RESEARCH AIM AND OBJECTIVES

The main aim of this research is to numerically investigate the wave behaviour in embedded timber utility poles (for both damaged and undamaged cases) in order to gain an insight into the wave propagation in the pole and, therefore, to develop a novel approach to produce reliable and precise assessments of the condition and embedment length of utility poles in the presence of uncertainties. Comprehensive numerical and experimental studies will be undertaken to investigate stress wave propagation in utility poles under special consideration of uncertainties such as complex material properties (for example direction of annual growth rings in timber or inhomogeneous characteristics), environmental conditions (for example temperature or humidity fluctuations), soil conditions (for example density, soil composition or moisture content), and damage or defects (for example voids, fungi decay or termite attack). For the numerical investigation, finite element analysis techniques will be utilised to model the complex nature of stress wave travel. Laboratory testing will be conducted in parallel with the numerical studies to experimentally verify the numerical models. Accordingly, numerical optimisation techniques will be used to classify the damage types as well as estimate the damage severity. The findings of the research will then be used to assist development of state-of-the-art NDT and analysis methods for the condition and length assessment of utility poles utilising the latest developments in the field including advanced signal processing and dynamic feature extraction. The specific objectives of the research are:

- FE modelling of timber material as an isotropic/orthotropic material (probabilistic FE modelling could also be considered)
- Modelling of stress wave interaction between timber pole and soil
- Modelling timber defects, deterioration and damage and investigation of damage signatures/patterns from wave propagation
- Identification of aforementioned damage by using optimisation techniques
- Possible residual life prediction for timber poles

1.4 ORGANIZATION OF THE THESIS

In Chapter 1, a general overview of the research work is presented including the background, research objectives and the significance of the research.

In Chapter 2, the state-of-the-art in NDT methods are outlined first and stress wave theory based NDT methods are briefly introduced. The numerical modelling of timber poles and soil as well as damage detection methods are reviewed extensively.

In Chapter 3, numerical investigation of stress wave propagation in simulated timber poles are presented. Parametric study and model verification is undertaken. Wave behaviour is studied under different boundary conditions and material characteristics.

In Chapter 4, a novel damage detection technique based on numerical results is proposed including damage classification and damage severity identification. Wavelet packet energy technique is briefly introduced.

In Chapter 5, damage prediction is conducted according to an optimisation technique. Two well-known algorithms are imported to estimate the damage severity based on the known parameters. The accuracy of the prediction results are outlined and compared.

In Chapter 6, loading capacities for damaged timber utility poles are analysed using numerical models. The loading is considered to be wind load based on the corresponding Australian standards (AS/NZS1170.2) and the Ausgrid manual (NS220).

In Chapter 7, a summary of the research work and recommendations for future work are provided.

2 Literature review

2.1 INTRODUCTION

This literature review includes some of the most significant works regarding the numerical modelling of embedded timber poles and the development of non-destructive damage detection methods in civil engineering applications. Some works which have been reported by other researchers forms the platform upon which the research work offered in this thesis is based.

This chapter starts with the traditional NDT methods for pile/pole structures. This is followed by a review of numerical modelling of embedded timber poles including modelling of timber material as well as soil. Damage types in timber poles are briefly introduced before reviewing damage detection methods. Some traditional damage detection methods are introduced and WPT based damage detection is reviewed extensively. Further to this, optimisation techniques with two relevant algorithms for damage detection are explored.

2.2 OVERVIEW OF TRADITIONAL NON-DESTRUCTIVE TESTING METHODS FOR POLES/PILES

Modern structural health monitoring (SHM) methods can be classified into two groups, the global methods well known as vibration based methods and local methods which include guided wave (GW) based methods (Raghavan and Cesnik, 2007). Local GW based methods, according to their features, are normally used in the condition that the potential damage location is known (Uhl et al., 2013). Both global methods and local methods are widely used in non-destructive testing (NDT) to assess the conditions of

structures. NDT is the means by which structures may be inspected without destruction of serviceability (Alvandia and Cremona, 2006).

The damage identification can be divided into four levels (Rytter, 1994) as shown in Figure 2-1.

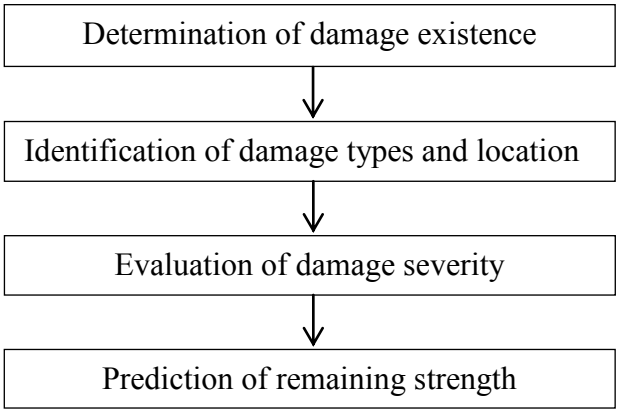

Figure 2-1 levels of damage detection

Non-destructive testing (NDT) methods are used in the field of civil engineering to assess the health state of civil infrastructures. Over the years, numerous specialised methods have been developed and have successfully been applied in practice.

Current NDT techniques for civil infrastructures rely on visual inspection, acoustics, ultrasound, magnetic fields, radiography or X-rays. These techniques are local methods and require that the damaged region is known a priori, and usual inspection techniques require the portion of the structure being inspected to be readily accessible and are, therefore, not appropriate due to interference with operational conditions (Doebling et al., 1998).

To assess the integrity of poles/piles, the most practised methods are visual inspection, sounding and stress wave methods. Among these methods, visual inspection and sounding are the most commonly used techniques. They are, however, highly subjective and greatly depend on the experience of the practitioner. Further, they cannot always detect decayed parts of timber, especially when these are located underground (Tanasoiu et al., 2002). In Australia, drilling is a normal method using visual examination and sounding to assess the condition of a pole between the ground line and 350mm below ground as shown in Figure 2-2 (Ausgrid, 2006). Drilling assessment is

based on the sound, smell and resistance where the drilling is taking place. All these features will indicate the condition of the timber and then justify whether it is sound or decayed timber. The limitations are: location has to be accessible for the drilling and the results are subjective depending on personal observations (Baraneedaran et al., 2009).

Figure 2-2 Inspection below ground line (Ausgrid, 2006)

Other advanced methods that are applied to examine the integrity of timber poles/piles are, for instance, radiographic methods, X-ray techniques, force application and ultrasonic tomography. The use of these advanced methods is currently very limited due to their high cost, complex operation and often poor and inconsistent results (Tanasoiu et al., 2002).

Stress wave methods, on the other hand, are considered as simple and cost-effective applications and a number of stress-wave based techniques have primarily been developed for the condition assessment of deep foundations. They are popular NDT methods and include sonic and ultrasonic techniques. Stress waves occur in a structure when sudden pressure or deformation is applied to its surface such as by impact excitation. The disturbance propagates through the structure in a manner analogous to how sound travels through air. The speed of stress wave propagation is a function of the modulus of elasticity, Poisson's ratio, the density, and the geometry of the structure (American Concrete Institute, 1998). Due to these dependencies, monitoring and analysis of stress wave propagation can be used to assess the condition of structures.

Over the past decades, the state-of-the-art for stress wave based NDT assessment of unknown foundation conditions mainly involved two methods: surface wave methods, where access is required only at the surface of the test structure, and borehole wave methods, where a borehole is drilled close to the test structure and wave reflections are monitored from the borehole. These methods were found to be able to accurately determine the unknown depths of exposed piles, drilled shafts, shallow abutments and piers. For field testing, however, the methods have a number of limitations. For example, it was found that traditional stress wave based NDT methods cannot detect the depth of foundations with underlying pile caps (Larry et al., 1998).

In general, surface wave methods can be categorised by the type of wave they analyse. In surface wave testing, the disturbance caused by impact excitation propagates through the structure as three different waves, they are: longitudinal, flexural and Rayleigh waves. Longitudinal and flexural waves are body waves and propagate into the structure along hemispherical wavefronts, while the Rayleigh wave travels away from the disturbance along the surface. The longitudinal wave, also called P-wave, compression or dilatational wave, is associated with the propagation of normal stress and particle motion is parallel to the propagation direction (see Figure 2-3 (a)). The flexural wave is related to shear stress and particle motion is perpendicular to the propagation direction (see Figure 2-3 (b)). The Rayleigh wave, also called R-wave, travels across surfaces and moves in ellipses in planes normal to the surface and parallel to the direction of propagation (see Figure 2-3 (c)) (Davis, 1998).

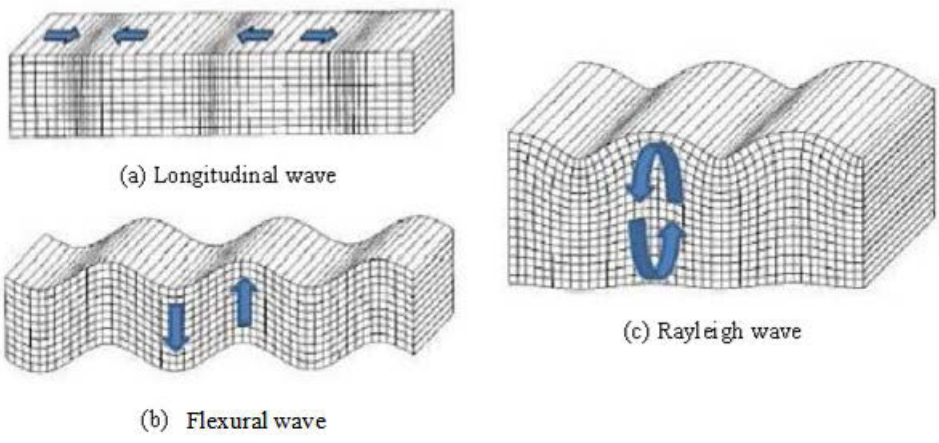

Figure 2-3 Different types of stress waves (ParkSeismic, 2012)

The most popular surface stress wave techniques used for the assessment of pile and foundation structures are: Sonic Echo method (Ni et al., 2006), Impulse Response method (Davis et al., 2005), Bending Wave method (Linjama, 1992), Ultraseismic method (Jalinoos et al., 1996) and Impact Echo method (Carino, 2001).

Due to the successful applications and positive results of surface methods to pile and foundation structures as well as their limitations and challenges, surface stress wave techniques are found to be quite suitable to detect the depth and service condition of free standing timber utility poles such as those investigated in this study. To give more detailed background information, the most popular surface stress wave methods are briefly described in the following section.

2.2.1 Sonic Echo/Impulse Response method

In SE/IR testing, an impact is imparted from the top of a pile/pole structure (generating longitudinal waves) and reflection measurements (echoes) from the bottom of the structure are evaluated to assess the condition/determine the length of the structure. The SE method (also known as Echo, Seismic Echo, Sonic, Impulse Echo, Pulse Echo method and Pile Integrity Test), is the earliest of all stress wave NDT methods to become commercially available (Steinbach and Vey, 1975). It was first developed for quality assurance of the integrity and length of driven piles of new constructions (Rausche et al., 1992). The Impulse Response (IR) method (termed also as Sonic Transient Response, Mobility, Transient Dynamic Response and Sonic method) was developed as an extension to a technique originally proposed by Davis and Dunn (Davis and Dunn, 1974).

The basic theory of both methods is that stress wave patterns and associated frequency domain data will change when stress waves propagate through different stiffness media (the bottom of a structure or defects/damage) according to the impedance function. The testing is performed by impacting the top of a pile foundation to generate longitudinal waves, which travel down to the bottom of the pile (see Figure 2-4 (a)). The wave will be reflected back from changes in stiffness, cross-sectional area and density. A crack or hollow section will have lower impedance, while rotten timber material, stiffer soil or bedrock layer will have higher impedance (Larry et al., 1998). The reflected longitudinal wave is recorded by a sensor, which is placed on top of the structure in

proximity to the impact location. For timber utility poles, the average diameter of a pole is around 300mm and the sensors have to be placed along the side of the pole to avoid the influence of the surface wave (see Figure 2-4(b)).

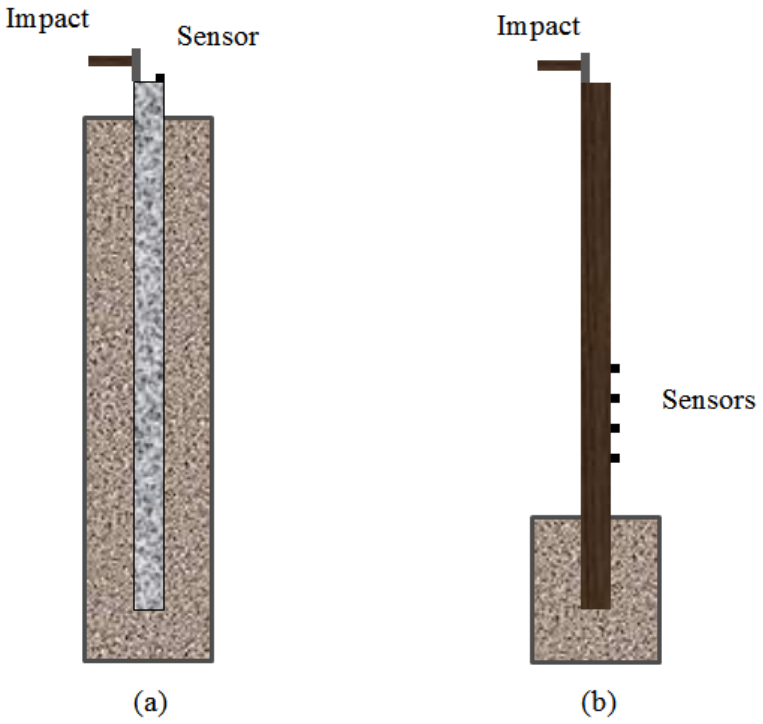

Figure 2-4 SE/IR testing applied to (a) a pile and (b) a timber utility pole

For the SE method, the length of a pile/pole structure can be calculated based on the time separation between the first wave arrival and the first wave reflection (echo) event or between any two consecutive reflection events according to the following equation:

$$L_t = \frac{\beta \times V \times T}{2} \qquad \text{Eq. 2-1}$$

where L_t is the length between the location of the sensor and the bottom of the pole or location of a defect; V is the velocity of the longitudinal wave; T is the time difference between the first arrival event and the first reflection event recorded by the sensor. β is a velocity adjustment factor and is normally set to 0.9 (Pandey and Anthony, 2005).

As the frequency domain counterpart of the SE method, the IR method transfers the measured time history data into the frequency domain by Fast Fourier Transform (FFT). The length of the pole can be estimated by:

$$L_t = \frac{\beta \times V}{2 \times F} \quad \text{Eq. 2-2}$$

where F is the measured frequency interval between two consecutive resonant frequency peaks of the pole; it is the inverse of T.

In timber, the velocity of the stress wave is affected by the moisture content in the wood. A typical timber pole in service contains a dry zone (above the ground), a saturated zone (below the ground), and a transient zone (an increasing amount of moisture). Therefore, the formula to estimate the length using measured data is modified to:

$$L_t = L_d + L_w = L_d + \left(\frac{\beta \times V_w}{2 \times F} \right) - \frac{V_w}{V_d} \times L_d \quad \text{Eq. 2-3}$$

where L_d is the length of pole in the dry zone, L_w is the length of pole in the wet zone, V_d is the wave velocity of the dry wood, and V_w is the wave velocity of the wet wood (Pandey and Anthony, 2005).

Texas A&M University (Briaud, 1997) conducted a series of comparative NDT testing on nine bored piles using the SE/IR method. The piles were tested at the National Geotechnical Experimental Sites at Texas A&M University with five piles being embedded in sand and four piles in clay. Five companies were invited to conduct the SE/IR testing. The condition and the length were not revealed to the testing companies and the results were obtained directly after the site testing. The comparison between length predictions and actual feature led to the following findings. Firstly, the length prediction will not be accurate when two damages are present in a pile. Secondly, the accuracy of the result heavily relies on the operators' experience. For defects detection, the comparison of the results also revealed some significant issues. Firstly, as mentioned the experience of the engineer plays an important role in the testing and the interpretation of the measurement results. Secondly, the size and location of the defect will affect the accuracy of the testing. Thirdly, the stiffness of the soil surrounding the pile will influence the results.

Federal Lands Highway Administration (Larry et al., 1998) tested several foundation piles of bridges. After collecting the data the researchers found that the SE/IR method works best for piles or drilled shafts without any structure on top. Typically, this

method is performed on piles for ratios of length-to-diameter (L/D) up to 20:1 and can only detect large damage with cross-sectional area changes greater than 5%. For higher L/D ratios of 30:1 or larger, the method is applicable for softer soils. A study conducted by the University of Houston at the National Geotechnical Experimentation Site also found that for a pile L/D ratio of less than 20, the pile length can be predicted more accurately and the success rate can reach at least 80%. If the L/D rate increases to 30, the success rate will decrease rapidly.

2.2.2 Ultraseismic method

The Ultraseismic (US) method is an extension of the SE/IR method (for longitudinal waves) and the BW method (for flexural waves). The method was developed as a response to overcome the difficulties with the SE/IR and BW methods when many reflecting boundaries are present (Olson and Aouad, 2001). The US method is used to predict the integrity and the length of foundation structures based on multi-channel seismic reflections. The method was developed for its application to drilled shafts, driven piles and shallow wall-shaped substructures with at least 1.5 m–1.8 m of the side of the structural element exposed for mounting instrumentation (Olson, 2014). Traditionally, several accelerometers with 15 cm–30 cm intervals are mounted on the side of the testing specimen. An impulse hammer is used as the source to generate stress waves (see Figure 2-5).

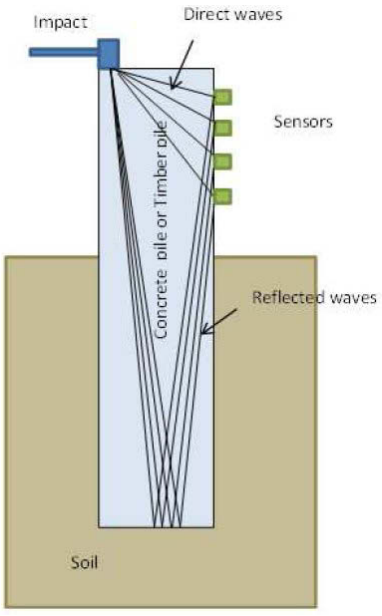

Figure 2-5 US testing of a pile

Three types of waves including longitudinal waves, flexural and Rayleigh waves can be recorded. Each type of wave will provide vital information on poles/piles for depth and defects prediction. Reflected wave forms from the pile/foundation bottom are identified and the effects of undesired wave reflections from other boundaries are minimized. Information on the initial arrival and reflection of waves are captured by multiple accelerometers, and after data processing, a stacked record of measured data of all sensors will be provided. In the stacked record, the slope lines of arrival wave and reflected wave are connected, and the length or the location of the defect can be predicted (see Figure 2-6).

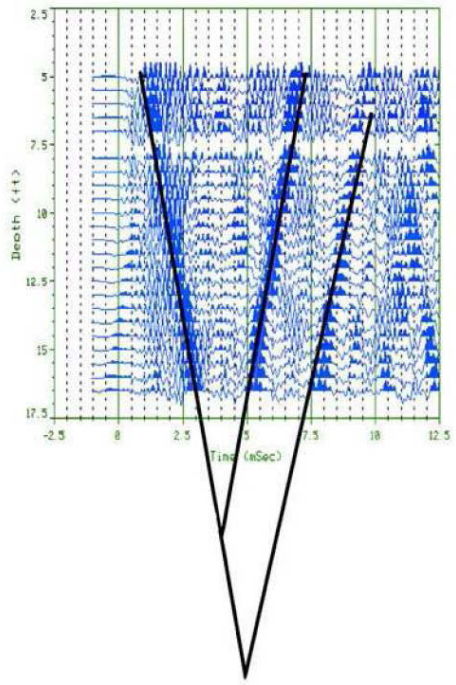

Figure 2-6 Stacked record of US testing (Olson, 2014)

According to the Federal Lands Highway Administration report in 1998, the US method was found to be able to provide much more accurate depth prediction than the SE/IR method under complex substructure condition. Research undertaken at the Chao Yang University of Technology in Taiwan found that the error to predict the depth of intact piles using the US method is within a range of 5% (Wang, 2003).

Despite the widespread use of stress-wave based NDT methods such as the SE/IR, BW and US method, for their application to pile and foundation structures, the transfer of these techniques to the condition assessment of free-standing timber utility poles is not

straight forward due to the inaccessibility of the top of the pole structure, the complexity of material property, geotechnical conditions and interaction behaviour between pole and soil. To gain an insight into the complex stress wave propagation in free-standing timber pole structures, numerical investigations with extensive studies on the wave behaviour in timber utility poles are essential to the successful development of a stress-wave based condition assessment technique for timber utility poles. Timber utility poles have different material characteristics as well as boundary conditions than piles. Hence, a study of the wave propagation behaviour in timber poles is needed in this research.

2.3 NUMERICAL MODELLING OF EMBEDDED TIMBER POLES

2.3.1 Introduction to numerical modelling

Many practical engineering problems are too complicated to be solved accurately by classical analytical methods. To deal with the problems, numerical modelling methods are imported. Finite element method (FEM), finite difference method (FDM), boundary element method (BEM) and spectral element method (SEM) are always considered in numerical analysis of wave propagation (Wang, 2009).

The first step of numerical analysis is discretisation which means dividing the medium of interest into a number of small subregions and nodes (Moaveni, 1999). FDM, using a differential equation for each node and replacing the derivatives by difference equations, is suitable for simple geometries and boundary conditions as well as simple material properties (Moaveni, 1999). BEM solving partial differential equations (Kirkup, 1998) for nodes is an effective method to simulate an infinite medium but has limitations in dealing with scattering problem in a finite medium (Wang, 2009).

SEM is considered an effective numerical method especially in wave propagation studies and is adopted by many researchers. SEM obtains accurate results with less computational time. However, it has serious drawbacks to limit its application such as:

- Exact shape functions are available only for relatively simple systems (this usually is a problem for multi-dimensional systems). Approximate methods may be used if accuracy decreases.
- The method cannot be applied directly to time variant, nonlinear systems

- The solution involves inverse time and deteriorates the solution quality (Stepinski et al., 2013).

The FEM (its practical application often known as finite element analysis that is FEA) is one of the most widely used methods to deal with complicated problems such as dynamic and nonlinear problems, for example impacts or blasts. Due to the characteristics of FEM, this method (can potentially) provide a solution for any geometry, as long as this geometry and its boundary conditions can be modelled. ANSYS is a very powerful and impressive FEA tool and can be widely used to solve various engineering problems.

A finite element analysis basically involves the following steps (Cook et al., 1989):

1. Discretise the structure or continuum into finite elements using a mesh generation program.
2. Formulate the physical behaviour of an element by assuming an approximate continuous function to represent allowable element deformation.
3. Assemble elements to obtain an FE model and construct the global stiffness matrix.
4. Apply boundary conditions and loads.
5. Solve linear or nonlinear algebraic equations to obtain nodal results such as displacement or temperature value for each node.

Moser and his team used FEM to model guided wave propagating in annular structures. The FE results were directly compared to an analytical solution as well as experimental results. All these comparisons confirm the high accuracy of FE solutions when applied to wave propagation problems (Moser et al., 1999). Bartoli and his colleagues applied FE analysis to simulate ultrasonic guided waves in rails to detect the defects. They found finite element modelling is an essential tool to predict the wave interactions with a variety of defects that would be impractical to replicate experimentally (Bartoli et al., 2005). Cerniglia and his colleagues studied ultrasonic wave propagation in multi-layered plates under intact and damaged conditions through finite element analysis. The numerical results matched with experimental results very well. They found that FEA was a powerful tool to obtain a better understanding of the wave propagation and interference phenomena (Cerniglia et al., 2010).

In this current research, the FEA software ANSYS was used to perform transient analysis to model timber poles and to investigate wave propagation behaviour. The material parameters of the poles were obtained from laboratory experimental testing undertaken by another PhD student of this project as well as some relevant literatures.

2.3.2 Numerical modelling of timber material

Timber is a natural composite material with anisotropic and inhomogeneous characteristics. The mechanical behaviour is complicated and the mechanics performance shows high nonlinear behaviour. Due to the lack of understanding of the nonlinear behaviour of wood, it is sometimes simulated as a homogeneous and isotropic material. However, the results will not be able to illustrate the real mechanics performance (Li, 2007).

Over the years, timber-based composite materials, such as timber composite beams, have been developed. These reconstituted materials are more homogeneous than raw wood and usually have been seen as orthotropic materials (Serrano, 2000). Research on timber-based composite materials is typically focused on the strength testing to determine the fatigue fracture parameters. In most research, timbers are normally simulated as orthotropic linear elastic materials in tension, and as orthotropic elasto-plastic materials in compression.

For analysing the failure and fatigue behaviour of timber structures, such as timber composite beams, it is well recognised that it is necessary to model timber as an orthotropic material (Serrano, 2000) with elastic-plastic behaviour (bilinear curve) based on Hill's criterion (Junior and Molina, 2010) (Figure 2-7).

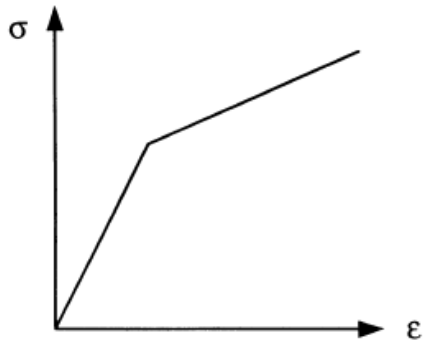

Figure 2-7 Stress-strain curve used to simulate the material behaviour of timber (Junior and Molina, 2010)

To establish a constitutive model for timber material, several models have been used by researchers to simulate the behaviour of timber poles:

1. Idealised isotropic and homogeneous continuum model,
2. Orthotropic and homogeneous continuum model,
3. Transversely isotropic (identical properties in tangential and radial directions) and homogeneous continuum model (Murray, 2007)

In the development of the material model of a timber pole, several assumptions are made as follows (Tabiei and Wu, 2000):

1. Wood is idealized as an orthotropic material instead of anisotropic material.
2. Wood is idealized as a homogeneous continuum.
3. Wood is intact with no growth defects.
4. Wood grain is oriented straight and parallel to the long axis of the timber pole.

Piao (Piao et al., 2005) developed finite element models to predict the performance of the uniform-diameter composite poles subjected to loads. Five orthotropic models created by ANSYS have been developed and verified with experimental results. Three-dimensional (3D) 10-node tetrahedral solid element is used in the modelling of wood laminated composite poles. This element type has a nonlinear displacement behaviour, plasticity, large deflection, and large strain capabilities. The predicted deflection by these models agreed well with those of the experiment, and the predicted normal stress agreed with those calculated. Pellicane and Franco used 3D finite element models to investigate the stress distribution and failure of wood poles subjected to cantilever

bending. Orthotropic and isotropic models with linear-elastic material properties were established and verified with theoretical results. They came to the conclusion that orthotropic models are more sensitive to support conditions influencing the bending stress distribution near the boundary (Pellicane and Franco, 1994). Bulleit and Falk developed an isotropic model to investigate the use of stress wave velocity measurements to distinguish between strength-reducing decay and non-strength-reducing growth ring separations (ringshake). The results from the field test and finite element analysis indicated that the stress wave velocity measurements alone were not sufficient to confidently differentiate between ringshake and decay (Bulleit and Falk, 1985).

2.3.3 Numerical modelling of soil

Modelling of soil

Soil is a complicated material and is composed of particles with various mineralogy, size and shape and as a consequence, the mechanical properties are complex (Airey et al., 2011). The detail of soil behaviour is discussed by Brinkgreve (Brinkgreve, 2005). Classical soil mechanics makes use of an idealised stress strain curve to simulate soil behaviour. In Figure 2-8, the curve OXY presents the typical shear stress and shear strain relationship of soil. Under working loads, the stress/strain behaviour is linear and elastic, which is presented as OA. The complete failure of soil with large deformation can be seen as perfectly plastic and is presented by OBC (Wood, 1990).

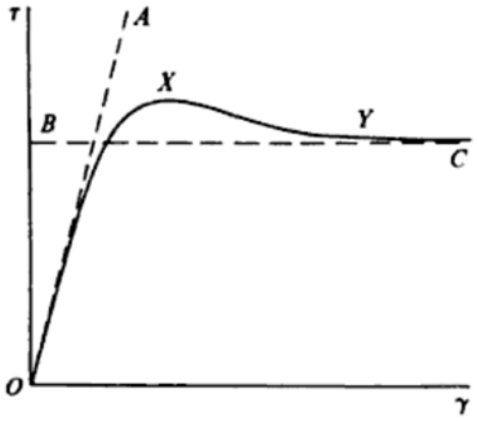

Figure 2-8 Shear stress strain curve for soil (Wood, 1990)

In general, the consideration for the soil modelling should always involve a balance between the requirements from the soil mechanics properties, reality of soil behaviour

from the laboratory testing and the effectiveness in computational application (Ti et al., 2009).

Several constitutive models are widely used in numerical analysis of geo-materials, such as linear elastic, nonlinear elastic or elasto-plastic. The Duncan-Chang model also known as the hyperbolic model (Duncan and Chang, 1970) is a nonlinear elastic model. This type of model is not widely accepted since it cannot consistently distinguish between loading and unloading (Schanz et al., 1999). Mohr-Coulomb model, which is an elasto-plastic model and always used to simulate general soil behaviour, provides a better representation for wave propagation problem (Balendra, 2005). Drucker-Prager model (Drucker and Prager, 1952) is the simplification of the Mohr-Coulomb model. The Modified Cam-clay is an elastic plastic strain hardening model and suitable for describing the deformation of the consolidated soft soils (Ti et al., 2009).

Soil modelling plays an essential part in pile testing research. High strain testing of piles is typically performed to evaluate the driving system for assessing the static or bearing capacity. For this kind of testing, soil behaviour is always considered as elasto-plastic and simulated by the Mohr-Coulomb model to describe the stability of foundation structures. Abdel-Rahman and Achmus created numerical models to simulate the pile foundations embedded in sand. An elasto-plastic model with Mohr-Coulomb failure criterion was used to illustrate the behaviour of medium dense sand when the piles are under an inclined load (Abdel-Rahman and Achmus, 2006). Kwon et al. used a Mohr-Coulomb elasto-plastic model to describe soil behaviour and pile foundation stability when a strong earthquake happened (Kwon et al., 2013). Low strain methods are used for the integrity assessment and length prediction of piles. For a very low strain level (less than 10^{-5}), elastic and linear behaviour is present (Luna and Jadi, 2000). As a result, soil can be simulated as linear elastic, which provides the most basic soil behaviour without considering the nonlinear and plastic behaviour at failure. Chow and his fellow researchers used a linear elastic model to describe the soil behaviour under integrity testing (Chow et al., 2003). In this current research, low strain testing was conducted and the strain level was less than 10^{-5}. Hence, the material constitutive in this research will be simulated as linear elastic.

Modelling of soil-pole interaction

Over the last 40 years, research in dynamic Soil-Structure Interaction (SSI) has attracted intensive interest among researchers and engineers in the fields of structural dynamics, wave mechanics and soil dynamics (Li et al., 2004). The interaction behaviour between contact surfaces is critical if a dynamic load is generated, particularly if there is a significant difference in stiffness between the different media or if the potential for slip or separation exists. The response of the compound system is highly dependent on the interface behaviour (Drumm et al., 2000). A three dimensional model under dynamic load is more important to understand the overall structure's behaviour (Dutta and Roy, 2002).

Many researchers have proposed improved laws for the modelling of contact problems and various models have been proposed to represent "discrete" interface. Among the early models, Goodman, Taylor and Brekke (Goodman et al., 1968) explored the idea of linkage element and derived the stiffness matrix for a more general joint element to model the behaviour of jointed rocks. Figure 2-9 displays the interface modelling of a simple one-dimensional line element with zero thickness. In this model, the constitutive relation matrix is presented by the joints stiffness per unit length in the normal and tangential directions. Thin layer interface element (Desai et al., 1984) was developed to demonstrate the soil-structure behaviour under a seismic or blast load. It considered the deformation at interface including stick, slip, de-bonding and re-bonding. Some researchers (Wu and Finn, 1997, Cai et al., 2000) developed 3D finite element models to investigate the response of the pile-soil system under a seismic load.

Several experimental investigations have been undertaken on the soil-structure interface behaviour, and it was found that the principal factors affecting the interface behaviour include the roughness of the contact body, the mineralogical and grading characteristics of soil, the soil density, and the normal pressure. Among these factors, the roughness of the contact body is the most critical one (Liu et al., 2006).

For soil-pile interaction, interfaces are commonly simulated in two ways; perfectly bonded interface or frictional interface. The frictional interface allows slipping and gapping between the soil and the pile, which represents the real behaviour more accurately and Coulomb's friction model is used to simulate slipping and gapping in FEA. However, it takes more computational time and computer resource. Hence, if

slipping and gapping is negligible or will not influence the analysis results, perfect bonding using the coupling method can be applied (Balendra, 2005).

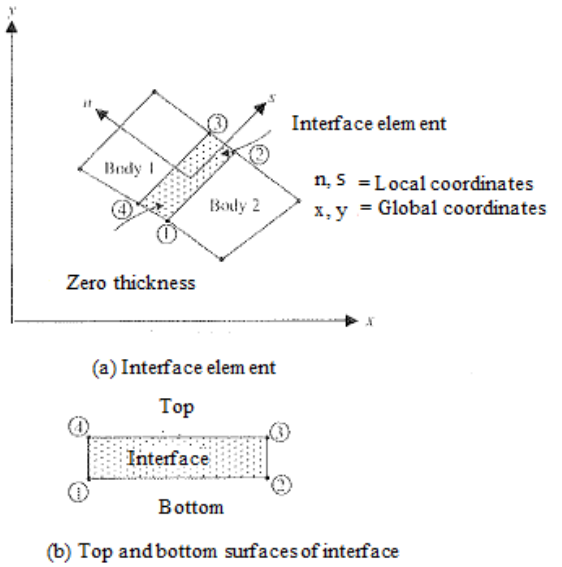

Figure 2-9 Interface element with zero thickness (Drumm et al., 2000)

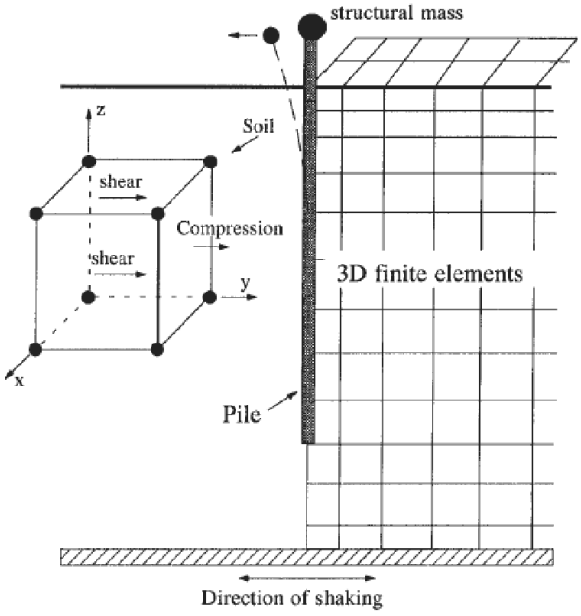

Figure 2-10 3-D model of pile-soil response (Wu, 1994)

For early research on pile-soil structure interaction, most of the studies have been done for the purpose of earthquake-resistant design (see Figure 2-10). In this specific field, the plastic deformations of the soil are represented by a series of non-linear springs. For the field study of pile integrity testing, the soil is always considered as a linear elastic material and the slip effect between pile and soil can be neglected (Schauer and Langer,

2012). In commercial FEA software ANSYS, the modelling of interaction behaviour can be achieved by contact analysis considering different contact conditions. Ji and Wang used surface contact element in ANSYS to simulate the integrity testing of a wharf pile based on one-dimensional stress wave theory. The results from numerical models matched with testing results quite well and the defects of the wharf piles could be detected accurately. The dynamic response of wharf piles caused by pulse load can be accurately simulated by ANSYS (Ji and Wang, 2010). Interface elements (contact pairs) in ABAQUS (a FEA software) was selected by Miao (Miao et al., 2007) to investigate the response of a single pile when subjected to lateral soil movements. These elements were allowed to separate if there was tension across the interface and the shear and normal force are set to zero once a gap is formed. The contact pairs in ANSYS have the same features as the interface elements in ABAQUS. Ninic studied the pile-soil interaction along the pile skin under an axial loading using a 3D frictional point-to-point contact formulation, where each pile integration point was associated with an adjacent target point in the soil element (Ninic et al., 2014). It has been shown that pile responses are comparable with the analytical models he developed.

2.4 DAMAGE TYPES IN TIMBER POLES AND DAMAGE DETECTION METHODS

2.4.1 Damages types in timber poles

Timber utility poles are connected in series and the collapse of a single pole will initiate a domino effect bringing down a large part of the power line and as a result the power supply will be disrupted (Datla and Pandey, 2006).

Damage to wood is normally caused by several factors such as fungi, climatic conditions, insects attack as well as mechanical damage from vehicles (Li et al., 2007). Decay caused by fungi once started can be very rapid as fungi can grow quickly over wood surfaces under ideal conditions (Nofal and Morris, 2003). These fungi can penetrate or destroy the cell walls of wood that will lead to significant loss of wood strength. If there is a connection point in wood, it will be susceptible to decay, such as when bracings are used to stabilise piles or poles. When these connection points are exposed to alternate moisture and dryness, they will be subjected to wetting and drying

cycles which make wood swell and shrink, and cause splitting, cracking or warping. (Nguyen et al., 2004)

Timber poles deteriorate over time by varying levels, and in most cases, the damage is invisible and often below ground (Baraneedaran et al., 2009), since the influence of soil factors on decay of timber poles below ground were identified after analysing failure data from industries (Chattopadhyay, 2007).

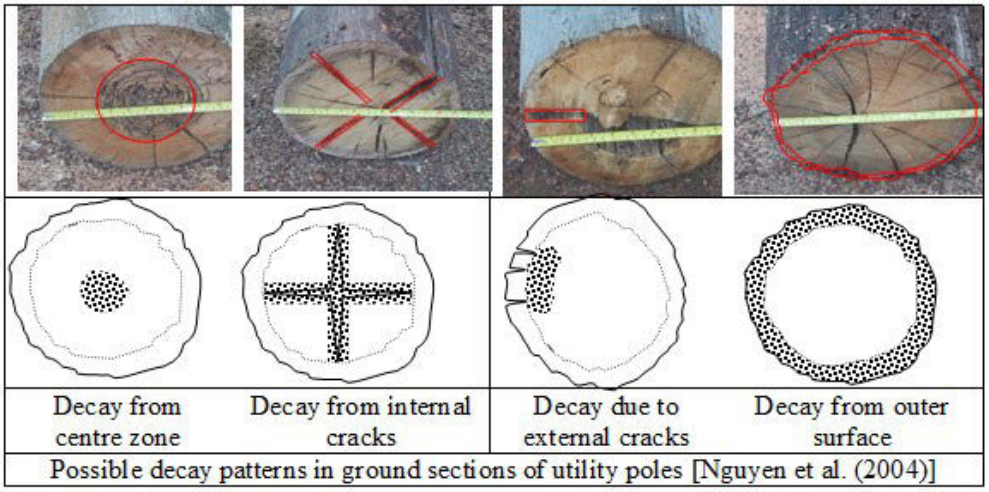

Figure 2-11 Possible decay patterns of utility poles below ground level (Nguyen et al., 2004)

Several types of decay on cross section of poles just below the ground level are shown in Figure 2-11. Wang et. al established a model to predict the decay according to the wood and climate information and thus the remaining life of a timber pole can be predicted (Wang et al., 2008) as shown in Figure 2-12. It can be found that the decay in the centre of a pole is much slower than the decay on the surface. Unfortunately, surface decay always has a significant influence on the strength of a pole.

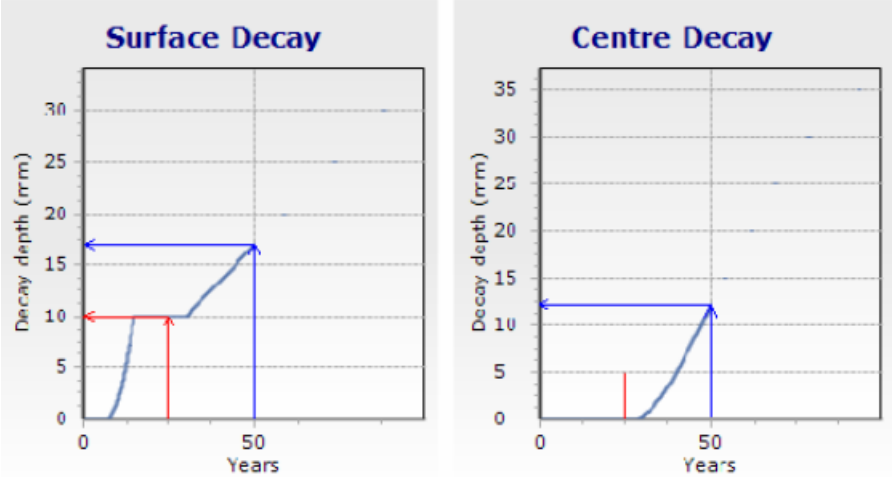

Figure 2-12 Details of decay rate from software developed by Wang (Wang et al., 2008)

2.4.2 Damage detection methods

To avoid the sudden failure of structural components, damage detection in structures at the earliest possible stage is pervasive throughout the researchers in civil, mechanical and aerospace engineering (Sinou, 2009). The effect of damage on a structure can be classified as linear and nonlinear. The linear damage situation is that linear elastic structure remains linear elastic after damage and can be analysed by model-based and non-model-based methods; while the nonlinear damage is that linear elastic structure demonstrates nonlinear behaviour after damage such as a fatigue crack (Doebling et al., 1998).

2.4.2.1 Overview of vibration based damage detection methods

Generally, the damage detection procedures are similar by analysing some parameters from measurement that are related to the condition of a structure. Much of the technical literature concerns the identification of structural damage by analysing the changes in measured structural vibration response including changes in modal frequencies, changes in measured mode shapes and changes in measured flexibility coefficients (Doebling et al., 1996).

The most well-known methods are modal testing measuring changes in modal parameters, such as frequencies, mode shapes and response to specific excitation (Sinou, 2009). The methods using natural frequencies are considered as one of the most popular damage detection methods since these methods are quite mature and easy to be conducted in experimental testing. The methods of frequency measurements extraction

are also well developed. Researchers have claimed that it was possible to identify the changes of structure properties from correlated measured frequency response functions (FRF) (Crema and Mastroddi, 1998). However, truncation could cause a significant change in FRFs even when there is no damage (Agneni, 2000).

Modal assurance criterion (MAC) is suggested by researchers for damage detection using mode shapes. MAC is a scale factor from 0 to 1.0 representing the correlation between two sets of modal vectors; 0 for uncorrelated and 1.0 for perfectly correlated. MAC was not able to detect the damage location explicitly and accordingly, the co-ordinate modal assurance criterion (COMAC) was developed. The location where a COMAC value is close to zero is the possible damage location. Ko and his colleagues presented a combined method using MAC and COMAC, and the damage in steel-framed structures was identified (Ko et al., 1994). However, Parloo and his colleagues indicated that combined MAC and COMAC could only detect the most severe damage in the case of a highway bridge in New Mexico and the noise presented in the measurement significantly affected the damage detection (Parloo et al., 2003).

The spatial location of damage can be identified by mode shape derivatives such as curvatures. Although this method was considered an efficient tool for damage localisation (Pandey et al., 1991), Parloo and his colleagues found this method not suitable for practical application since the measurement was influenced by the uncertainties, noise as well as ambient conditions (Parloo et al., 2003).

Modal strain energy measuring the changes in strain mode shape and change in resonant frequency was proposed by Dong and his colleagues (Dong et al., 1994). Although his method was more efficient than the previous methods mentioned above, it was found to be hard to detect the damage located near the supports or joints. In addition, this method became less efficient due to the noise and multiple damages (Sinou, 2009).

Dynamic flexibility using a dynamically measured flexibility matrix to estimate the changes in structural stiffness can be used as a damage detection method in the static behaviour of structure. Park and his colleagues applied this method to detect the damage of a ten-storey building, a bridge and an engine structure and the damage was predicted and located correctly (Park et al., 1998). However, it was found that the method became

less efficient if there was complex damage or simultaneous damages, or the damages were close to the joints (Alvandi and Cremona, 2006).

2.4.2.2 Overview of wave propagation based damage detection methods

The wave propagation based methods detect structural damage by sending stress waves in a structural geometry to compare the signal before and after damage and is more and more used in order to assess the state of various structures. Besides the SE/IR and ultraseismic methods mentioned in section 2.2, a number of studies are under investigation in damage detection mainly using Lamb wave. Lamb waves, was discovered by Horace Lamb in 1917, can exist in plate-like thin plate with parallel free boundaries (Su et al., 2006). Subsequently, Worlton introduced Lamb waves as a means of damage detection in 1961 (Worlton, 1961). Cuc and his peers successfully used piezoelectric wafer active sensors working in conjunction with guided Lamb wave to detect various types of damages in complex geometry structures (Cuc et al., 2007). Purekar and Pines successfully used Lamb waves associated with sensor arrays to identify the presence of delamination damage in a composite laminate (Purekar and Pines, 2010).

Time of flight (TOF) and amplitude are important indicators for damage detection using guided wave method. TOF is one of the most common and simplest techniques used in damage identification. Typically, a stress wave is induced by striking one side of the inspected structure with a hammer, which is instrumented with a sensor. The sensor emits a start signal to a timer when the impact is imparted. The wave travels to the opposite side of the structure and is captured by the sensor placed directly opposite to the impact location. When the sensor receives the arrival wave, a stop signal will be sent to the timer. According to the measured times and the known distance between the impact location and the second sensor, the velocity of the wave can be calculated and used to assess the structural condition. Normally, stress wave travels quickly if the structure is dense and solid. Damages will cause increased transmission times for wave propagation, and therefore, slow moving wave always indicates presenting of damages. This method can be used to detect the internal damage of timber structures; however, early stages of decay cannot be detected. The effectiveness of this method also depends on the type of damage, for example, brown rots are generally more easily detected than white rots (Dackermann et al., 2013). Ramadas and his peers used TOF to detect the

crack of a beam structure. It was found that if the crack is close to the boundary, it is difficult to identify the arrival time of the reflected wave group since interference happened between the boundary reflection and the reflection from the crack, and therefore, TOF become less reliable (Ramadas et al., 2008). Tang and Yan pointed out that TOF-based methods need to subtract the guided waves before damage from those after damage to obtain the damage-scattered waves. However, the environment such as temperature, load and noise, can significant influence the propagation of guided waves in the structure. Therefore, the guided waves of an intact structure under different environmental conditions could be different which will lead to suspicious identification of damage (Tang and Yan, 2013).

Guided waves are able to propagate long distances with little amplitude attenuation (Dodson, 2012). Hence, the wave amplitude based methods are widely used to extract damage features. Giurgiutiu and his peers used amplitude change to detect disbonding of a lap joint specimen. The amplitude of the transmitted wave signal can be an indicator of the bond quality. The amplitude of the received wave signal is large for a healthy bond. On the contrary, if disbonding presents, there will be a decrease in amplitude of the received wave signal proportional with the severity of the disbanding (Giurgiutiu et al., 2005). Li and his colleagues utilised the feature of amplitude reduction of the wave signals to detect the damage for composite laminates. The results demonstrated that the method is effective to identify the existence of delamination damages in composite laminate (Li et al., 2009). Ramadas and his peers used amplitude ratio to identify the damage location and severity of a beam. The results demonstrated that if the crack is near the boundary, the reflected waves from the crack and boundary interfere. The amplitude will be influenced by this interference phenomenon. Hence, amplitude based methods may give a wrong interpretation if damages are close to the boundary (Ramadas et al., 2008). Lee and his colleagues experimentally found the variation in temperature dramatically changes the amplitude of the piezoelectric sensor response (Lee et al., 2003). In their research, a principle component analysis method was used to detect damages, but the results demonstrated that the temperature variations cause larger changes in signals than the damage.

It is known that an incident wave reflects and refracts at an interface. Wave propagation in monitored structures is complex; multiple reflections and mode conversions in

complex structures may present due to the various interactions between waves and boundaries, and therefore it is difficult to interpret the results of damage detection. Lee and Staszewski, in their research, numerically verified that the propagating wave is significantly attenuated near the excitation source and very little attenuation can be found afterwards. When the incident wave hits the damage slot, it is observed that the wave reflected form the damage, transferred through the damage as well as diffracted by the damage. A change in direction of wave propagation can also be identified. The transferred wave changes direction twice undergoing refraction when it passes over the two boundaries of the damage slot, and the bending angles depend upon the relative speed that wave propagates in two media. The wave speed in the specimen is much larger than in air, as a result, the wave propagation slows down when it passes over the damage slot. The incident wave passes around the damage slot, and thus a change in direction of propagation associated with diffraction presents. When the wavelength of the incident wave is much larger than the damage slot, diffraction can be negligible. While, the incident wave passes through almost unaffected if the damage slot is much larger than the wavelength. The results also demonstrated that the angle of incident wave propagation is important to detect the damage since the incident and reflected waves are difficult to be separated if the angle of wave propagation is large (Lee and Staszewski, 2007).

Although the wave propagation based methods have demonstrated the great potential for structural damage detection, associated advanced signal processing methods are playing an important role to extract the damage feature effectively.

2.4.2.3 Overview of advanced signal processing and pattern recognition methods used in damage detection

With the rapid development of computer technologies, pattern-matching techniques using neural networks (NN) have drawn considerable attention in the field of damage assessment and structural identification. Wu and his colleagues reported the success of application of NN in damage detection using modal data (Wu et al., 1992). The basic strategy was to train a neural network to recognise the behaviour of the undamaged structure as well as the behaviour of the structure with various possible damage states. When the trained network is subjected to the measurements of the structural response, it should be able to detect any existing damage. Many pilot studies by researchers showed

that NN based methods for damage assessment were promising. However, for finite element analysis, the computational time and resource needed to train a NN model increases dramatically with increasing number of structural degrees of freedom. Therefore, most successful examples of damage detection using NN based methods in FEA were aimed for severe damage rather than small damage due to the mesh issue.

Analysis methods of the signal measured from structure components are well developed such as wavelet-based methods (Percival and Walden, 2000, Addison and Addison, 2002, Robertson et al., 1998), parametric system identification (Bisht, 2005), Hilbert-Huang transform (Huang et al., 1998, Yang et al., 2004), and the peak-picking method (Bisht, 2005).

Wavelet analysis can be viewed as an extension of the traditional Fourier transform with adjustable window location and size. It is capable of examining local data in multiple levels of details and approximations of the original signal. Therefore, transient behaviour of the data can be precisely described. Surace and Ruotolo used wavelet transform to detect the presence of a crack on the structure. They concluded that the method was more sensitive in detecting relatively small cracks (Surace and Ruotolo, 1994). Dutta and Okafor successfully applied wavelet transforms to detect the damage on a cantilevered aluminium beam with Gaussian white noise based on the mode shapes (Okafor and Dutta, 2000). Wavelet transform can be divided into continuous wavelet transform (CWT) and discrete wavelet transform (DWT). CWT was obtained by changing the scale of the analysis window, shifting the window in time, multiplying by the signal, and integrating over time history. Therefore, the computation amount is huge. DWT analysed a signal by filtering of different cut-off frequencies with high pass filters and low pass filters (Polikar, 2001). It provided flexible time-frequency resolution but suffered from a relatively low resolution in the high-frequency region, which lead to difficulty in differentiating high-frequency transient components (Gao and Yan, 2011). However, wavelet packet transform (WPT) provided good resolution in both the low frequency region and the high frequency region, thereby overcoming the problem (Gao and Yan, 2011).

Wavelet packet (WP) transform is a mathematical method that decomposes a signal into low and high frequency components at random time-frequency resolutions. Wavelet packets consist of a series of linearly combined usual wavelet functions. Sun and Chang

developed a more promising method for structural damage assessment using the wavelet packet (WP) energy method. The vibration signals caused by a pulse load were first decomposed into wavelet packet components. Signal energies of these components were calculated by their magnitudes and used as the inputs of NN models for damage detection. The numerical study was on a three span continuous bridge under impact excitation. The results showed that the WP energies are sensitive to structural damage and can be used to detect the damage occurrence, location as well as severity (Sun and Chang, 2002). Next, the authors extended the method to a pattern extraction to create a WP signature index based on vibration response using a statistical method. Two indicators based on component energy change were employed to determine the structure's condition. Statistical process control was applied to minimise the effect from excitation force. The novel method was validated by an experimental testing on a steel cantilever "I" beam and the results demonstrated that the indicators were able to discriminate the intact and damaged conditions of the structures accurately even with measurement noise (Sun and Chang, 2004).

In signal processing, the energy associated with each frequency component at a given decomposition level of WPT tree shows more robust features than the coefficients alone (Yen and Lin, 2000). The wavelet packet energy can be understood as the total energy of the signal decomposed into a summation of wavelet packet component energies that correspond to different frequency bands (Han et al., 2005). Yam and his peers combined wavelet packet transform as well as artificial neural networks (ANN) to identify the damage of composite laminated plate using vibration response. The damage feature vectors were created based on energy variation of the vibration responses decomposed using wavelet package before and after the occurrence of structural damage. The ANN was applied to establish the relationship between structural damage feature and damage status (location and severity). The results indicated that the damage index was basically monotonously changeable with the severity of crack damage in the plates and it was very sensitive to small damages, therefore, the method could be applied for online damage detection and health monitoring for various industrial structures (Yam et al., 2003). The sensitivity of WPT component energy related to the local change of system parameters has been derived analytically by Law and his colleagues. Both acceleration and strain responses have been used separately or in combination in numerical analysis. The acceleration was shown to be more sensitive to local change of structural

parameters during numerical as well as analytical analysis. An experimental result from a steel beam also indicated the effectiveness of the method (Law et al., 2005). Han and his colleagues employed WPT-based energy rate index to detect the damage of beam structures. After comparing with experimental results, they concluded that both simulated and experimental studies demonstrated that the WPT-based energy rate index was a good candidate index that was sensitive to structural local damage. Jiang and his colleagues used lifting WPT to achieve online damage detection of laminated composite plates. Structural damage feature vectors were obtained through energy variation of the decomposed vibration signals between the intact and damaged structures. The results demonstrate that the energy feature vector was sensitive to structural local damage (Jiang et al., 2010). Prakash used WPT-based method to identify the damage of a glass fibre reinforced polymer cantilever beam under ambient excitation. The effectiveness of this method was verified by changing the damage location and severity (Prakash, 2013). Facchini and his team used WPT as a feature extraction tool on a vibrating composite beam and pattern of the damaged beam was identified (Facchini et al., 2014). From the literature reviews, it can be found that WPT-based damage detection is a very effective tool for damage detection even for small damages regardless of the structural characteristics.

2.4.2.4 Optimisation techniques for structural damage detection

In the application of damage detection in structures, the aim is to formulate an objective function in terms of parameters related to the state of the structure. The objective function must be formulated in such a way that the measured value is close to the results that evaluated with the true parameters. An optimization procedure has to be employed to determine the values by following an iteration process. Once the procedure arrives at the solution, the values will indicate the state of the structure (Mares and Surace, 1996).

Comparing many other optimization algorithms, genetic algorithm (GA) converges to a global optimal solution and has been successfully applied in many applications including FE analysis (Marwala, 2010), since it has less possibility to fall into local optimisation. Friswell used GA combining with eigen-sensitivity method to identify location and severity of damage based on measured vibration responses. Through the numerical analysis as well as experimental testing, it is found the algorithm is effective and powerful (Friswell et al., 1998). Hao and Xia proposed a damage detection method

by comparing the frequencies and mode shapes before and after damage from measurement. A real-coded GA with real number encoding was used to minimise the objective function. A cantilever beam and a frame structure were tested and it was found the method with real-coded GA was more accurate to indicate damage of beam structure than other optimisation methods (Hao and Xia, 2002). Marwala used GA to successfully optimise FE model based on the wavelet data from experimental measurement of a suspended beam and the results indicated that GA is capable to find global optimum solutions (Marwala, 2002). Perera and Ruiz developed a multi-stage scheme for damage detection for large structures based on measured modal data (Perera and Ruiz, 2008). In their study, modal flexibilities and a damage location criterion dependent on frequencies and mode shapes were used as two objective functions. The method was successfully implemented in numerical analysis as well as in experimental testing of a real bridge. There are a series of parameters which need to be defined in GA, thus, the selection of proper parameters will significantly influence the accuracy of results.

Artificial fish swarm algorithm (AFSA) is also an intelligent population-based optimization algorithm inspired by the behaviours of fish swarm and shares similarities with GA. It is one of the best methods of optimization among the swarm intelligence algorithms with many advantages such as high convergence speed, flexibility, fault tolerance and high accuracy (Neshat et al., 2012). Li and Yu identified damage using AFSA on their two-storey portal frame model. The illustrated results show that the proposed AFSA based optimisation method can effectively locate damaged elements of structures. The method was able to identify the extent of damage under all damage scenarios with a good noise immunity (Li and Yu, 2014).

2.5 LOAD CAPACITY OF TIMBER UTILITY POLES

Timber utility poles form an essential component of lifelines in all communities, including electricity distribution and communication systems. While timber poles may have high initial strength, they often experience deterioration and decay over their designed service life due to the fungus or termite attacks in varying levels, which may significantly influence the load capacity of timber utility poles. To quantify the load capacity or strength of timber utility poles, limit-state design procedures of timber poles

in Australia was suggested by Crews and Horrigan in 1998 (Crews and Horrigan, 1998). Limit-states are the limiting conditions beyond which a pole ceases to fulfil its intended function, and are calculated using a load and resistance format that separates the effects of component strengths and their variability from the effects of external loadings and their uncertainty. The limit-states determined for a particular structure are used in the application of reliability-based design procedures which are aimed at achieving an acceptable risk of the structure failing for a particular loading condition (Francis and Norton, 2006).

Timber pole construction is typically utilised to provide support for gravity loads and resistance against lateral forces. Wind load acting on the timber utility poles is the most common lateral force during the service life of the poles, and thus, in this thesis, load capacity of the poles will be extensive studied under a design wind load. According to Australian Standard 1170.2, wind speed, aerodynamic shape factor and dynamic response factor of a structure are the critical issues to define a proper wind load. Load capacity design in Australian Standard 1720.1 for timber structures is based on modifying the characteristic capacities by the factors appropriate to the service condition as well as the material property type. The design capacity in bending of round timbers such as poles or piles for the strength limit state is defined in the standard. However, the main limitation of this criterion is that it does not consider the damage type of a timber pole influences on the strength performance. Actually, the effects on the load capacity of timber utility poles caused by different types of damage are distinctly different.

Timber utility poles are normally used for power and communication supply and thus different forms of cables are attached to the poles. As a result, wind loads acting on the cables have to be considered as well to analyse the load capacity of timber poles. These cables are more sensitive to wind loads than the pole structures and they have a uniformly distributed mass along the span. Generally, consideration of maximum wind load case along the cables distribution as well as normal to the cables distribution is necessary for load capacity design. According to Ausgrid NS 220, for network distribution application, at the termination of a distribution network or if the cables are attached to the poles at certain angles, stays are designed to take the full load applied and not just the portion by which the load exceeds pole capacity, and the purpose is to

avoid the collapse along the cables distribution. In this situation, the wind loads normal to the cables distribution are more likely to cause the utility poles collapse. Based on the review of related standards, this thesis will focus on estimation of load capacity or strength of damaged and undamaged utility poles considering the condition that the wind load is normal to the cables distribution.

This chapter briefly reviewed the well-known stress wave based NDT methods and the application limitations of these methods in certain conditions, discussed the numerical modelling consideration for timber utility poles including timber material modelling and soil modelling. This chapter also briefly introduced the issues that caused the damage of timber utility poles. Damage detection techniques including the vibration based methods and wave based methods were reviewed extensively. Some optimisation algorithms that are used in this research were introduced briefly and detailed discussions will be conducted in Chapters 4 and 5. Load capacity of timber utility poles will be extensively studied in Chapter 6.

2.6 IDENTIFIED RESEARCH GAPS

Based on literature review, it is clearly noticed that there has been limited studies on condition assessment of timber utility poles. In other words, limited resources in the public domain can be found in this field of research. As a starting point of this specific topic several gaps were identified and need to be fulfilled during the research work:

- Propagation behaviour of stress wave in timber utility poles is complex due to the material complexity and uncertainty, and there is limited research which can be found.
- Most of the research on timber modelling has been focused on the composite beams and the purpose is to study the fatigue and failure behaviour of timber beams; limited research has been reported on modelling of wave propagation in timber poles.
- Limited research can be found in the modelling of timber pole and soil interaction under low strain testing condition. Most relevant references relate to the modelling of pile integrity testing. However, pole and pile are different structures in relation to soil-structure interaction due to wave propagation,

especially considering complicated timber properties. The interaction behaviour between soil and the poles is different from that with the piles.

- Most damage detection methods and the associated research are based on vibration and vibration responses. Limited research has been found on utilising wave patterns for accurate and effective condition assessment of timber poles.
- Limited research has been found on damage severity estimation of timber poles.
- No research has been reported on strength prediction related to pole design/operation standard.

To achieve the objectives of this research, we start from the numerical simulation by developing FE models to investigate the wave behaviour in timber utility poles. After this, a novel damage detection method can be developed based on WPT and damage prediction will be carried out by an optimisation technique. Finally, the remaining load capacity of the damaged pole can be predicted by numerical analysis using Australian/New Zealand standards.

3 FE modelling for wave propagation study in timber poles

3.1 INTRODUCTION

To describe and study the wave propagation behaviour in a timber pole that is embedded in soil, three issues should be considered: modelling of the timber material, modelling of the soil and modelling of the soil-pole interaction. By obtaining proper modelling methodology, the investigation of wave behaviour in timber poles will become achievable.

The basic methodology of FEA is to divide a body into a finite number of small units (elements) which leads to a satisfactory approximate solution for the analysis. In this research, to capture the wavefront accurately, at least 40 elements should be considered per wave length (depending on the excitation frequency). After this, the time step is set due to the minimum grid point distance and the wave speed (Fischer et al., 2010).

As mentioned in Chapter 2, the timber will be considered as an homogeneous structure. 3D model is considered in this stage to make the simulation more accurate. Element SOLID 185 is used for general 3-D modelling of solid homogeneous structures in ANSYS and is defined by eight nodes with three degrees of freedom at each node in the nodal x, y, and z directions as shown in Figure 3-1:

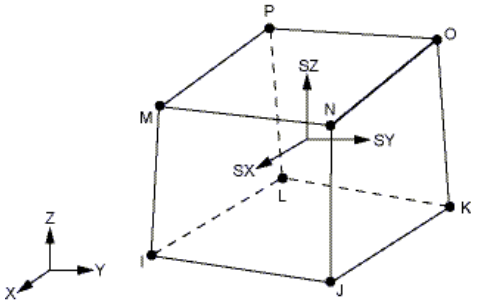

Figure 3-1 SOLID 185 homogeneous structural solid geometry (ANSYS, 2011)

3.2 GENERAL NUMERICAL MODELLING OF TIMBER POLES

3.2.1 Modelling of timber material

Wave propagation in timber is a complex dynamic process controlled by the properties, orientation and microstructure of the fibre, and perhaps more importantly, by the geometry of the material (Wang et al., 2005). Therefore, accurate simulation of timer materials is the priority issue to get insight into wave propagation behaviour in timber poles.

To investigate the influence of the material characteristics on the wave behaviour, FE modelling of material characteristics can be divided into three categories: isotropic, transversely isotropic and orthotropic. Isotropic materials have identical values of a property in all directions, none of the properties depend on the orientation and the material is perfectly rotationally symmetrical. Transversely isotropic materials (see Figure 3-2) have the same properties in one plane (for example the x-y plane) and different properties in the direction normal to this plane (for example the z-axis). An orthotropic material has at least two symmetric orthogonal planes, where material properties are unique and independent in the direction within each plane. A material without any symmetric planes is defined as anisotropic material (Efunda, 2014).

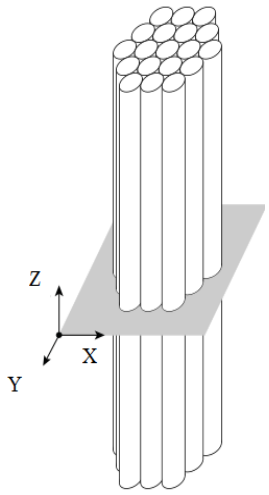

Figure 3-2 Transversely isotropic materials

Orthotropic materials can be expressed by the matrix below according to generalized Hooke's law.

$$\begin{bmatrix} \varepsilon_{LL} \\ \varepsilon_{RR} \\ \varepsilon_{TT} \\ \gamma_{LR} \\ \gamma_{LT} \\ \gamma_{RT} \end{bmatrix} = \begin{bmatrix} \frac{1}{E_L} & -\frac{\nu_{RL}}{E_R} & -\frac{\nu_{TL}}{E_T} & 0 & 0 & 0 \\ -\frac{\nu_{LR}}{E_L} & \frac{1}{E_R} & -\frac{\nu_{TR}}{E_T} & 0 & 0 & 0 \\ -\frac{\nu_{LT}}{E_L} & -\frac{\nu_{RT}}{E_R} & \frac{1}{E_T} & 0 & 0 & 0 \\ 0 & 0 & 0 & \frac{1}{G_{LR}} & 0 & 0 \\ 0 & 0 & 0 & 0 & \frac{1}{G_{LT}} & 0 \\ 0 & 0 & 0 & 0 & 0 & \frac{1}{G_{RT}} \end{bmatrix} \times \begin{bmatrix} \sigma_{LL} \\ \sigma_{RR} \\ \sigma_{TT} \\ \tau_{LR} \\ \tau_{LT} \\ \tau_{RT} \end{bmatrix} \quad \text{Eq. 3-1}$$

In the matrix, ε is the elastic strain vector, γ the shear strain vector, σ the stress vector, E the elastic modulus, G the shear modulus and ν the Poisson's ratio. The subscripts L, R and T represent grain directions, with L describing the direction along the grain (longitudinal direction), R across the grain (radius direction), and T tangential to the grain (tangential direction), respectively (see Figure 3-3).

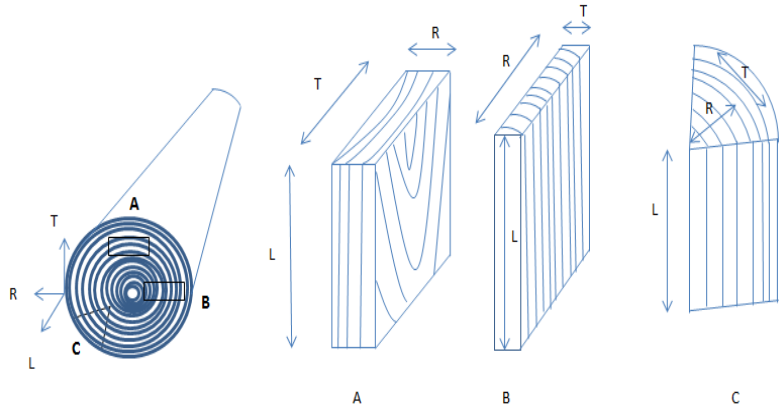

Figure 3-3 Three dimensional fibre of timber

The matrix can be simplified to the following equation:

$$\{\boldsymbol{\varepsilon}\} = [\mathbf{C}]_{\text{orth}}\{\boldsymbol{\sigma}\} \qquad \text{Eq. 3-2}$$

where $\{\boldsymbol{\varepsilon}\}$ is the strain tensor, $\{\boldsymbol{\sigma}\}$ is the stress tensor and $[\mathbf{C}]_{\mathbf{orth}}$ is the orthotropic elastic matrix (6×6). For orthotropic materials, the following is valid:

$$\frac{\nu_{ij}}{E_i} = \frac{\nu_{ji}}{E_j},\ i \neq j \quad i, j=L, R, T \qquad \text{Eq. 3-3}$$

Hence, the orthotropic elastic matrix $[\mathbf{C}]_{\text{orth}}$ can be written as a symmetric matrix, with nine parameters needed to define the wood material properties.

Experimental testing, which supports this research, was primarily conducted on test specimens of hardwood timber made from Spotted Gum. The density of Spotted Gum ranges from 950 kg/m^3 (dry wood) to 1150 kg/m^3 (green wood), and the elastic modulus varies from 18,000 MPa (green wood) to 23,000 MPa (dry wood) (Bootle, 1983). The typical stress-strain behaviour of hardwood timber can be illustrated by a hardwood species named Balau which has a density of 979 kg/m^3. The related stress-strain diagrams are depicted in Figure 3-4.

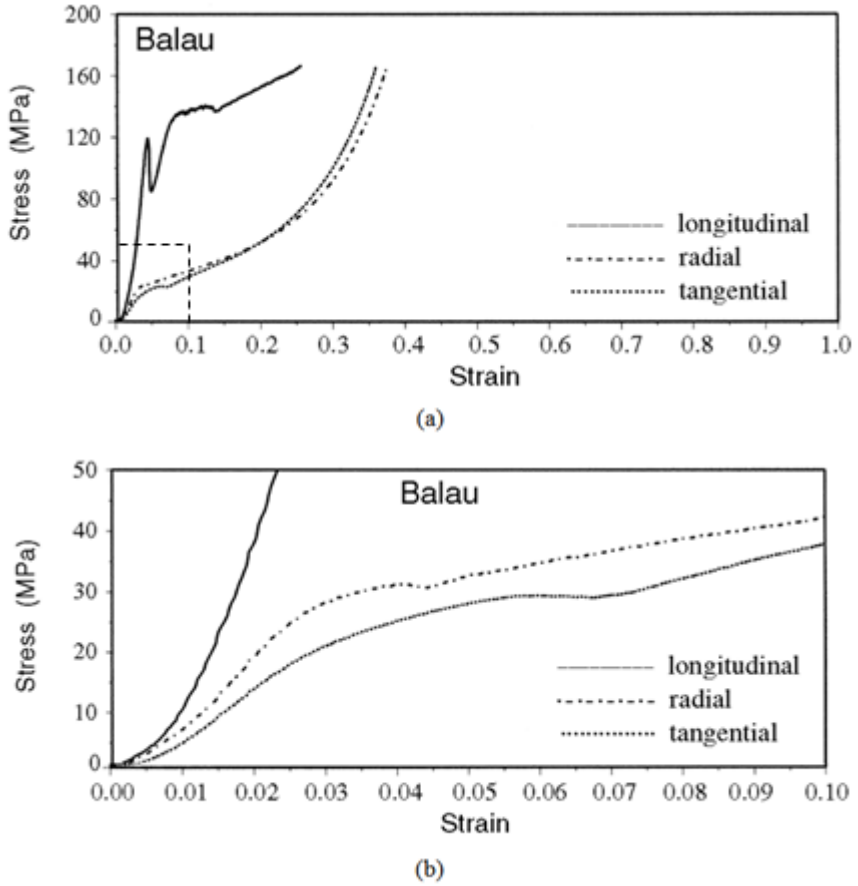

Figure 3-4 (a)Stress/strain relationship for Balau loaded in compression up to a strain level of 1.0, (b) Zoomed-in view of the stress/strain relationship (Ellis and Steiner, 2002)

It is well known that at a low strain level (for example, less than 0.03), timber exhibits linear elastic behaviour (Ellis and Steiner, 2002). In this project, by numerical analysis, it was shown that using an impact hammer to induce stress generates strain levels below 0.001 throughout the pole structure. Therefore, for this research, it is reasonable to use linear elastic models to simulate the timber material.

The material properties for the isotropic model are defined as 23,000MPa of Elastic modulus and 0.3 of Poison's ratio. For orthotropic and transversely isotropic material models, the parameters are listed in Table 3-1. The density for three different types of models is set to 950 kg/m^3.

Table 3-1 Properties for orthotropic and transversely isotropic material

orthotropic material								
Elastic modulus (Mpa)			Shear modulus (Mpa)			Poison's ratio		
E_R	E_T	E_L	G_{LR}	G_{RT}	G_{LT}	ν_{RL}	ν_{RT}	ν_{TL}
1955	850	23000	1513	357	1037	0.04	0.682	0.023
transversely isotropic material								
Elastic modulus (Mpa)			Shear modulus (Mpa)			Poison's ratio		
E_R	E_T	E_L	G_{LR}	G_{RT}	G_{LT}	ν_{RL}	ν_{RT}	ν_{TL}
1955	1955	23000	1513	581	1513	0.023	0.682	0.023

3.2.2 Modelling of boundary conditions

3.2.2.1 Modelling of soil

The timber utility pole, as found in the field, is embedded in soil. Under this condition, boundary influences from the surrounding soil must be considered in order to correctly model the wave propagation. Classical soil mechanics makes use of an idealised stress strain curve to simulate soil behaviour as mentioned in Chapter 2.

In this research, low strain testing was conducted to investigate the wave behaviour; as a result, the soil behaviour is assumed as linear elastic. To investigate the effect of soil modelling method, two models were created of a 5 m long pole using two different soil modelling methods (linear vs. non-linear), that is the elastic linear model and the Drucker-Prager model (see Figure 3-5). The Drucker-Prager model is used to represent the behaviour of dry soils, rocks, concrete and ceramics where the cohesion and compaction behaviour of the materials cause an increasing resistance to shear up to a limiting value of yield strength as the loading increases and the yield strength of these materials is highly dependent on pressure (ANSYS, 2012). The cohesion value of soil was set to 30 MPa and internal friction angle was 25 degrees (soil characteristics of Sydney region). All properties of materials used are listed in Table 3-2, and a comparison of calculated acceleration response captured by the measurement points at the same location of two models are shown in Figure 3-6.

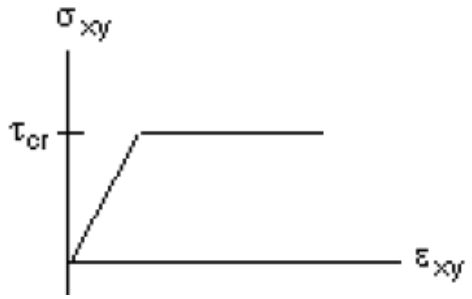

Figure 3-5 Drucker-Prager Model

Table 3-2 Material properties of soil models

	Density (kg/ m³)	Elastic modulus (MPa)	Poison's ratio
Linear-elastic	1520	100	0.3
Drucker-Prager	1520	100	0.3

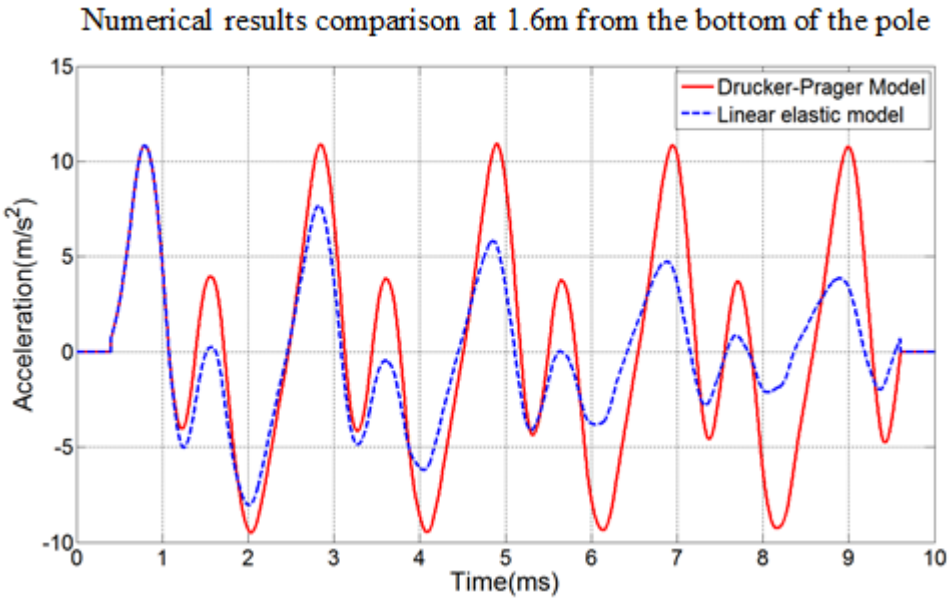

Figure 3-6 Comparison of numerical results according to different soil modelling methods

In Figure 3-6, the dashed curve presents the results of the elastic linear soil modelling and the solid curve presents the Drucker-Prager model. The results comparison shows that different soil modelling methods cause some difference in the structural response. However, the difference is about the amplitude rather than the wave pattern. From the figure, it can be seen that the acceleration amplitude of the Drucker-Prager model is larger than the linear elastic model, while the locations of the wave peaks are almost the

same. This allows the conclusion that different soil modelling methods have less influence on the accuracy of wave propagation in this study and the linear elastic model is resonable to represent soil performance.

3.2.2.2 Modelling of soil-pole interaction

Interaction behaviour simulation between soil and timber pole is one of the most important issues of modelling as it will directly influence the results. In commercial FEA software ANSYS, the modelling of interaction behaviour can be achieved by contact analysis considering different contact conditions. Finite Element Analysis is often used in the initial design stages of a new contact. This analysis will test the contact by simulation to generate a normal force curve based on the stress-strain curve provided by the material properties. To obtain effective results from a FEA study, the restraints and contact conditions have to be carefully defined.

Perfectly bonded contact analysis, considering two components are bonded together without friction, is based on small deflections or rotations and considers linear behaviour (Madenci and Guven, 2006). A set of coupled degrees of freedom DOFs contains a primary DOF and other DOFs, and coupling will only keep the prime DOF during the analysis and deletes other DOFs. The advantage of this method is to achieve an accurate solution with minimum computational resources. However, in a structural analysis, coupling DOFs to create a rigid region can sometimes cause apparent violations of equilibrium (ANSYS, 2011). For this research, coupled DOFs will be modelled if the interaction between pole and soil is not considered, which means that the DOFs of the pole and the soil act equally when impact is applied.

For the other contact analysis, the interaction between two contact surfaces can have several characteristics: no penetration; normal stress transmission and tangential stress transmission. In general, no normal tensile stresses are transmitted between contact surfaces, meaning that the contact surfaces can be separated and this can be considered as nonlinear behaviour. There are two difficulties during the analysis; one is that the contact region is unpredictable because of many factors such as loading, material properties, boundary conditions. The other complication is that friction needs to be considered and the response can be chaotic, which can make the solution not convergent (ANSYS, 2011).

In this research, bonded (coupling contact) and no separation (frictional contact) were considered to describe the contact status in ANSYS. The algorithm, namely, Lagrange Multiplier method applied on the contact normal and the penalty method (tangential contact stiffness) on the frictional plane was selected, since this method only allows a very small amount of slip for a sticking contact condition which is quite similar to the condition in this research.

"Node to node" contact in ANSYS is normally used when one node comes into contact with another node, which means the contact location must be known beforehand. In some conditions, a series of node to node contacts can be used to simulate surface contact, and the prerequisites for this type of contact are: the mesh must be the same on both contact surfaces, which means the nodes on two surfaces line up; the relative sliding is small; and the deformation is negligible, which were the case in this project. In this research, an investigation was conducted comparing the perfect bonded method against the node to node contact method. The contact behaviour was considered as no separation but sliding was permitted to simulate the potential situation in experimental testing. In terms of the computation algorithms in ANSYS, based on the understanding from experimental testing, the Lagrange Multiplier on normal plane and penalty on tangent plane were considered, as this algorithm is suitable for a very small amount of slip for a sticking contact condition. Figure 3-7 shows the node to node contact element created by ANSYS.

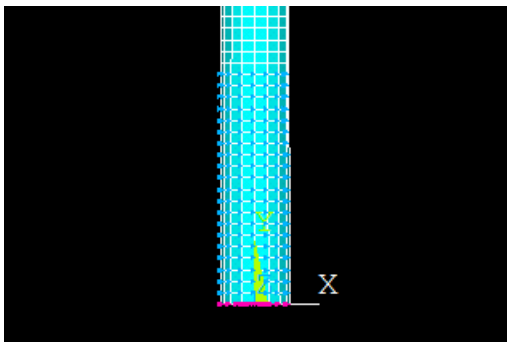

Figure 3-7 Contact element created by ANSYS

3.2.2.3 Comparison between soft boundary and hard boundary

The boundary conditions of timber poles play an important role on the wave propagation behaviour. The hard boundary will change the phase direction of wave

propagation compared to the soft boundary. To clearly present this phenomenon, two numerical models with the length of 12m were created.

The model with free end was achieved by modelling the pole hanging through two steel cables. Element LINK180 is a 3D spar and can be used in different engineering applications such as truss, sagging cables and links. The element is an uniaxial tension-compression element with three degrees of freedom at each node: translations in the nodal x, y, and z directions as shown in Figure 3-8. Tension-only (cable) and compression-only (gap) options were supported without considering bending effects (ANSYS, 2011).

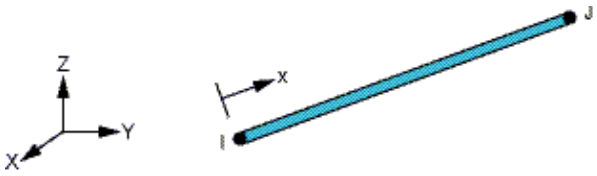

Figure 3-8 LINK180 geometry (ANSYS, 2011)

3D FE model with free end was created by ANSYS using element SOLID 185 and LINK 180 as shown in Figure 3-8. A hammer impact was applied on the centre of one edge of the pole.

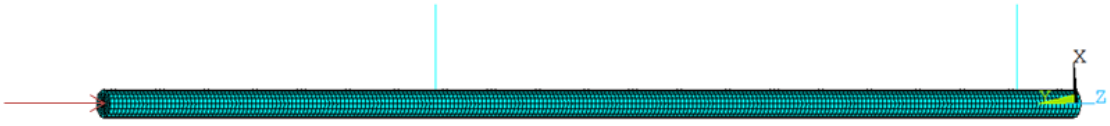

Figure 3-9 FE model with free end

The fixed boundary was achived by coupling the contact node of the pole and bedrock as mentioned in the previous section. The hammer impact was applied on the top centre of the pole (see Figure 3-9). The mesh conditions were exactly the same for the contact surface to make use of the coupling method as shown in Figure 3-10 and Figure 3-11.

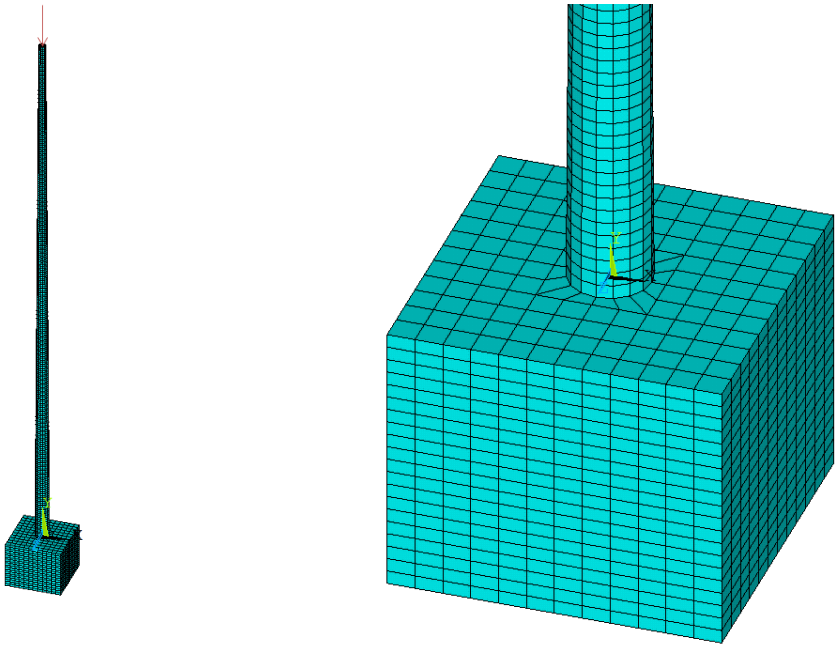

FE model with fixed boudary Zoom-in the contact part

Figure 3-10 FE model with fixed boundary

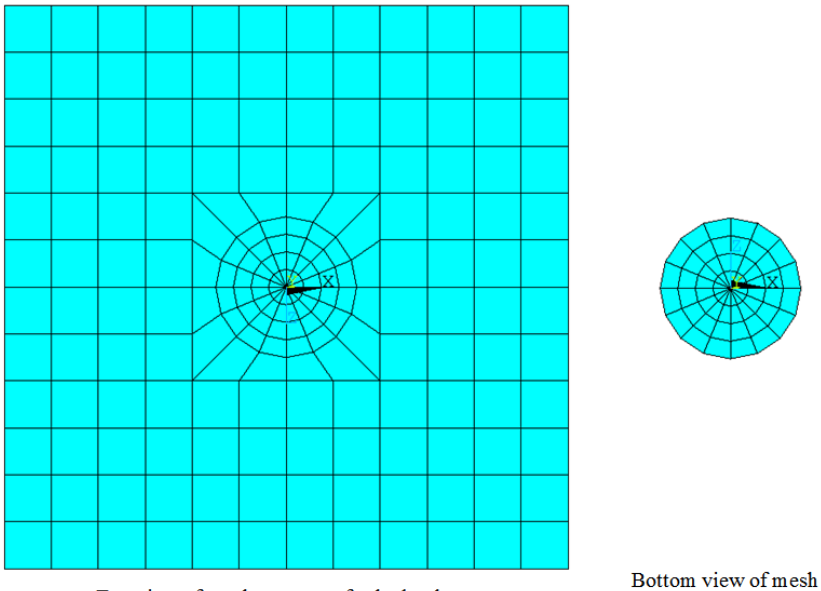

Figure 3-11 Mesh geometry of FE model for the contact suface

A measurement point (or called sensor) was located on the top of the pole and a hammer excitation was applied on the top centre of the two models. The sensors recorded the two kinds of wave behaviour based on time history and the results are plotted together for comparison(see Figure 3-12). The material properties are shown in Table 3-3.

Table 3-3 Material properties for three structural components

Material properties for the pole		
Elastic modulus (MPa)	Density (kg/m^3)	Poisson's ratio
23000	950	0.3
Material properties for the bedrock		
Elastic modulus (MPa)	Density (kg/m^3)	Poisson's ratio
32000	2400	0.2
Material properties for the steel cable (cross section area: 3.25E-4m^2)		
Elastic modulus (MPa)	Density (kg/m^3)	Poison's ratio
210000	7850	0.2

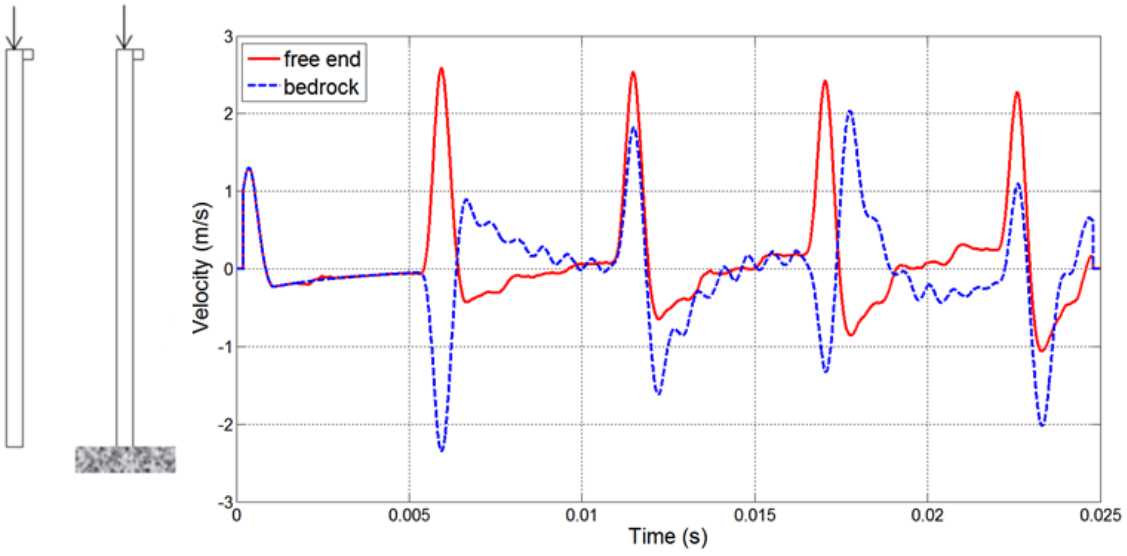

Figure 3-12 Results comparison between different boundary conditions

From Figure 3-12, it can be seen that the incident wave (generated by hammer impact directly) propagates the same until it reaches the boundary of the pole. For the free end boundary condition, the wave reflects back from the boundary and keeps the same phase direction as shown by the red solid curve: all the peaks are in the same direction. However, for the bedrock boundary condition, when the wave reflects back, the phase direction is opposite to the incident wave and the phase changes again when it reaches the hard boundary as shown by the blue dashed curve: the peak directions are opposite to each other. This phenomenon is explained intuitively according to Hirose and Lonngren's wave theory (Hirose and Lonngren, 1985): the wave pulse approaches the

fixed end, the internal restoring forces which allow the wave to propagate exert an upward force on the end of the pole. However, the bedrock is fixed and must be exerting an equal downward force on the end of the pole. This new force creates a wave pulse that propagates back, with the same speed and amplitude as the incident wave, but with opposite polarity (upside down).

3.3 NUMERICAL MODEL VERIFICATION AND VALIDATION

As metioned in previous sections, frictional contact and bonding contact are both considered to simulate the interaction between pole and soil. In order to find a more proper model to reflect the wave propagation in poles with surronding soil, experimental testing was conducted simultaneously and compared with numerical results. In the laboratory, a 5m long pole was always used because of the limitation of the ceiling height and embedded in sand by 1m. The dimensions of the cage that stored the sand was 1.2m by 1.2m by 3m, in which, 3m was the height of the cage.

Equipment

The equipment necessary to perform surface stress wave testing consisted of a modally tuned impact hammer, multiple sensors (accelerometers), a multi-channel signal conditioner, a multi-channel data acquisition system and a laptop (personal computer) equipped with signal acquisition software. For stress wave testing at UTS, the impact hammer used was a PCB model HP 086C05 of sensitivity 0.24 mV/N as shown in Figure 3-13 (a). The hammer was equipped with a load cell to measure the impact load. To record the structural response, piezoelectric accelerometers were used. The piezoelectric accelerometers employed were PCB model 352**C**34 (see Figure 3-13 (b), which had a high sensitivity of 100 mV/g and had a bandwidth of 0.5 Hz to 10 kHz . To amplify and condition the signals of the modal hammer and the piezoelectric accelerometers, a 12-channel signal conditioner, model PCB 483B03, was used (see Figure 3-13 (c)). The data acquisition system employed for stress wave testing at UTS was a middle range 8 channel system with 12-bit 4M sample/sec per channel model NI PCI-6133 (see Figure 3-13 (d)). It was essential to utilise a data acquisition system that was able to record signals with a minimum sampling frequency of 1M sample/sec per channel. For data processing, a personal computer equipped with the National

Instrument software LabVIEW was used (see Figure 3-13 (e)) (Dackermann et al., 2014).

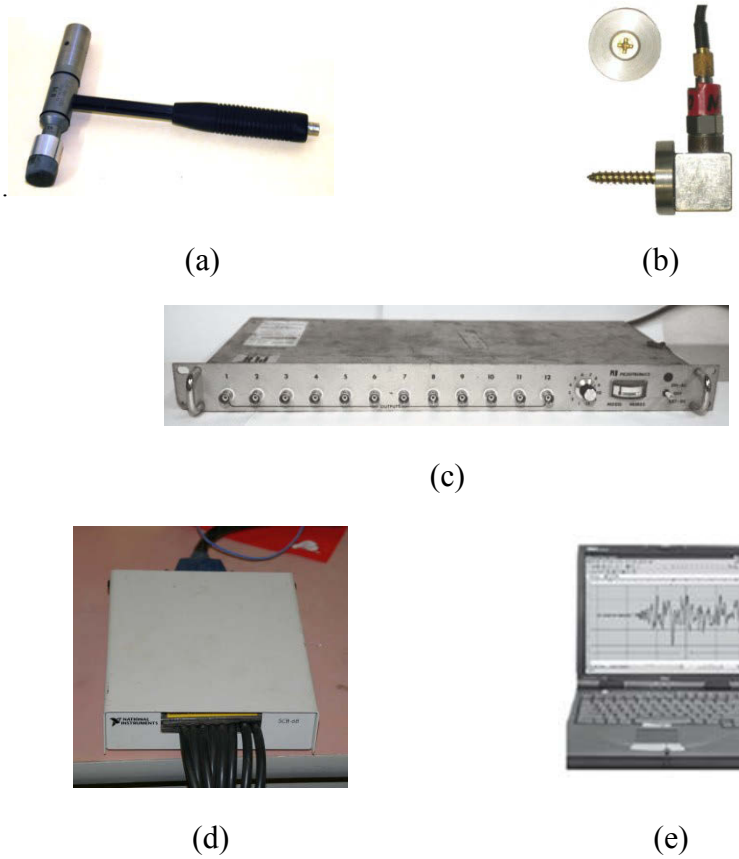

(a) (b)

(c)

(d) (e)

Figure 3-13 Testing equipment (a) impact hammer - PCB model HP 086C05, (b) piezoelectric accelerometer - model PCB 352C34, (c) multi-channel signal conditioner - model PCB 483B03, (d) multi-channel data acquisition system- model NI PCI-6133 and (e) laptop equipped with the National Instrument software LabVIEW (Dackermann et al., 2014)

Experimental testing procedure

For experimental tests, a step-by-step testing procedure, including the set-up of the equipment, the settings of the acquisition software and the execution of the tests, is described as follows (Li et al., 2011).

1. Setting up of laptop, data acquisition system and signal conditioner.
2. Attachment of sensors to the structure.

   Note: A series of accelerometers are mounted in a line 0.2 m off the ground with a spacing of 0.2 m between the sensors. To be assured that a firm connection between the structure and the sensors is established, sensor brackets are used. For the magnetic piezoelectric accelerometers used in laboratory, steel brackets are screwed

to the pole to provide an adhesive surface (see Figure 3-14). All sensors must be orientated to measure longitudinal vibration.

Figure 3-14 Sensors attached to the pole

3. Connection of the impact hammer and sensors to the signal conditioner, data acquisition system and laptop (see Figure 3-15) .

   Note: For magnetic piezoelectric accelerometers used in the laboratory, a voltmeter is used to check the voltage to enssure the voltage of the DC power suppply is between 6 to 12 mV.

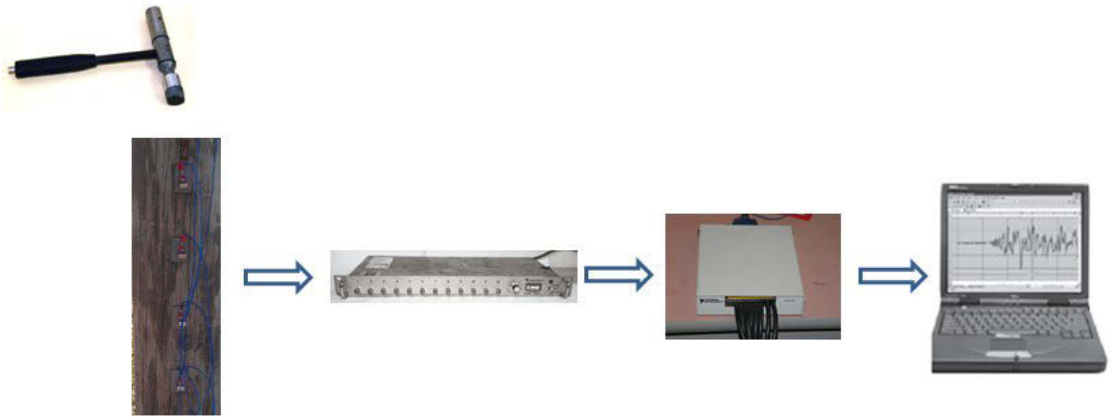

Figure 3-15 Experimental testing set up

4. Launching and setting up of data acquisition software (such as National Instrument LabView).

   Note: In the data acquisition software, the sampling rate must be set to at least 1 MHz for a frequency range of 100 Hz to 5 kHz and a minimum record duration of 0.5 s. To ensure that the entire impact excitation signal is recorded, a pre-trigger delay of 0.01% of the test duration is set.

5. Execution of trial tests.

   Note: To ensure that the testing equipment is set-up correctly and that all sensors are working properly, a number of trial tests should be performed before the real tests are conducted. The following features must be checked for the hammer and all sensor channels: noise-to-signal ratio of hammer and sensor signals (must be lower than 1%), amplitudes and shapes of hammer and sensor signals, DC offsets of sensor signals and consistency of sensor signals between different tests.

6. Execution of real tests.

   Note: The hammer strike must be performed in a straight manner to ensure precise longitudinal excitation. The duration of impact depends on the individual operator. The hammer impact is an impulse load and the duration measures the time period of the load applied on the pole. The average impact duration in this testing is around 500 μs, that is, the excitation frequency of the hammer impact is about 2KHz.

7. Saving of recorded data. Disconnecting, dismantling and packing of equipment.

FE models and experimental settings are shown in Figure 3-16. The isotropic material model was used for comparison and the corresponding material properties were mentioned in section 3.2.1. Bonded contact and frictional contact were used to represent the contact status, respectively.

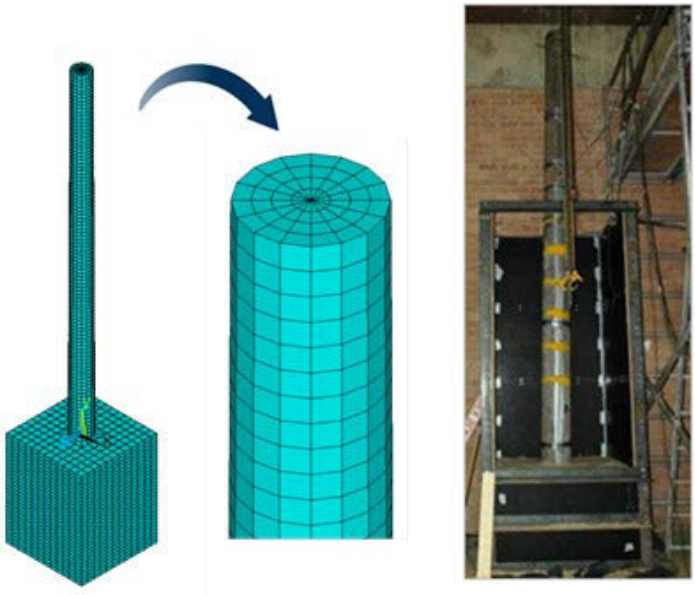

Figure 3-16 FE model vs. experimental settings

The measurement point was located at 1.6m from the bottom of the pole. The results obtained at the same meaurement points of FE models and the experimental specimen are shown in Figure 3-17 and Figure 3-18. The times at which peaks appear illustrate the arrival and reflection of wave propagation and it is a significant feature to present wave behaviour, and therefore, the time at which peaks appear is the most critical issue for the comparison.

The red thick curve presents the experimental result and the blue thin curve indicates the numerical result. After comparing the results from the model of frictional contact as well as bonded contact, it was found that the wave pattern from the model of bonded contact was more consistent with the experimental results. In addition, the curve for the model using frictional contact misses several peaks compared to the experimental result. As a result, bonded contact will be used in further study to simulate interaction behaviour between pole and soil.

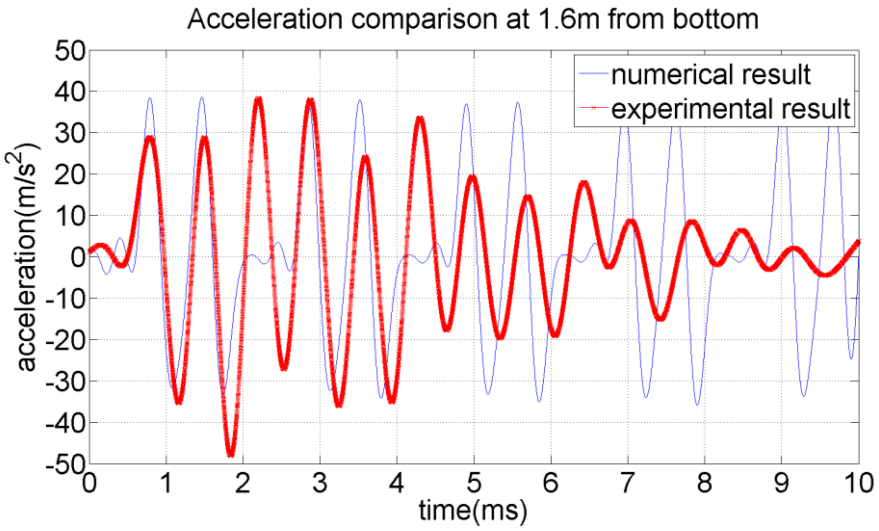

Figure 3-17 Comparison of experimental and numerical results using the frictional contact method

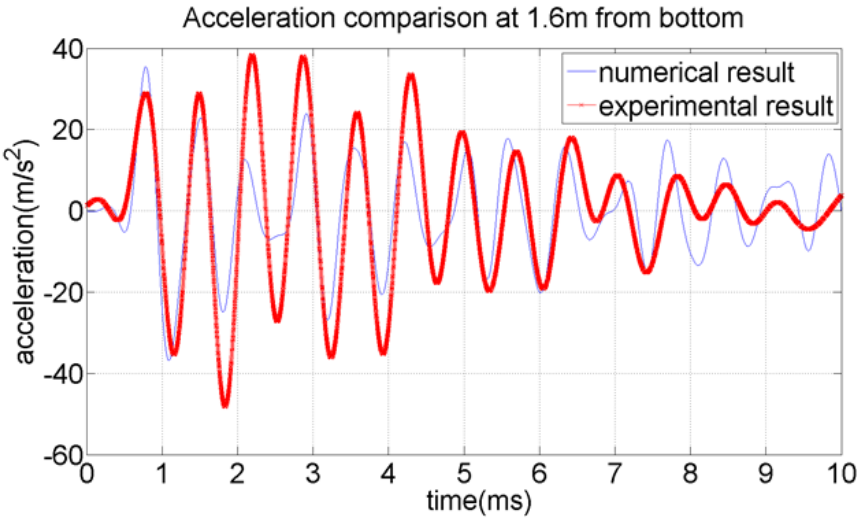

Figure 3-18 Comparison of experimental and numerical results using the bonded contact method

To obtain the best constitutive model representing the timber pole, model verification was carried out. Isotropic, orthotropic and transversely isotropic material models were created and compared with the results from experimental testing.

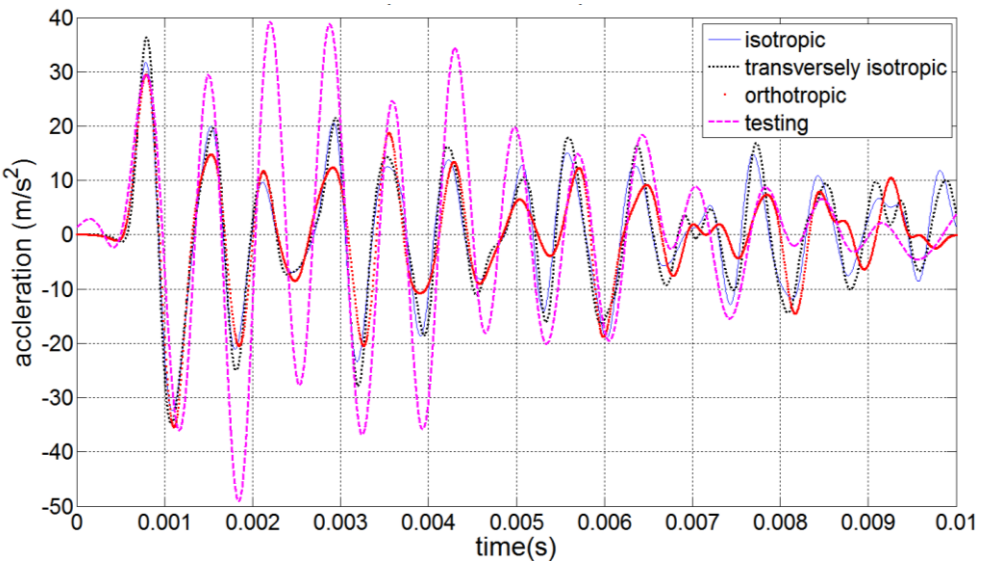

Figure 3-19 Comparison between the results from FE models and experimental testing

Figure 3-19 compares the results from a measured point located at 1.6m from the bottom of the pole using three different FE material models as well as the experimental specimen. Through comparison, it can be seen that the results for the isotropic material model and the transversely isotropic material model are quite close to each other for both wave pattern and the time at which peaks appear. It can also be observed that although the dark red curve representing the orthotropic material model missed some clear peaks, the times at which peaks appear are more consistent with experimental results than other material models.

Some conclusions can be drawn from the comparison results:

1. The behaviour of the longitudinal wave is quite similar for the three kinds of material models. Although the orthotropic material model gives the most accurate result compared with the experimental testing, the results from the three kinds of material models have no obvious difference.
2. In order to simplify the FE model and reduce computational time, the isotropic material model can be considered in the next research stage for study of longitudinal wave propagation in timber poles.

3.4 MATERIAL PARAMETRIC STUDY

Wood properties will be significantly affected by the diversity and variation between and within different species of woods in terms of the biological origin. Take Spotted Gum as an example: the elastic modulus is increased from 18,000 MPa for green wood to 23,000 MPa for dry wood; the density is decreased from 1150 kg/m^3 for green wood to 950 kg/m^3 for dry wood. With the environmental condition changed, the material properties changed as well. Damages can also cause the material properties to change. If the timber poles have been attacked by fungi and decayed, the parameters of the material properties such as elastic modulus and density will be changed, and accordingly, the wave behaviour in the decayed pole will be different with the intact pole. This phenomenon will give a fingerprint to detect the damage of the timber poles. Hence, investigation of material properties affecting the wave propagation behaviour is another important issue; accordingly, a parametric study is needed to be conducted. Elastic modulus, density and Poison's ratio will be considered as the candidate parameters that are changed by environmental conditions. Wave velocity of the incident wave is considered an index to illustrate the change of wave propagation behaviour. Since this study focuses on the longitudinal wave, the wave velocity mentioned in this thesis is always longitudinal wave velocity. One important issue which needs to be identified is that the velocity of the arrival wave and the reflected wave is not the same as well as the down-travel wave and up-travel wave in a tapered pole. The wave signal was obtained from the 5m pole with an excitation on the top centre, and the wave velocity was calculated based on the first arrival wave signal that was captured by a series of measurement points (nodes). To obtain a more accurate wave velocity, 30 nodes that were located between the ground level and 1.5m above ground level were selected.

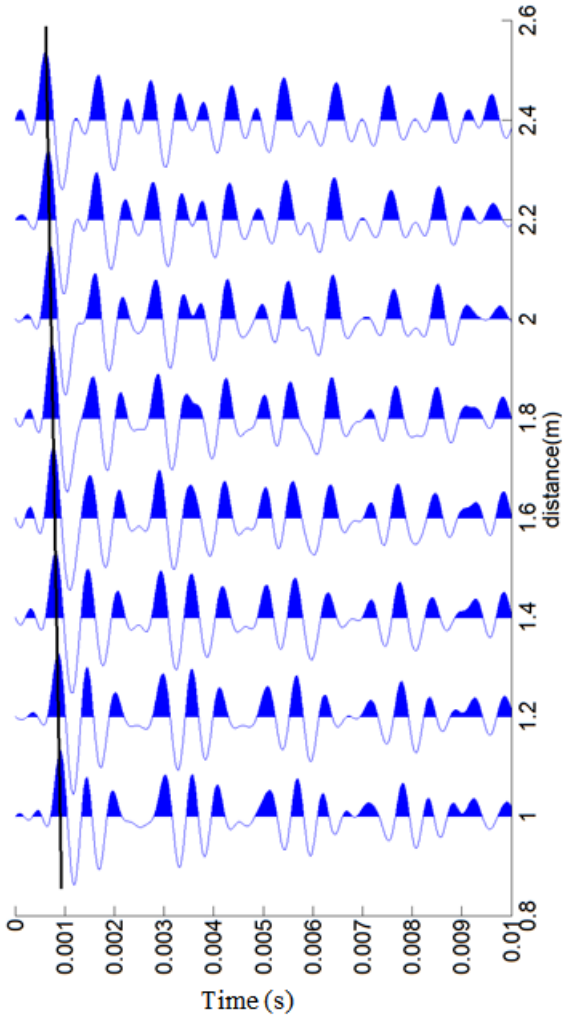

Figure 3-20 Diagram of nodes vs. time

The displacements from these nodes in the longitudinal direction were obtained from ANASYS to investigate the wave behaviour. Accelerations of the selected nodes were calculated by double differential and plotted in time versus nodes location diagram. The peaks indicate the time that the wave arrived at specific nodes. All the peaks were connected by a line and the slope of the line represented the average velocity of the wave propagated in the pole. Figure 3-20 shows an example of this method to calculate the wave velocity based on eight nodes. Through this method, the wave velocity can be calculated and compared under different material parameter scenarios.

3.4.1.1 Elastic Modulus

Both the isotropic and orthotropic models were considered to investigate the elasticity modulus influence on the wave behaviour. Three sets of data were used to compare the elastic modulus influences on the wave velocity. The parameters were selected within

the range of elastic modulus for Spotted Gum and were listed in tables. The elastic modulus for orthotropic material is independent of the directions of three orthogonal axes, therefore, the study along three directions was considered to find if a change in elastic modulus in each direction influenced the wave velocity. The time history diagram shows the wave signal that was captured by the measurement point located at 1.6m from the bottom of the pole.

Table 3-4 Parametric study of elastic modulus for isotropic model

Elastic modulus (MPa)	Reduction percentage (%)	Wave velocity (m/s)	Percentage change (%)
23,000	NA	4920	NA
21,000	8.7	4649	5.51
18,000	21.7	4306	12.5

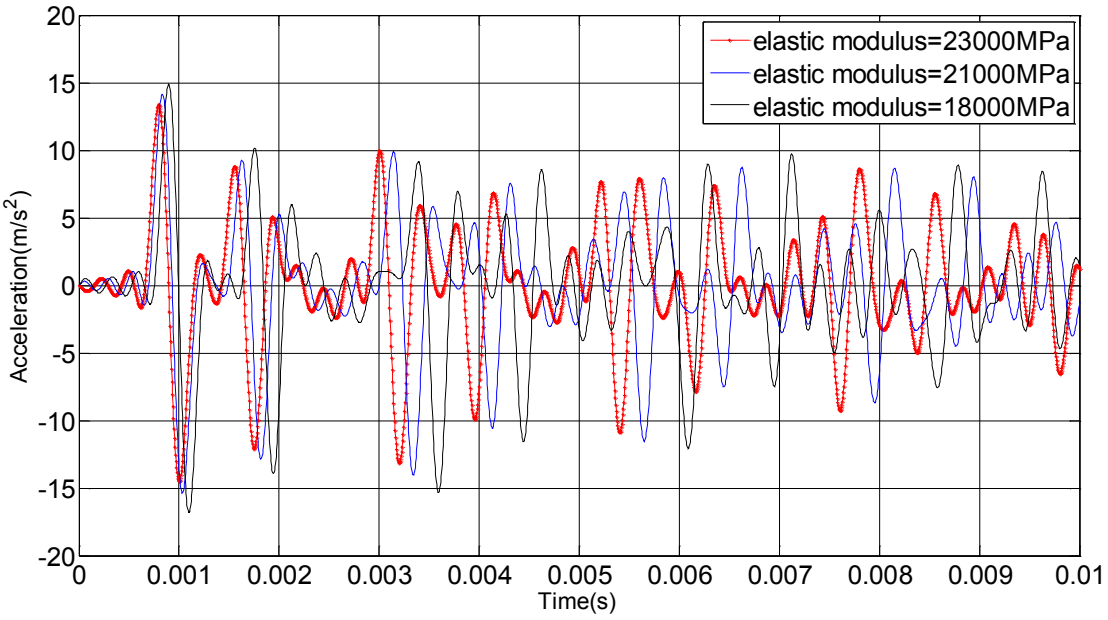

Figure 3-21 Elastic modulus influences on wave behaviour in isotropic material

In Table 3-4, reduction percentage shows the reduction ratio of the elastic modulus within the three models. Also the percentage change compares the velocity change ratio among the three models when the elastic modulus changes. It can be observed that if other parameters (for example density and Poisson's ratio) are set for the isotropic material, the higher elastic modulus will cause higher wave velocity. Figure 3-21 shows the time history diagram of wave signal captured at the measurement point. The dark

line illustrates the elastic modulus of 23,000MPa condition, the light solid line shows the elastic modulus of 21,000MPa and the dotted line represents the elastic modulus of 18,000MPa. The first peak of the curve indicates that at the specific time, wave propagates to the sensor location for the first time. From the figure, the dark curve reaches the peak firstly and is followed by the light solid curve and then dotted curve, which present the calculation results graphically confirming that higher elastic modulus will result in the higher wave velocity. It also can be found in the figure that the delay of wave peaks appearing is more obvious within the three materials after the waves travel up and down the poles several times.

Table 3-5 Parametric study of elastic modulus for orthotropic model (longitudinal direction)

Elastic modulus (MPa)	Reduction percentage (%)	Wave velocity (m/s)	Percentage change (%)
23,000	NA	5000	NA
21,000	8.7	4783	4.34
18,000	21.7	4410	11.8

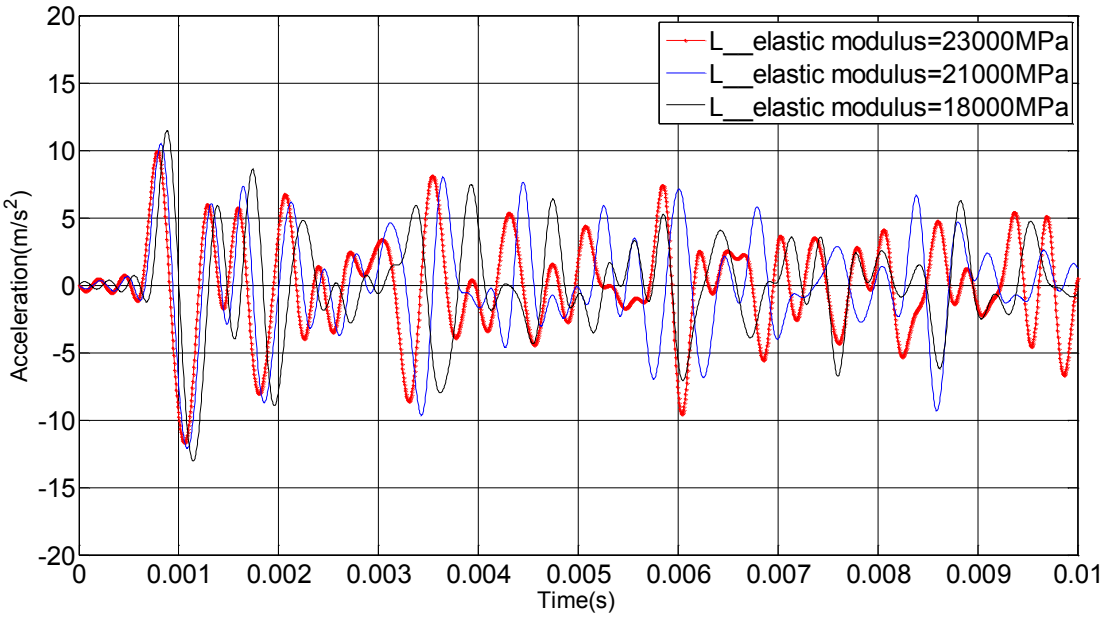

Figure 3-22 Elastic modulus in longitudinal direction influences on wave behaviour in orthotropic material

Table 3-6 Parametric study of elastic modulus for orthotropic model (radial direction)

Elastic modulus (MPa)	Reduction percentage (%)	Wave velocity (m/s)	Percentage change (%)
1955	NA	5000	NA
1785	8.7	5000	0
1531	21.7	5000	0

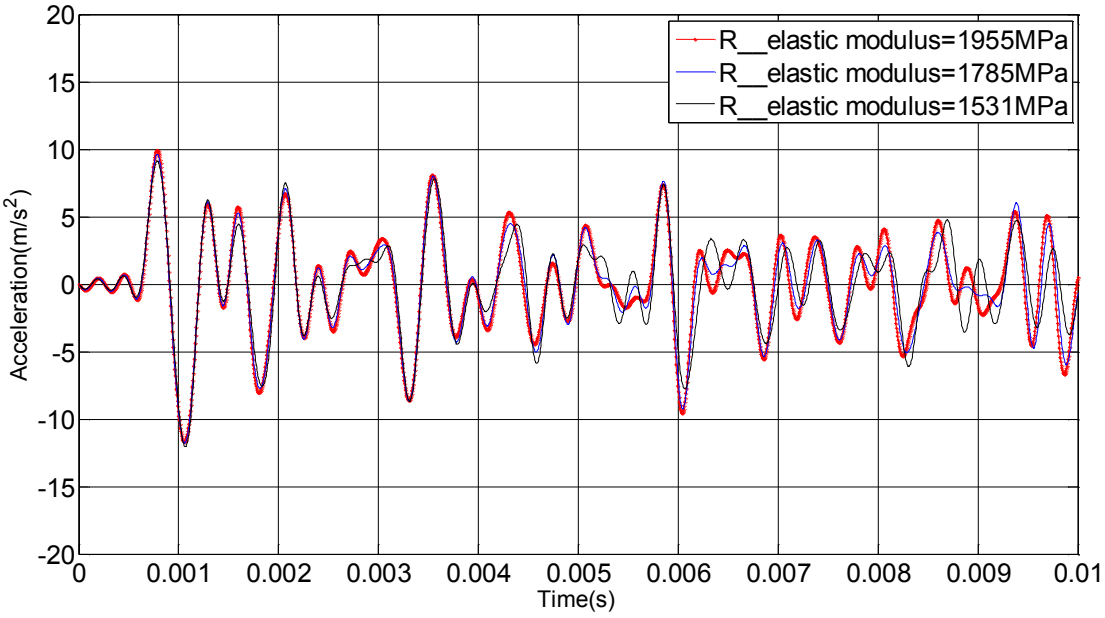

Figure 3-23 Elastic modulus in radial direction influences on wave behaviour in orthotropic material

Table 3-7 Parametric study of elastic modulus for orthotropic model (tangential direction)

Elastic modulus (MPa)	Reduction percentage (%)	Wave velocity (m/s)	Percentage change (%)
850	NA	5000	NA
776	8.7	5046	0.92
665	21.7	5044	0.88

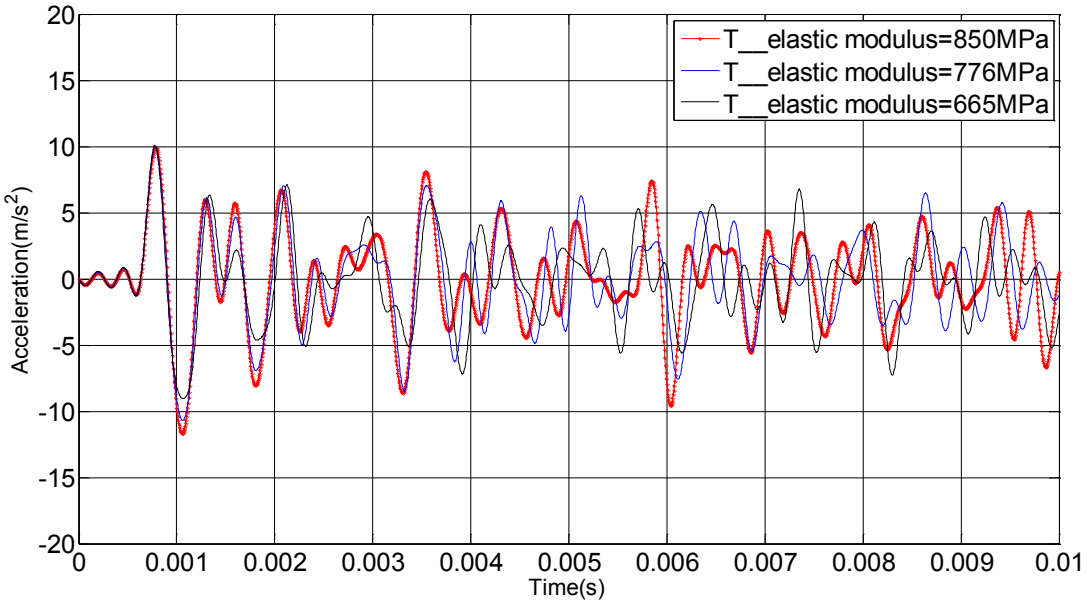

Figure 3-24 Elastic modulus in tangential direction influences on wave behaviour in orthotropic material

For the orthotropic material model, the elastic modulus in the longitudinal direction (Table 3-5) plays a more important role in changing wave velocity, and the phenomenon is quite similar to the isotropic model. The changes in elastic modulus in the radial and tangential directions provide less influence on wave velocity. In Figure 3-23 and Figure 3-24, it is illustrated that the first peak of the curves are totally overlapped; however, according to the shape of the wave patterns in these two figures, the wave propagation is slightly affected by the changes of elastic modulus in the tangential direction.

As it was mentioned previously, longitudinal waves are mainly studied in this research. Velocity of longitudinal waves highly depends on the elastic modulus in longitudinal direction. Damage or decay may lead to change of elastic modulus of material in different degrees. In this context, the elastic modulus in the longitudinal direction is more sensitive to the decay than the ones in other directions. The general relationship between strength and the effect of decay indicates that an initial rapid loss of strength occurs in the early stages and then this is followed by a gradual decrease in the rate of the strength loss at higher weight losses (Ouis, 1999, Kim et al., 1994). As a result, for the purpose of damage detection, further research in parameter study of elastic modulus needs to be done experimentally to investigate the wave behaviour signatures in a specific strength scenario.

3.4.1.2 Density

After considering the parameter of elastic modulus influences on wave behaviour, the parameter of density was considered. The parameters were selected within the range of density for Spotted Gum as listed in Table 3-8 and Table 3-9. The isotropic model and orthotropic model were imported, respectively. The same measurement point as the parametric study of elastic modulus was used to record the time history of wave propagation.

Table 3-8 Parametric study of density for isotropic model

Density (kg/m^3)	Reduction percentage (%)	Wave velocity (m/s)	Percentage change (%)
950	NA	4920	NA
1050	8.7	4685	4.8
1150	17.4	4428	10

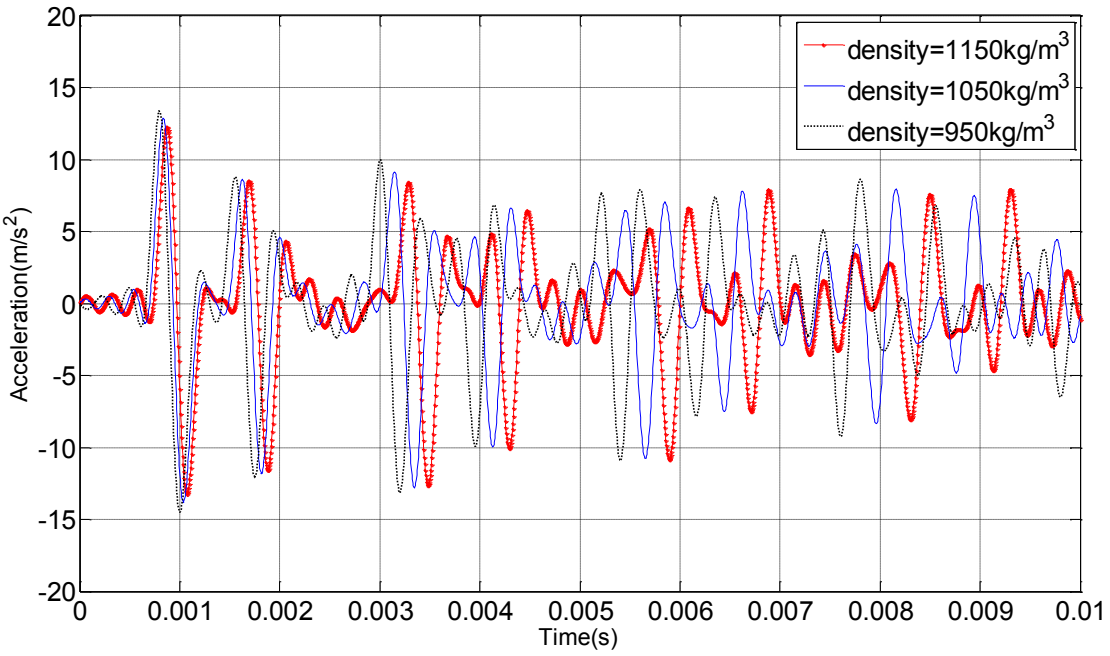

Figure 3-25 Density influences on wave behaviour in isotropic material

Table 3-9 Parametric study of density for orthotropic model

Density (kg/m³)	Reduction percentage (%)	Wave velocity (m/s)	Percentage change (%)
950	NA	5000	NA
1050	8.7	4789	4.22
1150	17.4	4619	7.62

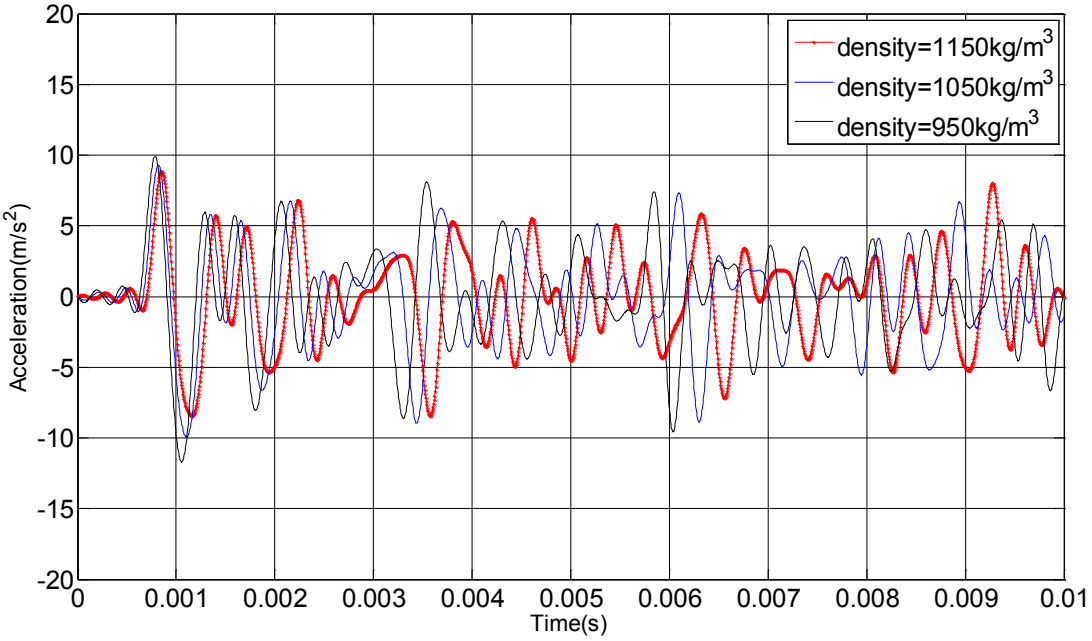

Figure 3-26 Density influences on wave behaviour in orthotropic material

In Figure 3-25 and Figure 3-26, the dotted curve reaches the peak first and is followed by the light solid curve and then the dark dotted curve, which intuitively demonstrates the calculation results in Table 3-8 and Table 3-9; higher wave velocity can be obtained from the model with lower density regardless of the material characteristics. It should be noticed that decay of wood will cause the strength loss at first and then a gradual decrease in the rate of the strength loss at higher weight losses as mentioned before. The range of parametric study for density in this paper is within the intact pole of Spotted Gum. The lower limit of the density is still higher than intact soft wood. If there is decay in the wood, the density of the decayed wood should be much lower than the intact wood; as a result, a wider range of density parameter should be studied in future for damage detection.

3.4.1.3 Poisson's ratio

Poisson's ratio is normally set as 0.3 for the isotropic model; as there is no reference range of Poisson's ratio for the same species of wood, 0.35 was set for comparison. In the orthotropic model, three independent Poisson's ratios obtained from related literature were firstly defined for three directions, and then the Poisson's ratios obtained from experimental testing were used for comparison to investigate the wave behaviour under different sets of Poisson's ratio. The same measurement point mentioned before was used to indicate the time history.

Table 3-10 parametric study of Poison's ratio for isotropic model

Poisson's ratio	Wave velocity (m/s)	Percentage change (%)
0.3	4920	NA
0.35	4879	0.83

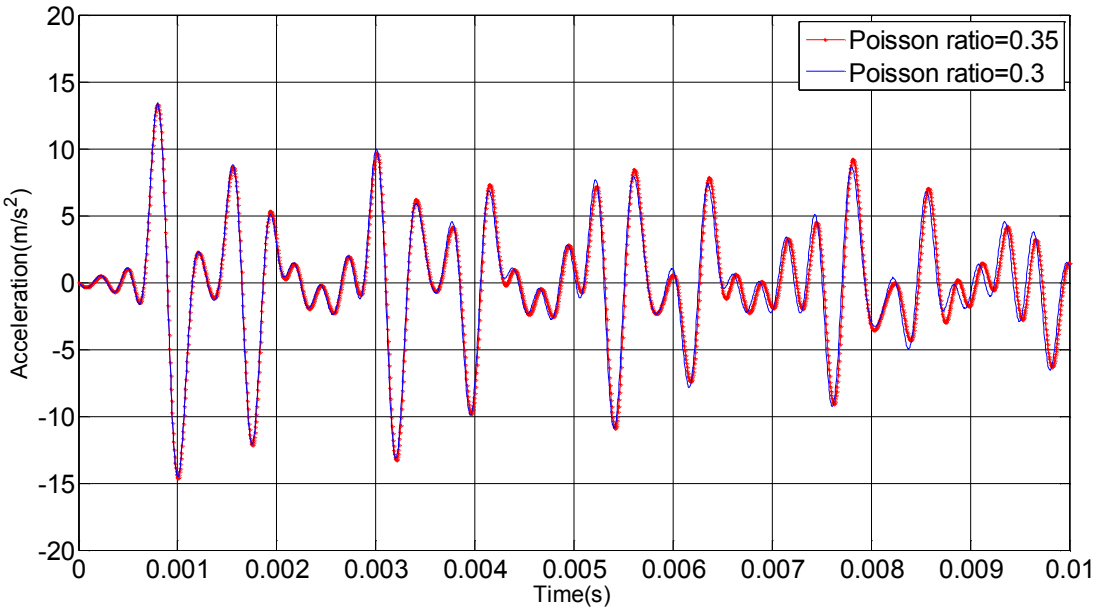

Figure 3-27 Poisson's ratio influences on wave behaviour in isotropic material

Table 3-11 Parametric study of Poison's ratio for orthotropic model

Poisson's ratio			Wave velocity (m/s)	Percentage change (%)
ν_{RL}	ν_{RT}	ν_{TL}		
0.044	0.682	0.023	5000	NA
0.04	0.66	0.05	4874	2.52

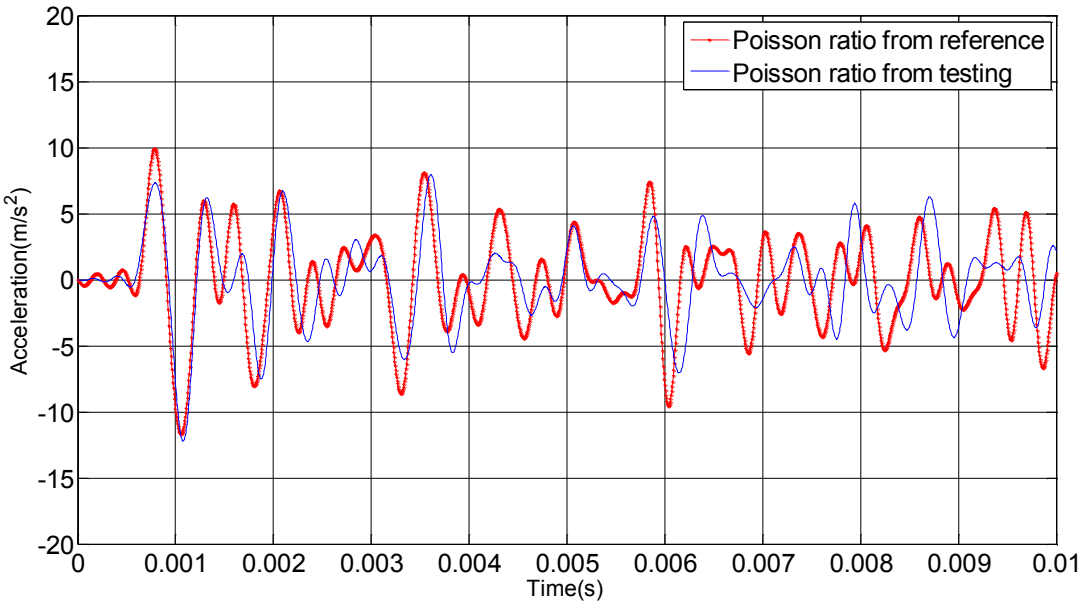

Figure 3-28 Poisson's ratio influences on wave behaviour in orthotropic material

From Table 3-10, the longitudinal wave velocity did not change much due to the change of Poison's ratio for the isotropic model. In Figure 3-27, the dark red curve shows Poison's ratio of 0.35 and light blue solid curve shows the ratio of 0.3. It can be seen that the two curves are almost overlapped at this measurement point. For the orthotropic model (Table 3-11), as can be observed, the Poisson's ratio in the longitudinal and radial direction were quite similar, however, in the tangential direction, the ratio changed by almost 50%, and the longitudinal wave velocity changed accordingly. From Figure 3-28, it can be found that the wave pattern also changed slightly due to the change of Poisson's ratio. A conclusion can be drawn that longitudinal wave velocity is more sensitive to the Poisson's ratio in the orthotropic model than in the isotropic model.

Through the parametric study above, some conclusions can be drawn:

1 higher elastic modulus (longitudinal direction for orthotropic material) always yields higher wave velocity regardless of the material characteristics
2 elastic modulus changes in the radial and tangential directions for the orthotropic material have less influence on longitudinal wave propagation
3 lower density will always generate higher wave velocity regardless of the material characteristics
4 change of elastic modulus and density has less influence on the wave velocity for the orthotropic material models compared with the isotropic material models. For example, the percentage change of the wave velocity is 10% for the isotropic model with density reduction percentage of 17.4%, while the percentage change of the wave velocity is 7.62% for the orthotropic model under the same reduction percentage of density. However, change of Poisson's ratio for the orthotropic material model has more effects on the wave velocity than for the isotropic model.

3.5 INFLUENCE OF IMPACT LOCATION ON WAVE PROPAGATION

3.5.1 Introduction

One of most challenging issues of this research is caused by the practical restriction to where stress waves can be generated. In laboratory testing, a 5m long pole is always used because of the limitation of the ceiling height. Impact on the top of the pole will generate a pure longitudinal wave, which makes analysis of wave behaviour straightforward. However, in-situ utility poles are normally 12m long with 1.2-1.5m embedment length, which makes top excitation unfeasible due to practical restrictions. Therefore, the excitation was imparted at 1.5 m from the ground level at an angle of 45 degrees through a waveguide, and it caused more complicated problems. To investigate the wave propagation behaviour caused by different excitation locations, a series of numerical models were created.

To study and investigate the wave propagation behaviour, different impact locations were created including top impact (for 5m pole), top side impact with 45 degrees (for 5m pole) and side impact with 45 degrees (for 12m pole). The impact was imparted on the node at the top centre with load F to simulate the top impact (Figure 3-29 (a)). The impact on the node at the top side of the pole with incline load F was applied to

simulate top side impact (Figure 3-29 (b)). In ANSYS, the incline load F amount can be defined as corresponding component loads in horizontal and vertical directions (x and y direction). In addition impact on the node at the side surface of the pole can be used to simulate the field testing for 12m poles (Figure 3-29 (c)). The isotropic model was 5m with 1m embedded in the soil and all material properties were the same as with previous studies. Wave signals were captured by the measurement point at 1.6m from the bottom of the pole. The results from these numerical models were discussed and compared with analytical results according to the wave theory.

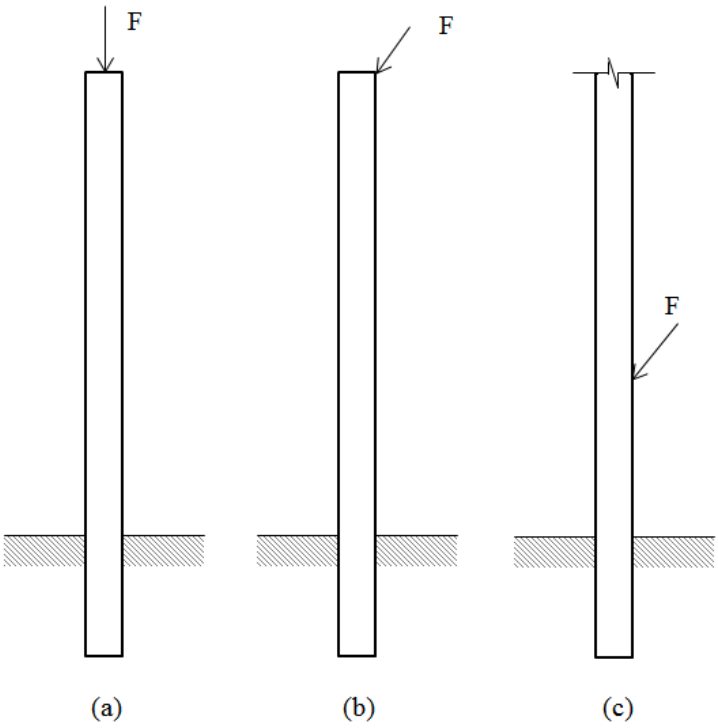

Figure 3-29 Three different impact locations

3.5.2 Influence of impact location on wave propagation

3.5.2.1 Study of wave behaviour in isotropic material model

Guided wave (Dieulesaint and Royer, 1980) propagation in a structure combined different types of wave shapes due to the wave reflection from boundaries (Graff, 1975). The function of displacement components for a GW in an isotropic cylindrical coordinate system (r, θ, z) is provided by Hanifah (Hanifah, 1999) as below,

$$u_r = \left[A_1 \alpha Z_p'(\alpha r) - A_4 \xi Z_p'(\beta r) + A_6 \left(\frac{p}{r}\right) Z_p(\beta r)\right] \cos p\theta \; e^{i(\xi z - \omega t)}, \quad \text{Eq. 3-4}$$

$$u_\theta = \left[-A_1 \left(\frac{p}{r}\right) Z_p(\alpha r) + A_4 \left(\frac{p\xi}{\beta r}\right) Z_p(\beta r) - A_6 \beta Z_p'(\beta r)\right] \sin p\theta \; e^{i(\xi z - \omega t)}, \quad \text{Eq. 3-5}$$

$$u_z = i\left[-A_1 \xi Z_p(\alpha r) - A_4 \beta Z_p(\beta r)\right] \cos p\theta \; e^{i(\xi z - \omega t)} \quad \text{Eq. 3-6}$$

where u_r, u_θ and u_z are the displacement components along radial, tangential and longitudinal directions. Z is the ordinary and modified Bessel function of the first kind and A1, A4 and A6 are undetermined coefficients. A1 represents longitudinal effects while A4 and A6 represent shear effects. The three equations above identified that if axisymmetric waves (such as longitudinal wave, i.e. p=0) were generated, u_θ components become zero. In other words, in longitudinal waves, the displacement only contains radial and longitudinal components. Moreover, only longitudinal components can be obtained if the waves are captured in the longitudinal direction. However, if non-axisymmetric waves (such as bending wave) were generated (p = 1), the displacement contains all three components (Subhani, 2014). According to the guided wave theory above, the pure longitudinal component of the longitudinal wave can be captured at a specific location.

To verify this phenomenon, two isotropic models with different impact locations were created. The sensors were placed from 1m to 2.4m from the bottom of the pole with the interval distance of 200mm and aligned with the impact line which was named as 0° and the sensor opposite to 0° was set as 180°, while the sensors located between 0° and 180° around the circumference from the impact location was defined as 90° (see Figure 3-30). The setup and the physical parameters were the same as previous models and the wave was captured in the longitudinal direction to obtain the longitudinal components. Firstly, a hammer impact was imparted on the top centre which generates a pure longitudinal wave (Figure 3-30 (a)). Secondly, the impact was applied on the top side with an angle of 45° (Figure 3-30 (b)). In this condition, the longitudinal wave and the bending wave were generated at the same time. Sensors were placed in the longitudinal, radial and tangential directions to capture corresponding wave components as shown in Figure 3-31.

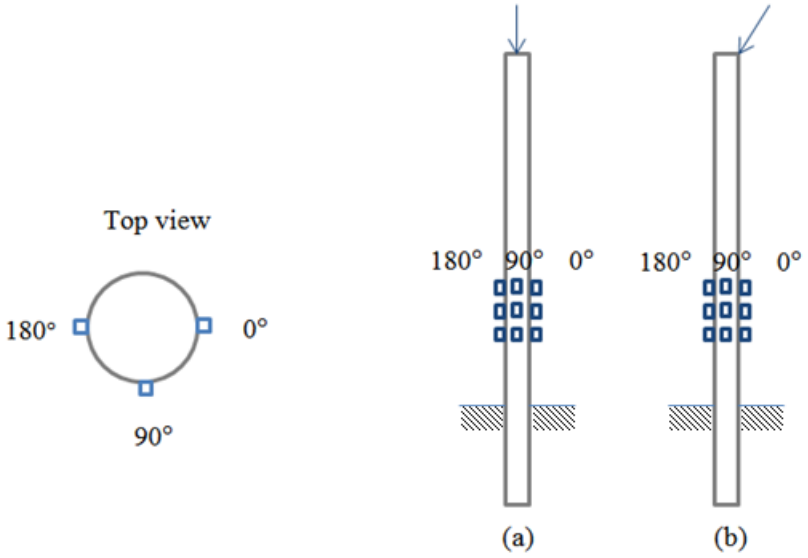

Figure 3-30 Different locations of impact and sensor arrangement

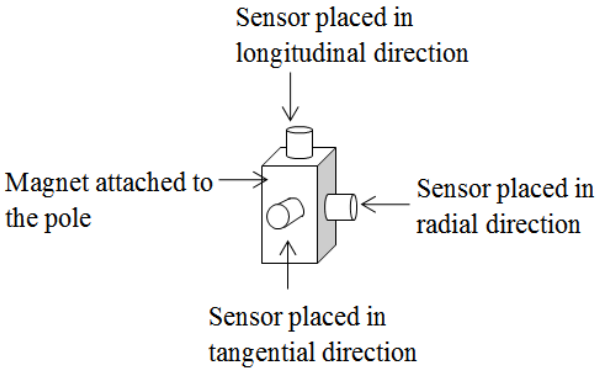

Figure 3-31 Sensor measurement directions

Impact at top centre

Figure 3-32, Figure 3-33 and Figure 3-34 compare the wave patterns captured at 0, 180 and 90 degrees in three orthogonal directions with the height of 1.6m from the bottom of the pole under top centre impact. From these three figures, it can be observed that the value of the tangential component under this impact condition is zero which is consistent with the wave theory that a longitudinal wave does not contain a tangential component but has radial and longitudinal components.

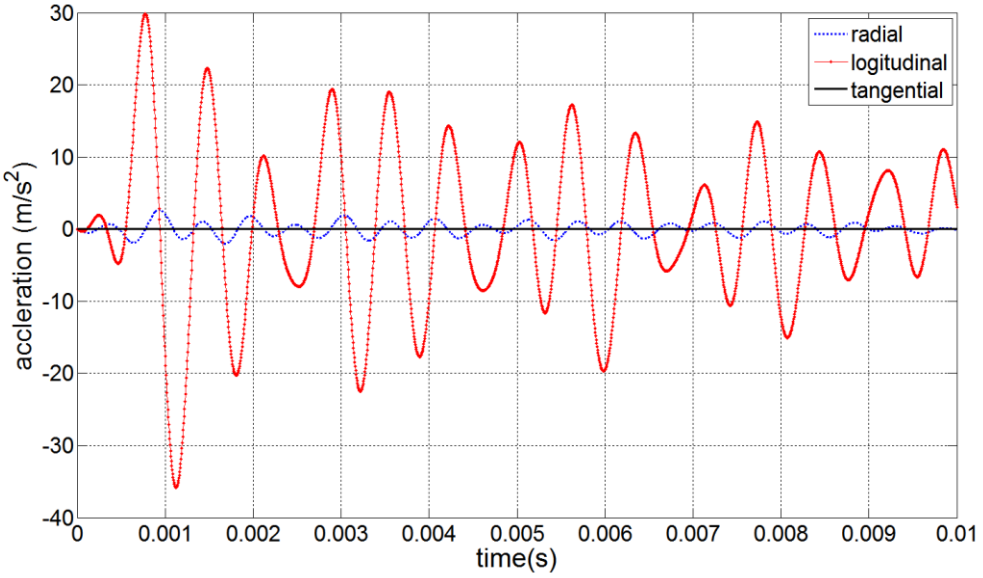

Figure 3-32 Comparison of wave patterns at 0 ° in three orthogonal directions

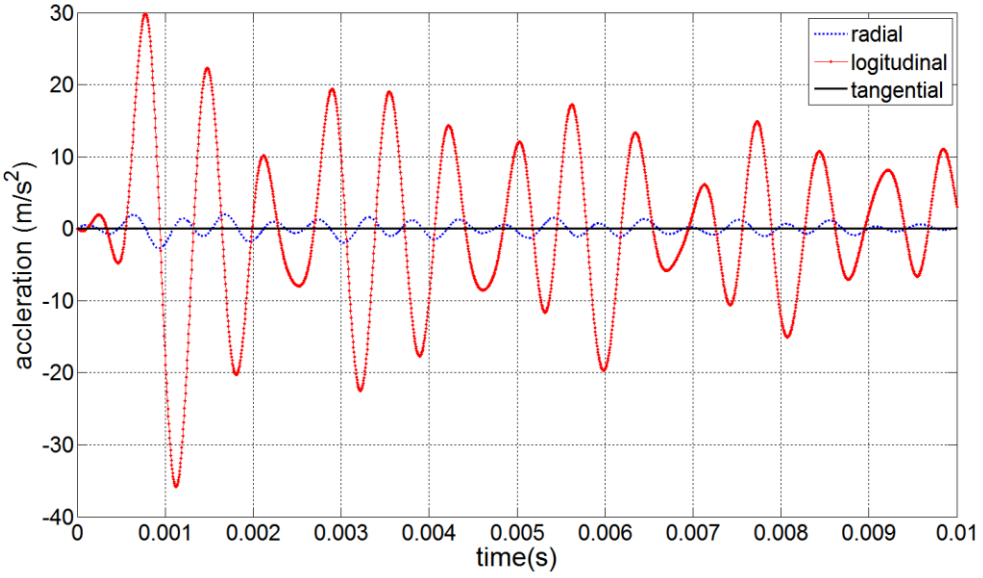

Figure 3-33 Comparison of wave patterns at 180 ° in three orthogonal directions

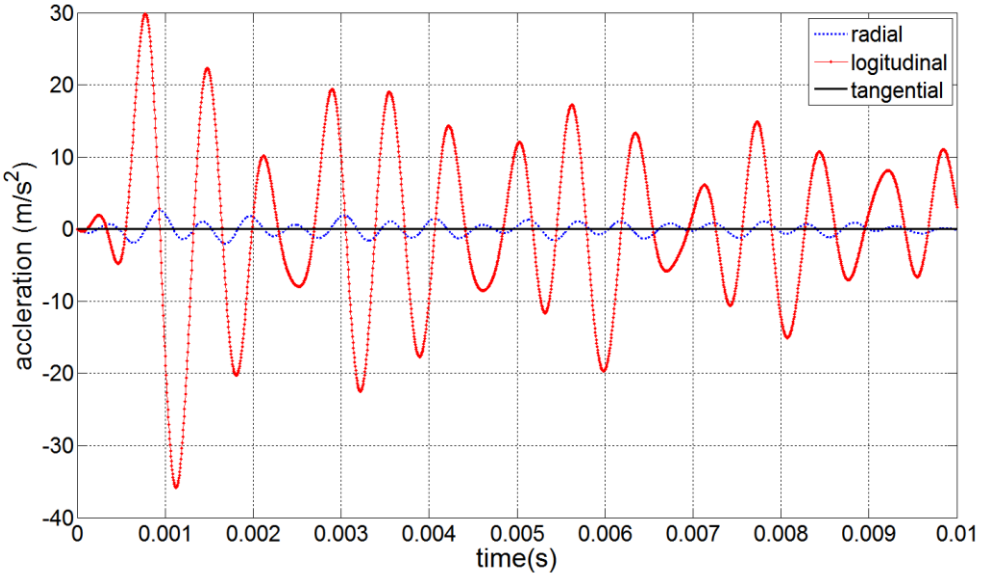

Figure 3-34 Comparison of wave patterns at 90 ° in three orthogonal directions

Figure 3-35 illustrates the comparison of the longitudinal component from the sensors at the same height at 0, 90 and 180 degrees. It can be observed that the wave patterns are the same and overlapped. This indicates that in the longitudinal wave, only the longitudinal component can be obtained if the sensors are placed in the longitudinal direction regardless of the orientation location of the sensors. Figure 3-36 presents the wave patterns captured by all the sensors in the longitudinal direction with the three orientations. It clearly shows that at the same height level the wave patterns are the same regardless of the orientations. This again verifies the wave theory that for the longitudinal waves, in the longitudinal direction, the wave pattern will not be influenced by the orientation.

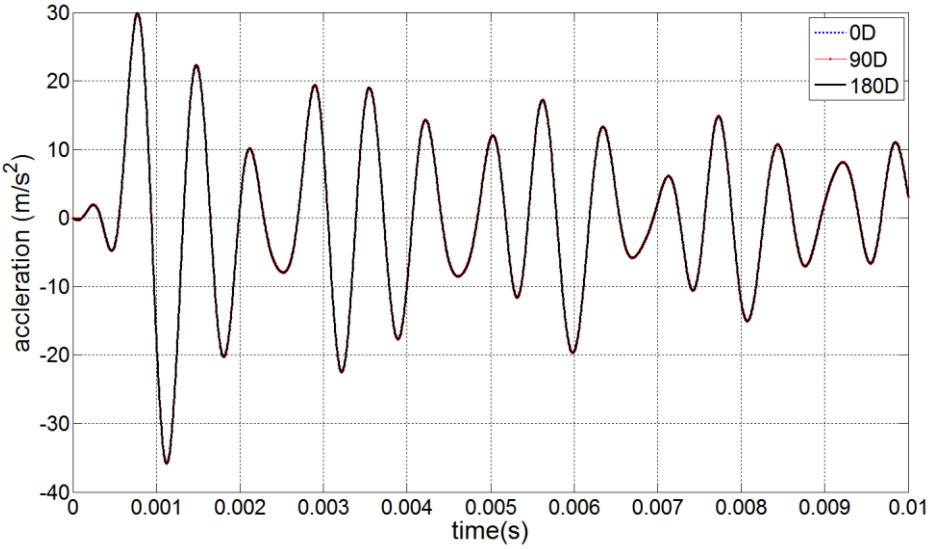

Figure 3-35 Comparison of wave patterns in longitudinal direction

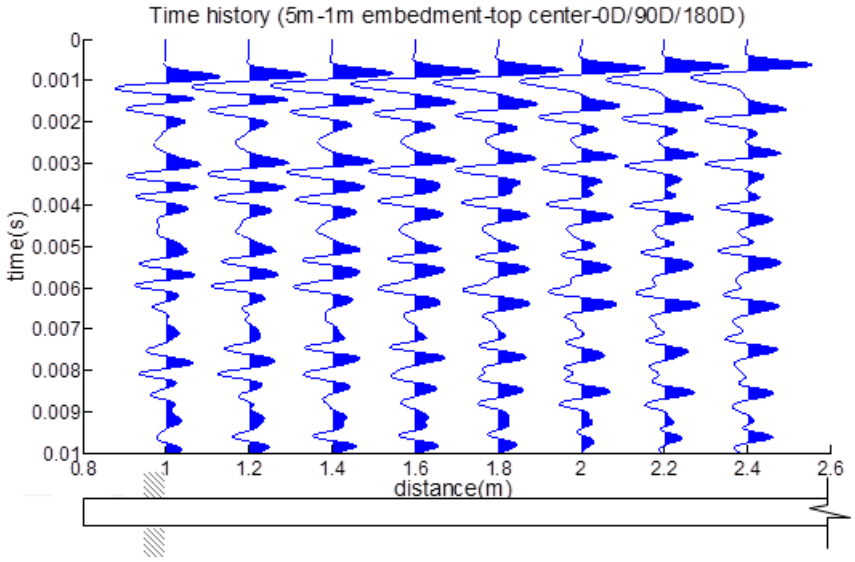

Figure 3-36 Wave patterns captured from all sensors in longitudinal direction with three orientations

Figure 3-37 compares the wave patterns in the radial direction with orientation of 0, 90 and 180 degrees. The radial component of longitudinal wave is presented by measuring the wave signals in the radial direction. The waves have the same phase in three orientation locations even if it presents the opposite phase direction at 0 and 180 degrees due to the contraction effect. Thus, the symmetric behaviour of the longitudinal wave is identified.

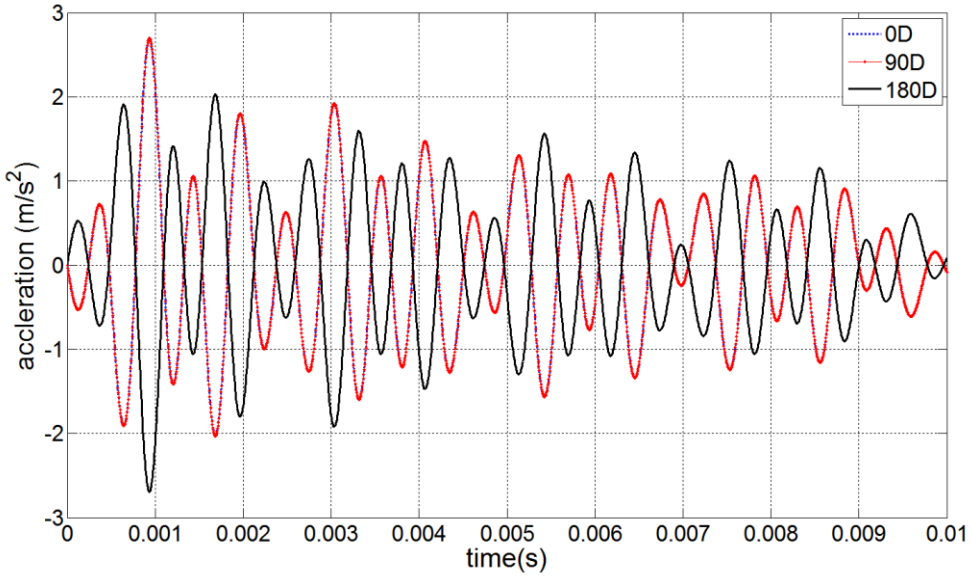

Figure 3-37 Comparison of wave patterns in radial direction

As a conclusion, according to Eq. 3-4 – Eq. 3-6, the circumferential component of the longitudinal wave is zero, and thus the longitudinal wave will not be affected by the impact angle and measurement orientation.

Impact at top side at 45 degrees

Figure 3-38, Figure 3-39 and Figure 3-40 compare the wave patterns captured at 0, 180 and 90 degrees in three orthogonal directions at the height of 1.6m from the bottom of the pole under impact at top side at 45 degrees. Although the wave signal is not as clear as in the previous scenario due to the flexural waves, it still can be observed that at 0 and 180 degrees, the tangential component becomes zero and at 90 degrees all three components appear which is caused by the flexural waves and is in line with the theory and equations mentioned above.

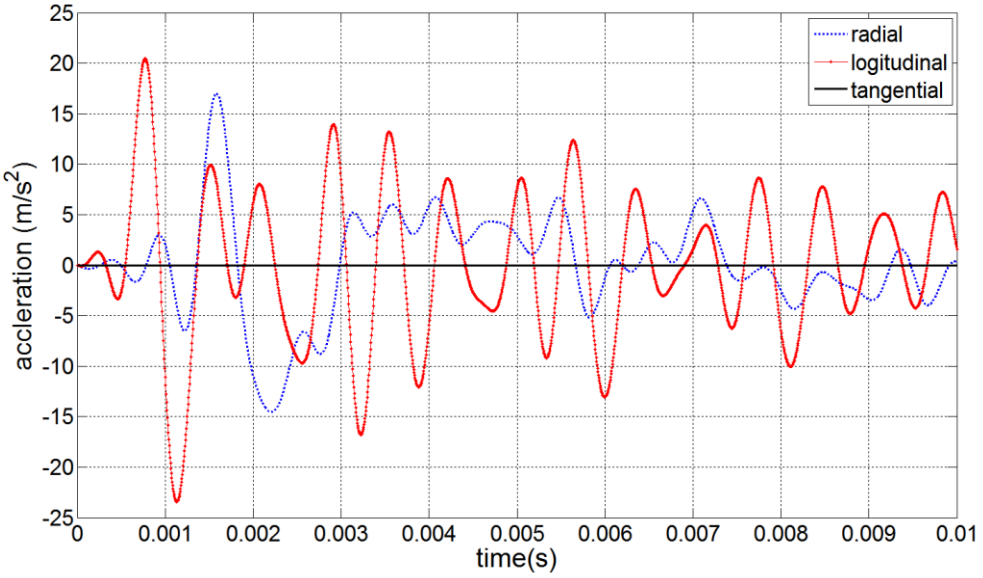

Figure 3-38 Comparison of wave patterns at 0 ° in three orthogonal directions

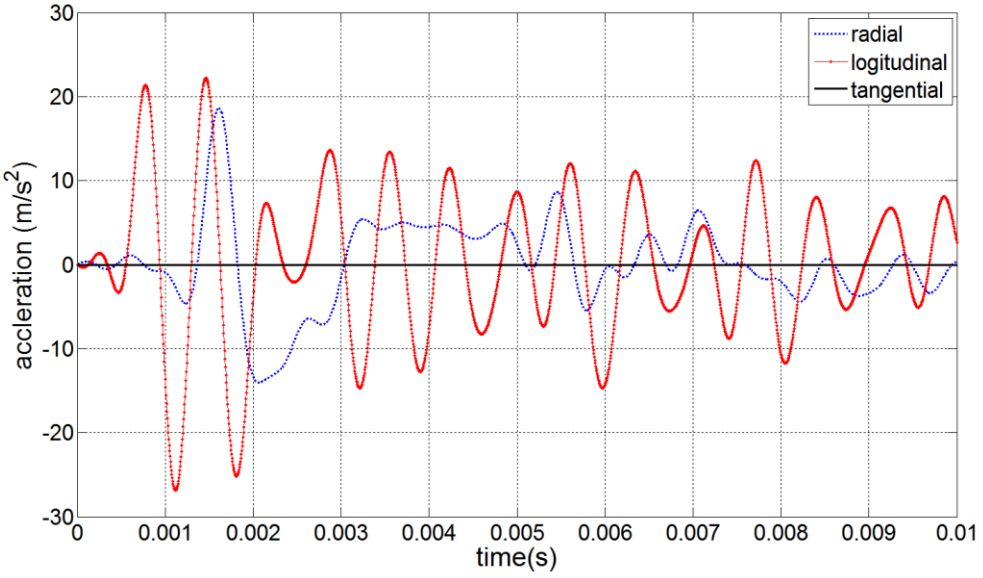

Figure 3-39 Comparison of wave patterns at 180 ° in three orthogonal directions

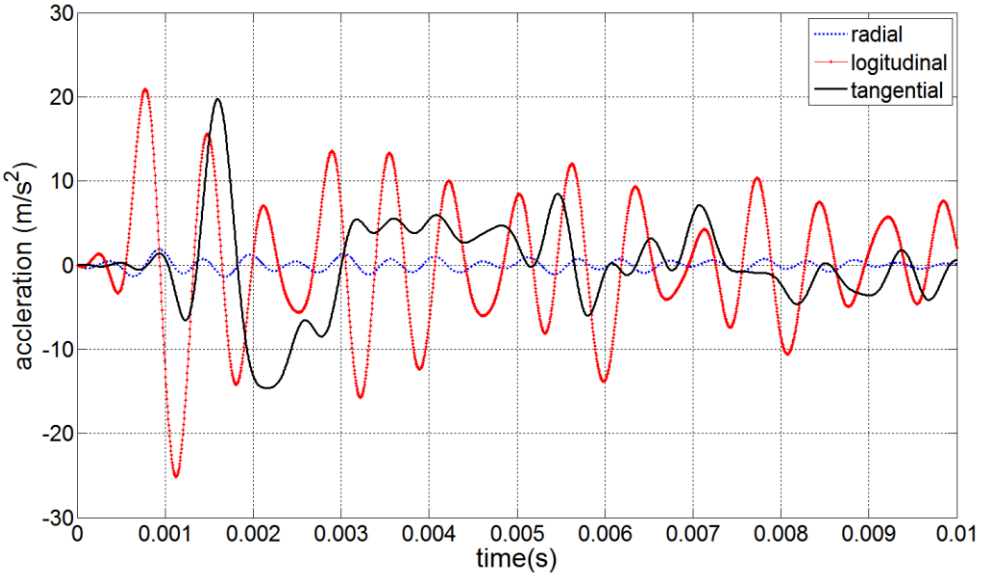

Figure 3-40 Comparison of wave patterns at 90 ° in three orthogonal directions

Figure 3-41, Figure 3-42 and Figure 3-43 compare the wave patterns in longitudinal, radial and tangential directions along three orientations. In the longitudinal direction, the wave patterns are not overlapped along the three orientations. Although the amplitudes of wave patterns are different, the wave velocity is not influenced too much according to the locations of peaks. In the radial direction, the wave patterns at 0 and 180 degrees are almost the same which is due to the flexural wave behaviour.

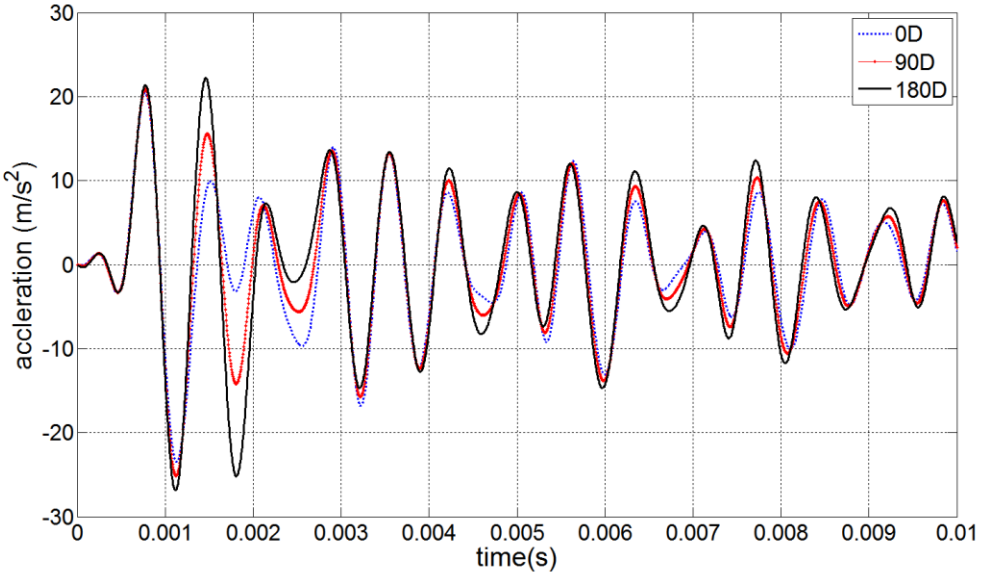

Figure 3-41 Comparison of wave patterns in longitudinal direction

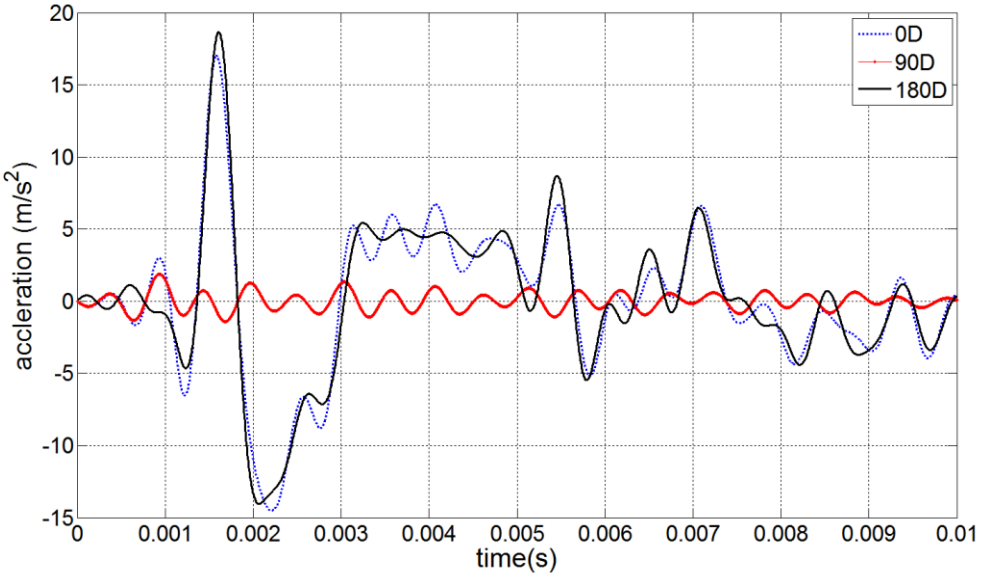

Figure 3-42 Comparison of wave patterns in radial direction

The radial component has small amplitude in longitudinal wave propagation as shown before and confirms that the radial component is dominated by the bending / flexural waves behaviour. According to the Eq. 3-4 – Eq.3-6, the tangential component becomes zero at 0 and 180 degrees and only appears at 90 degrees which is clearly presented in Figure 3-43.

As a conclusion, for the impact at 45 degrees, according to the wave behaviour characteristics, an effective method can be conducted to separate the longitudinal component from the other components at the location of 90 degrees.

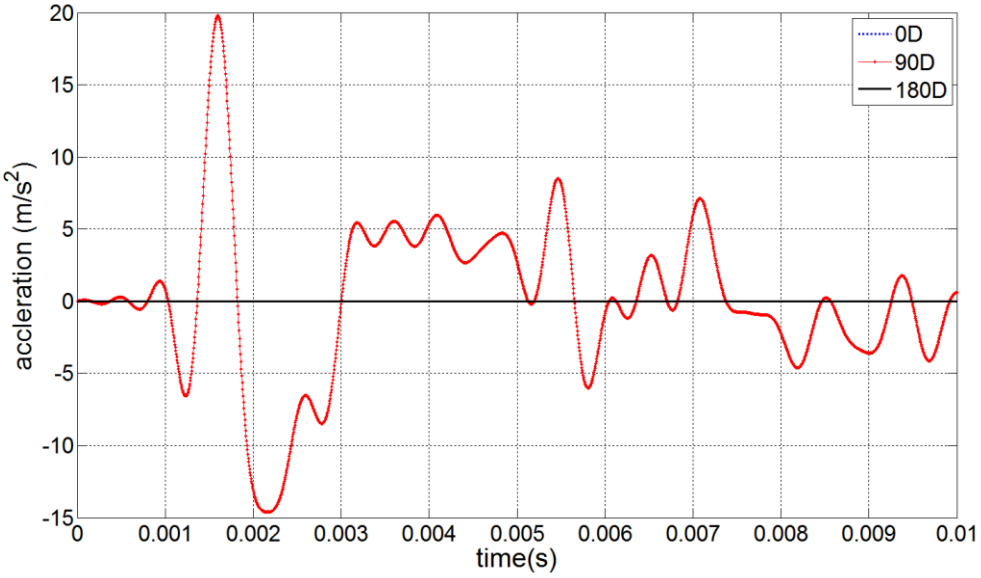

Figure 3-43 Comparison of wave patterns in tangential direction

Wave pattern comparison between different impact locations

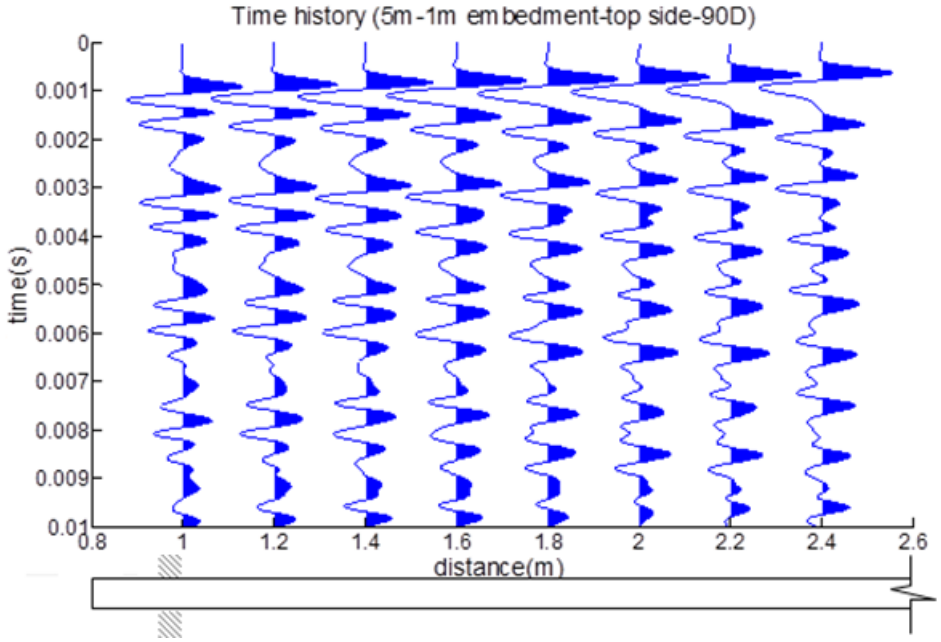

Figure 3-44 Top side impact at 45 ° and measurement in longitudinal direction at 90 °

Figure 3-44 shows the time history of calculated acceleration from all sensors in the longitudinal direction at 90 degrees when impact is at the top side at 45 degrees. To get a clear overview and comparison between the wave signal caused by top side impact and top centre impact, the results of sensors located at 2.4m (sensor1) and 1.6m

(sensor5) from the bottom of the pole were selected and compared between two impact scenarios as shown in Figure 3-45.

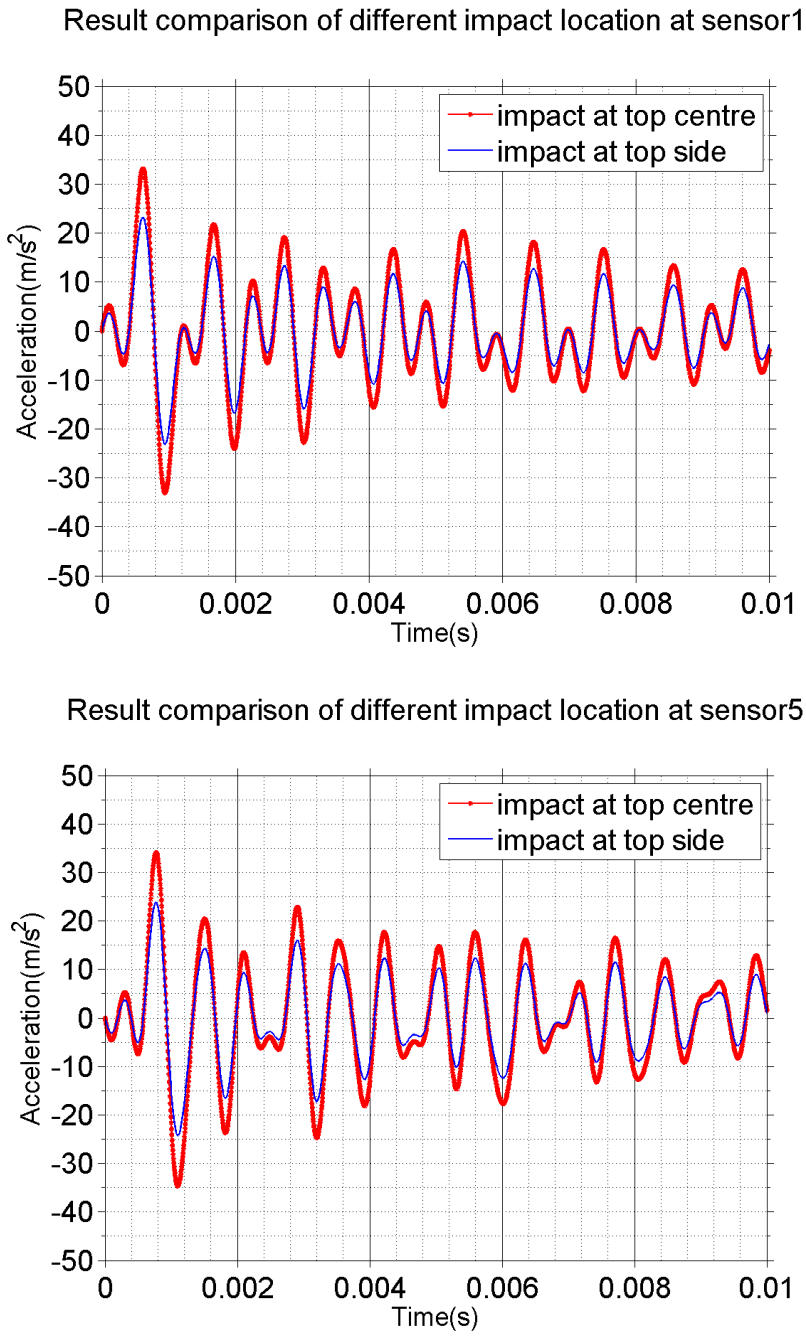

Figure 3-45 Comparison of different impact scenarios via measuring in the longitudinal direction at 90°

From Figure 3-45, it can be seen that the wave patterns are almost the same except for the amplitude. The impact forces for these two scenarios are the same which is around 2kN and to apply the inclined force to the model in ANSYS, the x component and y component force are applied at the same time.

Under this situation, the load in the y direction generating a longitudinal wave by incline impact is smaller than the top centre impact condition. As a result, the amplitude of the longitudinal wave generated from incline impact is smaller than the top centre impact.

From the comparison figure above, a conclusion can be drawn that in the longitudinal direction at 90 degrees, the longitudinal wave can be captured even when the inclined impact is conducted.

3.5.2.2 Study of wave behaviour in transversely isotropic material model

Guided wave propagation in a transversely isotropic cylindrical structure has more complicated behaviour as shown in equations below:

$$u_r = \left\{ \begin{array}{c} A_p\left[\left(s_1\frac{p}{r} + i\xi a s_1\frac{p}{r}q_1\right)J_p(s_1r) + (-s_1 - i\xi a q_1 s_1)J_{p+1}(s_1r)\right] \\ +B_p\left[\left(s_2\frac{p}{r}q_2 + i\xi a s_2\frac{p}{r}\right)J_p(s_2r) + (-s_2q_2 - i\xi a s_2)J_{p+1}(s_2r)\right] \\ +C_p\left[\left(\frac{p}{r}\right)J_p(s_3r)\right] \end{array} \right\} \cos(p\theta)e^{i(\xi z-\omega t)}, \quad \text{Eq. 3-7}$$

$$u_z = \left\{A_p\left[(i\xi + aq_1s_1^2)J_p(s_1r)\right] + B_p\left[(i\xi q_2 + as_2^2)J_p(s_2r)\right]\right\}\cos(p\theta)e^{i(\xi z-\omega t)}, \quad \text{Eq. 3-8}$$

$$u_\theta = \left\{A_p\left[\left(-\frac{p}{r} - i\xi a\frac{p}{r}q_1\right)J_p(s_1r)\right] + B_p\left[\left(-\frac{p}{r}q_2 - i\xi a\frac{p}{r}\right)J_p(s_2r)\right] + C_p\left[\left(-\frac{p}{r}\right)J_p(s_3r) + s_3J_{p+1}(s_3r)\right]\right\}\sin(p\theta)\,e^{i(\xi z-\omega t)} \quad \text{Eq. 3-9}$$

where $q_1$and q_2 are constants that depend on the elastic constants of the material. From the equations above, it can be seen that even though the expression for wave behaviour in a transversely isotropic material is more complicated than the isotropic material, the same behaviour characteristics appear.

Impact at top centre

Figure 3-46 to Figure 3-48 show the comparison of wave patterns under different directions and orientations when longitudinal waves are generated (p = 0) and illustrates the same features as the isotropic model: only longitudinal and radial components are

present; the wave patterns are overlapped in the longitudinal direction regardless of the orientations (Figure 3-49); the wave phase direction has a difference of 180 degrees between orientation of 0 degrees and 180 degrees in measurement of the radial direction (Figure 3-50).

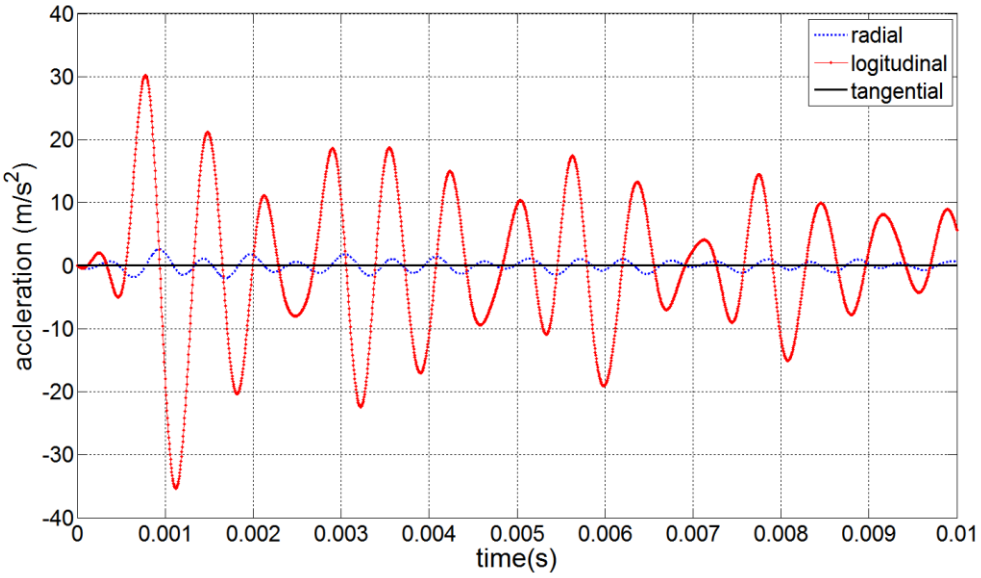

Figure 3-46 Comparison of wave patterns at 0 °in three orthogonal directions (Transversely isotropic model)

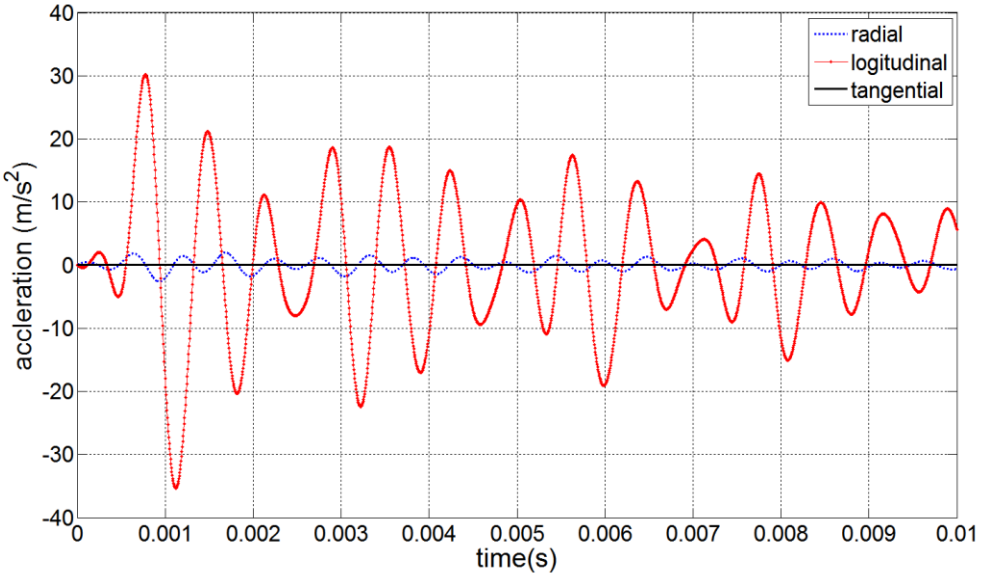

Figure 3-47 Comparison of wave patterns at 180 ° in three orthogonal directions (Transversely isotropic model)

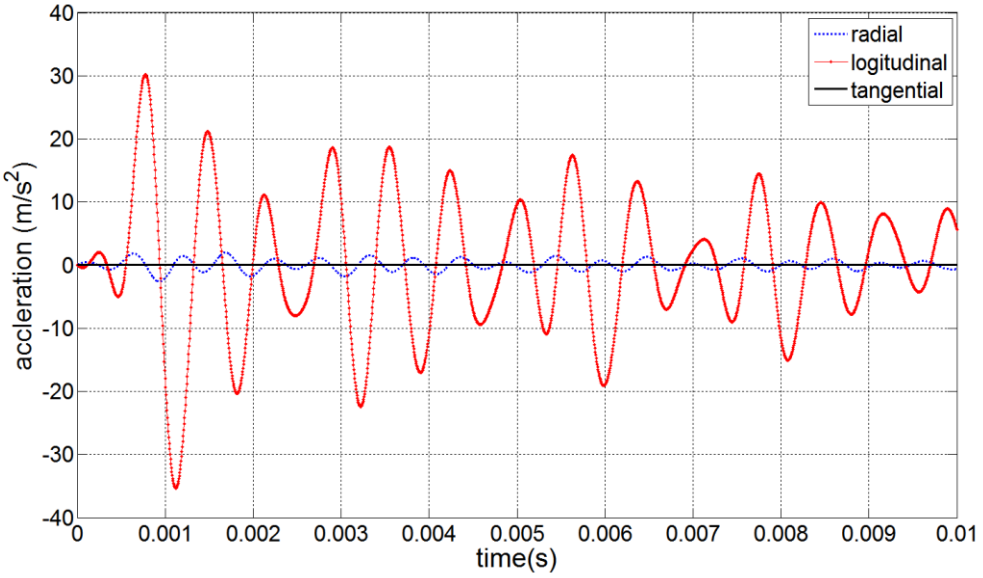

Figure 3-48 Comparison of wave patterns at 90 °in three orthogonal directions (Transversely isotropic model)

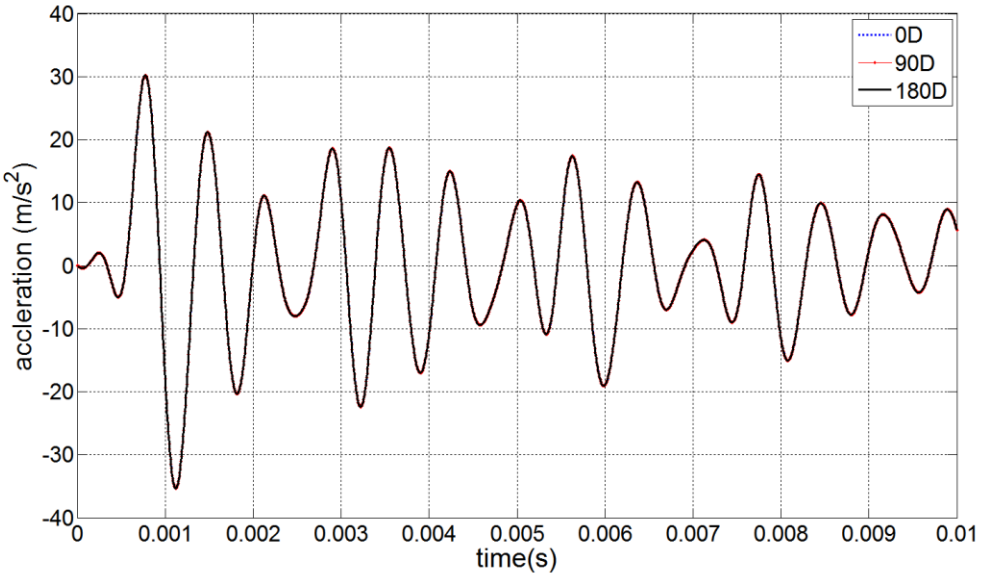

Figure 3-49 Comparison of wave patterns in longitudinal direction (Transversely isotropic model)

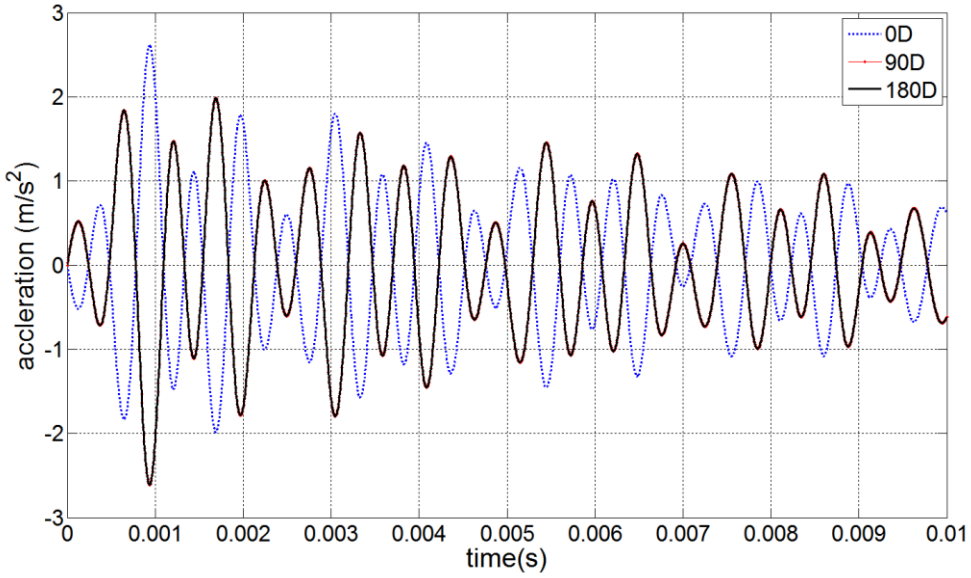

Figure 3-50 Comparison of wave patterns in radial direction (Transversely isotropic model)

Impact at top side at 45 degrees

Figure 3-51 to Figure 3-56 compare the wave patterns under different directions and orientations when flexural waves are generated (p = 1) and the same wave behaviour as the isotropic model can be observed. The tangential component becomes zero at 0 degrees and 180 degrees but appears at 90 degrees which is clearly indicated in Figure 3-51, Figure 3-52, Figure 3-53, and Figure 3-54.

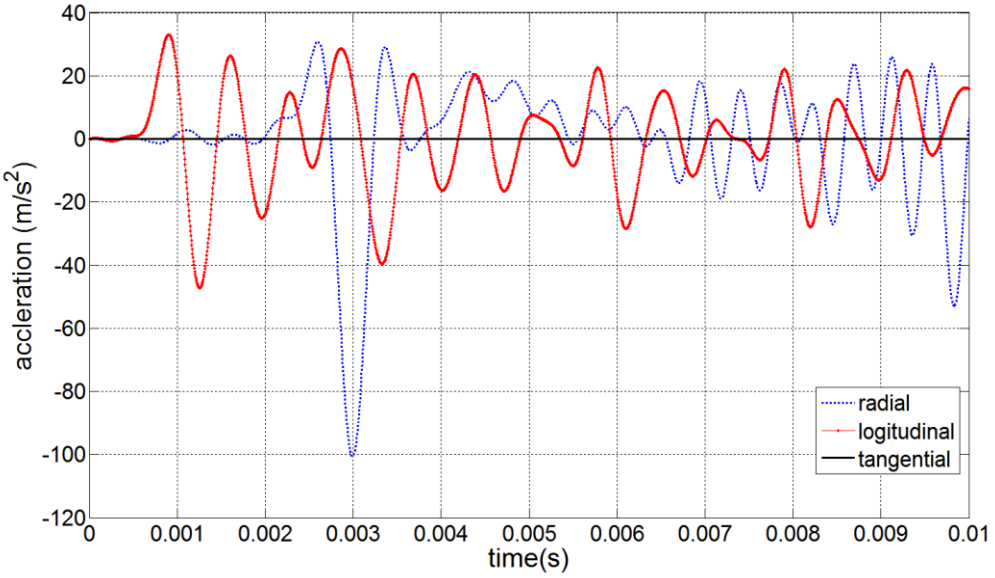

Figure 3-51 Comparison of wave patterns at 0 ° in three orthogonal directions (Transversely isotropic model)

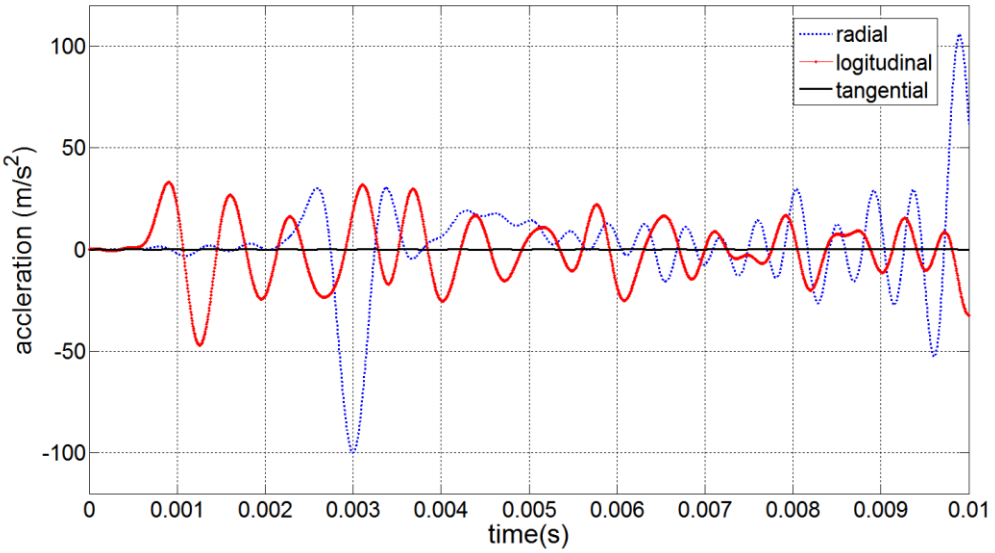

Figure 3-52 Comparison of wave patterns at 180 ° in three orthogonal directions (Transversely isotropic model)

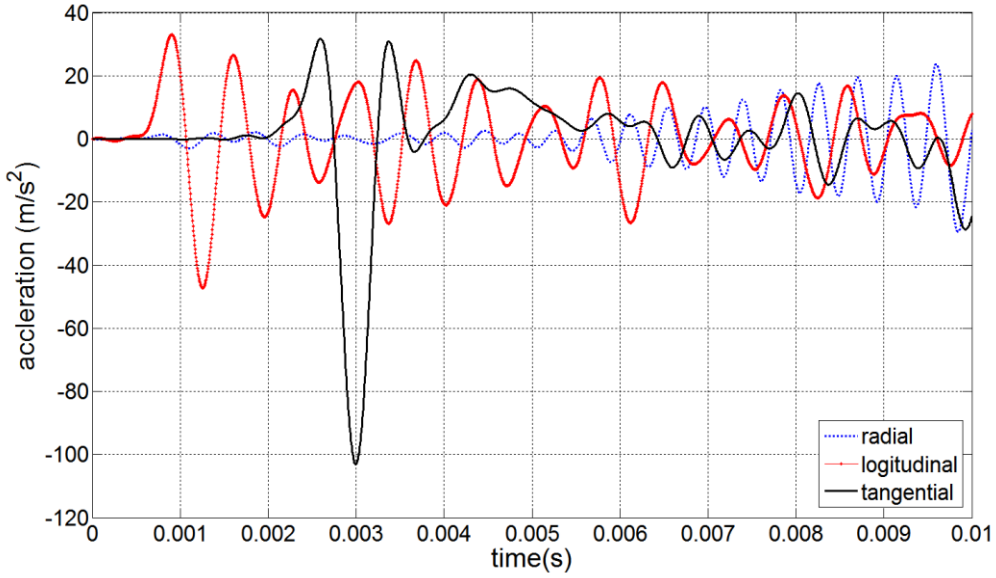

Figure 3-53 Comparison of wave patterns at 90 °in three orthogonal directions (Transversely isotropic model)

Figure 3-54 presents the wave patterns in the longitudinal direction at three orientations and it can be seen that the wave patterns are not overlapped. Both the amplitudes and peak locations are different from each other which indicates that the characteristics of the transversely isotropic material will affect the wave speed in the propagation directions and this will be identified in the next step. In the radial direction, the wave patterns also confirm that the wave behaviour is influenced by the transversely isotropic material properties as shown in Figure 3-55. Also the tangential component becomes zero at 0 and 180 degrees and only appears at 90 degrees (Figure 3-56) which is clearly the same phenomenon as the isotropic model.

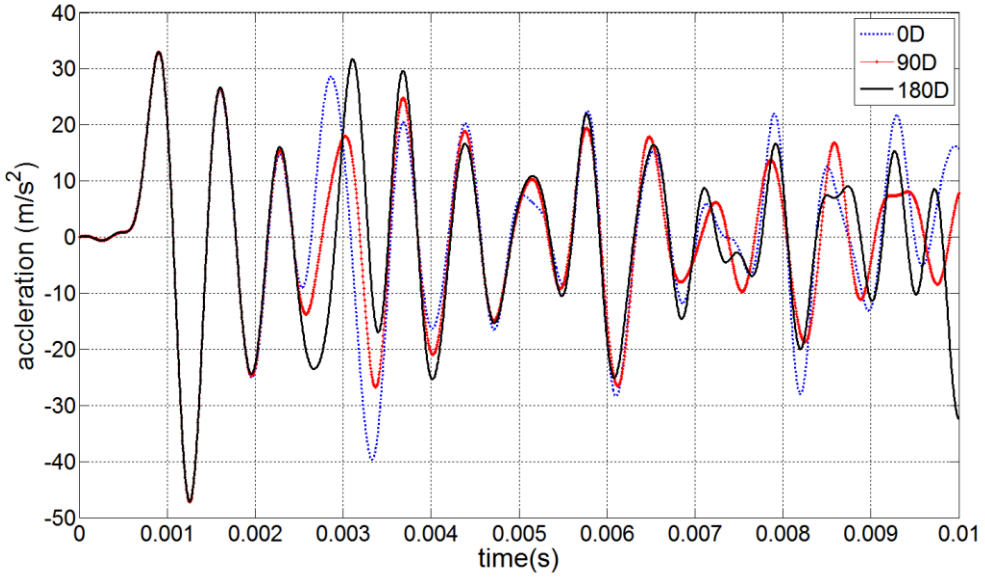

Figure 3-54 Comparison of wave patterns in longitudinal direction (Transversely isotropic model)

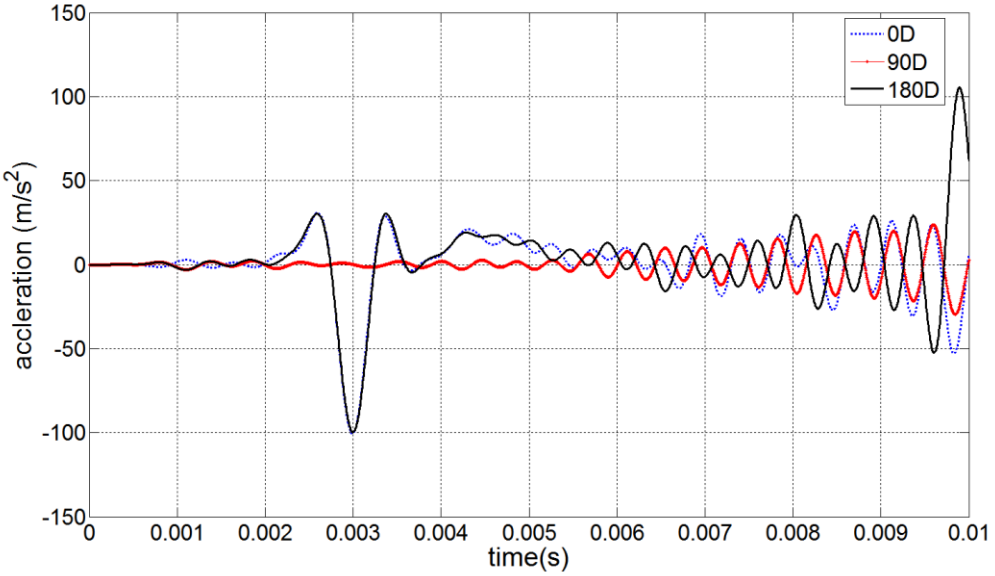

Figure 3-55 Comparison of wave patterns in radial direction (Transversely isotropic model)

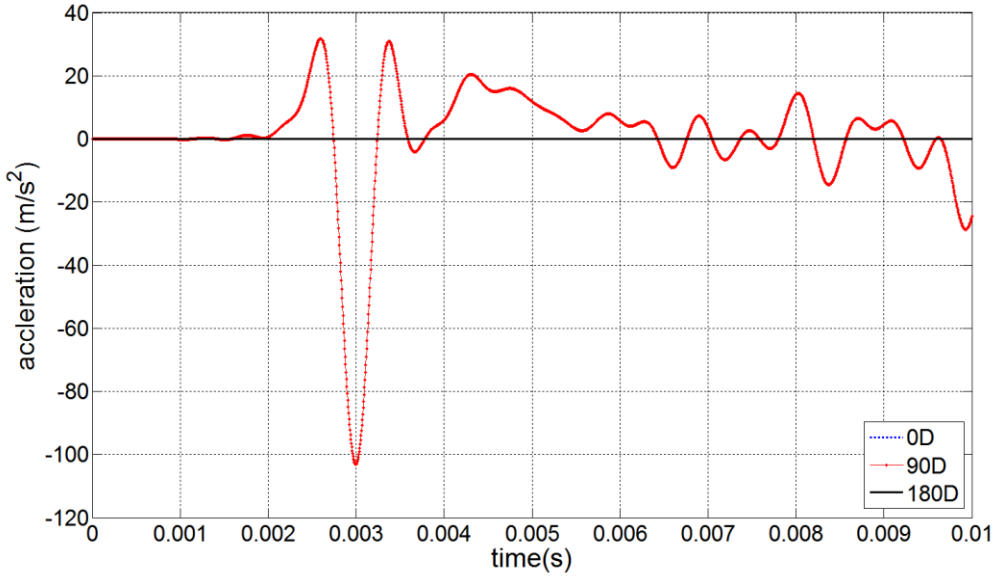

Figure 3-56 Comparison of wave patterns in tangential direction (Transversely isotropic model)

Wave pattern comparison between different impact locations

In the longitudinal direction at 90 degrees, the longitudinal component can be obtained in the transversely isotropic model according to the equations in this section. Figure 3-57 compares the longitudinal wave patterns captured from the same sensor under top centre impact and topside impact. The dotted curve representing top side impact is delayed comparing with the solid curve referring to top centre impact. This phenomenon explicitly demonstrates that in a transversely isotropic material, the wave propagation is affected by the orientation material properties.

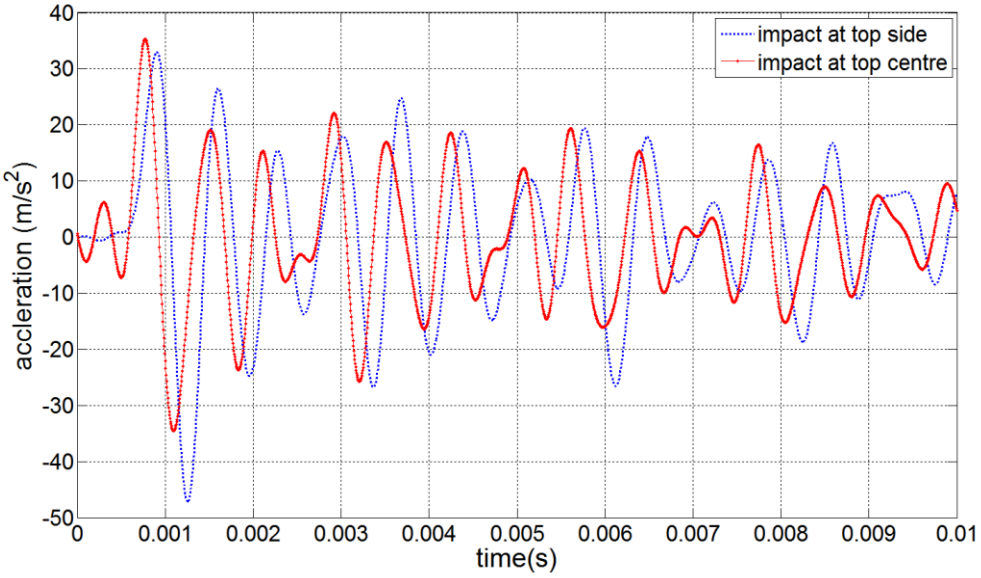

Figure 3-57 Comparison of wave patterns generated by top centre impact and topside impact

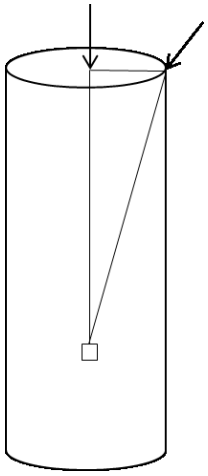

Figure 3-58 Wave propagation under top centre and topside impact

As mentioned before, an isotropic material has the same material properties in three orthogonal directions, so the wave speed is the same in each direction. However, transversely isotropic material properties in the plane are different than the properties in the normal to the plane and the wave speed will be different in these two directions. The longitudinal direction representing the fibre direction has a higher elastic modulus, and thus, wave propagation in this direction is faster. Under top centre impact, the direction of wave propagation is close to the longitudinal direction, while the direction of wave propagation caused by the incline impact combines the longitudinal and tangential directions and as a result, the wave speed is slower (see Figure 3-58).

A conclusion can be drawn from the study above that although the wave behaviour is more complicated in a transversely isotropic material, the feature of wave behaviour is similar with the isotropic material. For both material constitutive models, at 90 degrees in the longitudinal direction, a pure longitudinal wave can be captured regardless of the top centre impact or inclined impact but the speed of wave propagation will be affected by the material properties.

3.5.2.3 Study of wave behaviour in orthotropic material model

Study of wave propagation in orthotropic material is the most challenging work since the wave behaviour is very complicated in this kind of material. To understand the wave behaviour in an orthotropic material, the 5m pole with top centre impact was studied first. Impact on the top centre of pole will generate a longitudinal wave, which makes analysis of wave behaviour straightforward. To investigate the wave behaviour caused by top centre excitation on the 5m pole, both the isotropic and orthotropic models were created. The cylindrical pole was tapered in shape with 1m embedded in soil. The diameter at the top was 270mm and at the bottom was 300mm and the material properties of the isotropic and orthotropic model were the same as the parameters in section 3.2. Figure 3-59 provides a typical example of FE results of wave propagation in a full sized 5m pole. Figure 3-59 (a) is the wave trace for the isotropic model and (b) is for the orthotropic model. Although the material characteristics of the two models are different, the wave behaviour is quite similar.

The displacements from all nodes along a line in the longitudinal direction at 90 degrees are selected as output to investigate the wave behaviour in the entire timber pole. Accelerations of the selected nodes were calculated and plotted in time versus node location diagram (Figure 3-59). In the diagram, the peaks of the accelerations are indicated by darker colour in the time history of the wave traces. The intersections of incident and reflection waves (the adjacent two oblique lines) indicate the reflection of boundaries including the top of the pole and bottom of the pole beneath the soil. According to the distance from the point to the soil level, the embedment length can be predicted. The slope of these lines presents the velocity of the waves. The solid line is the ground level; after reaching the bottom of the pole, wave reflection and refraction occurs at the boundary (the bottom of the pole), that is, some wave reflects back and some wave propagate into the soil. It also confirms that, due to the tapered shape of the

pole, up-going wave and down-going wave have different velocities. For the 5 m pole with the excitation on top centre, the velocity of the incident wave or called down-going wave was 4920m/s and the reflected wave or called up-going wave was 4864m/s. In application, the measurement area is located between the soil level and 1.5m above the soil (demonstrated by dotted line), and the signal captured by the measurement points within this area would be easily distinguished to obtain effective wave information including the incident wave and reflected wave. Accordingly, the embedded length of the pole could be predicted.

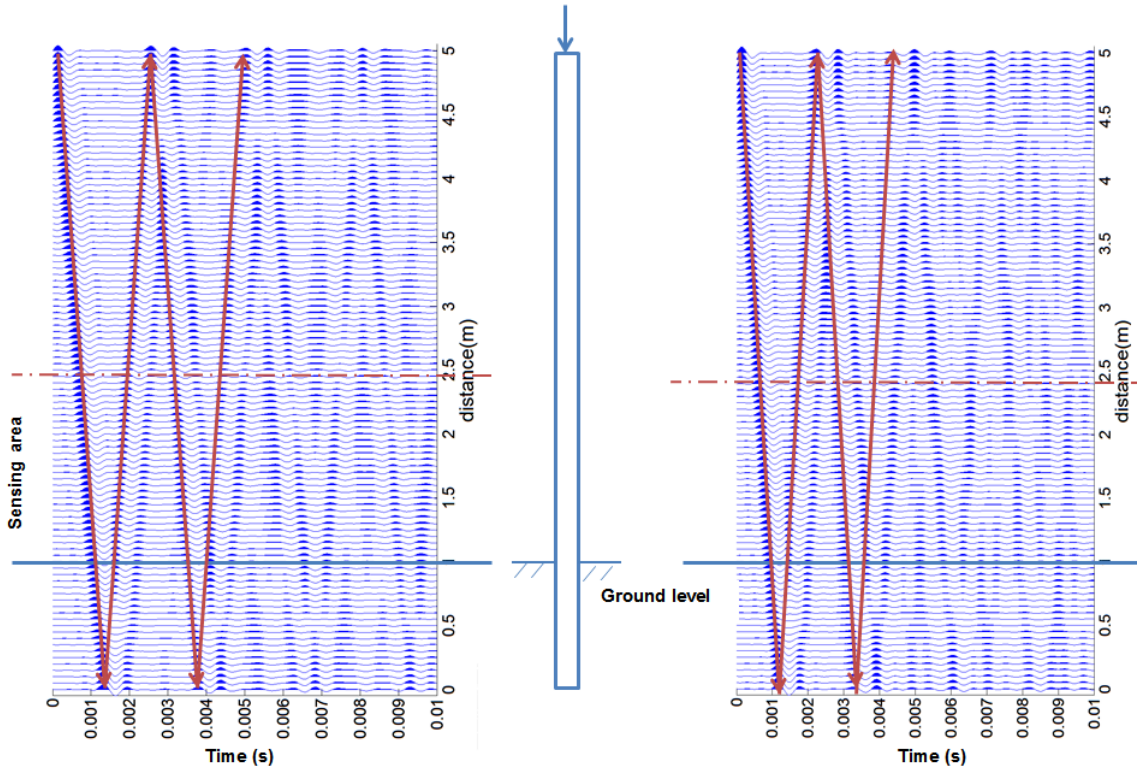

(a) (b)

Figure 3-59 Wave trace for 5 m pole (a) isotropic model (b) orthotropic model

However, in-situ utility poles are normally 12m long with 1.2-1.5m embedment length, which makes top excitation unfeasible due to practical restrictions. Therefore, the excitation has to be imparted at 1.5 m from the ground level at an angle of 45 degrees through a waveguide, and it will cause more complicated problems. It will generate two types of waves: longitudinal wave and bending wave; it will generate two directional waves as well: up-going wave and down-going wave. To investigate this wave propagation behaviour, a full sized utility pole model of 12m was created. The pole was

of tapered cylindrical shape with the top diameter of 228 mm and the bottom diameter of 300 mm, respectively. The impact excitation has been imparted at 1.5 m from the ground level at an angle of 45 degrees. Both isotropic (Figure 3-60 (a)) and orthotropic models (Figure 3-60 (b)) were created and compared.

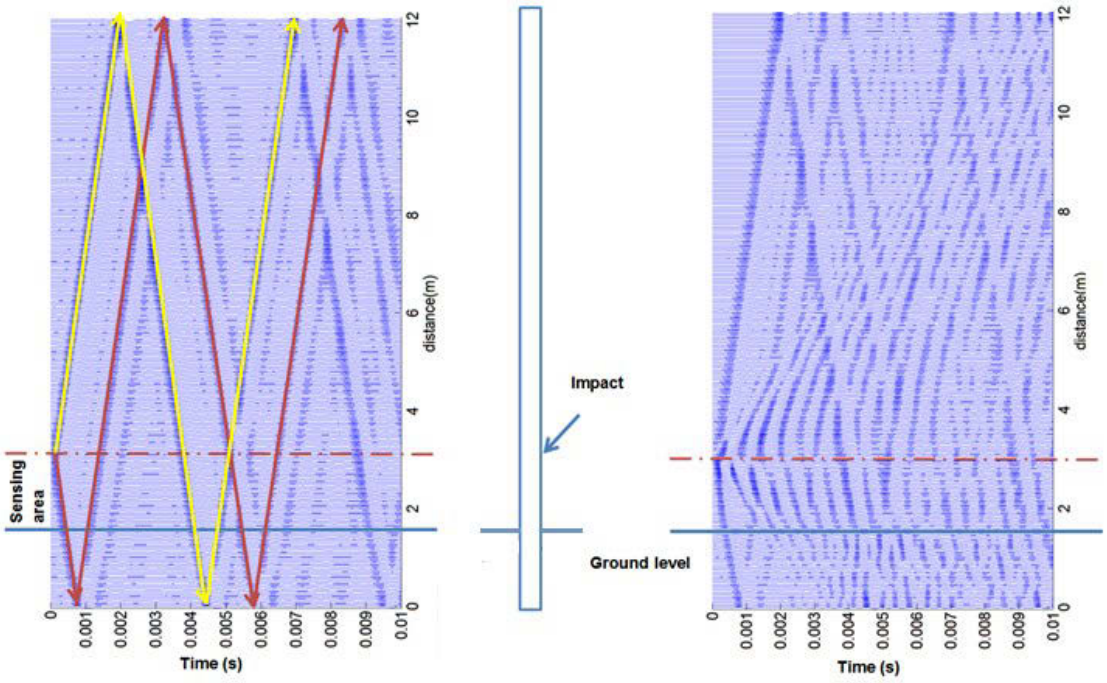

(a) (b)

Figure 3-60 Wave trace for 12 m pole (a) isotropic model (b) orthotropic model

Again the displacements from all nodes along a line in the longitudinal direction at 90 degrees are selected as output to investigate the wave behaviour in the entire timber pole. Calculated accelerations are plotted in time versus node location diagram. The dotted line is the level where the impact takes place and the solid dark line stands for the soil level. In the isotropic model (Figure 3-60 (a)), from the impact point, it can be seen clearly that the up-going and down-going waves are generated simultaneously. The down-going wave propagates down to the bottom of the pole and the wave velocity in the pole will be slowed down slightly by surrounding soil when it reaches the part that is embedded in soil which is the same phenomenon as the wave behaviour in the 5m pole. The up-going wave propagates in the pole at the same time; when it reaches the top of the pole, it will be reflected back.

The results also show the wave behaviour in the measurement zone where the sensors are located between the impact location and ground level, that is, the sensors will capture the down-going wave first and then its reflection wave before capturing the up-going wave reflected from the top of the pole.

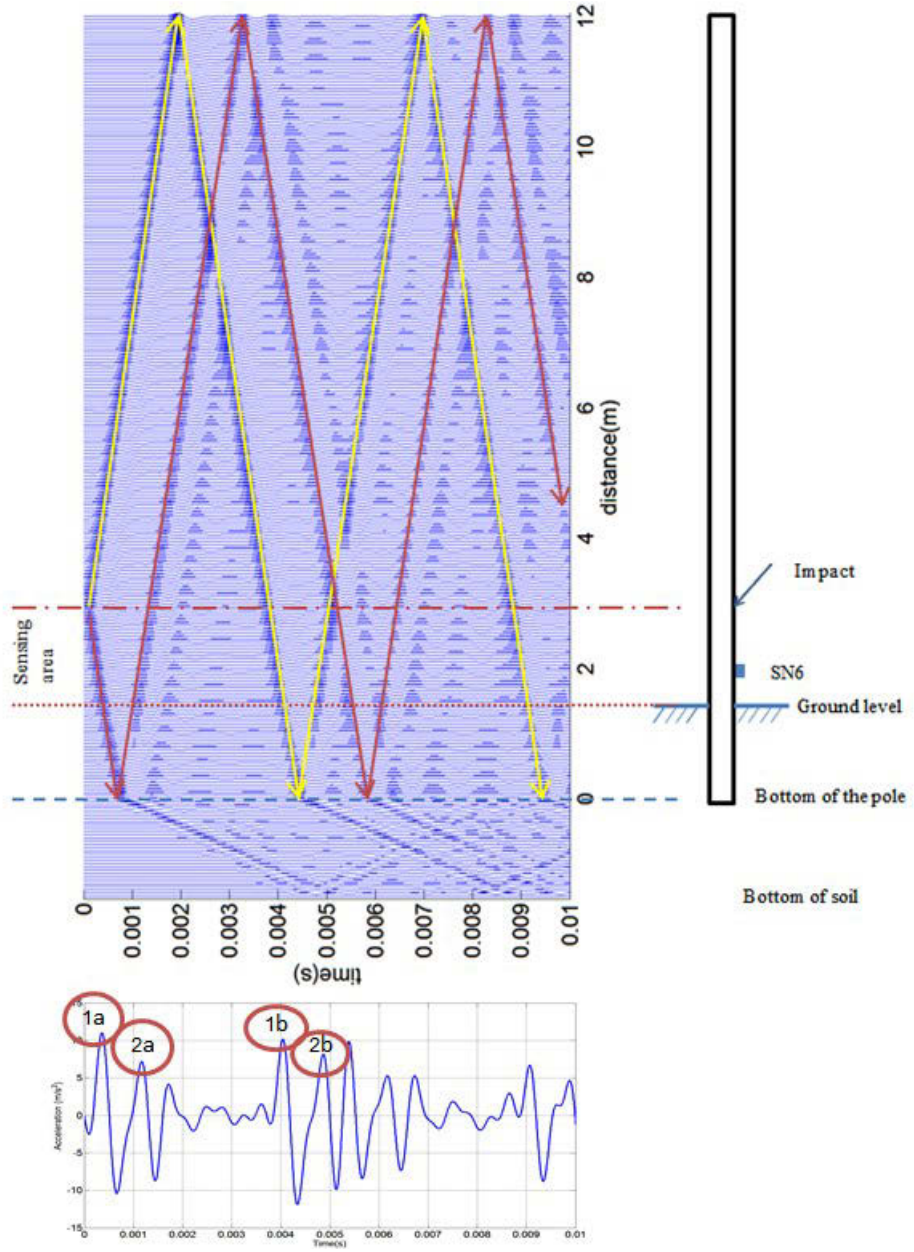

Figure 3-61 Wave trace in12m timber pole and soil

In Figure 3-61, the signal from the sensor No. 6 is used to illustrate the wave propagation behaviour. Sensor 6 is located at 400 mm above the soil level and the figure above shows the time history of the signal captured by sensor 6. The travel-down wave will be captured first by the sensor and in the time history graph is shown as the first

peak named 1a. The wave is then reflected from the bottom of the pole and captured by the same sensor, shown as the second peak named 2a. In the meantime, the travel-up wave reflected from the top of the pole will then reach sensor 6 as a peak named 1b followed by its reflections from the bottom of the pole as a peak named 2b. Figure 3-61 also indicates the wave propagation in the soil that is below the pole. From the interface between the pole and soil (dashed line), it can be clearly seen that some of the incident wave is reflected by the bottom boundary of the pole and some of the wave is refracted into the soil and according to the wave trace, it can be observed that the wave in poles captured by sensors will not be influenced by the wave reflected from the bottom boundary of soil since the wave speed in soil is extremely slow and the reflected energy is also very small and thus can hardly be detected by the sensors within the recording time.

From the wave trace, it can be found that although the wave signal in the 12m isotropic pole with side excitation is more complicated than the wave signal in the 5m pole with top excitation, the interference zone of the up-going and down-going waves and their reflection wave can still be identified to avoid errors during the signal processing.

The most complicated situation is the wave behaviour in the 12m orthotropic pole with side excitation. From Figure 3-60 (b), it can be observed that from the impact point, two types of waves were generated at the same time: longitudinal waves and bending waves. In addition, different modes of waves are generated due to the orthotropy feature of the material, that is, reflection and refraction occurs at the same time inside the orthotropic material. Also because of the different types of waves and various modes of waves, reflected wave identification becomes difficult. Therefore, further study in signal processing needs to be done to effectively separate longitudinal and bending waves as well as different modes.

3.6 WAVE DISPERSION IN TIMBER POLE

3.6.1 Introduction

The dispersion is a normal phenomenon in wave propagation problems and is defined as waves with different wavelengths (frequencies) travelling at different speeds in the same material (Puckett, 2000).

When stress wave based NDT methods are applied, the premise of results interpretation is assuming a one-dimensional wave is generated (Wang and Chang, 2008). One-dimensional wave illustrates that wave propagates through a string or a plane in infinite space and the lateral displacement is not considered. The boundary condition can only affect the wave amplitude but not the wave speed when reflection and transmission happens during the wave propagation. The wave equation is shown below:

$$\frac{\partial^2 y}{\partial t^2} - {c_0}^2 \frac{\partial^2 y}{\partial x^2} = 0 \qquad \text{Eq. 3-10}$$

where c_0 is a constant value and is described as the wave speed, while y is displacement. The equation indicates that one-dimensional waves are functions of time and space. The full solution is (Plumb, 2003):

$$y(x,t) = Re\left[y_+ e^{i(kx-\omega t)} + y_- e^{i(kx+\omega t)}\right] \qquad \text{Eq. 3-11}$$

Where y_+ y_- are constant complex amplitudes, k is wavenumber and 2π/k is wavelength, ω is angular frequency and satisfies equation 3-9 and describes the dispersion relation for the wave:

$$\omega^2 = k^2 {c_0}^2 \qquad \text{Eq. 3-12}$$

Eq. 3-11 describes some characteristics in a progressive wave (Plumb, 2003):

- At a given instant t, it is a sinusoidal wave disturbance with the wavelength of 2π/k
- At a given location x, it is an oscillation of $y_\pm e^{ikx} e^{\pm i\omega t}$ with period of 2π/ω, $y_\pm e^{ikx}$ is the complex amplitude.
- The wave propagates with the phase velocity of c = ω/k = $\pm c_0$ and indicates non-dispersive feature, i.e. the phase velocity keeps constant regardless of the wavenumber and angular frequency.

However, the waves propagated in timber poles are three dimensional waves. Pochhammer first derived a three-dimensional wave equation for an infinite cylindrical bar in 1876. He developed frequency equations for the three-dimensional wave and described all modes during wave propagation in a three-dimensional traction free infinite cylinder. In a finite medium, the boundary of a structure will cause the reflection

of waves and changing of wave type. Guided wave exists in all finite media including elastic and inelastic materials (Wang, 2004) and all guided waves are dispersive in finite media except light in a vacuum (Brillouin, 1960). Due to the excited longitudinal waves by hammer within a low frequency range, the wave velocity does not change too much with frequency (Finno et al., 2001). Accordingly, it is acceptable to assume that longitudinal waves in pole /pile structures are one-dimensional with constant velocity.

3.6.2 Dispersion study of wave propagation

3.6.2.1 Simplification of numerical model

Concentration on traction free condition

To investigate the dispersion phenomenon of a longitudinal wave in a cylindrical structure, some research work has been done and the dispersion relations are obtained under specific conditions. A key description of a dispersion phenomenon is a dispersion curve which shows the relationship between the phase velocity or group velocity and the wavelength or the frequency of a specific material with certain geometry (Puckett, 2000). In this research, only the longitudinal wave is studied in numerical analysis and the dispersion curve is presented by the relationship between phase velocities versus frequencies. Hanifah and Chao (Hanifah, 1999, Chao, 2002) have verified that in the traction free (without surrounding soil) and embedded conditions, phase velocity is almost not affected. Subhani (Subhani, 2014) also presented the same phenomenon through analytical analysis (see Figure 3-62).

The connection between soil and timber material plays an important role to generate the dispersion curves. In this research, rigid connection is employed as mentioned in Chapter 3 since the low strain produced by excitation.

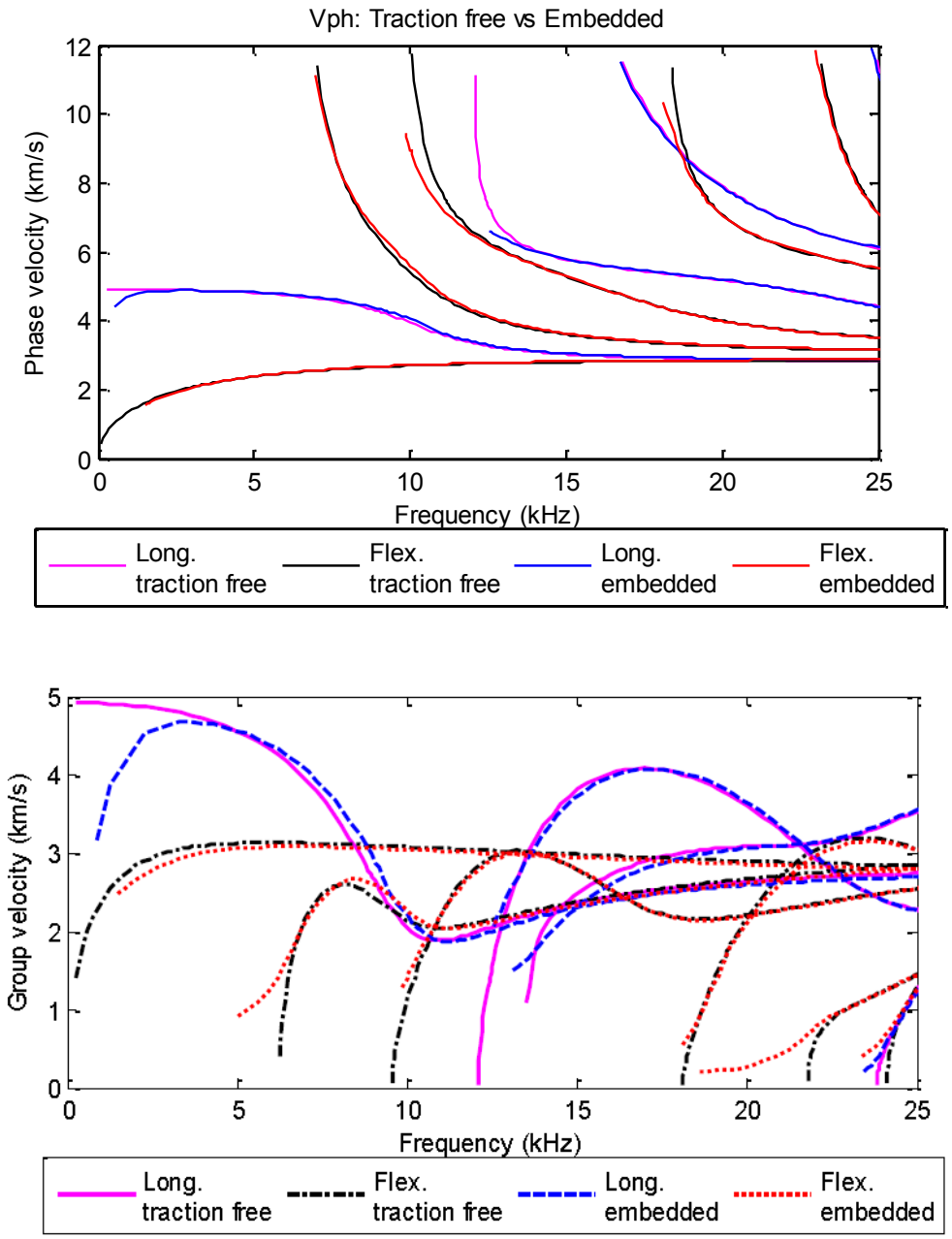

Figure 3-62 Comparison of phase velocity and group velocity curves between traction free and embedded condition (Subhani, 2014)

Figure 3-62 compares the wave velocities based on analytical analysis between the traction free and embedded situation of an isotropic model (Subhani, 2014). The pink solid line and the blue dashed line present the longitudinal wave in the traction free and embedded condition, respectively. The figure clearly illustrates that phase velocity of longitudinal waves is almost unaffected in the traction free and embedded conditions. Since the real part of wavenumber for both traction free and embedded cases is not

affected significantly by the density or shear modulus of the surrounding medium. However, in the embedded situation, imaginary part of the wavenumber has a large value and causes attenuation due to the rigid connection between soil and timber pole. Group velocity represents the propagation of energy and attenuation presents in the embedded structure, hence, infinite value of group velocity presents at cut-off frequency. In this condition, group velocity cannot be obtained directly, on the contrary, leakage of the energy in the surrounding medium is high, and thus, energy velocity was calculated (Subhani, 2014). From the figure, it was found the energy velocity of longitudinal wave is less affected by the surrounding medium except in very low frequency range. In this research, traction free condition is considered to simplify the numerical models.

Model simplification from 3D to 2D

To balance the computational time and accuracy, 2-D axisymmetric models are considered. In general, more accurate results are obtained from a finer mesh density. Although 3D models deliver more accurate results compared to 2D models, they require more computational time and resources. For the modelling of timber poles for stress-wave-based damage detection, at least 30 elements must be created per wave length (depending on the excitation frequency) in order to capture the wave front accurately. Hence, a large number of elements are required, which results in an extremely long computation time. To overcome this problem, a 2D axisymmetric numerical model is developed. In ANSYS, the axisymmetric model is defined in the X-Y plane with positive X values. The geometry can be created by a cross-section, which, when rotated along the Y axis of the global Cartesian system, forms the actual model as shown in Figure 3-63 (ANSYS, 2012).

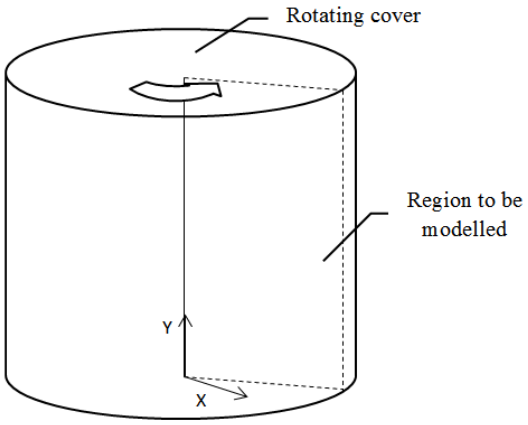

Figure 3-63 Two-dimensional axisymmetric numerical model

To verify that a 2D model will be able to represent a 3D model, a comparative study between 2D and 3D models was undertaken (see Figure 3-64). A 5 m free standing timber pole was simulated and a Gaussian excitation $P(t)$ (see Eq. 3-13) with a central frequency of 20 kHz was applied on the top centre of the pole to generate longitudinal waves.

$$P(t) = \frac{A}{\sigma\sqrt{2\pi}} e^{-\frac{1}{2}\left(\frac{t-\mu}{\sigma}\right)^2} sin(2\pi t f) \qquad \text{Eq. 3-13}$$

where σ is standard deviation, μ is mean (where Gauss distribution is a maximum), A is amplitude and f is central frequency. The time step is 1 μs and the deviation is 0.000125. The excitation signal is shown in Figure 3-65.

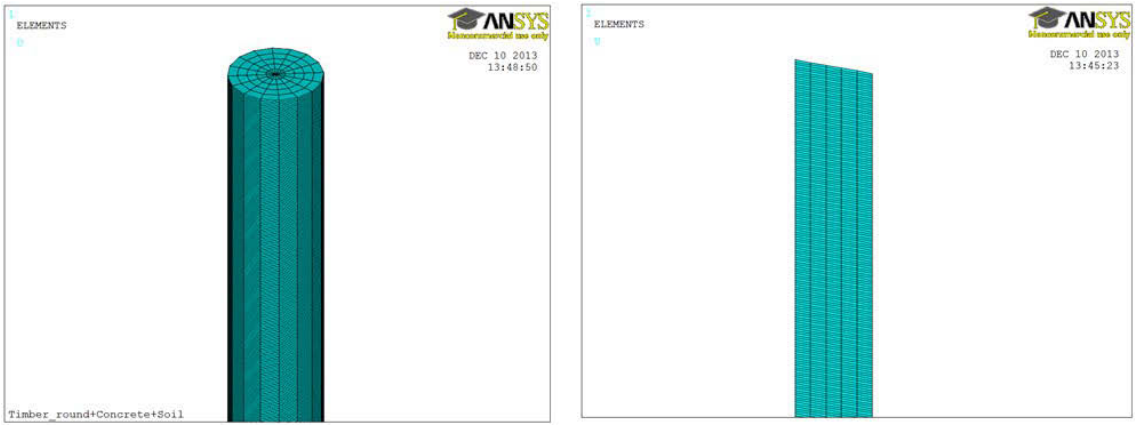

Figure 3-64 3D and 2D axisymmetric models created with ANSYS

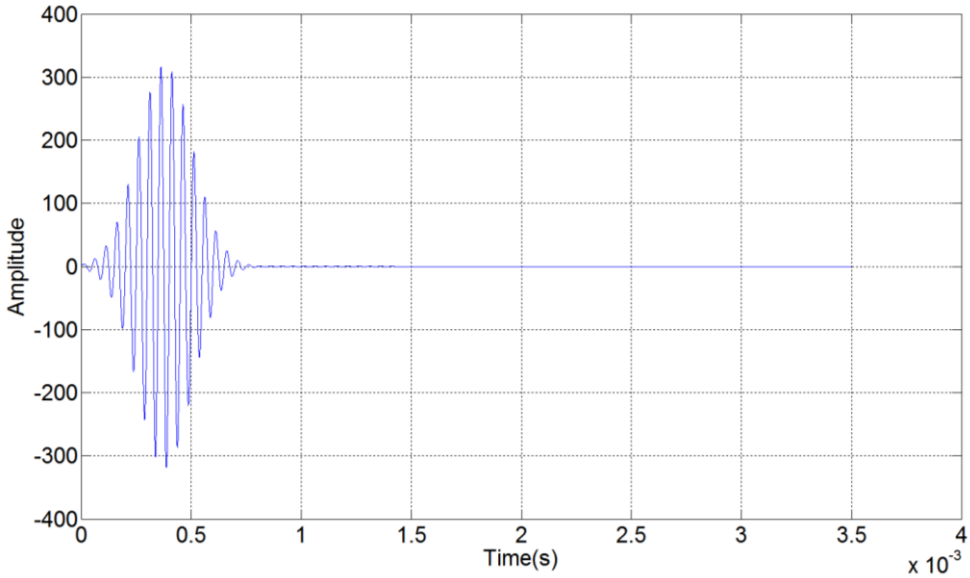

Figure 3-65 Excitation with central frequency of 20 kHz

Figure 3-66 shows the recorded acceleration results from a sensor located at a distance of 1 m from the bottom of the pole. It can be seen from the figure that even though the amplitudes are slightly different, the wave patterns of the two models are consistent. Based on these results, it is confirmed that a 2D axisymmetric model can be used for further studies.

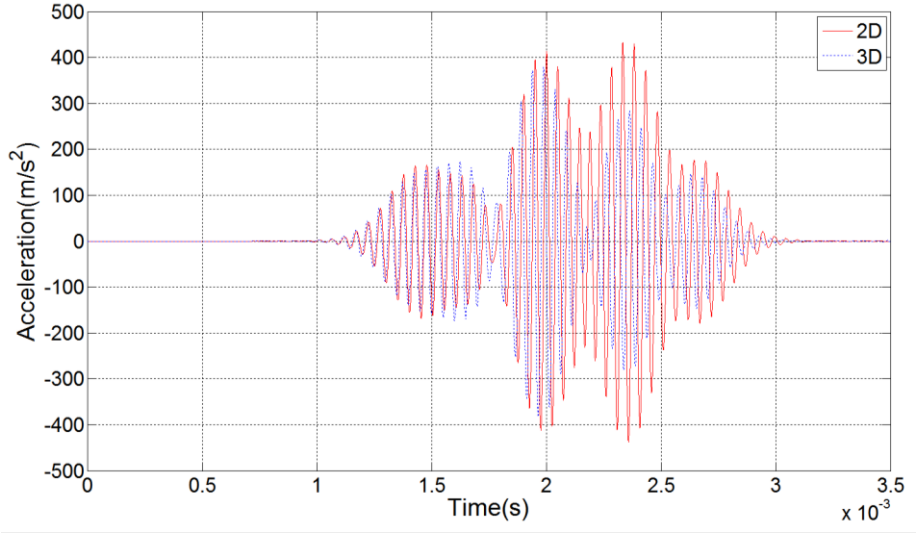

Figure 3-66 Result comparisons between 2D and 3D models of 5 m long pole

3.6.2.2 Dispersion study

To create the dispersion curve, accurate wavenumbers have to be collected. In the longitudinal direction of the pole, 2000 elements were created and 500 nodes were

selected to compute the wavenumber. The time step is 0.2μs to capture the wave front. The method of obtaining the wavenumber in this study references Dr Puckett's work who did dispersion study of longitudinal wave in a cylindrical structure by numerical methods. In this study, to collect clear wave numbers, pure sinusoidal waves with different frequencies (2kHz, 4kHz, 6kHz, 8kHz, 10kHz, 12kHz, 14kHz 16kHz, 18kHz and 20kHz) as excitation were in turn applied on the top centre of the pole in traction free condition. The excitation frequency excited all modes whose cut-off frequencies were below this excitation frequency. The corresponding acceleration was obtained and a frequency spectrum in time was created by applying a Fourier transform. The amplitude of a specific frequency was taken from each of the frequency spectrum for the nodes along the pole and these points were used to create the wavenumber spectra in the space domain by applying another Fourier transform (Puckett, 2000). The wavenumber for specific frequency (according to the excitation frequency) was determined by the spectrum in space domain. Accordingly, the phase velocity was calculated by Eq. 3-12 and the procedure was repeated when another excitation was applied. After obtaining the phase velocities under all excitations, the dispersion curve was plotted. The wave data obtained from ANSYS were processed according to the method above through MATLAB. The longitudinal wave propagated in a 5m isotropic model with traction free condition was considered. The calculated wave number and phase velocity is listed in Table 3-12 and the dispersion curve is plotted accordingly.

From the calculations, it can be found that the second mode appears from an excitation frequency of 12 kHz and the third mode is present from 14 kHz. However, the velocity value exceeds the range of figure settings so it did not appear in the dispersion curve.

Figure 3-67 compares the numerical and analytical results. From the comparison, it can be seen that although there are some errors appearing, most numerical results are quite consistent with the analytical results. At lower frequencies (below 10 kHz), only one mode appears for each frequency, while in the higher frequency range, more modes are presented. The phase velocity is always around 5000 m/s in the lower frequency range such as below 8 kHz. In the higher frequency range, the phase velocity of the first mode (red) is decreased to 3000 m/s. In addition, the second mode (black) and the third mode (blue) are presented in this range with higher phase velocities.

Table 3-12 Calculated wavenumber and phase velocity under different excitations

Frequency (kHz)	Wavenumber	Phase velocity (m/s)	Wavenumber	Phase velocity (m/s)	Wavenumber	Phase velocity (m/s)
2	2.45	5121				
4	5.22	4818				
6	7.82	4819				
8	10.74	4680				
10	17.79	3532				
12	23.32	3233	9.05	8331		
14	29.76	2956	14.88	5912	3.68	23890
16	34.36	2926	18.41	5461	8.44	11915
18	38.66	2925	20.71	5461	11.35	9965
20	44.03	2854	24.08	5219	16.05	7830

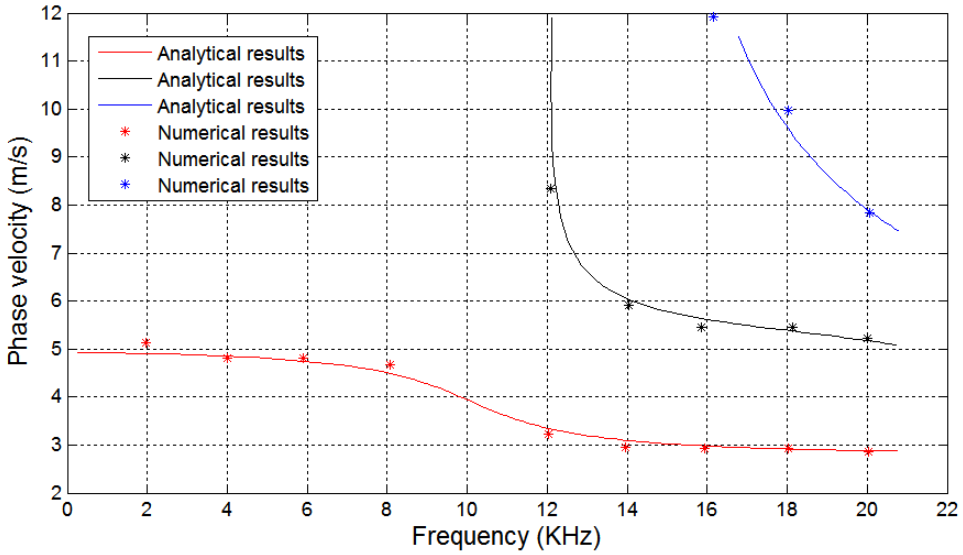

Figure 3-67 Comparison between analytical and numerical results

From the calculated results and the dispersion curve, it can be observed that the phase velocity decreases when the frequency increases in each mode; the second and third modes have a higher phase velocity than the first mode.

For the transversely isotropic and orthotropic model, there is no obvious peak of wavenumber and, thus, it can hardly be detected and obtained, as a result, the phase velocity cannot be calculated accurately. Hence, the results are not shown in this thesis. This phenomenon may be due to the limitation of the numerical analysis method. In

analytical analysis, the wavenumber is obtained from structure's physical information directly such as geometry and material properties. However, in numerical analysis, the wavenumber is calculated from captured wave data that is generated by different excitations and can be influenced by the energy of the wave propagation as well as the errors of finite element analysis. For the transversely isotropic and orthotropic material, the wave behaviour is more complicated as shown in section 3.5. The energy of longitudinal wave propagation may not be as concentrated as it propagates in an isotropic material, and, therefore, the peak of the wave number is not prominent.

3.7 CONCLUSIONS

This chapter discussed the critical issues for creating numerical models of timber poles such as material characteristics and boundary conditions. The behaviour of wave propagation in a complex material (such as timber) is dependent on the location of excitation where the stress wave is initiated. For the excitation on the top centre with low frequency (such as hammer impact), wave behaviour is quite similar in isotropic and orthotropic materials. As the starting stage of this research topic, the isotropic model was considered as the priority selection and will be used in the next research stage.

To simplify the numerical model and reduce the computational time, a 2D model was imported to represent a 3D model. Comparison study has verified that the wave pattern from the 2D model is quite close to the 3D model. Therefore, the 2D model will be used in the next research stage for developing a novel damage detection method.

Dispersion study demonstrates that the velocity of a longitudinal wave will not be influenced directly regardless of the boundary condition for an isotropic material. Accordingly, in the next research stage, the model will be created without considering the soil influence.

According to the outcomes of the investigation on wave propagation characteristics in this chapter, a novel damage detection method will be proposed based on numerical models developed.

4 Damage detection based on wavelet packet energy

4.1 INTRODUCTION

Significant economic loss, threats to human injury and property damage due to the sudden collapse of the civil infrastructure highlights the importance of developing applicable techniques for damage detection and condition monitoring of structures. Timber utility poles are one of the key civil infrastructures which provide an essential component of lifelines in all communities and, therefore, damage detection for the poles is very important. As mentioned in Chapter 2, there are several typical damages for timber poles (see Figure 2-11)

Some similar damage scenarios can be simulated by ANSYS (see Figure 4-2). In this chapter, wavelet and wavelet packet (WPT) theories are briefly reviewed, and then mesh density affecting wave behaviour is studied. The internal and external artificial damages with axisymmetric characteristics were created such as the damage scenarios shown in Figure 4-1 on the left. A novel damage detection method based on WPT was developed including an effective damage classification technique based on SVM with optimisation algorithm.

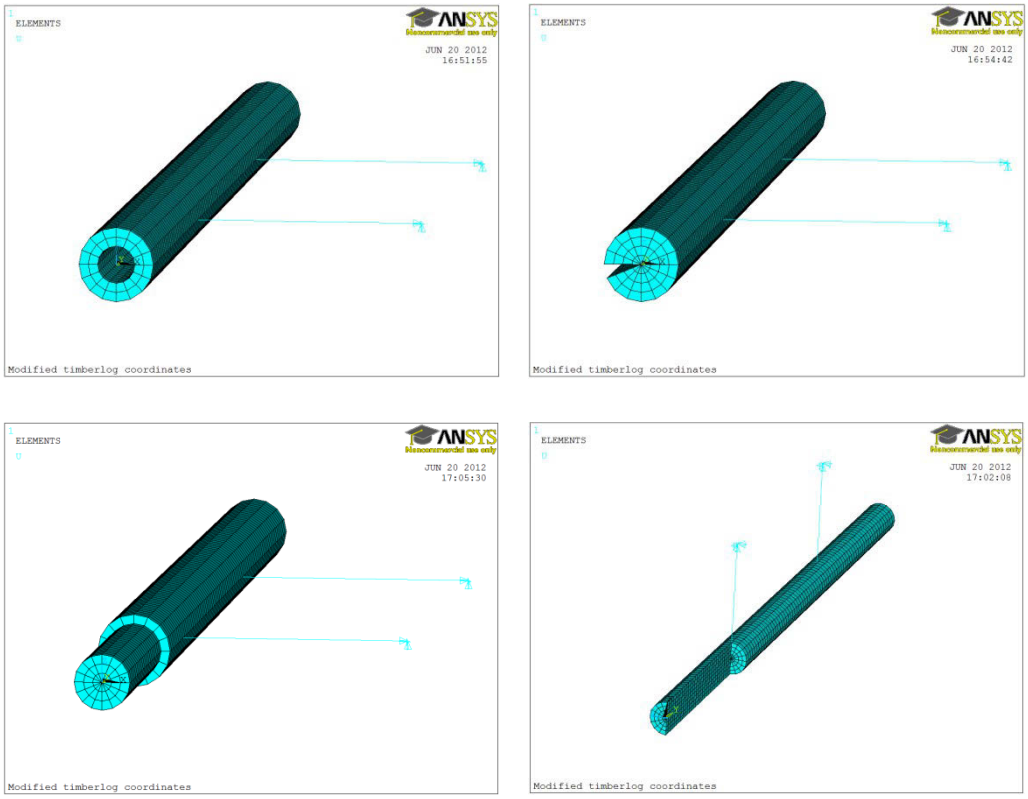

Figure 4-1 Damage scenarios created by ANSYS

4.2 OVERVIEW OF WAVELET AND WAVELET PACKET

Spectral analysis using Fourier transform has been one of the most important and most widely used tool in different engineering fields including damage detection. However, in some specific conditions, Fourier transform cannot provide enough information to identify the problem. Over the past few years, researchers have become aware of the limitations of this technique and have developed wavelet transform to deal with the non-stationary signals and non-linear systems. Wavelets are a natural extension of the Fourier transform and are used widely for signal analysis in the time and frequency domain simultaneously. A wavelet packet transform is a simple generalization of a wavelet transform and offers a great deal of freedom in dealing with different types of transient signals (Learned and Willsky, 1995). In this section, the theory of wavelet transform is briefly explained.

4.2.1 Continuous wavelet transform (CWT)

Continuous wavelet transform maps the original time series into a function of time and frequency providing highly redundant information and, therefore, will cause long computational time. Continuous wavelet transform is defined as follows:

$$CWT_x^{\varphi}(\tau, s) = \Psi_x^{\varphi}(\tau, s) = \frac{1}{\sqrt{|s|}} \int x(t)\varphi^*\left(\frac{t-\tau}{s}\right)dt \qquad \text{Eq. 4-1}$$

Where τ and s are translation and scale parameters, respectively. Translation is related to the location of the window and corresponds to time information. Scale corresponds to frequencies and is used to collect information in detail (high frequency/low scale) or globe (low frequency/high scale). $\varphi(t)$ is the mother wavelet and is a prototype for generating the other window functions. Some mother wavelets are well known and widely used such as Mexican hat wavelet, Morlet wavelet, Daubechies wavelet.

The wavelet analysis measures the similarity between the wavelets and the signal. If the signal has a major component of the frequency corresponding to the current scale, then the wavelet at the current scale will be similar to the signal at the particular location where this frequency component appears. As a consequence, the CWT coefficient in the time-scale will be a large number (Polikar, 2004) and hard to implement.

4.2.2 Discrete wavelet transform (DWT)

The discrete wavelet transform is easier to implement compared with CWT and makes significant reduction in the computation time. DWT is a tool that separates a signal into different frequency components, and then studies each component with resolution matched to its scale (Kociołek et al., 2001).

DWT converts a signal into different frequency bands with a high pass wavelet filter and a low pass wavelet filter as in the equations below:

$$y_{high}[k] = \sum_n x[n] \cdot g[2k-n] \qquad \text{Eq. 4-2}$$

$$y_{low}[k] = \sum_n x[n] \cdot h[2k-n] \qquad \text{Eq. 4-3}$$

Where $y_{high}[k]$ and $y_{low}[k]$ are the outputs of a signal converted by the high pass and low pass wavelet filters, respectively. $x[n]$ is the original signal while g and h are

wavelet filters. The DWT analyses the signal at different frequency bands with specific resolutions by decomposing the signal into an approximate and detail components. The original signal is first passed through a half band high pass filter and low pass filter. After the filtering, half of the samples can be eliminated according to the Nyquist's rule. This procedure provides a good time resolution at high frequencies and good frequency resolution at low frequencies. Figure 4-2 indicates the procedure that DWT processes a time domain signal. DWT coefficients are sampled from the CWT on a dyadic grid; that is $s = 2^j$ and $t = k * 2^j$, j is the number of the final decomposition level. Also, due to the successive subsampling by 2, the signal length must be a power of 2. The length of the signal determines the number of levels that the signal can be decomposed to (Polikar, 2004).

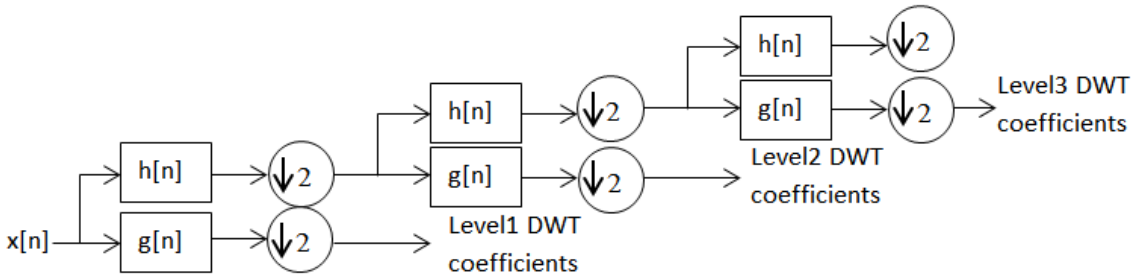

Figure 4-2 3 level decomposition by DWT

From the figure above, it can be found that in DWT, after down sampling, low frequency components will be decomposed into the next level decomposition. However, the information in high frequency components is not desirable and accordingly may cause problems in certain applications in which the main information is located in high frequency components. To overcome this problem, an alternate analysis method needs to be employed.

4.2.3 Wavelet packet transform (WPT)

4.2.3.1 Wavelet packet decomposition

Wavelet packet transform is a generalization of DWT and the necessary frequency resolution can be achieved. In WP analysis, both high frequency and low frequency components can be split, and this, therefore, provides sufficient information for signal analysis. Figure 4-3 shows the wavelet packet tree of a time domain signal $f(t)$ up to 3 levels of decomposition. As shown in the figure, both high and low frequency components are decomposed.

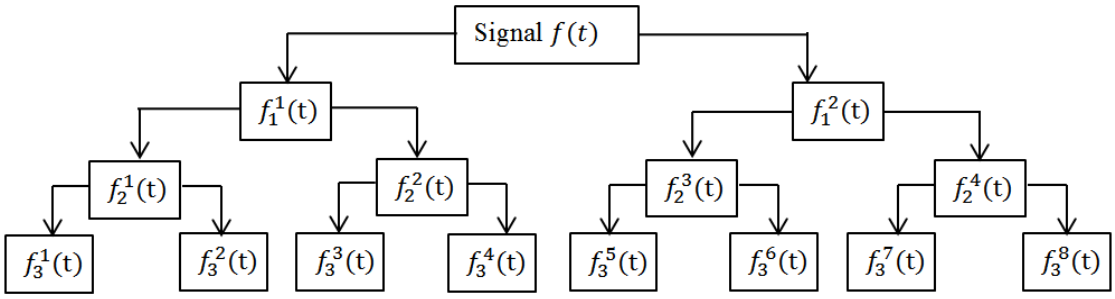

Figure 4-3 WP decomposition tree

Each component in this wavelet packet tree can be viewed as output of a particular filter and the whole tree can be viewed as a filter bank. At the top of the tree, the good time resolution of the WP components is obtained but at the expense of poor frequency resolution whereas at the bottom of the tree with high decomposition level, the frequency resolution of the decomposed component is good but the time resolution is poor (Amiri and Asadi, 2009).

A wavelet packet is presented by Eq. 4-4

$$\varphi_{j,k}^{i}(t) = 2^{j/2}\varphi^{i}(2^{j}t - k) \qquad \text{Eq. 4-4}$$

where i, j, k are the modulation, scale and translation parameters, respectively. The wavelet φ is defined by the recursive relations as:

$$\varphi^{2i} = \sqrt{2}\sum_{k} h(k)\,\varphi^{i}(2t - k) \qquad \text{Eq. 4-5}$$

$$\varphi^{2i+1} = \sqrt{2}\sum_{k} g(k)\,\varphi^{i}(2t - k) \qquad \text{Eq. 4-6}$$

where $h(k)$ and $g(k)$ are called group-conjugated orthogonal filters (Fan and Zuo, 2006) and are quadrature mirror filters associated with the scaling function and mother wavelet function (Ghodrati et al., 2008).

The wavelet packet coefficients corresponding to the signal $f(t)$ can be obtained from:

$$C_{j,k}^{i}(t) = \int_{-\infty}^{\infty} f(t)\,\varphi_{j,k}^{i}(t)dt \qquad \text{Eq. 4-7}$$

where $C_{j,k}^{i}$ is wavelet packet coefficients and satisfies the orthogonality condition:

$$\varphi_{j,k}^{m}(t)\varphi_{j,k}^{n}(t) = 0, (m \neq n) \quad \text{Eq. 4-8}$$

The wavelet packet component of a signal at a specific node of the decomposition tree is:

$$f_j^i(t) = \sum_{k=-\infty}^{\infty} c_{j,k}^i(t)\varphi_{j,k}^i(t) \quad \text{Eq. 4-9}$$

After the decomposition of j^{th} level, the original signal $f(t)$can be constructed by the sum of 2^jcomponents as in Eq. 4-10

$$f(\mathrm{t}) = \sum_{i=1}^{2^j} f_j^i(t) \quad \text{Eq. 4-10}$$

An entropy based criterion is used to determine the most suitable decomposition of a given signal and also an adaptive filtering algorithm (Amiri and Asadi, 2009).

4.2.3.2 Wavelet packet component energy

Yen and Lin (Yen and Lin, 2000) have shown that the energy associated with each component at a certain level of WP tree represents a more robust signal feature for classification than using the WPT coefficients alone. In this study, the wavelet packet energy index is proposed to identify the damage severity. The signal energy at j^{th} level can be defined as:

$$E_{f_j} = \int_{-\infty}^{\infty} f^2(t)\,dt = \sum_{m=1}^{2^j}\sum_{n=1}^{2^j}\int_{-\infty}^{\infty} f_j^m(t)\,f_j^n(t)dt \quad \text{Eq. 4-11}$$

where f_j^m and f_j^n are decomposed wavelet components. Substituting Eq. 4-9 into Eq. 4-11 when the orthogonal condition is satisfied:

$$E_{f_j} = \sum_{i=1}^{2^j} E_{f_j^i} \quad \text{Eq. 4-12}$$

The component energy $E_{f_j^i}$ can be considered as the energy stored in the component signal $f_j^i(t)$ and can be obtained by:

$$E_{f_j^i} = \int_{-\infty}^{\infty} f_j^i(t)^2 dt \qquad \text{Eq. 4-13}$$

The component signal $f_j^i(t)$ is a superposition of wavelet function $\varphi_{j,k}^i(t)$ of the same scale as j but translated into the time domain ($-\infty < k < \infty$). The total signal energy can be decomposed into a summation of wavelet packet component energies that correspond to different frequency bands which are determined by the wavelet function.

In this study, the mother wavelet BiorSplines 6.8 was selected due to its features of good orthogonality and symmetry as well as high vanishing moments (Li et al., 1995). The sampling rate was set to 5 MHz to capture the wave front accurately and the decomposing scale was set to 10 accordingly. Shannon entropy based criterion was selected to decompose the wave signal.

4.3 DAMAGE DETECTION BASED ON WAVELET PACKET ENERGY

4.3.1 Sensitivity study of mesh density for 2D models

In FE analysis, the mesh density significantly influences the numerical results. Therefore, several different mesh densities were studied under different excitation frequencies. The wave signal from a fine mesh of 40 elements per wavelength (Fischer et al., 2010) (depending on the input frequency) was set as a benchmark. The signals from the models with different mesh densities will be compared to the benchmark. Several measurement points for capturing wave signals were selected which were located from 1.7 m to 2.7 m near the bottom of the pole with a distance of 200 mm between two points. To evaluate the results, the cross-correlation coefficient was used, which is a similarity measurement of two signals or waveforms. If two signals are exactly the same, the coefficient will be 1.0; if the signals do not match at all, the coefficient will be 0. In this study, this methodology was used to identify the differences between signals that were obtained from two mesh conditions with the same measurement point. For example, a wave signal obtained at 2.1m of the model with fine mesh is set as benchmark; the wave signal from the same location of a coarse mesh model is compared with the benchmark signal and the difference between these two signals will be qualified by cross-correlation coefficient. If the coefficient closes to 1, there is no significant difference between two signals; while the coefficient closes to 0

indicates that the signal from the coarse mesh is obvious different with the benchmark signal.

Figure 4-4 provides an intuitive example of mesh density influencing on the wave signal captured by different measurement points. The excitation frequency is 25 kHz, accordingly the wave length is extremely small. In this situation, the mesh density will affect the wave signal significantly. In the figure, the results from four measurement points are taken and plotted which are located at 1.9m, 2.1m, 2.5m and 2.7m. Coarse mesh1, 2 and 3 present the mesh density of 4*2000, 20*800 and 20*1000, respectively. For coarse mesh1, the cross correlation coefficient of the signal captured by the measurement points at 1.9m is less than 0.5, and coefficients from other measurement points are always less than 0.9. For other coarse mesh conditions, the coefficients of some measurement points are less than 0.9. It is clearly shown that for coarse mesh conditions, the accuracy of some measurement points is significantly decreased. For medium mesh condition (mesh density of 40*1000), the cross correlation coefficients are always above 0.9 regardless of the measurement location.

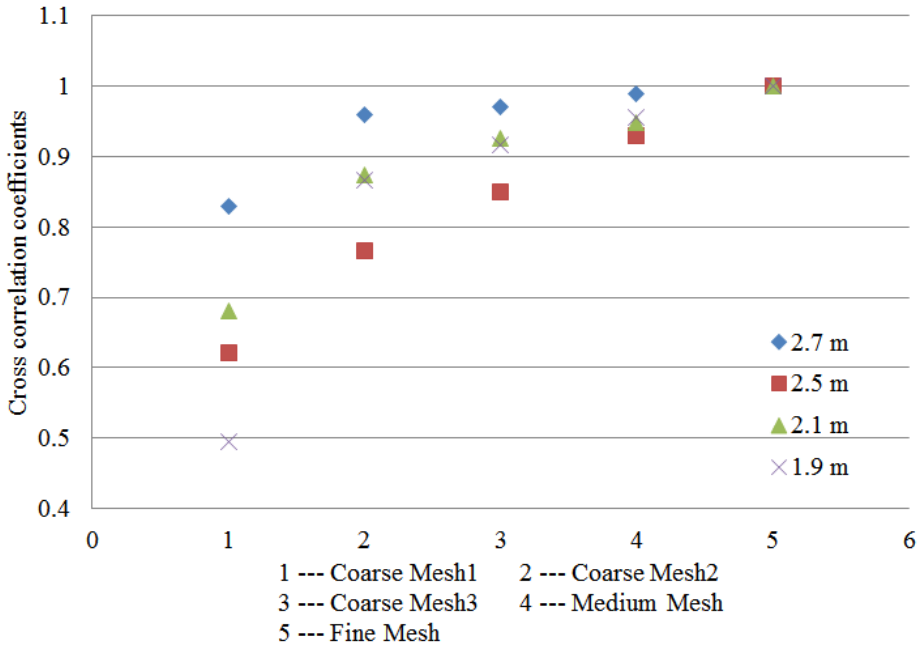

Figure 4-4 Mesh density influence on wave signal under excitation of 25 kHz

Table 4-1 shows the cross-correlation coefficients between the standard mesh condition (fine mesh) and different medium and coarse mesh conditions. In the table, λ represents the wavelength; w and h indicate the width and the height of an element, respectively.

In the table, the cross-correlation coefficients of three excitation frequencies are listed. For the 2D model, the mesh density can be increased or decreased in the radial and longitudinal direction.

Table 4-1 Comparison of cross-correlation coefficients under different mesh densities

Excitation: 25kHz		λ=0.12 m	Measurement Points					
Mesh dimension		Element size [w(m)/h(m)]	2.7m	2.5m	2.3m	2.1m	1.9m	1.7m
fine	60×2000	0.0025/0.0025	1	1	1	1	1	1
medium	40×1000	0.00375/0.005	0.988	0.929	0.986	0.947	0.955	0.983
	24×1000	0.00625/0.005	0.980	0.895	0.985	0.938	0.936	0.979
	20×1000	0.0075/0.005	0.970	0.850	0.983	0.925	0.917	0.975
coarse	20×800	0.0125/0.00625	0.958	0.766	0.971	0.874	0.866	0.965
	4×2000	0.0375/0.0025	0.829	0.622	0.876	0.680	0.496	0.608
Excitation: 12kHz		λ =0.25 m	Measurement Points					
Mesh dimension		Element size [w(m)/h(m)]	2.7m	2.5m	2.3m	2.1m	1.9m	1.7m
fine	60×2000	0.0025/0.0025	1	1	1	1	1	1
medium	20×800	0.0075/0.00625	0.976	0.986	0.977	0.978	0.956	0.951
coarse	12×800	0.0125/0.00625	0.964	0.980	0.973	0.971	0.943	0.939
	12×500	0.0125/0.001	0.953	0.976	0.962	0.968	0.926	0.927
	4×2000	0.0375/0.0025	0.830	0.937	0.911	0.953	0.818	0.870
Excitation: 8kHz		λ =0.5 m	Measurement Points					
Mesh dimension		Element size [w(m)/h(m)]	2.7m	2.5m	2.3m	2.1m	1.9m	1.7m
fine	60×2000	0.0025/0.0025	1	1	1	1	1	1
medium	20×500	0.0075/0.01	0.976	0.973	0.973	0.970	0.971	0.961
coarse	8×1000	0.02/0.001	0.973	0.973	0.973	0.966	0.962	0.957
	4×2000	0.0375/0.0025	0.971	0.965	0.954	0.951	0.950	0.943
	8×200	0.02/0.025	0.955	0.954	0.955	0.947	0.939	0.944

The cross-correlation coefficient study of different mesh densities leads to the following findings.

1. From the coefficients, it can be seen that for high frequency excitations, such as 25 kHz, the coarse mesh generates larger errors compared to the fine mesh condition. For the low frequency excitation, such as 8 kHz, the coarse mesh is still quite accurate to represent the wave behaviour. This indicates that to capture the wave front accurately, the mesh density plays a crucial role.

2. An optimised mesh density in all directions is more important than the total number of elements. The results of the model with an excitation frequency of 12 kHz supports this phenomenon. When comparing the two coarse mesh conditions, it is found that the

mesh dimensions of 12×500 contains a much smaller number of elements than the dimensions of 4×2000, but the results are more accurate.

Hence, from the cross-correlation coefficient results, it is concluded that a medium mesh delivers a good balance between computation time and result accuracy and is, therefore, used in further studies.

4.3.2 Proposed damage classification algorithm

Wavelet packet energy (WPE) methods are traditionally used with vibration-based methods to identify damage in a structure. Thereby, a number of sensors are attached at various locations of the structure, typically covering the entire area that needs to be inspected. Significant energy changes indicate the occurrence of damage in the proximity of the measurement point (see Figure 4-5). This WP based method is able to indicate the damage location as well as the severity as mentioned in Chapter 2. However, the application of these methods on the wave signal is limited especially in that sensors/measurement points cannot cover the entire area where damage has to be assessed.

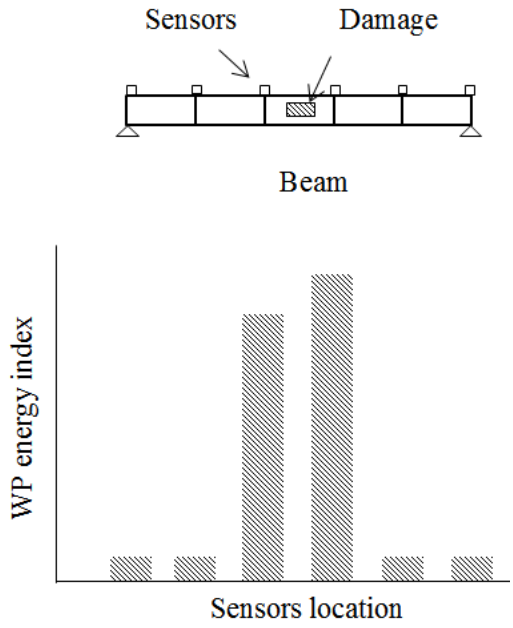

Figure 4-5 Damage detection for beam structure using WP energy method

For embedded utility poles, however, the part that is buried in soil, which is indeed most prone to damage, cannot be covered with sensors (see Figure 4-6). Therefore, in this study, the damage detection can only rely on the wavelet packet energies from the

reflected wave signal, and a novel damage detection algorithm is investigated for application to utility poles.

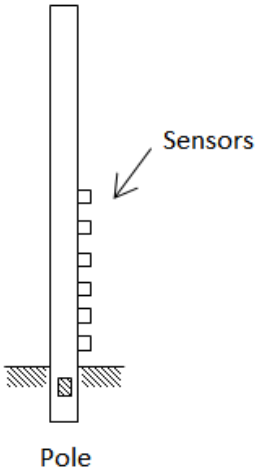

Figure 4-6 Damage detection for utility pole structure

4.3.2.1 Damage classification

Since the damage detection in this study can only rely on the wavelet packet energies from the reflected signal, it results in some complications in identifying the damage since interference may occur between the incident wave and the reflected wave, and, thus, the energy change may not only be caused by damage but also by other factors. To overcome this issue, the use of a sensor network is proposed to minimise the effect of the interference between the incident wave and reflected wave.

In the current study, the isotropic model was considered without surrounding soil influence. The pole was 5m long with diameter of 300mm, and seven measurement points (sensors) were placed at 1.7 m to 2.9 m from the bottom of the pole with a distance between each sensor of 200 mm. Wave signals were generated with a continuous sine wave excitation of 8 kHz, applied on the top centre of the pole. According to the dispersion study of isotropic material, it was found that longitudinal wave with 8kHz had only one mode as well as a smaller wave length. The wave signal generated by a continuous sine wave of 8 kHz was easy to analyse and was more sensitive to small damage. Damage was simulated by removing specific elements. Different damage types with varying size of damage were simulated with a damage width of 15 mm, 30 mm, 45 mm, 60 mm, 75 mm, 90 mm, 120 mm, 150 mm, 180 mm and 210 mm, respectively, and a constant damage height of 200 mm. An example of

damage size of 150mm is shown in Figure 4-7. To make it easy to demonstrate, if there is no specific description, the damage size in this thesis refers to the width of damage. Four investigated damage types are illustrated in Figure 4-8, among them damage type 2 is the major damage type in timber utility poles that has been reported and type 1 is designed to verify the capability of the proposed method for damage classification. For all damage scenarios, the wave signals were captured by the sensors and the wavelet packet component energies of each sensor were calculated according to the equations in section 4.2.3.1.

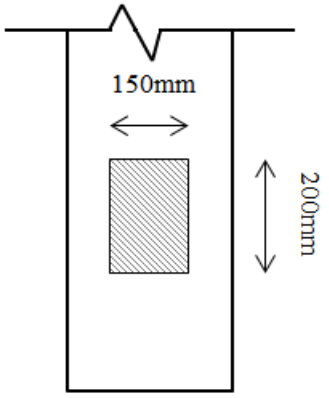

Figure 4-7 Damage with 150mm in width and 200mm in height

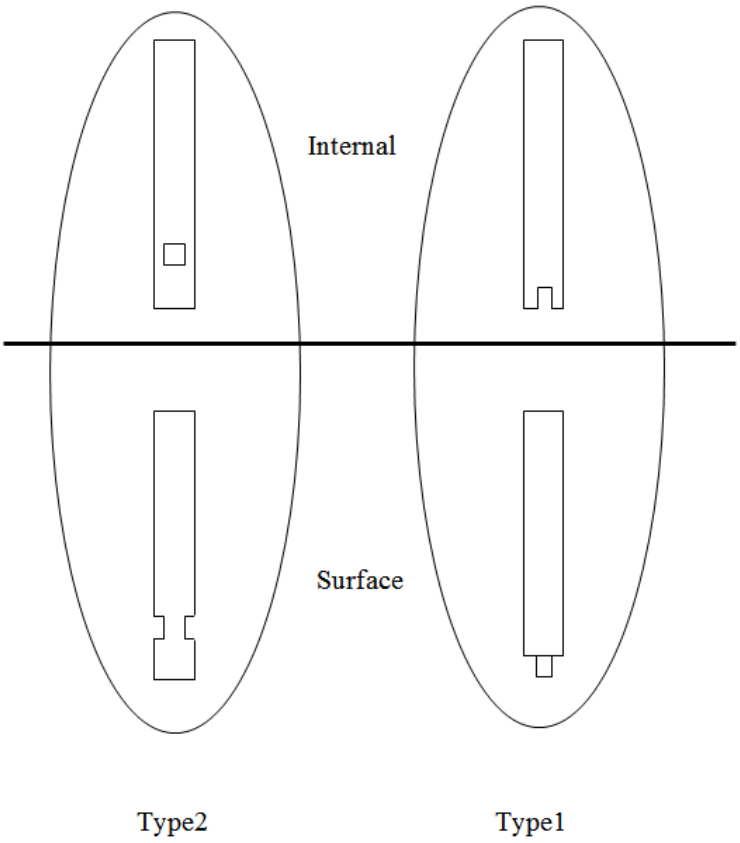

Figure 4-8 Damage classifications

These four types of damage, named internal type 1, internal type 2, surface type 1 and surface type 2, are simplified to an axisymmetric form. In reality, some damage caused by decay or insects attack occurs internally and some is present on the surface. For some utility poles, different degrees of protective measures have been taken to deal with fungi and insect attack at the bottom part; and, therefore, much decay occurs above the protected area such as damage type 2. Also, in this research, for damage type 2, the damage location was designed at 400mm from the bottom of pole (see Figure 4-9).

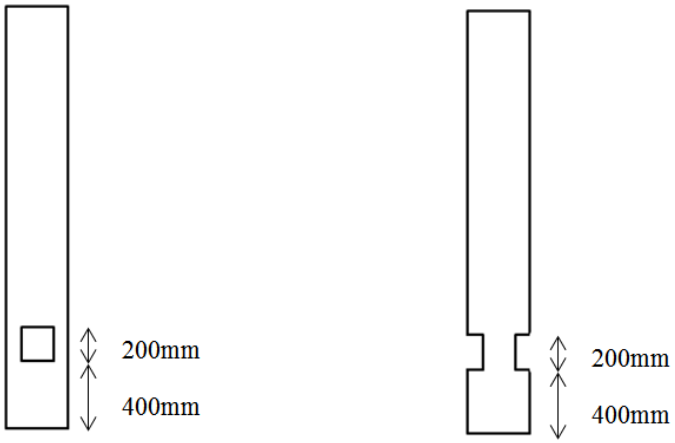

Figure 4-9 Damage localization for type 2

To classify the damage type, WP energy and natural frequency parameters were used as classification features. Since the change of these parameters was hard to be identified for small damage, the damage classification started from damage size of 90mm (that is 30% of cross section) up to 210mm (70% of cross section) with increasing step size of 30mm, that is five damage sizes of 90mm, 120mm, 150mm, 180mm and 210mm with 4 damage types were used for damage classification.

After 10 levels of wavelet packet decomposition, 1024 frequency bands, that is 1024 energy components, were obtained for each sensor. The WP energy feature was obtained by the following equations:

$$EF = \sqrt{\frac{\sum_{i=1}^{N}\left(\frac{E_{Di}}{E_{Si}} - 1\right)^2}{N}} \qquad (i = 1,2,3,\dots,N) \qquad \text{Eq. 4-14}$$

where EF is the parameter of energy feature for each damage scenario, N is the total number of sensors, E_{Di} and E_{Si} are the total WP energy for each sensor under damaged and intact conditions, respectively. According to Eq. 4-14, four types of damage with 5 different damage sizes were obtained. Take the damage of 150mm for example:

Table 4-2 WP energy components from 7 sensors under intact and damaged (150mm) conditions

Intact						
E_{S1}	E_{S2}	E_{S3}	E_{S4}	E_{S5}	E_{S6}	E_{S7}
23037436	25982776	19224989	18895091	26673383	20301733	12763184
Internal type1						
E_{D1}	E_{D2}	E_{D3}	E_{D4}	E_{D5}	E_{D6}	E_{D7}
22555072	26400639	19724970	18088275	26489639	21700297	12356134
Internal type2						
E_{D1}	E_{D2}	E_{D3}	E_{D4}	E_{D5}	E_{D6}	E_{D7}
21614681	22381054	20705352	19422246	19634374	18476699	17216786
Surface type1						
E_{D1}	E_{D2}	E_{D3}	E_{D4}	E_{D5}	E_{D6}	E_{D7}
22013525	26735355	20814719	17372529	26050506	23525945	12500371
Surface type2						
E_{D1}	E_{D2}	E_{D3}	E_{D4}	E_{D5}	E_{D6}	E_{D7}
22740350	21548495	19591743	21860683	22432128	15345537	17276525

In Table 4-2, the energy components from sensors of damage type 2 have more obvious difference with the intact ones compared with damage type 1. For example, the energy component from sensor 4 of intact condition is 18895091, and for the same sensor, the damage of internal type 1 has the value of 18088275 and internal type 2 has the value of 19422246. The surface type 1 has the value of 17372529 while the surface type 2 has the value of 21860683. From these parameters, it can be seen that the values change considerably under damage type 2. According to Eq. 4-14, the EF index of these damage types are 0.036, 0.18, 0.078 and 0.19 respectively. The results from different sensor arrangements are quite consistent.

Figure 4-10 indicates that damage type 1 and damage type 2 can be almost separated by EF index of 0.1 using 7 sensors. Figure 4-11 and Figure 4-12 demonstrate the results from different sensor arrangements and a similar phenomenon can be observed.

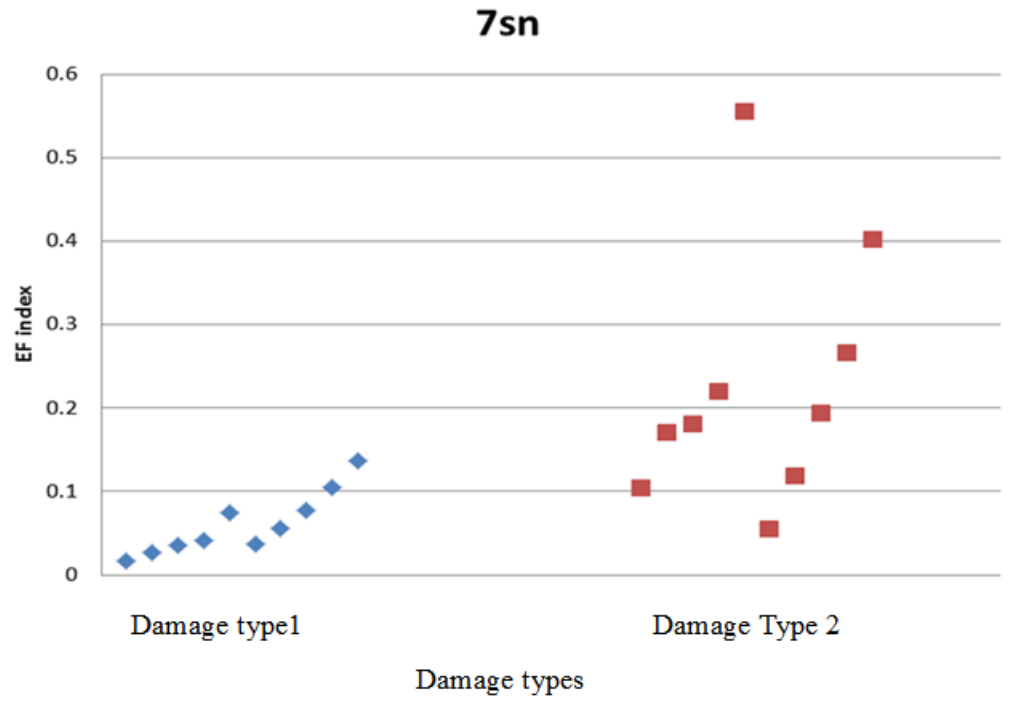

Figure 4-10 Energy feature obtained from 7 sensors

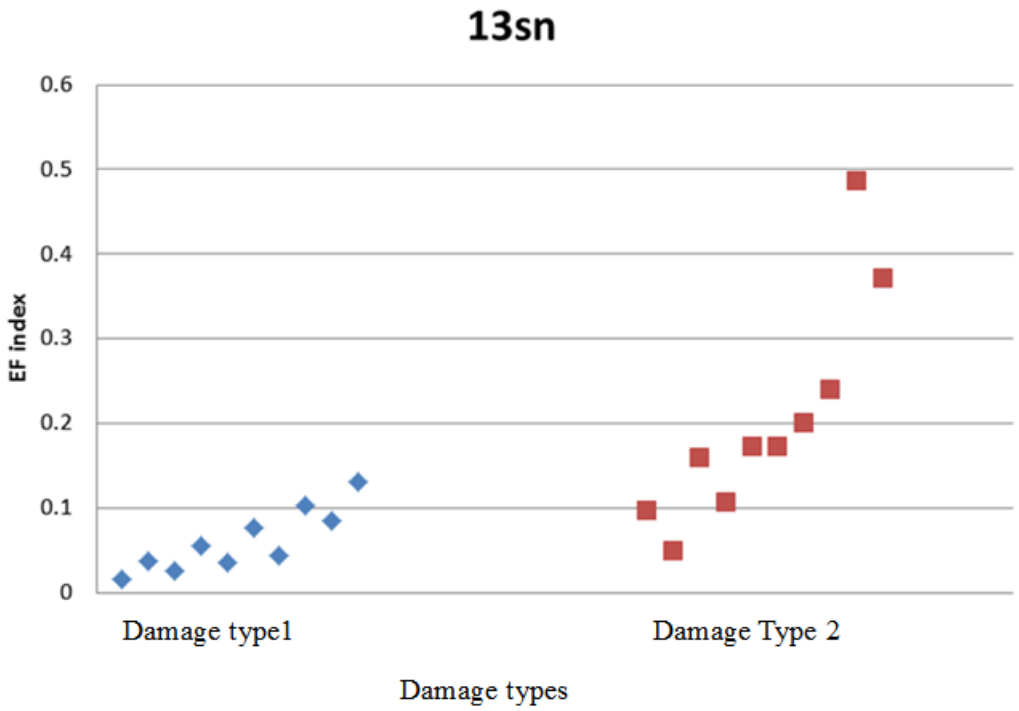

Figure 4-11 Energy feature obtained from 13 sensors

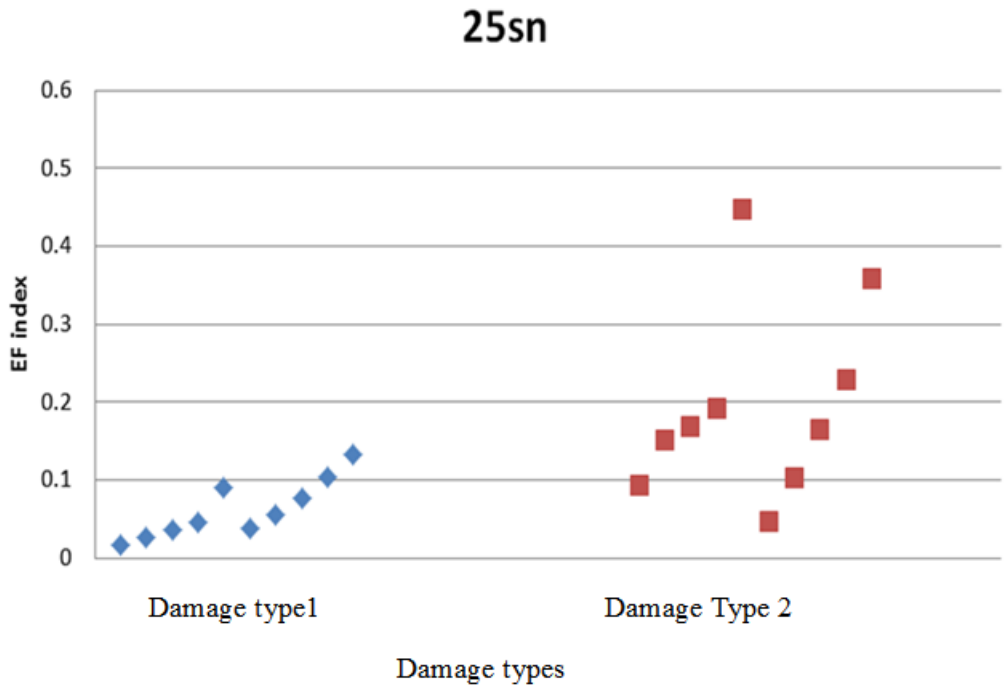

Figure 4-12 Energy feature obtained from 25 sensors

To further classify the damage, the parameters of the natural frequency feature need to be collected. The natural frequency was obtained by applying transient analysis through a hammer impact with a sampling frequency of 10 kHz. Frequency Response Function (FRF), a common transfer function measurement similar to Fast Fourier Transfer (FFT), was then used to process the acceleration, and the frequencies of the first four modes clearly appeared. Modal analysis based on the physical parameters of the models was conducted as well to compare the results with the transient analysis. The modes in this research were concentrated on the longitudinal modes only. The errors between these two methods were around 7%-8% and two examples are shown below:

Table 4-3 Comparison between transient and modal analysis under intact condition

Intact	Transient Analysis (Hz)	Modal Analysis (Hz)
1st mode	246	246
2nd mode	726	739
3rd mode	1175	1231
4th mode	1577	1721

Table 4-4 Comparison between transient and modal analysis under severe damage condition

Damage (210mm)	Transient Analysis (Hz)	Modal Analysis (Hz)
1st mode	235	235
2nd mode	696	707
3rd mode	1133	1183
4th mode	1530	1663

From the tables above, it can be seen that the results from the two methods are close to each other in the lower frequency range (first 2 modes) while the error increases at the 3rd and 4th modes. The results of transient analysis are corresponding to the sampling frequency as well as data processing through FRF, while for the modal analysis the frequencies of each mode are obtained from the structural characteristics directly; as a result it will generate some numerical errors during the transient analysis.

The natural frequencies obtained from transient analysis were used for frequency feature acquisition:

$$FF = \sqrt{\sum_{i=1}^{4}\left(\frac{f_{Di}}{f_{Si}} - 1\right)^2} \qquad (i = 1,2,3,4) \qquad \text{Eq. 4-15}$$

where FF is the parameter of the frequency feature for each damage type, f_{Di} and f_{Si} are the frequency at specific modes under damaged and intact condition, respectively.

Take the same damage size (150mm) as an example again:

Table 4-5 Natural frequencies (Hz) for intact and damaged condition

	Intact	Internal type1	Internal type2	Surface type1	Surface type2
1st mode	246	242	241	215	211
2nd mode	726	715	717	651	665
3rd mode	1175	1159	1169	1084	1134
4th mode	1577	1558	1580	1491	1571

From Table 4-5, it can be seen that the frequencies change significantly under surface damage compared with internal damage. For example, at the 2nd mode, the frequency under the intact condition is 726Hz, while the values under surface damages are 651Hz and 665Hz, respectively. However, under the internal damage conditions, the values are 715Hz and 717Hz. The change of frequencies under surface damage is more obvious. Based on Eq. 4-15, the FF indices are 0.029, 0.024, 0.188 and 0.169, respectively. Figure 4-13 indicates that internal and surface damage can be almost separated by the FF index.

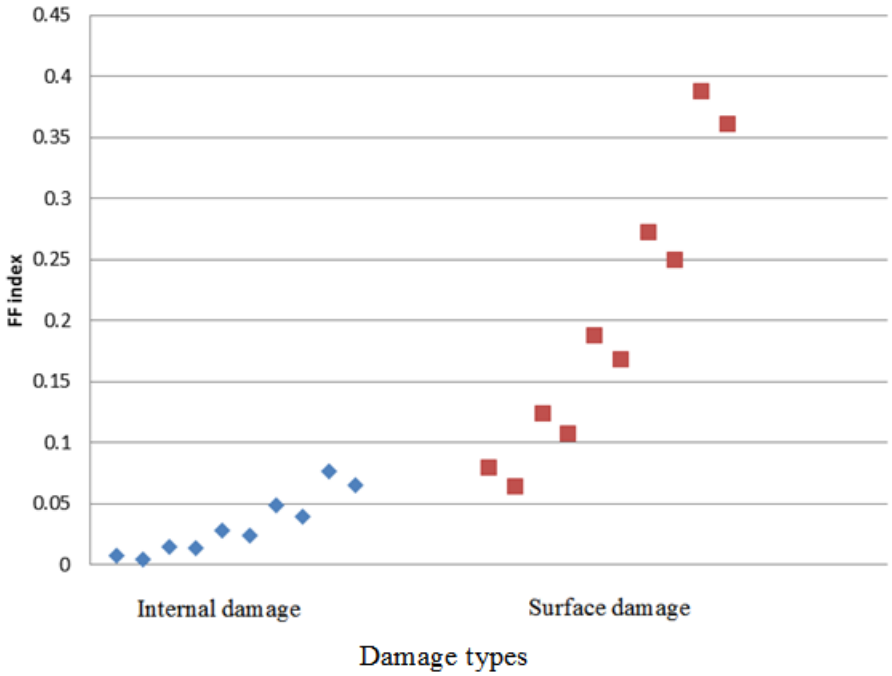

Figure 4-13 Frequency feature obtained from all damage scenarios

Combining the frequency feature with the energy feature, more obvious damage classification is obtained. It can be seen that each damage type covers a particular area in Figure 4-14. To verify the effectiveness of these features, damage of 160mm and 200mm with four damage types were imported. The damage classification shows consistent results with previous models. In Figure 4-15, the particular damage type again falls into the corresponding area that is formed by the specific features.

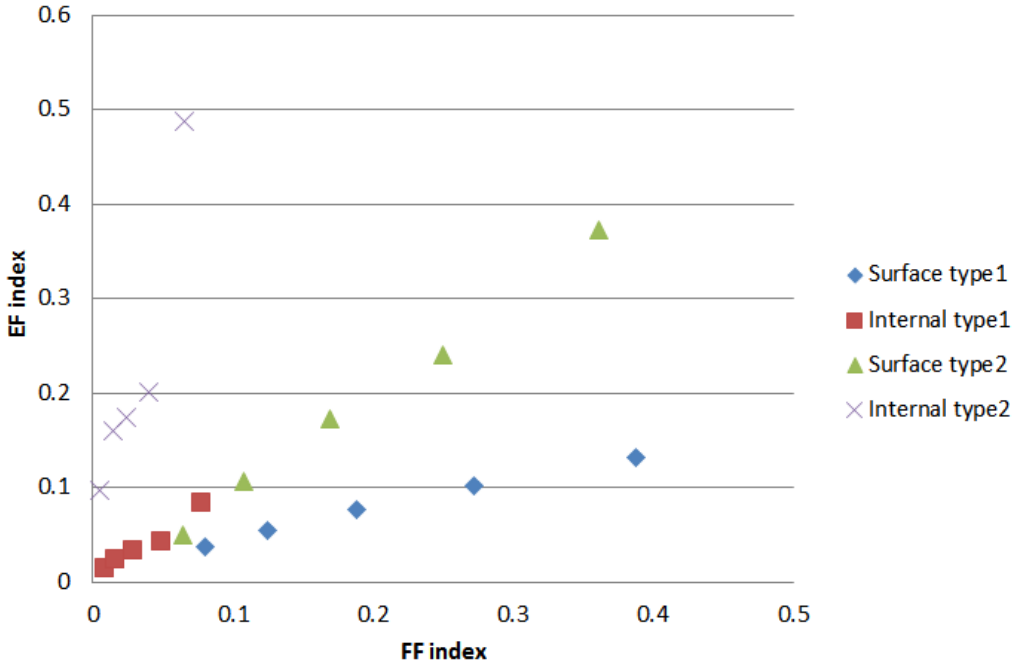

Figure 4-14 Combined feature to identify the damage classification (5 damage sizes)

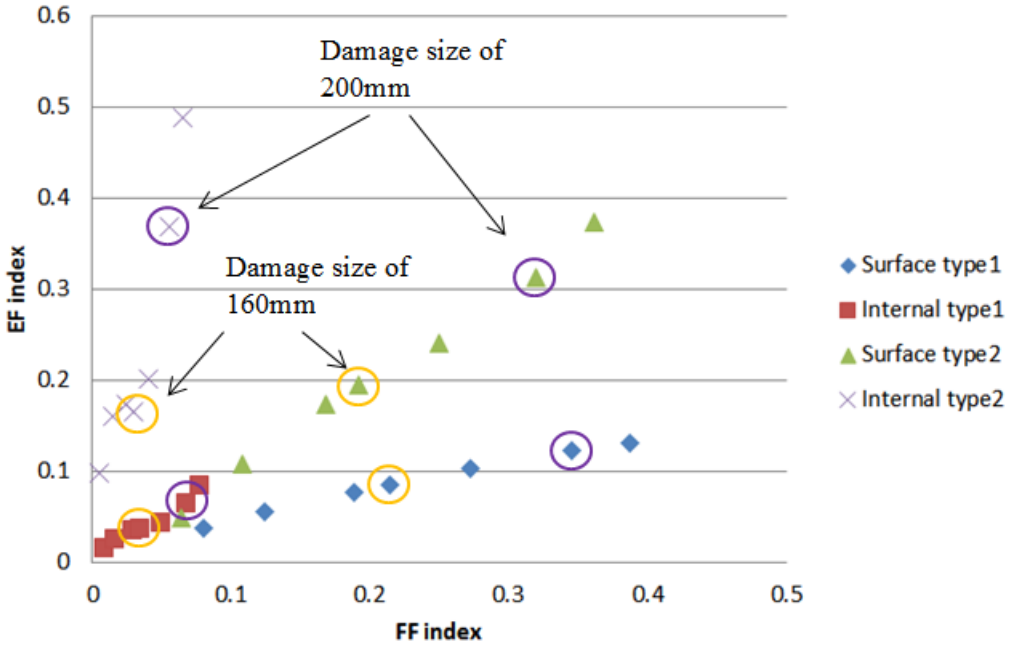

Figure 4-15 Combined feature to identify the damage classification (7 damage sizes)

According to combined energy and frequency feature, the damage classification can be identified systemically using a support vector machine (SVM).

4.3.2.2 Support vector machine

Support vector machines (SVM) are Kernel-based techniques and represent a major development in machine learning algorithms. It makes use of limited sample

information in a training model to seek the best compromise between accuracy and generalization performance and shows a unique advantage in solving the problem of small sample, nonlinear and high dimension, and, therefore, is the most effective machine learning method so far. SVM was firstly developed by Vapnik and his collaborators (Boser et al., 1992) based on the statistical learning theory in the early 90's and has grown in its popularity due to simple geometric interpretation, competitive classification accuracy in practice and has been successfully used in many applications of data mining, pattern recognition, fault diagnosis, intelligent control and signal processing (Lee, 2011). It also has operational characteristics such as sparsity and duality and makes the SVM solution more efficient for data reduction at the testing stage and allows coherent handling of high dimensional data (Lee, 2011).

The SVM can be considered to create a line or hyperplane boundary between two sets of data with maximum margin for classification.

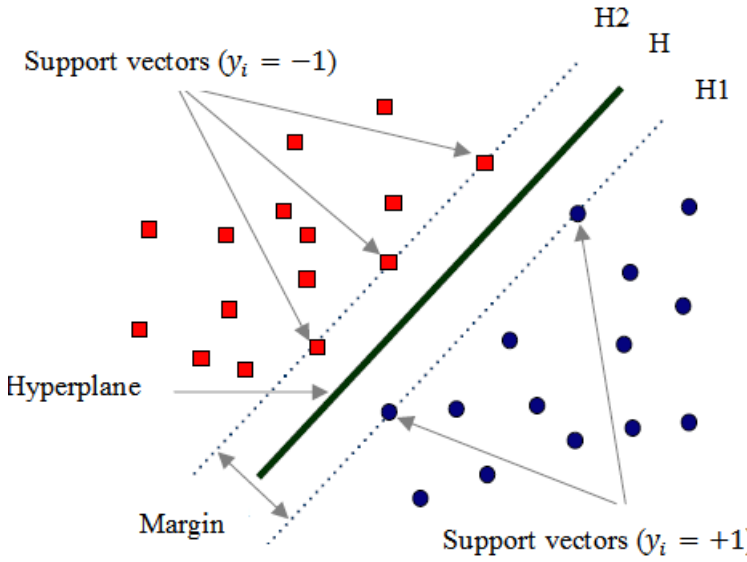

Figure 4-16 Classification of data by SVM (linear)

Figure 4-16 shows a series of symbols for two classes, circles and squares. The SVM attempts to separate the two different classes by placing a linear boundary (solid line), and orient it to achieve a maximum margin (represented by dotted lines). Support vectors (SVs) are used to define the margin and the boundary H is then placed in the middle of the margin. The boundary H can be expressed as Eq. 4-16

$$x \cdot w + b = 0, w \in R^N, b \in R \quad \text{Eq. 4-16}$$

where w defines the boundary, x is the input vector of dimension N and b is a scalar threshold. For two classes at the margins, H1 and H2, can be expressed by Eq. 4-17 and Eq. 4-18

$$x \cdot w + b = +1 \quad \text{Eq. 4-17}$$

$$x \cdot w + b = -1 \quad \text{Eq. 4-18}$$

Since SVs correspond to the extremities of the data for a given class, the decision function can be used to classify any data point in either class:

$$f(x) = \pm(x \cdot w + b) \quad \text{Eq. 4-19}$$

The distance between H and H1 is:

$$\frac{|x \cdot w + b|}{\|w\|} = \frac{1}{\|w\|} \quad \text{Eq. 4-20}$$

The distance between H1 and H2 is $\frac{2}{\|w\|}$

In order to maximise the margin, $\|w\|$ has to be minimised according to (Scholkopf, 1998):

$$\tau(w) = \frac{1}{2}\|w\|^2 \quad \text{Eq. 4-21}$$

And subjected to a constrained optimization problem:

$$y_i\big((w \cdot x_i) + b\big) \geq 1, i = 1, \ldots, l \quad \text{Eq. 4-22}$$

where l is the number of training sets. Eq. 4-22 defined the constrained condition as a "rigid margin". A Rigid margin requires the distance of all sample points and the classification plane exceeds a certain value. However, if there are a few stray samples which exist, it becomes no longer a linear problem, and this kind of classification problem is called "approximately linearly separable". A Rigid margin may make the whole optimization problem with no solution in dealing with this kind of problem. "Soft margin" is used to overcome this problem by introducing non-negative slack variables, ξ_i, satisfying $\xi_i \geq 0$. Eq. 4-21 and Eq. 4-22 lead to equations below;

$$\tau(w) = \frac{1}{2}\|w\|^2 + C\sum_{i=1}^{l}\xi_i \quad \text{Eq. 4-23}$$

$$y_i\big((w \cdot x_i) + b\big) + \xi_i \geq 1, \;\; i = 1, \ldots, l \quad \text{Eq. 4-24}$$

where C is a penalty multiplier and accordingly the optimization becomes a trade-off between a large margin and a small error penalty.

If the linear boundary cannot separate two classes properly, a hyperplane allows linear separation in the higher dimension by a transformation $\emptyset(x)$. Substituting $\emptyset(x)$ into Eq. 4-24 yields;

$$y_i\left(\big(w \cdot \emptyset(x_i)\big) + b\right) + \xi_i \geq 1, \;\; i = 1, \ldots, l \quad \text{Eq. 4-25}$$

By using the Lagrangian multiplier method, the solution of the constrained optimization problem can be obtained as follows:

$$L(w, b, \xi, \alpha, \beta) = \frac{1}{2}\|w\|^2 + C\sum_{i=1}^{l}\xi_i \quad \text{Eq. 4-26}$$

$$-\sum_{i=1}^{l}\alpha_i\,[y_i(w \cdot \emptyset(x_i) + b) + \xi_i - 1] - \sum_{i=1}^{l}\xi_i\,\beta_i$$

where x_i are SVs obtained from training, α_i is Lagrange Multipliers, and the optimization solution can be obtained from the saddle point of the Lagrange function:

$$\begin{cases} \dfrac{\partial L}{\partial w} = w - \displaystyle\sum_{i=1}^{l}\alpha_i y_i x_i = 0 \;\rightarrow w = \sum_{i=1}^{l}\alpha_i y_i \emptyset(x_i) \\ \dfrac{\partial L}{\partial b} = \displaystyle\sum_{i=1}^{l}\alpha_i y_i = 0 \;\rightarrow \sum_{i=1}^{l}\alpha_i y_i = 0 \\ \dfrac{\partial L}{\partial \xi_i} = 0 \rightarrow C - \alpha_i - \beta_i = 0 \rightarrow 0 \leq \alpha_i \leq C \end{cases} \quad \text{Eq. 4-27}$$

Substituting it into Eq. 4-25 a dual form can be obtained:

$$\max_{\alpha}\sum_{i=1}^{l}\alpha_i - \frac{1}{2}\sum_{i=1}^{l}\sum_{j=1}^{l}\alpha_i\,\alpha_j y_i y_j K\big(x_i \cdot x_j\big) \quad \text{Eq. 4-28}$$

$$\sum_{i=1}^{l}\alpha_i y_i = 0 \qquad 0 \leq \alpha_i \leq C, i = 1,2, \ldots, l \quad \text{Eq. 4-29}$$

where $K(x_i \cdot x_j)$ is a kernel function to reduce the computational load and at the same time retain the effect of higher-dimensional transformation (Samanta, 2004). The kernel is related to the transform $\emptyset(x_i)$ by

$$K(x_i \cdot x_j) = \emptyset(x_i) \cdot \emptyset(x_j) \quad \text{Eq. 4-30}$$

The optimization should also satisfy:

$$\begin{cases} \alpha_i[y_i(w \cdot \emptyset(x_i) + b) + \xi_i - 1] = 0 \\ \xi_i \beta_i = 0 \ \rightarrow \ (C - \alpha_i)\xi_i = 0 \end{cases} \quad \text{Eq. 4-31}$$

Combining Eq. 4-28, Eq. 4-29 and Eq. 4-31, the hyper plane in high dimension is obtained:

$$f(x) = \sum_{i=1}^{l} w \cdot \emptyset(x) + b$$

$$= \sum_{i=1}^{l} \alpha_i y_i(\emptyset(x_i) \cdot \emptyset(x)) + b \quad \text{Eq. 4-32}$$

$$= \sum_{i=1}^{l} \alpha_i y_i K(x_i \cdot x) + b$$

Sign function is always used to determine the classification of samples

$$y(x) = sgn[f(x)] \quad \text{Eq. 4-33}$$

4.3.2.3 Design of classifier for damage type classification

Typical application of support vector machine (SVM) uses a binary classifier, that is identifying the samples belonging to positive or negative class. In this research, identification of damage types is a multi-class classification problem. The most direct way is to establish an objective function to obtain multiple hyperplanes. The sample space will be divided into several regions and each region will correspond to a category. However, this method is not applicable since it requires a large computational resource.

In application, the methods used in multi-class classification can roughly be divided into two approaches: one-against-the rest (OAR) and one-against-one (OAO). The implementation procedure is reducing a multi-class classification problem to a binary

problem and the binary classifier also can be called the sub-classifier. Using OAR to solve an n-class classification problem, n sub-classifiers have to be constructed and each of them will be trained to separate one class from the rest. The i^{th} sub-classifier is trained with all the training examples of the i^{th} class with positive labels, and all the others with negative (Liu and Zheng, 2005). This method needs fewer sub-classifiers, but may cause overlapped categories or no category at all. OAO on the other hand constructs a sub-classifier for each possible pair of classes resulting in $n(n-1)/2$ sub-classifiers. When a sample is tested, each sub-classifier gives one vote to the winning class and finally the sample will be labelled with the class having the most votes. It can be found that OAO needs more sub-classifiers if the total number of categories increases.

Considering the damage types are not many, OAO was selected in this research to establish the classifier for damage type classification.

In practical applications, most classification problems are non-linear separation problems. Kernel methods map data from the original space onto the kernel space so that classifiers could find a linearly separable hyperplane (Liu et al., 2012). Kernel function has to be determined in advance to create classifiers and some common kernels include:

- Linear kernel $K(x, y) = x \cdot y$
- Polynomial kernel $K(x, y) = [(x \cdot y) + c]^d, c \geq 0$
- Gaussian radial basis function (Gaussian RBF) $K(x, y) = exp\left\{\frac{-\|x-y\|^2}{2\sigma^2}\right\}$
- Hyperbolic tangent $K(x, y) = tanh[k(x \cdot y) - \delta], k \geq 0$

For the choice of kernel function, there is a lack of recognised principle to guide the choice. This research adopts the Gaussian radial basis kernel function, because it has a strong capability of nonlinear approximation.

After selecting the kernel function, two parameters have to be set which are penalty multiplier C and the value of σ^2, respectively. C is a trade-off between training error and the flatness of the solution. Increasing C will cause less final training error, but it may also result in a risk of losing the generalization properties of the classifier since it

will try to fit as best as possible all the training samples. In addition, the time needed for training will also be increased. As a result, it is important to find a C that keeps the training error small, but also generalizes well. For Gaussian RBF, selecting appropriate parameter σ is essential and crucial to determine the robust performance of classifiers. Small σ will cause over-fitting while large σ will lead to under-fitting for classifiers (Liu et al., 2012). Gird search is the most intuitive and practical way for parameter selection by defining search ranges in advance; however, improper ranges will cause failure in searching appropriate parameters (Liu et al., 2012). In this research, the parameter selection was considered as an intelligent optimization problem and particle swarm optimization (PSO) algorithm was introduced.

Particle swarm optimization is a population based stochastic optimization technique originally attributed to Dr Eberhart and Dr Kennedy in 1995 and was intended to simulate social behaviour of bird flocking or fish schooling (Huang and Dun, 2008). The PSO algorithm uses particles representing a potential solution moving in an n-dimensional search space to search for solutions for n-variable function optimization problem. Each particle flies through the search space with a velocity adjusted by its own flying velocity and position according to its own flying experience as well as those of the other companion particles in the swarm (Liu et al., 2011). PSO is initialized with a population of random solutions and searches for optima by updating generations which are quite similar with other evolutionary computation techniques such as genetic algorithm (GA), but embraces the excellent advantages of simplicity and fast speed (Zhai et al., 2008).

In this case, the particle swarm optimization (PSO) was adopted to make the classifier parameters arrive at their optimums in the meantime. Then the classifier was constructed on the basis of these optimal parameters for pole damage classification. In other words, the PSO algorithm attempted to explore the optimal parameters to guarantee the sub SVM model fitted the training samples with maximal mean classification accuracy. The specific process of SVM based on PSO was composed of the following steps:

Step 1. Choose the kernel function and initialize the parameters of the SVR model: RBF function, C and σ.

Step 2. Initialize parameters of PSO algorithm, including particle population size P, the maximal allowable velocity v_{max}, the maximal iteration number N_{iter}. In this case, P=20, v_{max}=2 and N_{iter}=100.

Step 3. Randomly assign the position and velocity vectors of each particle by the following equation:

$$\begin{aligned} x_i &= x_l + rand \cdot (x_u - x_l) \\ v_i &= rand \cdot v_{\max} \end{aligned} \quad \text{Eq. 4-34}$$

where x_u and x_l denote the upper and lower boundaries of the estimated parameter vector, respectively. In this work, x_l =[0, 0] and x_u =[100, 100].

Step 4. Input the training data and corresponding outputs and calculate the fitness value of each particle. Evaluate and record the $pbest_i$ and $gbest$ according to the following equation:

$$pbest_i^{k+1} = \begin{cases} pbest_i^k, & if\ f(x_i^{k+1}) \geq f(pbest_i^k); \\ x_i^{k+1}, & or\ else \end{cases} \quad \text{Eq. 4-35}$$

Step 5. Check the termination rule. There are several rules available to terminate the PSO algorithm. Here, the maximal iteration is regarded as the stopping condition. If the condition is satisfied, the calculation will be terminated, $gbest$ is stored as the best solution and the operation will go to Step 7. Or else, repeat Steps 4-6.

Step 6. Update the velocity and position of each particle

Step 7. Set up the forecast model according to the optimal values of C and σ.

Step 8. Save the optimal parameters and trained model, and the classifier setup is finished.

In conclusion, the process of sub model setup for damage type classification can be illustrated in Figure 4-17.

The design of classifier was crucial for damage type classification and the procedure of damage classification is shown in Figure 4-18. Four damage types are named as C1, C2, C3 and C4 for convenience and, therefore, six classifiers are created to achieve binary classification including C1-C2 classifier, C1-C3 classifier, C1-C4 classifier, C2-C3 classifier, C2-C4 classifier and C3-C4 classifier, respectively. When a sample data with

the feature of specific damage type is tested, each sub-classifier gives one vote to the winning damage type and finally the sample will be labelled with the damage type having most votes.

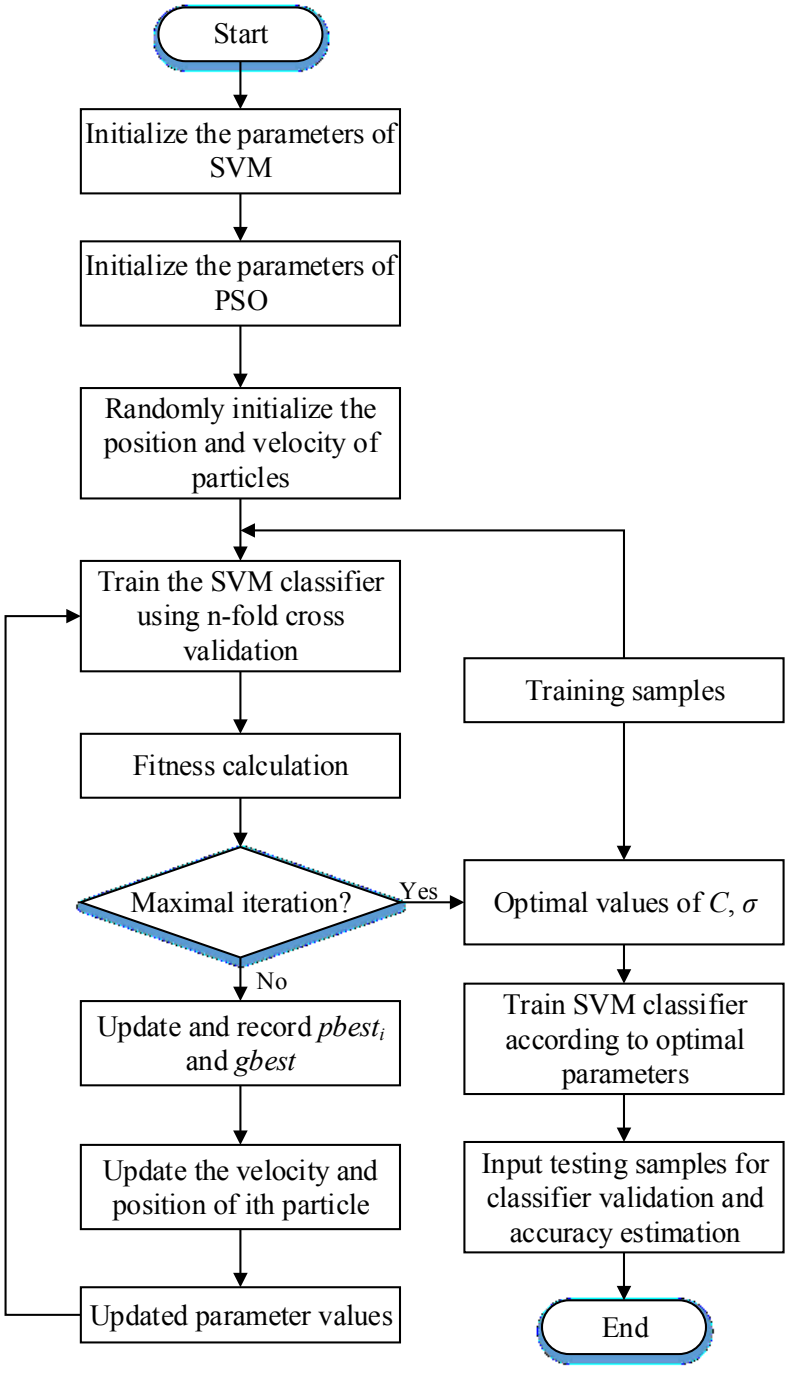

Figure 4-17 Parameter optimization process of SVM classifier

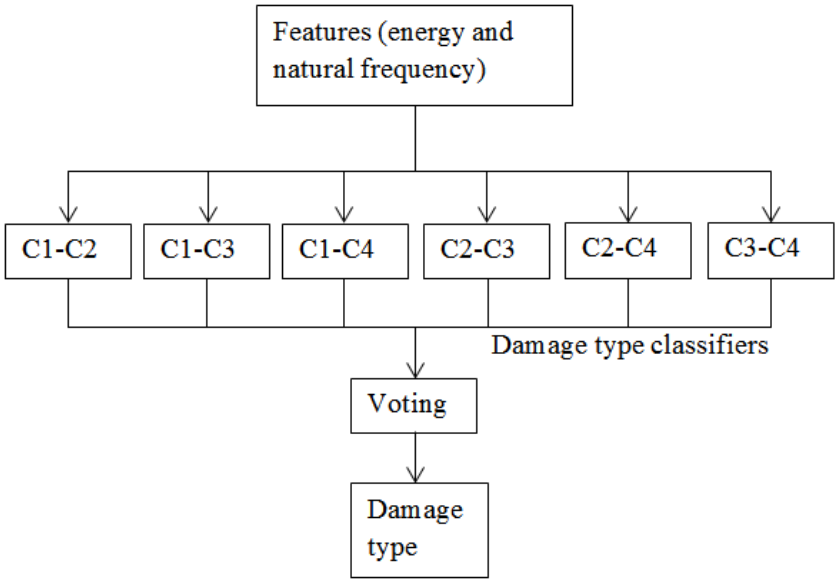

Figure 4-18 Design of classifier for damage type classification

Figure 4-19 to Figure 4-24 describe the parameter optimization process of six sub SVM classifiers. The left figures show the algorithm convergence during the iteration while the right figures exhibit the variance trend of each parameter for six cases. It is obvious that for all the cases the optimal fitness gradually increases with the increase of iteration number though some fluctuations still exists in the mean fitness (classification accuracy). In addition, it is easily found that two parameters (C and σ) always arrive at their optima in the meantime. Figure 4-25 depicts the visualization classification results of six sub SVM classifiers. It is noticeable that all categories of timber pole condition of training samples are clearly separated by an optimal hyperplane in each sub classifier although more support vectors are occupied in the training samples due to the limited data. Table 4-6 gives the classification results of all sub SVM classifiers by n-fold cross validation. It can be seen that the classification accuracies of all classifiers are above 90% and the average classification accuracy can reach 97.22%. In order to evaluate the performance of built multi-classifier, a damage case of 160mm and 200mm for four types of damage was adopted to extract the feature, which was then inputted into the classifier for damage type identification. Table 4-7 illustrates the identification results of a new group of damage cases (damage of 160mm and 200mm for four types). The results demonstrate that all damage types are correctly identified, which is regarded as a satisfactory result for its engineering application.

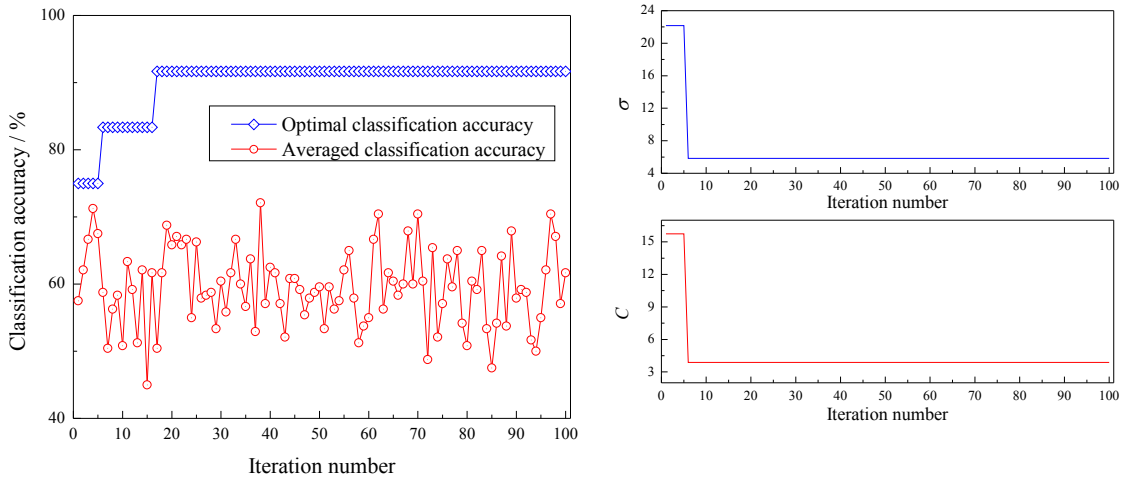

(a) Convergence rate (b) Parameter optimization

Figure 4-19 Parameter optimization process of sub SVM 1

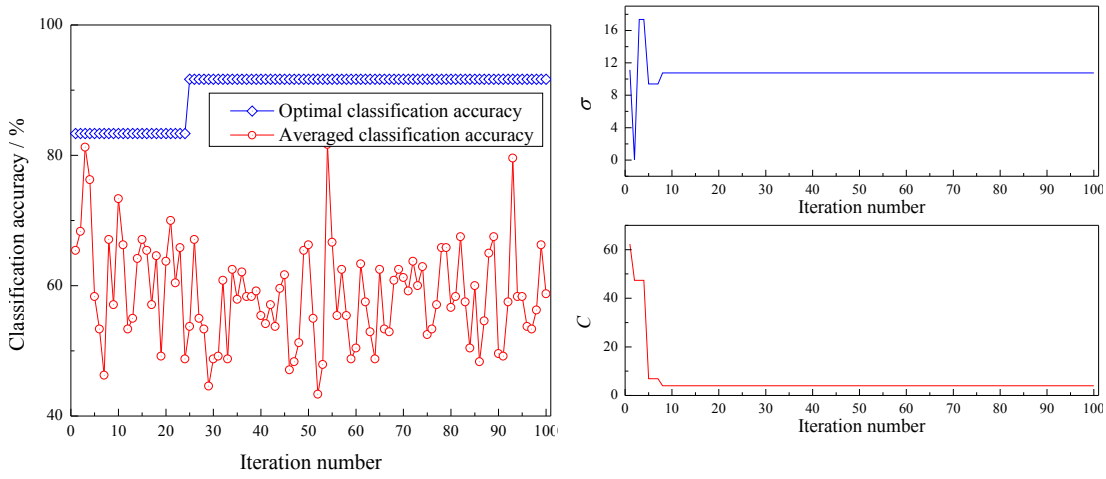

(a) Convergence rate (b) Parameter optimization

Figure 4-20 Parameter optimization process of sub SVM 2

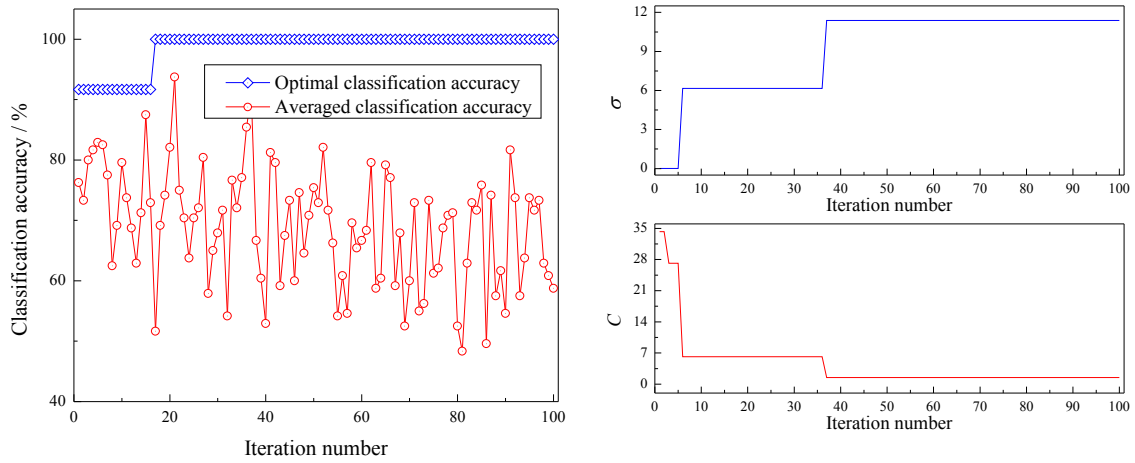

(a) Convergence rate (b) Parameter optimization

Figure 4-21 Parameter optimization process of sub SVM 3

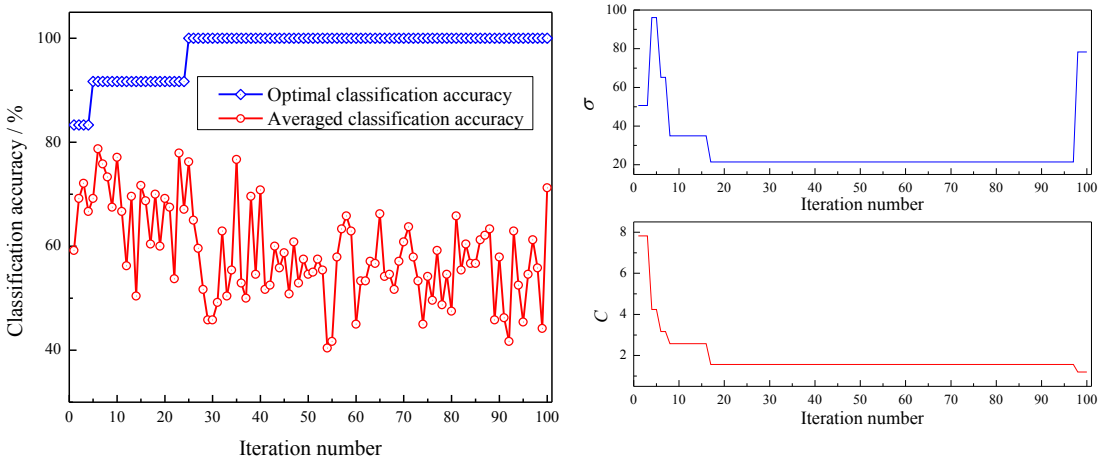

(a) Convergence rate (b) Parameter optimization

Figure 4-22 Parameter optimization process of sub SVM 4

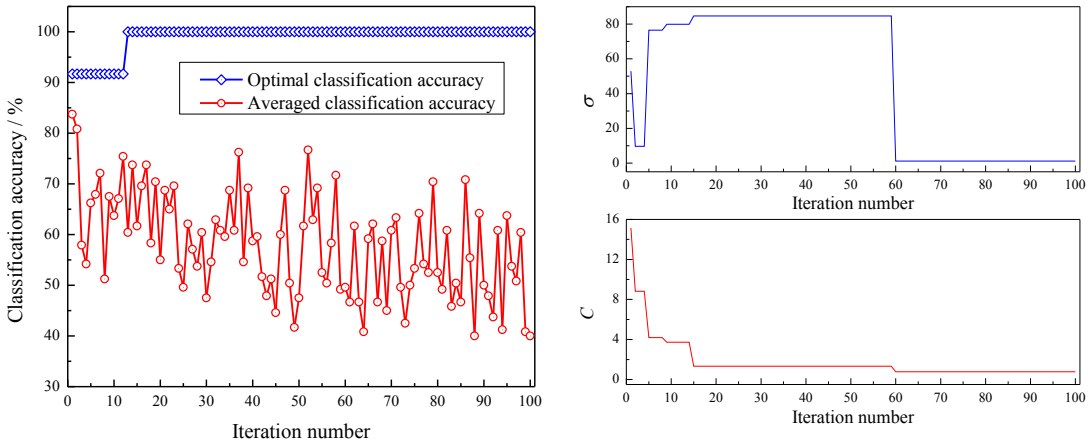

(a) Convergence rate (b) Parameter optimization

Figure 4-23 Parameter optimization process of sub SVM 5

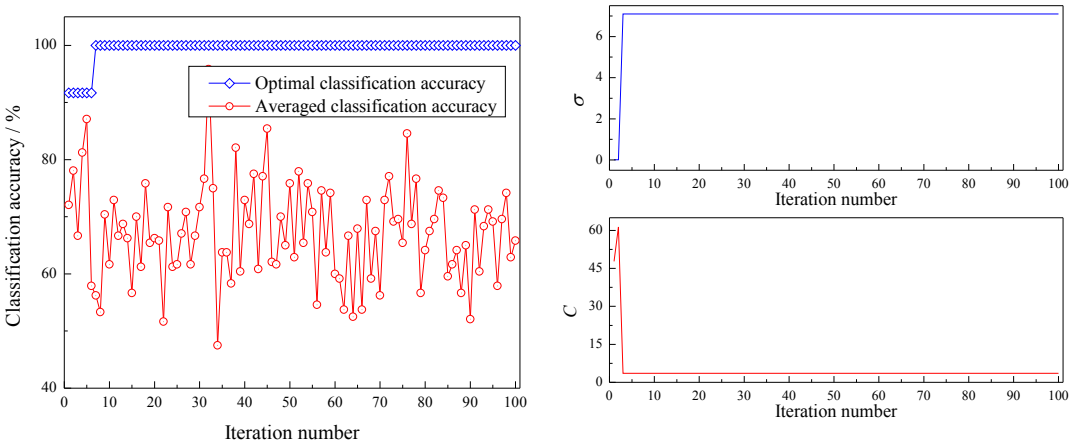

(a) Convergence rate (b) Parameter optimization

Figure 4-24 Parameter optimization process of sub SVM 6

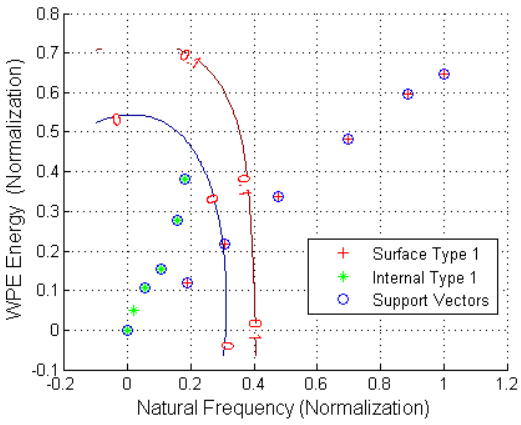

(a) Sub SVM 1

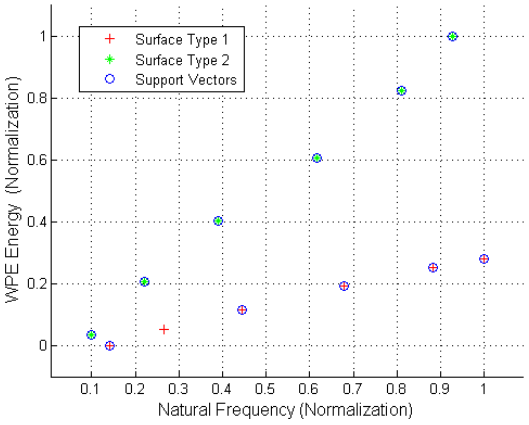

(b) Sub SVM 2

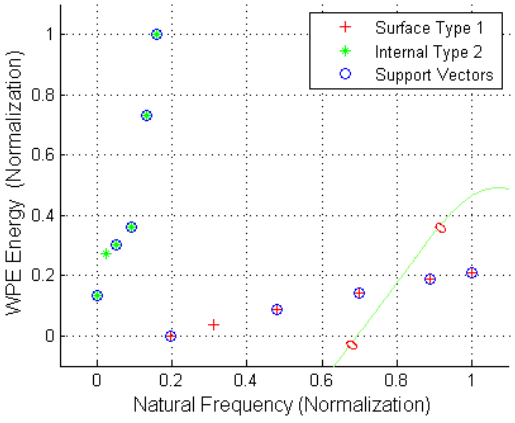

(c) Sub SVM 3

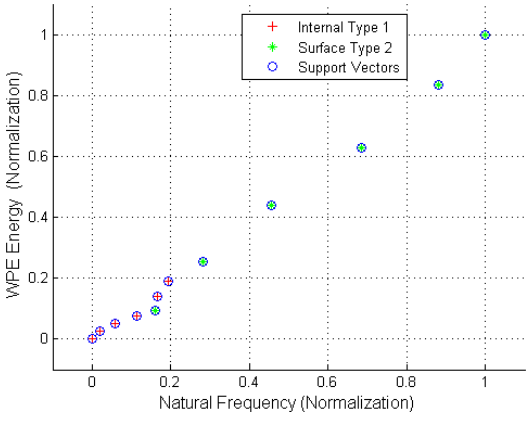

(d) Sub SVM 4

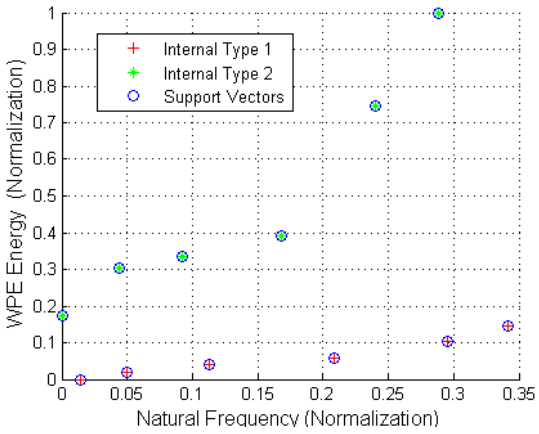

(e) Sub SVM 5

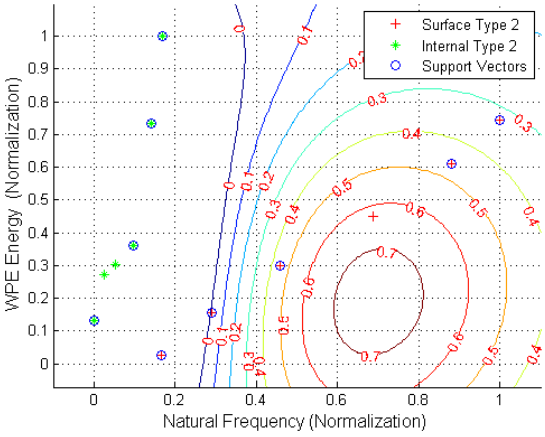

(f) Sub SVM 6

Figure 4-25 Visualization classification results of six sub SVM classifiers

Table 4-6 Classification results of all sub SVM classifiers using n-fold cross validation

	Sub SVM 1	Sub SVM 2	Sub SVM 3	Sub SVM 4	Sub SVM 5	Sub SVM 6	Mean
Classification accuracy	91.67% (11/12)	91.67% (11/12)	100% (12/12)	100% (12/12)	100% (12/12)	100% (12/12)	97.22% (70/72)

Table 4-7 Identification results of a new group of cases

Damage of 160mm				
Real damage type	Surface type 1	Internal type 1	Surface type 2	Internal type 2
Identification result	Surface type 1	Internal type 1	Surface type 2	Internal type 2
Damage of 200mm				
Real damage type	Surface type 1	Internal type 1	Surface type 2	Internal type 2
Identification result	Surface type 1	Internal type 1	Surface type 2	Internal type 2

4.3.2.4 Damage classification using experimental data

To verify the effectiveness of the damage classification method proposed in section 4.3.2.1, a set of experimental data was used. This experimental testing was conducted at the "Federal Institute for Materials Research and Testing" in Berlin, Germany by Dr Ulrike Dackermann and

Dr Saad Subhani (Dackermann et al., 2015). Various types of wave excitation including Mexican hat, sine wave were applied as excitations for the purpose of damage detection. Due to the set-up of utility poles, a hammer impact can only be imparted from the side of a pole, as a result, two types of waves including longitudinal wave as well as flexural wave were generated. Using tractile transducers (see Figure 4-26) as wave excitation source can overcome the major issues associated with a hammer impact. The Experimental settings and the dimensions was shown in Figure 4-27.

The specimens were soft wood with the density of 520 kg/m^3 and the elastic modulus of 11000 MPa in longitudinal direction. All the poles had a length of 3 m and a diameter of 0.25 m. One pole was intact and the other two poles were inflicted with two types of artificial damage simulating internal termite voids and external circumferential fungi decay (see Figure 4-28).

For all testing, four tractile transducers were used as excitation source and 12 accelerometers measured the wave signals. The four tractile transducers were mounted to the sensor wedges via a screw connection and were firmly attached to the pole structure in a ring formation with equal spacing using a ratchet strap. The specific excitation setting was trying to minimise the effect of flexural wave. The accelerometers were attached to the pole in a line. The applied excitation signals were narrow-band frequency burst signals and narrow-band continuous wave signals in the shape of a Mexican hat and a sine wave (Dackermann et al., 2015).

(a) (b)

Figure 4-26 (a) tractile transducer, (b) tactile transducer mounted on sensor wedge (Dackermann et al., 2015)

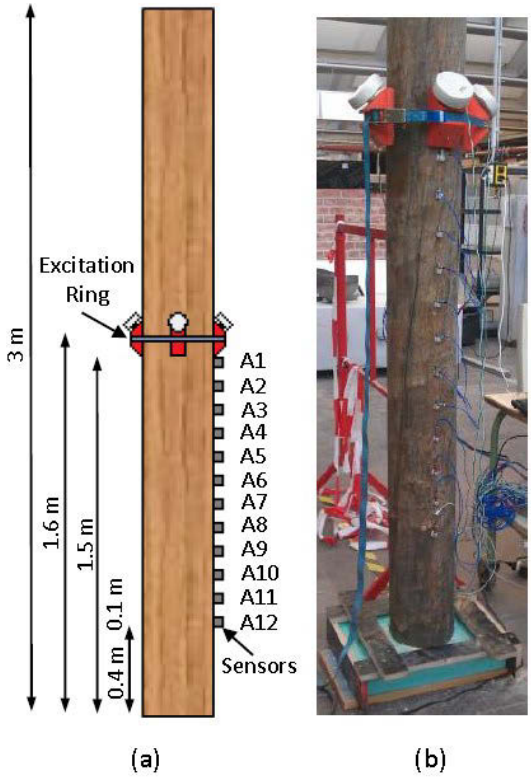

Figure 4-27 Testing set up and dimensions - (a) and (b) line measurement set-up (Dackermann et al., 2015)

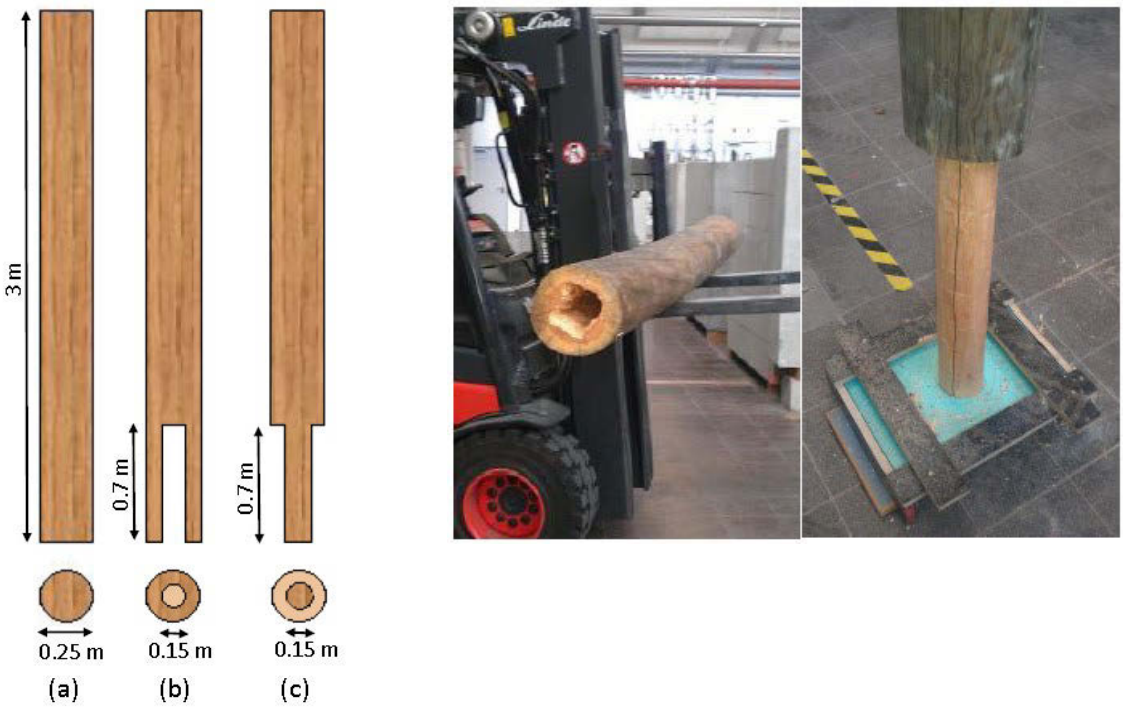

Figure 4-28 Damage configurations and dimensions of tested poles in longitudinal-section and cross-section view (a) intact pole (b) internal void damage (c) external circumferential cross-section loss damage (Dackermann et al., 2015)

The energy feature index and frequency feature index were calculated using the wave signal generated by different excitations and were listed in Table 4-8 and Table 4-9. The excitation frequencies include 5 kHz and 7 kHz; while the excitation waves are continuous sine wave, continuous Mexican hat wave, sine burst wave as well as Mexican hat burst wave. Table 4-8 indicates the damage classification using *EF* index, and the indexes are obviously different especially under the situation of high frequency excitations. Table 4-9 provides the natural frequencies of the intact and the damaged poles according to the wave signal generated by hammer impact. Due to the broadband excitation as well as the measurement noise, the natural frequencies are less accurate. Therefore, the difference of *FF* index between two damage types is not as obvious as the numerical results shown in section 4.3.2.1.

Table 4-8 *EF* index of damage classification

	Cont. sine wave 7k	Cont. sine wave 5k	Cont. Mex hat wave 7k	Cont. Mex hat wave 5k
Internal void damage	1.90	1.44	141.49	28.49
External cross-section loss damage	46.41	7.59	13.87	4.64

	Sine burst wave 7k	Sine burst wave 5k	Mex hat burst wave 7k	Mex hat burst wave 5k
Internal void damage	5.44	21.64	355.97	254.89
External cross-section loss damage	1.07	8.25	90.40	90.02

Table 4-9 Natural frequencies (Hz) and *FF* index

	1st mode	2nd mode	3rd mode	4th mode	*FF* index
Intact condition	442	564	824	1353	
Internal void damage	378	577	862	1236	0.18
External cross-section loss damage	396	747	991	1373	0.40

4.3.3 Proposed damage severity identification algorithm

The wave signals were generated with a continuous sine wave of 8 kHz that was applied at the top centre of the pole. The wave measurements were captured by the seven sensors and the WP component energies of each sensor were calculated. After 10 levels of WP decomposition, 1024 frequency bands, that is 1024 energy components, were obtained for each sensor.

Each sensor had an energy component matrix E_{si}. The difference of each energy component (*DEC*) between any two sensors under the same condition were calculated using Eq.4-36. For the seven sensors, it generated 21 combinations of *DECs* (see Table 4-10) and each *DEC* formed a new energy signal. The comparison of each combination of *DECs* between the intact and the damaged conditions then indicated the damage severity. The cross-correlation coefficient was considered as a comparison parameter and was defined by Eq. 4-37.

$$DEC = E_{s,i} - E_{s,j} \qquad (i, j = 1,2, \dots 7) \tag{Eq. 4-36}$$

$$R = max\left|\sum_{n=1}^{N-1} DEC_{ci}\,(n) DEC_{cd}(n+\tau)\right| \tag{Eq. 4-37}$$

where R is cross-correlation coefficients of two *DEC* signals, and indicates the similarity of *DECs* under intact and different damage conditions, DEC_{ci} presents the results from the intact condition and DEC_{cd} is obtained from the damaged condition. $\boldsymbol{\tau}$ is the lag of two *DECs* and N is the length of each *DEC.* A damage severity index based on a set of R is calculated by:

$$Index = \sqrt{\frac{\sum(1-R)^2}{Ns}} \tag{Eq. 4-38}$$

This method eliminates the wave interference effect by calculating *DECs* under intact and damaged conditions, respectively. Also, the difference of *DECs* between intact and specimen with unknown state will only be caused by damage.

Table 4-10 Calculation of *DECs*

	E_{s1}	E_{s2}	E_{s3}	E_{s4}	E_{s5}	E_{s6}	E_{s7}
E_{s1}	-						
E_{s2}	$E_{s1}-E_{s2}$	-					
E_{s3}	$E_{s1}-E_{s3}$	$E_{s2}-E_{s3}$	-				
E_{s4}	$E_{s1}-E_{s4}$	$E_{s2}-E_{s4}$	$E_{s3}-E_{s4}$	-			
E_{s5}	$E_{s1}-E_{s5}$	$E_{s2}-E_{s5}$	$E_{s3}-E_{s5}$	$E_{s4}-E_{s5}$	-		
E_{s6}	$E_{s1}-E_{s6}$	$E_{s2}-E_{s6}$	$E_{s3}-E_{s6}$	$E_{s4}-E_{s6}$	$E_{s5}-E_{s6}$	-	
E_{s7}	$E_{s1}-E_{s7}$	$E_{s2}-E_{s7}$	$E_{s3}-E_{s7}$	$E_{s4}-E_{s7}$	$E_{s5}-E_{s7}$	$E_{s6}-E_{s7}$	-

4.3.3.1 Results and discussion

After calculating different damage scenarios (different damage sizes of 15mm, 30mm, 45mm, 60mm, 75mm, 90mm, 120mm, 150mm, 180mm, 210mm and 240mm with the same damage length of 200mm), the results are plotted in Figure 4-29. From the figure, it can be seen clearly obviously that the index increases as the damage size increases regardless of the damage type. To verify the consistency of the results under different sensor arrangements, 13 sensors and 25 sensors were used to capture the wave data. After calculating and comparing with the indices obtained from 7 sensors, the results were quite consistent and show the same phenomenon.

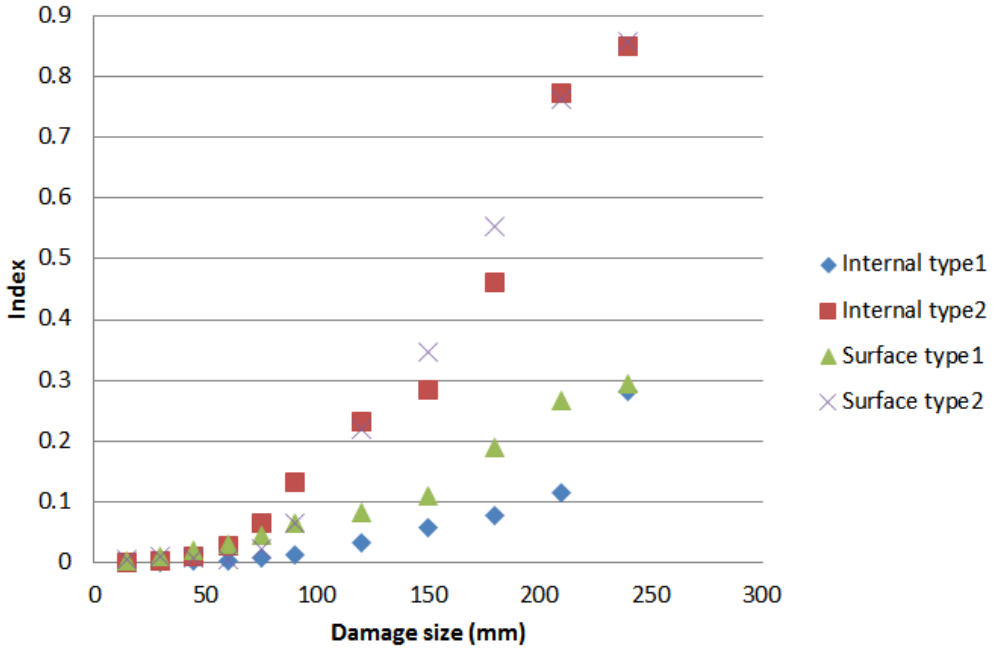

Figure 4-29 Damage severity identification

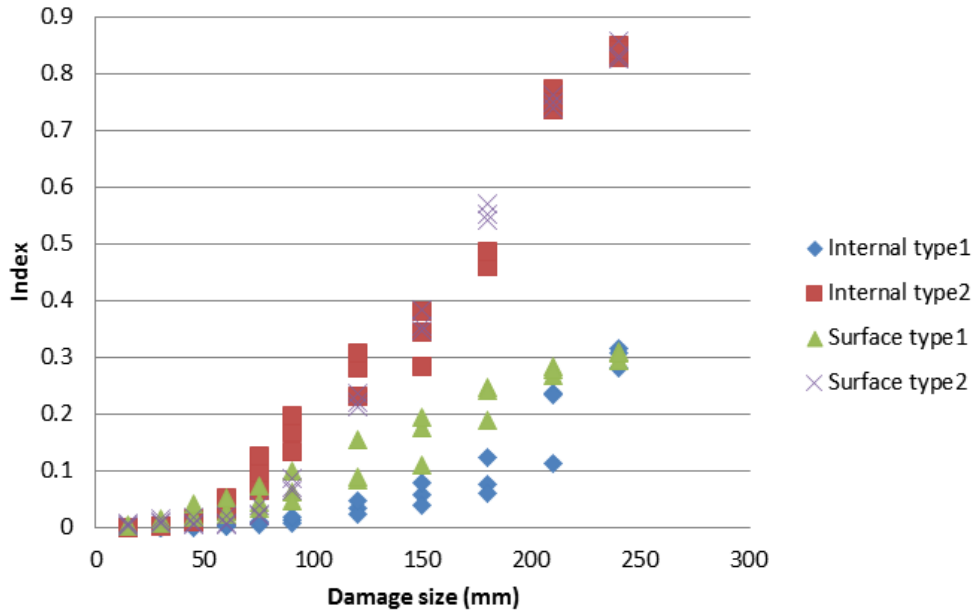

Figure 4-30 Damage severity identification using different sensor arrangement

In Figure 4-30, there are three symbols under the same damage type and size which indicate three different arrangements of sensors, which are 7 sensors, 13 sensors and 25 sensors. All the results identify the same phenomenon that the index increases as the damage size increases.

To verify whether the phenomenon still exists if the length of damage increases or the location of damage changes, other damage scenarios were created.

Firstly, the length of damage type 2 was increased from 200mm to 300mm at the same location (Figure 4-31) with different damage sizes of 30mm, 60mm, 90mm, 120mm, 150mm, 180mm and 210mm. 25 sensors were used to calculate the indices.

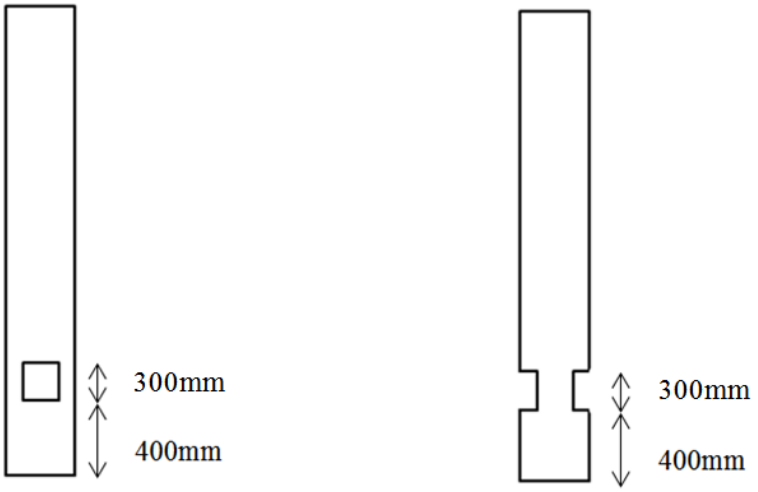

Figure 4-31 Length and localisation of damage for type 2

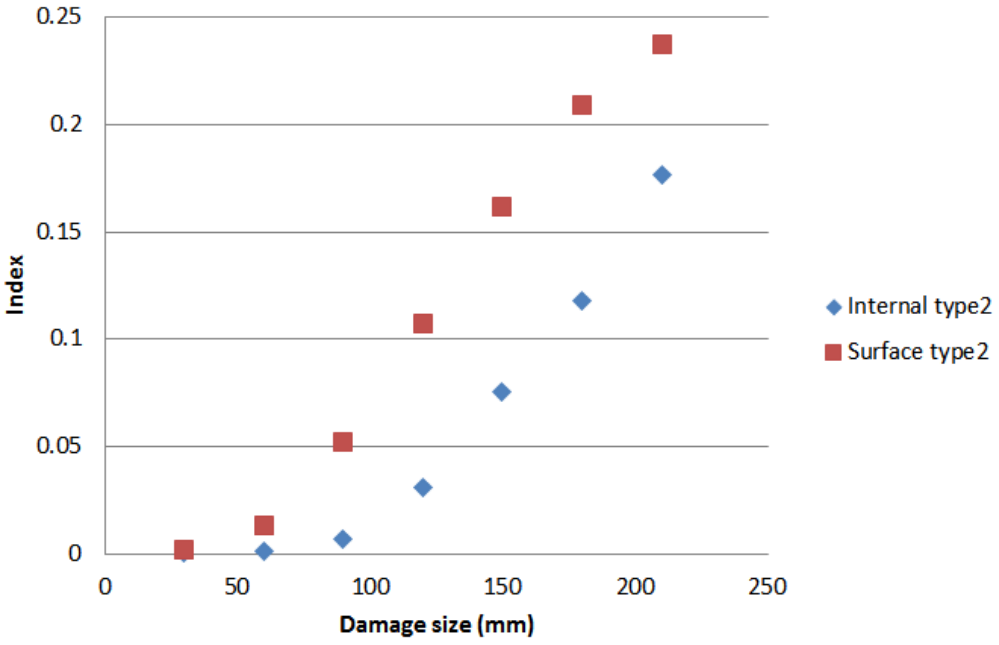

Figure 4-32 Damage severity identification for damage length of 300mm

Figure 4-32 indicates the results that the index is still able to describe the damage severity when the length of damage increases. This verifies that the change of damage length will not influence the identification of damage severity.

Secondly, the length of damage was kept at 200mm and the location of damage was at 600mm and 800mm from the bottom of the pole as shown in Figure 4-33.

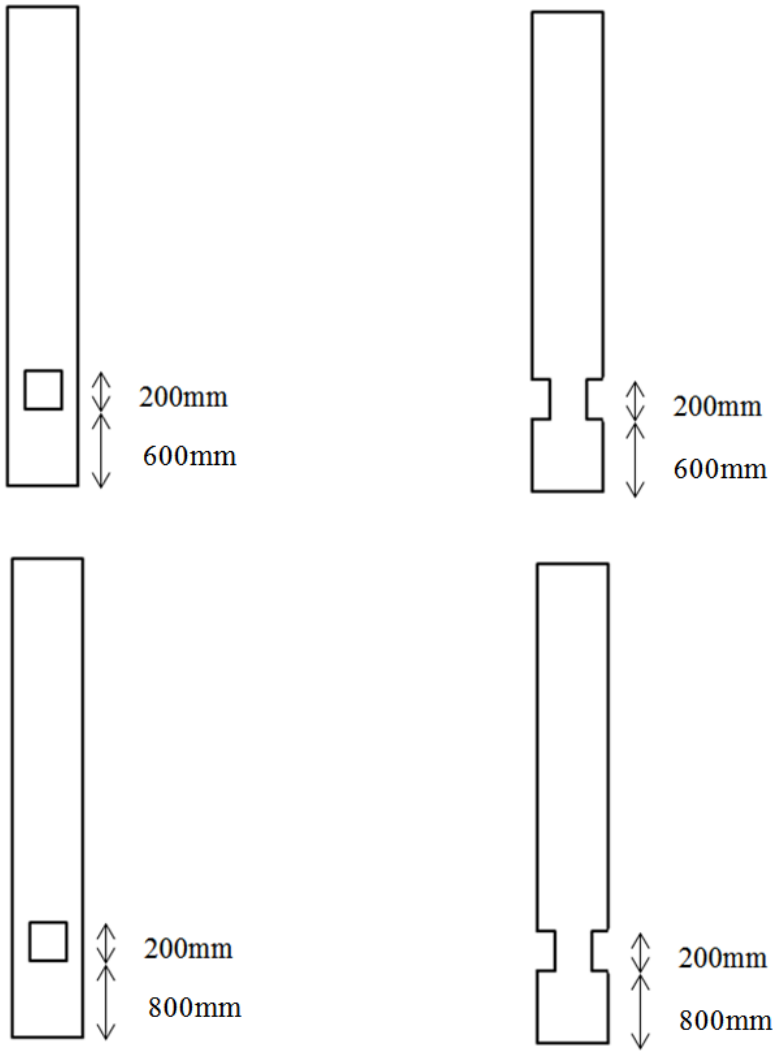

Figure 4-33 Change of location for damage type 2

The results are shown in Figure 4-34 and Figure 4-35, respectively. From the figures, it can be seen that the same phenomenon is occurring. The index always increases when the damage size is increased, and, therefore, the change of damage location will not influence the identification of damage severity. One important issue is the pick-up period. The pick-up period has to be satisfied that all the sensors capture the incident wave and reflected wave from the damage area and the bottom of the pole (see Figure 4-33). The wave reflects from the top of the pole should not be included. In this case, the wave signals captured by all the sensors contain the same information of the pole. For

these verification models, the pick-up period was shortened to avoid capturing the reflected wave from the top of the pole.

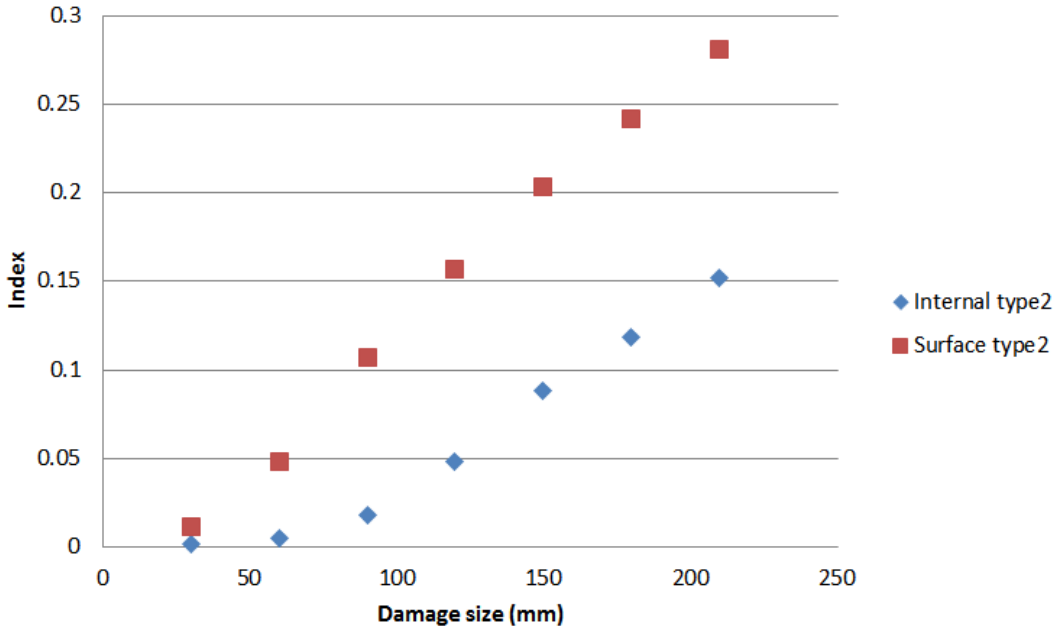

Figure 4-34 Damage severity identification for damage location at 600mm from the bottom

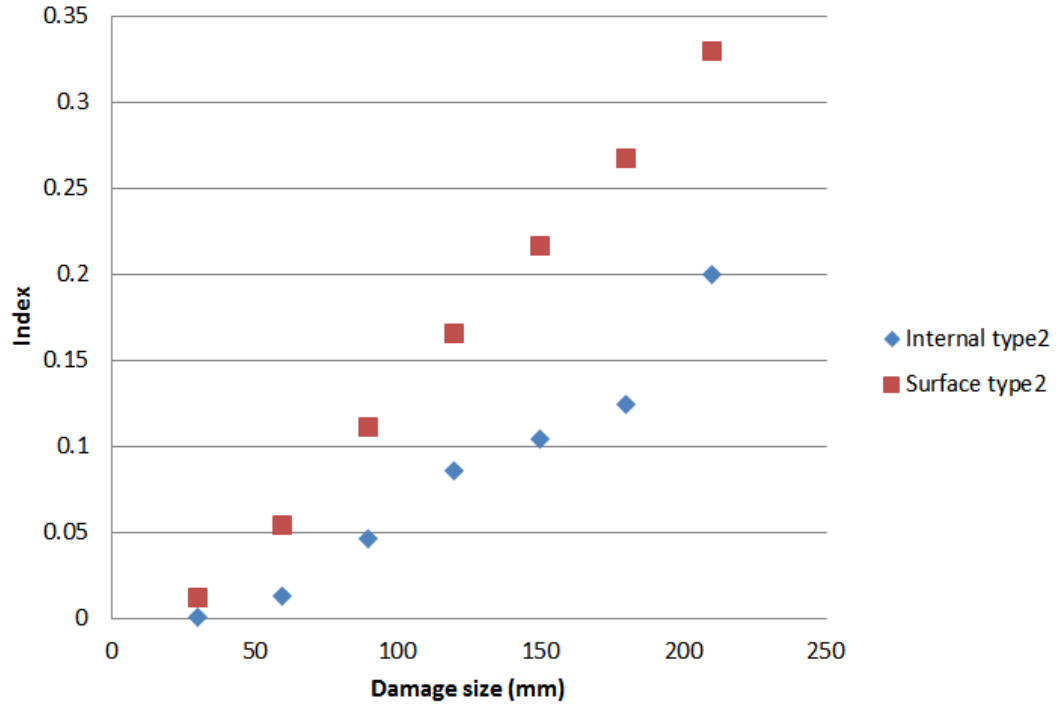

Figure 4-35 Damage severity identification for damage location at 800mm from the bottom

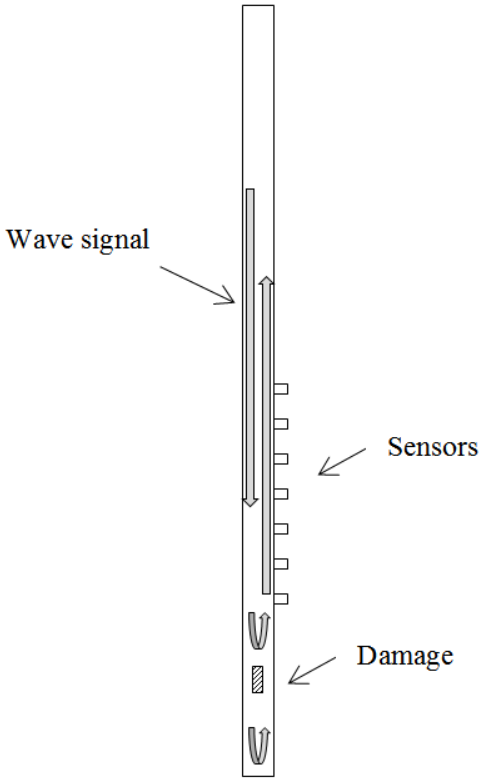

Figure 4-36 Pick-up wave signal

4.4 CONCLUSIONS

In this chapter, finite element models of intact and damaged poles were developed and employed to investigate, numerically, the effectiveness of the proposed damage detection method using WPE analysis. The damage detection is divided into two steps: damage classification and damage severity identification. To achieve damage classification, four damage types were defined. WPE and natural frequency data were combined to classify the damage types through support vector machine (SVM) technology. The comparison of WPE change gives the indicator for damage severity. There are several advantages of the presented method:

- The proposed method is able to identify the damage in an area where the sensors cannot be placed.
- The novel method is capable of removing the interference of incident wave and reflected wave. Accordingly, the damage can be identified more accurately.
- WPE information combining natural frequency data gives a conspicuous and indicative feature for damage classification, especially for internal and surface

damage types. Damage classification based on the experimental testing data also verifies the effectiveness of the proposed method. These two damage types play different roles in affecting the strength of utility poles which will be discussed in Chapter 6.

- Damage severity can be identified through wave data using the novel WPE based method.

According to the findings in this chapter, damage prediction will be applied in the next chapter.

5 Damage prediction using advanced optimisation techniques

5.1 INTRODUCTION

The proposed method in Chapter 4 shows its capability to identify the damage severity under different damage scenarios. This method will be more applicable if the damage severity can be predicted through the measurements from an unknown condition. In this chapter, damage prediction using optimisation technique is conducted. Four kinds of damage size under different damage types are imported to validate the accuracy of the proposed method.

5.2 APPLICATION OF OPTIMISATION TECHNIQUES

Standard analytical techniques use mathematical models to approximate the relationships between the specific damage conditions and the structural responses. This procedure can be taken as an inverse problem (Sandhu et al., 2001).

Inverse problems can be considered as optimisation problems. Solving an inverse problem is a procedure of determining the parameters of a model according to measurements performed on the structure (Friswell, 2008).

5.2.1 Optimisation algorithm

There are quite a number of algorithms used in optimisation; among them, genetic algorithm (GA), particle swarm optimisation (PSO) and simulated annealing (SA) are widely used in most of the optimisation problems. In this research, GA was firstly

selected as the algorithm for model optimisation. A new algorithm named artificial fish-swarm algorithm (ASFA) was also considered to compare the results with GA.

5.2.1.1 Genetic algorithm

Among different optimisation algorithms, genetic algorithm (GA) is well known and has been widely used. GAs are inspired by Darwin's theory about evolution and were formally introduced by John Holland in the 1970s (Holland, 1975). A GA searches through a space of "chromosomes" (a set of solutions or called population), each of which represents a candidate solution to a given problem. Solutions from one population are taken to establish a new population according to the specific fitness score, which makes sure that the new population will be better than the previous one. When solutions are taken from the current population, the chance of being selected is proportional to the chromosomes fitness, and, therefore, roulette wheel selection is usually used. To form a new population, a GA also applies "natural selections" with genetic operators such as mutation and crossover to evolve the solutions. Each chromosome consists of "genes" and each gene (an instance of a particular "allele") can be represented by a string of zeros or ones. Accordingly, one population of chromosomes will be formed by a series of zeros and ones. For example, parent chromosomes can be described as: 10000100 and 11111111. Crossover exchanges subparts of two chromosomes, so if it happens after the third locus in each parent chromosome, the offspring will be produced as 10011111 and 11100100; mutation changes the allele value of some locations randomly and if the offspring is 00000100 originally, the mutated one could be 01000100, and each bit has same probability of mutating. The general process to apply GA is show in Figure 5-1 and can be simply summarised as:

- Start with a large "population" of randomly generated "attempted solutions" to a problem
- Repeat following steps:
    - Evaluate each of the attempted solutions
    - Keep a subset of the best solutions
    - Use these solutions to generate a new population
- Quit when a satisfactory solution is obtained

Each iteration of this process is called a generation. A GA can be iterated from several to hundreds of generations. It can also be applied several times on the same problem to get the average result since randomness plays a large role in processing. Another issue which needs to be briefly introduced is selection in the GA. There are several selection methods such as roulette wheel selection, rank selection, steady-state selection and elitism. However, as mentioned before, roulette wheel selection is normally used to select parents due to its characteristics of being quicker in convergence and easier in operation. The fittest chromosomes have a greater chance to be selected (see Figure 5-2) and this replicates nature in that fitter individuals will tend to have more possibility to survive and breed (Newcastle University, 2014).

GAs have been applied in different fields since they are easy to implement and less likely to get stuck in a local optimum. Therefore, GA was selected to achieve damage prediction in this research.

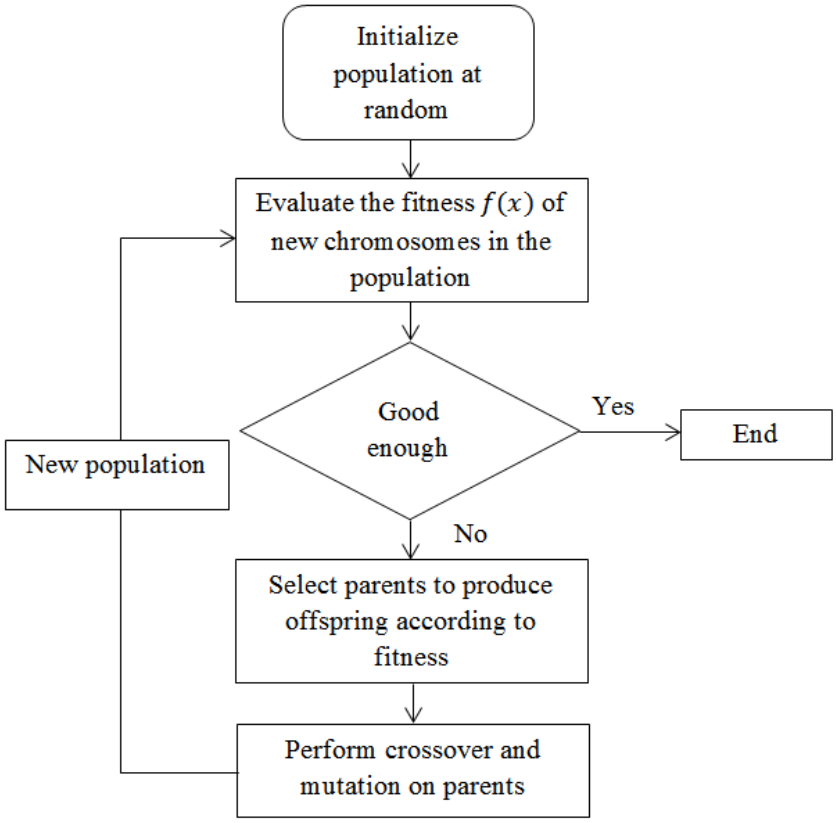

Figure 5-1 Flow chart for applying GA

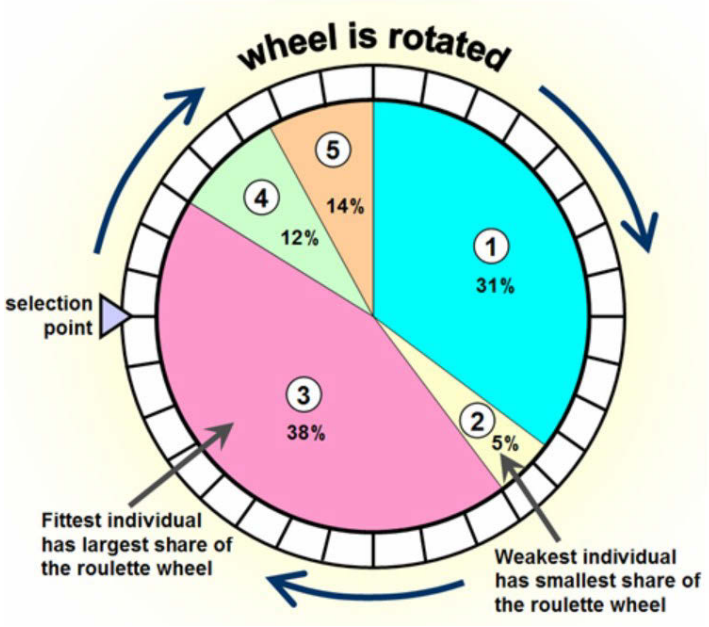

Figure 5-2 Roulette wheel approach: based on fitness (Newcastle University, 2014)

5.2.1.2 Artificial fish-swarm algorithm (AFSA)

Artificial fish swarm algorithm, firstly proposed by Li in 2002 (Li et al., 2002), is a novel intelligent optimization algorithm originated from foraging behaviour of fish groups in nature, such as preying, swarming and chasing. AFSA has been applied in various fields like optimization, control, image processing, data mining, improving neural networks, networks, scheduling, and signal processing and so on (Neshat et al., 2012). AFSA is an effective swarm intelligent optimization algorithm. The main characteristics of AFSA is that artificial fish movements solely depend on their current positions and other members of the group situations but not their past movements and experiences (Azizi, 2014).

AFSA has similar features to GA such as independence from gradient information of the objective function and the ability to solve complex nonlinear high dimensional problems (Neshat et al., 2012). Moreover, AFSA has lower computing complexity, faster convergence speed and greater precision.

AFSA searches the problem space with foraging behaviour and the objective function for the algorithm is to find the maximum food density. The algorithm simulates the biological behaviour: the artificial fish can perceive the change of the food concentration Y, and then change the current position X through evaluation function of

their own behaviour in order to obtain the global optimum location, that is the maximum concentration of food (Yu and Li, 2014). The behaviour of AF searching for maximum food concentration can be shown as Figure 5-3. If X_v has better food concentration than the current position, AF moves one step towards X_v, which results in displacement of AF from the original location to X_{next}. Otherwise, AF selects another position in its visual distance if the current location is better than X_v (Azizi, 2014).

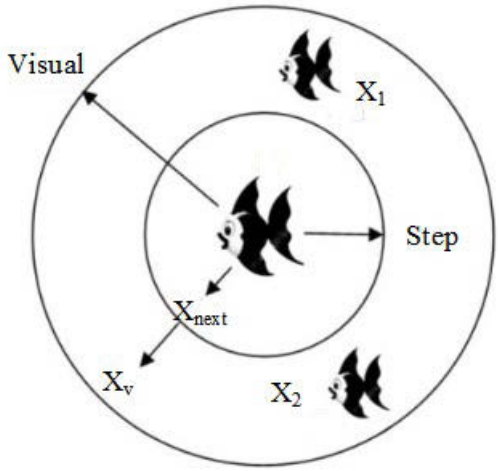

Figure 5-3 Artificial Fish behaviour (Azizi, 2014)

Suppose N artificial fish (AF) are initialised for the problem space presented as $X_i = X_1,\ldots,X_N$, where X_i indicates the AF current position. X_j is an intended position in its visual distance. The food concentration $Y=f(X)$ stands for the objective function. Several critical parameters are required to be defined in AFSA:

try-number	the maximum tentative time for AF each foraging
visual	visual distance of individual AF
step	length of AF movement
δ	crowd factor of AF ($0<\delta<1$)

The behaviour of AF can be explained as follows:

1 Preying: X_i represents the current state of AF and X_j is a random state within the visual distance. The relationship is expressed as:

$$X_j = X_i + rand(0,1) \times visual \qquad \text{Eq. 5-1}$$

If $f(X_j) < f(X_i)$, AF moves from X_i to X_j, i.e. $X_i^t \rightarrow X_i^{t+1}$, and forms:

$$X_i^{t+1} = X_i^t + rand(0,1) \times step \times \frac{X_j^t - X_i^t}{\|X_j^t - X_i^t\|} \quad \text{Eq. 5-2}$$

If $f(X_j) > f(X_i)$, AF randomly selects another state again. If it cannot satisfy the requirement within a given try-number, AF moves one step randomly as:

$$X_i^{t+1} = X_i^t + rand(0,1) \times step \quad \text{Eq. 5-3}$$

It is important to understand that try-number can be adjusted for several times to avoid getting in the local optimisation.

2 Swarming: the current state of AF is X_i and nf is the number of its companions within the visual distance d_{ij} between X_i and X_j , i.e. $d_{ij} < visual$. If $nf \neq 0$, there is

$$X_{centre} = \sum_{j=1}^{nf} \frac{X_j}{nf} \quad \text{Eq. 5-4}$$

$$y_{centre} = f(X_{centre}) \quad \text{Eq. 5-5}$$

X_{centre} and y_{centre} indicate the fitness of the centre position.

If $nf \times y_{centre} < \delta \times y_i$, it means that the companion centre is not crowded.

If $y_{centre} < y_i$, AF moves one step towards the centre position:

$$X_i^{t+1} = X_i^t + rand(0,1) \times step \times \frac{X_c^t - X_i^t}{\|X_c^t - X_i^t\|} \quad \text{Eq. 5-6}$$

3 Chasing: suppose X_m is the best state of AF individual within X_i 's visual distance and $y_{min} = f(X_m)$. nf is the number of X_m's companions within the visual distance. If it is satisfied

$$y_m < y_i \; and \; nf \times y_m < \delta \times y_i \quad \text{Eq. 5-7}$$

AF moves one step towards X_m. Otherwise, it goes to the behaviour of preying (Wu et al., 2011).

$$X_i^{t+1} = X_i^t + rand(0,1) \times step \times \frac{X_m^t - X_i^t}{\|X_m^t - X_i^t\|} \quad \text{Eq. 5-8}$$

From the behaviour above, it can be concluded:

- Swarming behaviour helps to get rid of local extremum and search for other extremum and finally get global extremum.
- Chasing behaviour helps AF to move towards an extremum rapidly and, therefore, speed up the optimization searching.

- AFSA evaluates two behaviours above and then selects a proper behaviour. Hence, it is a fast optimisation method with high efficiency.

5.2.2 Procedure of optimisation technique

As mentioned in Chapter 4, different indexes correspond to damage severities. Damage severities from unknown conditions could be predicted through an optimisation technique. In this procedure, the analysis of the entire FE model was avoided. A mathematical model can be generated to accurately describe the relationship between the damaged sample and the corresponding index, and accordingly can be used to predict the damage severity based on the obtained index from an unknown condition such as in Figure 5-5.

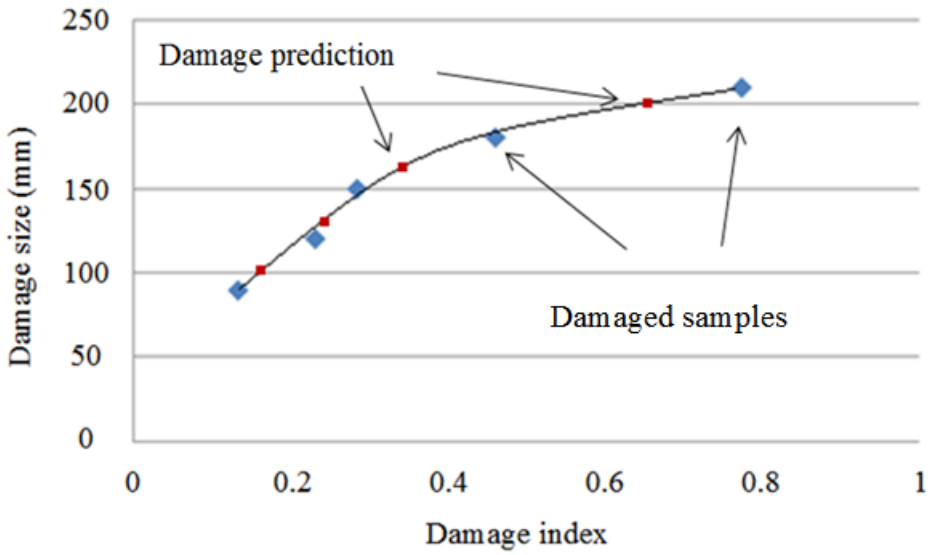

Figure 5-4 Damage severity index

The objective function can be expressed as follows:

$$J = min \sum_{i=1}^{N=5} [f(x_i) - y_i]^2 \qquad \text{Eq. 5-9}$$

where $f(x_i)$ is the mathematical model in the form of a polynomial and is shown below; x_i refers to specific index and y_i represents the corresponding damage size.

$$f(x) = ax^2 + bx + c \qquad \text{Eq. 5-10}$$

Damage prediction was concentrated on the damage size from 90mm to 210mm and five scenarios of damage size with corresponding indexes were obtained. The

mathematical model was established and evaluated based on the damage samples and their corresponding indexes. The damage prediction procedure can be presented by the flowchart shown below in Figure 5-5.

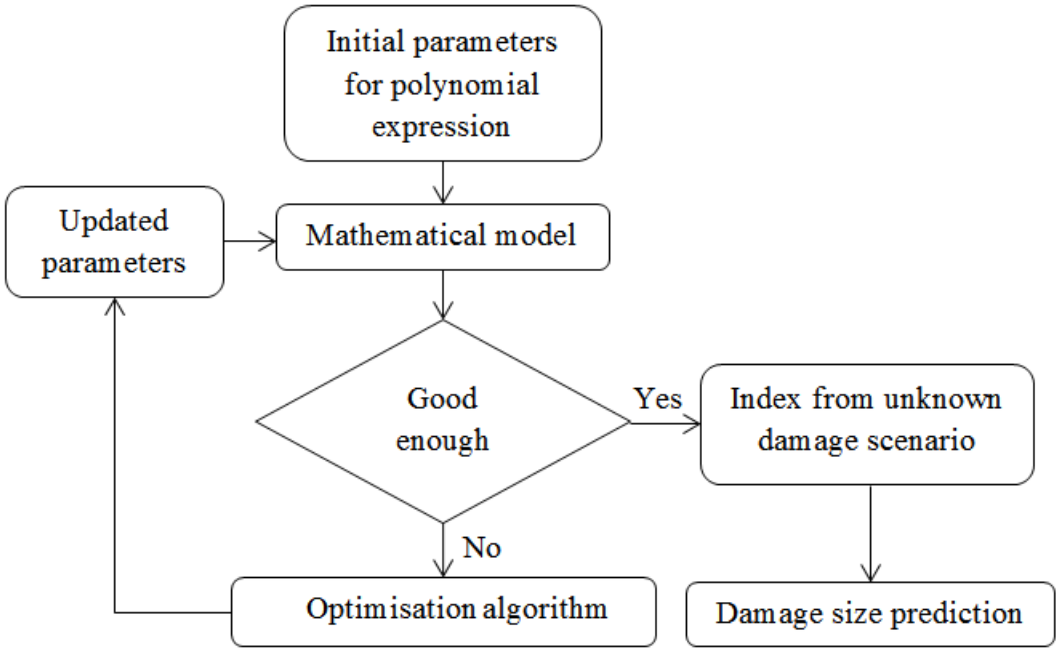

Figure 5-5 Damage prediction by optimisation technique

Parameters in the polynomial function were updated by an optimization algorithm to find a best model defining the relationship between the index and the damage size. Then, the index from an unknown damage condition was used as an input variable and the corresponding damage size could be obtained as an output.

5.2.2.1 Optimisation technique using GA

There is no theoretical principle to guide the choice of the parameters in GA; some recommendations for parameters selection were proposed by some researchers (Boyabatli and Sabuncuoglu, 2004) and can be divided into three aspects:

Crossover rate:

Generally, the crossover rate should be high around 80%-95%; however, some results show that the crossover rate of about 60% is the best choice for some problems.

Mutation rate:

Mutation rate, on the other hand should be very low. Best mutation rates reported are about 0.5% to 1%.

Population size:

Very big population size usually does not improve the performance of GA and the speed of finding a solution will be slowed down. Good population sizes are about 20-30. However, population sizes of 50-100 sometimes are reported as the best choice. Some researchers also mentioned that the best population size depends on the encoding, that is the encoded string.

The crossover, the mutation rate as well as the population size were selected after several testings. As mentioned before, randomness plays a large role in the processing so each procedure has been run five times and the average results were obtained as the prediction of the damage size.

In the optimisation procedure, the information of the damage samples including the damage size and index was used for searching the optimal model to present the relationship between damage size and index. Four damage sizes of 100mm, 130mm, 160mm and 200mm under four damage types located 400mm from the bottom of the poles were selected for damage prediction. The indexes of *DEC* for each damage size under specific damage types were calculated and the predicted damage sizes were compared with the given damage sizes. The results are listed in the tables below (Table 5-1 to Table 5-4).

Table 5-1 Damage size prediction for the damage type of internal type 1

Parameter setting						
Mutation rate: 0.005	Crossover rate: 0.85	Population size: 70	Generation: 500			
Damage size :100mm						
Prediction1	Prediction2	Prediction3	Prediction4	Prediction5	Average	Error
109	105	106	110	110	108	8.0 %
Damage size :130mm						
Prediction1	Prediction2	Prediction3	Prediction4	Prediction5	Average	Error
128	129	129	129	130	129	0.8 %
Damage size :160mm						
Prediction1	Prediction2	Prediction3	Prediction4	Prediction5	Average	Error
152	145	148	147	147	148	7.6 %
Damage size :200mm						
Prediction1	Prediction2	Prediction3	Prediction4	Prediction5	Average	Error
193	196	193	195	191	194	3.0 %

Table 5-2 Damage size prediction for the damage type of internal type 2

Parameter setting						
Mutation rate: 0.005	Crossover rate: 0.85	Population size: 70	Generation: 500			
Damage size :100mm						
Prediction1	Prediction2	Prediction3	Prediction4	Prediction5	Average	Error
107	104	108	104	107	106	6.0 %
Damage size :130mm						
Prediction1	Prediction2	Prediction3	Prediction4	Prediction5	Average	Error
135	133	135	136	133	134	3.4 %
Damage size :160mm						
Prediction1	Prediction2	Prediction3	Prediction4	Prediction5	Average	Error
151	145	147	143	145	146	8.6 %
Damage size :200mm						
Prediction1	Prediction2	Prediction3	Prediction4	Prediction5	Average	Error
205	206	205	206	205	205	2.7 %

Table 5-3 Damage size prediction for the damage type of surface type 1

Parameter setting						
Mutation rate: 0.005	Crossover rate: 0.85	Population size: 70	Generation: 500			
Damage size :100mm						
Prediction1	Prediction2	Prediction3	Prediction4	Prediction5	Average	Error
97	97	98	97	100	98	2.2 %
Damage size :130mm						
Prediction1	Prediction2	Prediction3	Prediction4	Prediction5	Average	Error
130	137	132	132	138	134	2.9 %
Damage size :160mm						
Prediction1	Prediction2	Prediction3	Prediction4	Prediction5	Average	Error
165	166	166	164	165	165	3.2 %
Damage size :200mm						
Prediction1	Prediction2	Prediction3	Prediction4	Prediction5	Average	Error
196	195	196	192	196	195	2.5 %

Table 5-4 Damage size prediction for the damage type of surface type 2

Parameter setting						
Mutation rate: 0.005	Crossover rate: 0.85	Population size: 70	Generation: 500			
Damage size :100mm						
Prediction1	Prediction2	Prediction3	Prediction4	Prediction5	Average	Error
107	102	107	108	100	105	4.8 %
Damage size :130mm						
Prediction1	Prediction2	Prediction3	Prediction4	Prediction5	Average	Error
128	128	128	124	128	127	2.2 %
Damage size :160mm						
Prediction1	Prediction2	Prediction3	Prediction4	Prediction5	Average	Error
161	157	158	161	159	159	0.5 %
Damage size :200mm						
Prediction1	Prediction2	Prediction3	Prediction4	Prediction5	Average	Error
203	203	201	200	202	202	0.9 %

From the tables above, it can be seen that the maximum error is less than 10% for all damage scenarios. The maximum error, which is 8.6%, exists in the damage type of internal type 2 with the damage size of 160mm. The errors for the damage type of internal type 1 with damage size of 100mm and 160mm are also quite large, which are 8%

and 7.6% respectively. Prediction errors for other damage scenarios are mainly around 2.5% to 3.0%.

From each damage scenario, it can be seen that some of the prediction results have large fluctuations and this phenomenon indicates that randomness plays an important role in the optimisation process. Thus, each procedure has to be run several times to get reliable results if GA is used as the prediction algorithm.

5.2.2.2 Optimisation technique using AFSA

AFSA has the same problem as GA which is no theoretical principle for guiding parameters selection. Some researchers (Azizi, 2014) provided recommendations in different application fields; after summarising, it can be concluded that:

- Small step always gives good precision.
- Visual does not influence too much if step is small
- Small crowd factor always helps to eliminate the local optimisation
- Large try-number is good for obtaining the convergence precision

The same damage samples were used to create the mathematical model as was used in GA. Randomness also exists in the optimisation procedure, and, therefore, each procedure has been run five times and the average results were obtained as the prediction of the damage size. According to the recommendations above, the corresponding parameters were defined. The same damage conditions which are 100mm, 130mm, 160mm and 200mm under four damage types were used for the damage prediction. All the damages are located at 400mm from the bottom of the poles. The calculation results are listed in the tables below (Table 5-5 to Table 5-8).

Table 5-5 Damage size prediction for the damage type of internal type 1

Parameter setting						
Visual: 2.5 Step: 0.3 Artificial fish: 30 Generation: 50 Crowd factor: 0.25 Try-number: 100						
Damage size :100mm						
Prediction1	Prediction2	Prediction3	Prediction4	Prediction5	Average	Error
98	98	98	99	99	98	1.6 %
Damage size :130mm						
Prediction1	Prediction2	Prediction3	Prediction4	Prediction5	Average	Error
130	130	130	130	130	130	0.0 %
Damage size :160mm						
Prediction1	Prediction2	Prediction3	Prediction4	Prediction5	Average	Error
159	160	159	160	160	160	0.3 %
Damage size :200mm						
Prediction1	Prediction2	Prediction3	Prediction4	Prediction5	Average	Error
206	206	207	206	206	206	3.1%

Table 5-6 Damage size prediction for the damage type of internal type 2

Parameter setting						
Visual: 2.5 Step: 0.3 Artificial fish: 30 Generation: 50 Crowd factor: 0.25 Try-number: 100						
Damage size :100mm						
Prediction1	Prediction2	Prediction3	Prediction4	Prediction5	Average	Error
101	101	101	101	101	101	1.0 %
Damage size :130mm						
Prediction1	Prediction2	Prediction3	Prediction4	Prediction5	Average	Error
138	138	138	138	138	138	6.2 %
Damage size :160mm						
Prediction1	Prediction2	Prediction3	Prediction4	Prediction5	Average	Error
149	148	148	148	148	148	7.4 %
Damage size :200mm						
Prediction1	Prediction2	Prediction3	Prediction4	Prediction5	Average	Error
205	206	206	206	206	206	2.9 %

Table 5-7 Damage size prediction for the damage type of surface type 1

Parameter setting						
Visual: 2.5 Step: 0.3 Artificial fish: 30 Generation: 50 Crowd factor: 0.25 Try-number: 100						
Damage size :100mm						
Prediction1	Prediction2	Prediction3	Prediction4	Prediction5	Average	Error
98	98	97	98	98	98	2.2 %
Damage size :130mm						
Prediction1	Prediction2	Prediction3	Prediction4	Prediction5	Average	Error
128	128	128	128	128	128	1.5 %
Damage size :160mm						
Prediction1	Prediction2	Prediction3	Prediction4	Prediction5	Average	Error
164	164	164	164	164	164	2.5 %
Damage size :200mm						
Prediction1	Prediction2	Prediction3	Prediction4	Prediction5	Average	Error
196	196	197	197	197	197	1.7 %

Table 5-8 Damage size prediction for the damage type of surface type 2

Parameter setting						
Visual: 2.5 Step: 0.3 Artificial fish: 30 Generation: 50 Crowd factor: 0.25 Try-number: 100						
Damage size :100mm						
Prediction1	Prediction2	Prediction3	Prediction4	Prediction5	Average	Error
100	99	100	100	100	100	0.2 %
Damage size :130mm						
Prediction1	Prediction2	Prediction3	Prediction4	Prediction5	Average	Error
128	129	128	128	128	128	1.4 %
Damage size :160mm						
Prediction1	Prediction2	Prediction3	Prediction4	Prediction5	Average	Error
159	159	159	159	159	159	0.6 %
Damage size :200mm						
Prediction1	Prediction2	Prediction3	Prediction4	Prediction5	Average	Error
202	203	202	202	202	202	1.1 %

From the tables above, it can be seen that the maximum error is less than 8% for all the damage scenarios. The maximum error, which is 7.4%, exists in the damage type of internal type 2 with the damage size of 160mm. The error for the same damage type with the damage size of 130mm is also quite significant, which is 6.2%. Prediction errors for other damage scenarios are quite small, mainly below 3%. From each damage scenario, it can be found that the prediction results have little fluctuation and the prediction results are almost the same after running five times. According to this phenomenon, the prediction procedure can be run fewer times to obtain reliable results; and therefore, this algorithm is less time consuming compared to GA.

To further verify the effectiveness of damage prediction using AFSA, two more damage cases were investigated: 1) the damage is located at 600mm from the bottom of the pole with the damage length of 200mm; 2) the damage is located at 200mm from the bottom of the pole with the damage length of 300mm. In these two cases, damage prediction is conducted for the damage type 2 including the surface as well as the internal damage since they are the most common damage types existing in timber utility poles.

Table 5-9 to Table 5-12 gives the damage prediction results of two damage cases. It can be found that all the errors are below 6% in case 1 and the maximum error presents in the surface damage of 130mm. For damage case 2, all the errors are less than 3% and the maximum error appears in the surface damage of 100mm. It can be observed that the optimisation method is effective to predict the damage severities under different damage conditions using numerical results.

Table 5-9 Damage size prediction for case 1 with surface damage type 2

Parameter setting						
Visual: 2.5 Step: 0.3 Artificial fish: 30 Generation: 50 Crowd factor: 0.25						
Try-number: 100						
Damage size :100mm						
Prediction1	Prediction2	Prediction3	Prediction4	Prediction5	Average	Error
99	99	100	100	100	100	0.4 %
Damage size :130mm						
Prediction1	Prediction2	Prediction3	Prediction4	Prediction5	Average	Error
129	130	128	127	128	128	1.2 %
Damage size :160mm						
Prediction1	Prediction2	Prediction3	Prediction4	Prediction5	Average	Error
159	158	159	159	159	159	0.7 %
Damage size :200mm						
Prediction1	Prediction2	Prediction3	Prediction4	Prediction5	Average	Error
202	203	202	202	202	202	1.1 %

Table 5-10 Damage size prediction for case 1 with internal damage type 2

Parameter setting						
Visual: 2.5 Step: 0.3 Artificial fish: 30 Generation: 50 Crowd factor: 0.25						
Try-number: 100						
Damage size :100mm						
Prediction1	Prediction2	Prediction3	Prediction4	Prediction5	Average	Error
101	99	99	99	99	99	0.6 %
Damage size :130mm						
Prediction1	Prediction2	Prediction3	Prediction4	Prediction5	Average	Error
136	136	137	137	137	137	5.1 %
Damage size :160mm						
Prediction1	Prediction2	Prediction3	Prediction4	Prediction5	Average	Error
153	153	154	154	154	154	4.0 %
Damage size :200mm						
Prediction1	Prediction2	Prediction3	Prediction4	Prediction5	Average	Error
206	205	205	205	205	205	2.5 %

Table 5-11 Damage size prediction for case 2 with surface damage type 2

Parameter setting						
Visual: 2.5 Step: 0.3 Artificial fish: 30 Generation: 50 Crowd factor: 0.25 Try-number: 100						
Damage size :100mm						
Prediction1	Prediction2	Prediction3	Prediction4	Prediction5	Average	Error
98	97	97	97	97	97	2.8 %
Damage size :130mm						
Prediction1	Prediction2	Prediction3	Prediction4	Prediction5	Average	Error
132	132	132	132	131	132	1.4 %
Damage size :160mm						
Prediction1	Prediction2	Prediction3	Prediction4	Prediction5	Average	Error
163	163	163	164	164	163	2.1 %
Damage size :200mm						
Prediction1	Prediction2	Prediction3	Prediction4	Prediction5	Average	Error
196	196	195	196	196	196	2.1 %

Table 5-12 2Damage size prediction for case 2 with internal damage type 2

Parameter setting						
Visual: 2.5 Step: 0.3 Artificial fish: 30 Generation: 50 Crowd factor: 0.25 Try-number: 100						
Damage size :100mm						
Prediction1	Prediction2	Prediction3	Prediction4	Prediction5	Average	Error
102	102	103	103	102	102	2.4 %
Damage size :130mm						
Prediction1	Prediction2	Prediction3	Prediction4	Prediction5	Average	Error
133	133	133	132	132	133	2.0 %
Damage size :160mm						
Prediction1	Prediction2	Prediction3	Prediction4	Prediction5	Average	Error
155	156	156	156	156	156	2.6 %
Damage size :200mm						
Prediction1	Prediction2	Prediction3	Prediction4	Prediction5	Average	Error
202	203	203	203	203	203	1.4 %

5.3 CONCLUSIONS

This chapter discussed the damage prediction based on the advanced optimisation technique. The mathematical model was optimised to represent the relationship between the damage sizes and the indexes according to the damage samples. Accordingly, the damage size can be predicted through the obtained index from an unknown condition.

Two optimisation algorithms, genetic algorithm (GA) and artificial fish swarm algorithm (AFSA) were selected. Through the comparison of the results, it can be found that both algorithms gave quite accurate prediction results regardless of the damage type and size. Based on this study, the method is able to estimate the severity of damage with reasonable confidence using numerical data.

Combining with the damage detection method proposed in Chapter 4, it can be seen that although the detection or prediction of damage was based on the simplified numerical models, the proposed method provided a potential possibility for condition assessment of the timber utility poles. A novel signal processing technique which tries to separate multiple modes of wave signals in an orthotropic material has to be developed in future research. The proposed damage detection method will be more reliable and applicable when combining with the novel signal processing method in future research work.

6 Load capacity prediction for in-situ timber poles

6.1 INTRODUCTION

Timber poles may have high initial strength. However, they may experience deterioration and decay over their designed service life due to the fungus or termite attacks in varying degrees. In most cases, the damage is not visible and is often below the ground. This chapter introduces the common types of degradation of the timber utility poles in the Sydney region and presents relevant deterioration models which simulate the loss of sections of the timber poles. This chapter is aimed to determine the remaining load capacity of the damaged utility poles based on the numerical models and provides investigations on estimation of strength of damaged and undamaged utility poles through some corresponding standards. The purpose of this chapter is to explore theoretical factors of damage influencing the strength of timber utility poles.

6.2 LOAD CAPACITY ANALYSIS OF INTACT AND DAMAGED TIMBER POLES

The load capacity analysis in this chapter is firstly achieved by calculating the maximum stress under a design wind load and comparing this with the corresponding fibre strengths of timber poles provided by the Australian/New Zealand standard.

6.2.1 Wind load design

Wind loading is among the dominant environmental loads for utility pole structures. Severe tropical cyclones known in some parts of the world as hurricanes and typhoons generate extremely strong winds over some parts of the tropical oceans and coastal regions. Thunderstorms also contribute significantly to the strongest gusts recorded in

many countries, including the United States, Australia and South Africa (Holmes, 2001). Damage to structures produced by wind forces, either overloads caused by overstressing under peak loads or fatigue damage under fluctuating loads of a lower level, has been a fact of life, therefore, appropriate wind load design is needed in this research.

6.2.1.1 Wind speed

The establishment of appropriate wind speed is a critical first step towards the calculation of design wind loads for structures. AS/NZS 1170.2 provides a method to calculate wind speed as is shown below:

$$V_{sit,\beta} = V_R M_d (M_{z,cat} M_s M_t) \quad \text{Eq. 6-1}$$

where

$V_{sit,\beta}$ --- site wind speed

V_R --- regional gust wind speed for annual probability of exceedence of 1/R, R is return period

M_d --- wind directional multiplier for the 8 cardinal directions (β)

$M_{z,cat}$ --- terrain/height multiplier

M_s --- shielding multiplier

M_t --- topographic multiplier

Regional wind speed (V_R) and wind direction multiplier (M_d)

Normally, structures are designed to resist a strong wind with a very long return period, such as 100 years or more. The design wind speed is determined from historical records using extreme value theory to predict future extreme wind speeds. The term "return period" is introduced for describing annual risk of exceedence. A wind speed with a 50-year return period V_{50} indicates an expected risk of exceedence of 0.02 (1/50) in any 1 year (Holmes, 2001). Australia is divided into several regions based on the maximum wind speed expected during peak storm activity as shown in Figure 6-1. This research concentrated on the strength analysis of timber utility poles under a design wind load in Sydney and, thus, the corresponding regional wind speed has to be selected based on the region where Sydney is located, that is region A2. Industry practice is to consider wind loads on structures based on a 3 second wind gust that occurs over a certain return period typically 50-200 years. However, for a 50 year return period, there is a 63%

probability that actual wind speeds will exceed design wind speed during a 50 year design life. Hence, the regional wind speed with a 50 year return period will not be considered in industry practice. Wind Speed for Region A and annual probability of exceedence is listed in the Appendix Table A1. In this study, the regional wind speed with 100-year-return period can be considered as appropriate which is 41m/s.

Figure 6-1 Wind regions (Australian/New Zealand Standard 1170.2, 2011)

Wind-tunnel and full scale studies have verified the variation of structural response as a function of wind direction as well as speed (Holmes, 2001). To describe the influence of direction on wind speed, a direction multiplier M_d is introduced and the values are in the range from 0.8 to 1.0 depending on wind direction. In Region A, and where the final orientation of the building is unknown, M_d has to be set to1.0. For ultimate limit states design which is a conservative approach, the wind speed and multipliers for the worst direction should be used, that is, the multiplier has to be considered as 1.0.

Terrain/height multiplier ($M_{z,cat}$)

Different terrains as categorized according to their associated surface roughness also influence the wind speed. At great heights (a few hundred meters) above the ground, frictional effects can be negligible. Closer to the ground surface the wind speed is affected by frictional drag of the air stream over the terrain. It is known that the wind speed increases with increase in height above ground level. There is a boundary layer within which the wind speed varies from almost zero, at the surface, to the gradient

wind speed at a height known as the gradient height (Mendis et al., 2007). Terrain categories (TC) with corresponding wind speed under a certain range of height are defined in AS/NZS standard 1170.2 and listed in the Appendix Table A2 and A3.

The length of timber utility poles used for network distribution in the residential areas of Sydney is normally from 11m to 14m with 1.5 to 2m embedded in soil. In this case, TC1, TC 2.5 and TC 3 are the proper terrain categories where the timber utility poles are placed. For ultimate limit state design, the worst situation was considered and the multiplier was set to 1.12.

Shielding Multiplier (M_s)

The shielding multiplier describes the situation where design wind speed is reduced by the protection afforded by buildings located on the upwind directions. Thus, this parameter highly depends on the location where the timber poles are placed. In this situation, the multiplier is set to 1.0 (meaning no shielding) due to timber poles having varying shielding and often no shielding.

Topographic Multiplier (M_t)

The topographic multiplier demonstrates a local geographic effect and increases the design wind speed based on the gradient upwind of the site. Especially, if the intended structures are located on a hill or escarpment, the topographic multiplier has to be evaluated properly and a multiplier of 1.0 is not a conservative assumption anymore. In this research, due to lack of information on the exact location of timber utility poles, the multiplier cannot be determined by assumption.

6.2.1.2 Wind pressure

According to the Australian standard, the wind pressure can be obtained based on wind speed. Similar to calculation of wind speed, a series of coefficients need to be determined for calculating wind pressure. It has been discovered that the design wind speed depends on the geographic region, terrain category, shielding and the topographic location of the structures, whereas the wind pressure coefficients are dependent upon the characteristics of the intended structures.

Timber utility poles are normally used for power and communication supply in Australia and thus different forms of cables are attached to the poles as shown in Figure 6-2. Wind loads on these structures result from two components: wind loads on the poles as well as on the cables. These cables are more sensitive to wind loads than the pole structures and they have a uniformly distributed mass along the span (Davenport, 1979).

Figure 6-2 Cables attached to timber utility poles for network distribution

For network distribution application, at the termination of a distribution network or if the cables are attached to the poles at certain angles, stays are designed (see Figure 6-3) to take the full load applied and not just the portion by which the load exceeds pole capacity. Generally, consideration of maximum wind load case and the corresponding tensions on the cables is analysed. Accordingly, this prevents the poles from collapse along the cables distribution. However, if the wind storm is normal to the cable distribution direction and no stays are in place (such as an intermediate in-line pole), the situation can be a problem, since the cables are subjected to wind loads and in turn, these loads are transmitted to the poles. In this case, the poles are more likely to collapse (see Figure 6-4). Hence, the situation that the wind storm direction normal to the cables which are supported by the intermediate in-line poles was concentrated on in this study.

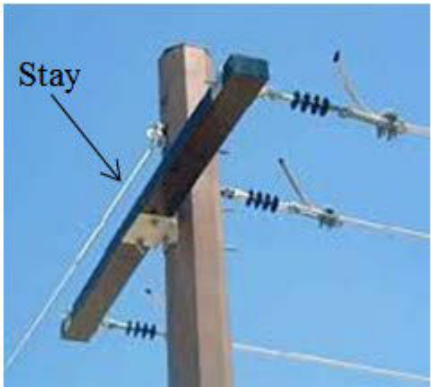

(a) Stay applied at the termination of distribution network

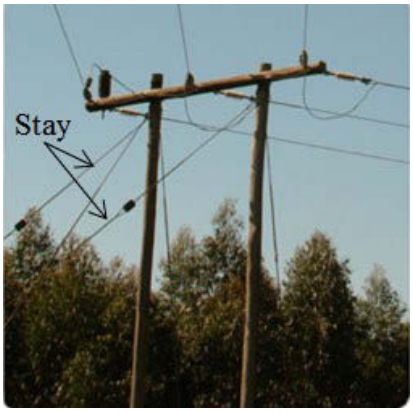

(b) Stay applied when the cables attached to the pole at a specific angle

Figure 6-3 Stays applied to distribution system

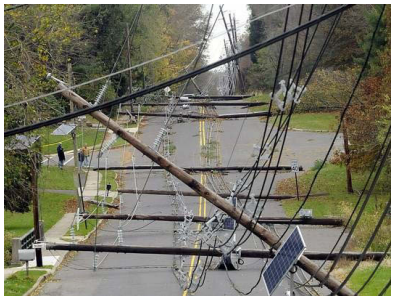

Figure 6-4 Collapse of timber utility poles

AS/NZS1170.2 gives an equation to determine the wind pressure based on the wind speed and some characteristic coefficients of a structure.

$$P = 0.5\rho V^2 C_{fig} C_{dyn} \qquad \text{Eq. 6-2}$$

where

P --- design wind pressure (Pa)

ρ --- air density and shall be taken as 1.2 kg/m^3

V --- wind speed

C_{fig} --- aerodynamic shape factor of a structure

C_{dyn} --- dynamic response factor of a structure

Aerodynamic shape factor (C_{fig})

Aerodynamic shape factor is used to determine the pressure applied to each surface of a structure. In this research, the pole structure can be classed as a cylinderical structural member in shape according to AS/NZS 1170.2. The pole structure above ground is around 10m high and the average diameter is 0.315m. According to the criteria below, the value of C_{fig} can be set to 0.2.

$$if\ b \times V < 7m^2/s,\ C_{fig} = 0.5 \quad \text{Eq. 6-3}$$

$$if\ b \times V \geq 7m^2/s,\ C_{fig} = 0.2 \quad \text{Eq. 6-4}$$

where

V --- design wind speed

b --- breadth of a structure usually normal to the wind stream

Dynamic response factor (C_{dyn})

Based on the uncertainties associated with dynamic features of structures and the target limit state, dynamic response factors for tall building and wind sensitive structure design are required. The factor would primarily account for deviations in the actual wind loads from the nominal wind loads and for uncertainties associated with the load effects. The factor is determined for structures or elements of structures with natural first-mode fundamental frequencies. If the frequency is greater than 1.0 Hz, the factor will be set to 1.0. In this study, the natural first-mode frequency of timber utility pole was around 1.9Hz, so the dynamic response factor was set to 1.0.

6.2.1.3 Wind load

To determine the wind force, a vector sum of the forces calculated from the pressures applicable to the assumed area is used for structural surface or elements:

$$F = \sum (P_z A_z) \quad \text{Eq. 6-5}$$

where

P_z --- design wind pressure at height z

A_z --- a reference area at height z, upon which the pressure at the height z acts

In this study, the intended pole structure has circular shape and the wind load can be calculated directly by:

$$F = 0.5\rho V^2 C_{fig} C_{dyn} A_{ref} \quad \text{Eq. 6-6}$$

where A_{ref} is the projected area normal to the wind direction.

From the previous studies, it can be found that the wind action highly depends on the characteristics of the location where the structures are placed as well as the characteristics of the structures. Due to the shortage of solid information about where utility poles are placed, it was hard to determine the design wind load accurately and only according to AS/NZS 1170.2. Therefore, other references have to be employed.

This project is funded by Ausgrid, which is a State Owned Corporation whose stakeholder is the New South Wales Government. The Ausgrid electricity network provides power to 1.6 million homes and businesses throughout Sydney, the Hunter and the Central Coast. The network is made up of more than 200 large electricity substations, 500,000 power poles, 30,000 small distribution substations and almost 50,000 km of below and above ground electricity cables (AUSGRID, 2014). Network standard NS220 which facilitates the design of the Ausgrid's overhead distribution network was compiled by staff and accredited service providers. It outlined key line design parameters and provided information on mechanical loadings, pole/structure capacity, and preferred practice. Therefore, the design principles it provided were not only according to Australian standard but also based on lots of practical experience and criteria. Hence, the information and corresponding parameters provided by Ausgrid standard were also adopted in this research.

In the Ausgrid standard, for round timber poles, a design wind pressure of 1.3kPa is used based on practical experience. The wind load on a round pole, resolved to its tip is given by:

$$F_T = 0.5 h D_{av} P \quad \text{Eq. 6-7}$$

where

F_T --- tip load due to wind load on pole (kN)

h --- pole height above ground (m)

P --- design wind pressure on pole (kPa)

D_{av} --- average diameter of pole (m)

Ausgrid generally uses CCA-treated (a chemical timber preservative coating containing chromium, copper and arsenic) timber poles for distribution lines and there are some typical types of length used for different applications (see Appendix Table A4).

In general, heavier poles (8 or 12kN working strength) are used for terminations and line deviations, whereas, lighter poles (6kN working strength) are used for intermediate in-line sites.

As mentioned previously, the utility poles used for intermediate in-line sites are studied in this chapter, lighter poles are considered in this situation and can be set to 12m long with average diameter of 0.315m. Normally the embedment length of a pole is 1.5m to 2m, so the height above ground level can be considered as 10m. The tip load due to the wind load on the pole can be calculated which is 1.95kN.

After considering the wind load directly acting on timber poles, wind load influencing the poles through conductors should be taken into account.

Transverse wind force applying on the poles through the conductors can be calculated by Eq. 6-8 provided by Ausgrid:

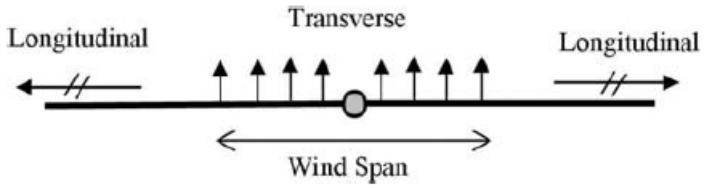

Figure 6-5 Wind Force on Conductor

$$W_T = 0.5LdPCF_{SR}\cos^2\alpha \qquad \text{Eq. 6-8}$$

where

W_T --- transverse force applied to pole due to conductor windage (kN)

L --- span length (m)

d --- projected diameter of conductor (m)

P --- design wind pressure on conductor (kPa)

C --- drag coefficient of conductor (default value of 1.0)

F_{SR} --- span reduction factor (SRF, default to 1.0, reducing for long spans)

α --- angle between wind direction and normal to the conductor

The poles intended for use in an urban area were studied in this chapter and thus the maximum span length was set to 80m (typical length of 65m); in this case, the SRF can be ignored as the span lengths tended to be short. For an urban area, wind pressure of 900Pa is used widely by the industry for distribution line design and drag coefficient is always set to 1.16. Suppose the wind direction is normal to the conductors, the angle α shall be 0 degrees and the value of $\cos^2 \alpha$ shall be 1.0. In this situation, W_T depends on the model of the conductors or the cables.

Conductor Low Voltage Aerial Bundled Cable (LVABC) 95mm^2 is normally used in residential areas. It is a preferred cable type for new low voltage mains and unsuitable for long spans, so this cable is typically used in an urban area for distribution application. One or two cables can be attached to the utility poles for network distribution, and one cable attached is normally used in residential areas and were considered in this study. For the straight line intermediate situation (see Figure 6-6), the maximum wind load on the LVABC is 2.62kN according to Ausgrid NS220. This value covers the majority of situations except the situation of extremely long span and includes the ultimate limit state.

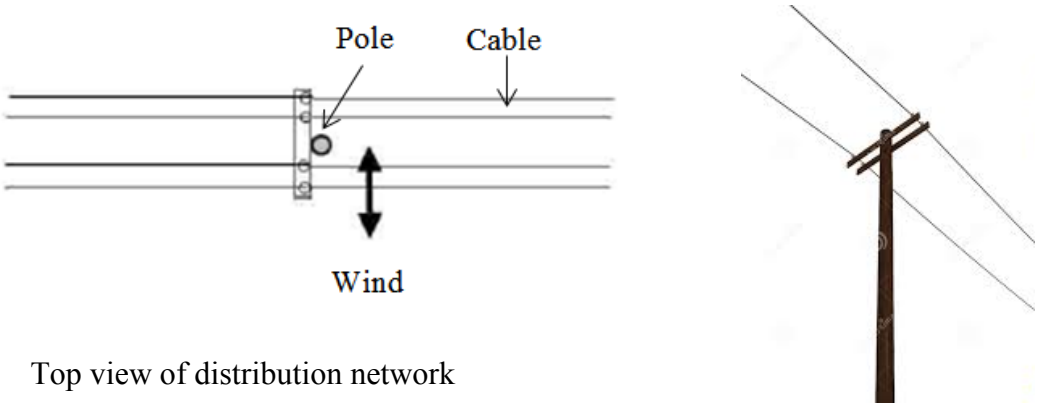

Top view of distribution network

Figure 6-6 Straight line intermediate

Accordingly, the total wind load applied on network distribution can be calculated based on the previous study which is 4.57kN.

6.2.2 Load capacity analysis of timber poles under wind load

Load capacity design in Australian Standard 1720.1 for timber structures is based on modifying the characteristic capacities by the factors appropriate to the service condition as well as the material property type. The design capacity in bending of round

timbers such as poles or piles for the strength limit state has to satisfy the following equation:

$$M_d \geq M^* \quad \text{Eq. 6-9}$$

where

$$M_d = \emptyset k_1 k_4 k_6 k_9 k_{12} k_{20} k_{21} k_{22} f_b^{'} Z \quad \text{Eq. 6-10}$$

and

M^* --- bending produced by strength limit states design loads

$\emptyset$ --- capacity factor, and 0.6 for round timber intended to fulfil an essential service

k_1 to k_9 --- strength modification factors

k_{12} --- stability factor, and 1.0 for round timber

k_{20} --- immaturity factor, and 1.0 for hard wood with mid-length diameter greater than 0.125m

k_{21} --- shaving factor, and 0.85 for hard wood considering bending stress

k_{22} --- processing factor, 0.85 if poles are steamed otherwise it shall be 1.0

$f_b^{'}$ --- characteristic strength in bending, evaluated by in-grade testing

Z --- section modulus of a round timber, $\frac{\pi d_p^3}{32}$, d_p is the diameter of the pole at the relevant section

The main limitation of this criterion is that it does not consider the damage type of a timber pole influences on the strength performance. Suppose there are two types of damage and they both cause the same loss of cross section but one of the damages is on the surface and the other is internal. In this situation, the calculated section modulus (Z) of these two damage scenarios will be the same as well as the bending capacity. However, the effects caused by these two types of damage are distinctly different. Ausgrid NS220 highlights this difference based on Eq. 6-11 and Eq. 6-12

$$F_T = \frac{k f_b^{'} \pi D^3 \times 1000}{32h} \quad \text{Eq. 6-11}$$

$$F_T = \frac{k f_b^{'} \pi (D^4 - d^4) \times 1000}{32hD} \quad \text{Eq. 6-12}$$

where

F_T --- ultimate tip strength (kN)

D --- ground line diameter (m)

d --- diameter of internal hollow (m)

h --- tip height above ground (m)

k --- factor accounting for load duration, degradation, shaving, immaturity and processing, 0.8 is set for assessing the in-service pole

Ausgrid NS220 uses tip strength to assess the strength of a pole instead of bending capacity used in AS1720.1. Eq. 6-11 is used to determine the tip strength of a pole if there is an external damage at the ground level whereas Eq. 6-12 is used for the internal damage condition. From these two equations, it can be seen that Ausgrid NS220 mainly considers the damage which happens at the ground level (see Figure 6-7) even though it highlights the different effects caused by the internal and the external damage.

Figure 6-7 Typical example of ground line decay

Actually, the damage occurring at ground level is more likely than any other area and can cause severe consequences. Hence, it is reasonable to concentrate on the study of the effects on strength when there is damage at the ground level for practical applications. However, for academic research, effects caused by other damage locations are interesting as well.

6.2.3 Strength analysis of damaged timber poles

In this section, different damage influencing the strength of the poles are concentrated on including different damage size and locations. The maximum strength in bending under a wind load is used to assess the effects of damage on the strength of the poles.

In order to investigate the damage influencing the strength of the timber poles, a number of numerical models with different damage conditions were created.

- Two damage types were considered: external damage and internal damage
- Three locations of damage were considered: ground level, middle and the top area (2m from the top of the pole)
- Five types of damage size (diameter) were considered
- Five types of damage length were considered

Different types and locations of damage are shown in Figure 6-8. In this study, considering transverse wind load will be applied on the pole, the 2D axisymmetric model was not appropriate, and thus the 3D orthotropic material models were created. The maximum stress in the longitudinal direction of the pole was obtained to represent the strength in bending for the pole under a design wind load.

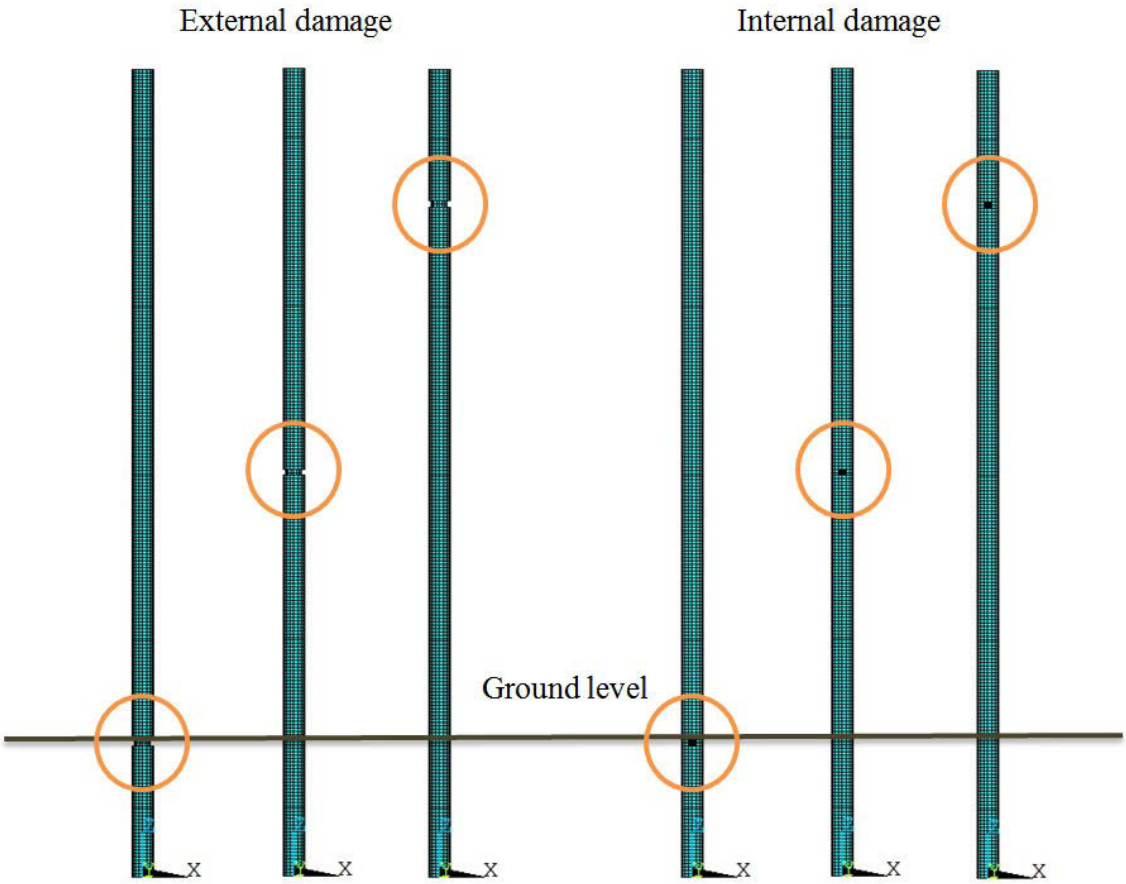

Figure 6-8 Different damage types and locations

The intended pole structure is a hardwood named spotted gum with unseasoned condition and in strength group S2 according to AS1720.1 and the strength in bending is normally considered as 80MPa for distribution applications in the Ausgrid standard, and the strength factor is set to 0.6 considering the maximum wind load is of interest in this research. Thus, the ultimate design strength in bending can be obtained which is 38MPa.

For numerical analysis, a design wind load was applied, and the maximum stress in bending was obtained. A safety ratio was considered to determine the damage effect on the strength of a pole which can be expressed as:

$$\text{Safety ratio} = \frac{\text{Obtianed bending strength}}{\text{Ultimate design strength}} \qquad \text{Eq. 6-13}$$

Firstly, the strength of the intact pole under a design wind load was studied and the results are listed in Table 6-1:

Table 6-1 Strength analysis for an intact pole

Ultimate design strength in bending: 38MPa				
L (m)	D_{av} (mm)	Wind load (kN)	Max. strength in bending (MPa)	Safety ratio
12	315	4.57	16	42%

Note: L --- length of the pole; D_{av} --- average diameter of the pole;

The material properties used to create the FE models were defined in Chapter 3. Table 6-1 provides the maximum strength in bending for an intact pole with specific dimension under a design wind load. The design wind load as mentioned previously includes the wind action on the pole as well as the cables attached. It can be found that the maximum stress caused by wind load is much less than the ultimate design strength, and the safety ratio of 0.42 indicated the pole is safe under the design wind load.

6.2.3.1 Damage at ground level

As mentioned previously, damage at ground level is more likely to happen and will significantly influence the load capacity of a utility pole. Hence, the damage at ground level was studied prior to the other locations. Table 6-2 indicates the acceptable tip load of timber utility poles for the intact pole as well as the damaged poles according to equations 6-11 and 6-12.

Table 6-2 Maximum acceptable tip load for the intact pole and the poles with damage at ground level

Intact timber pole: F_T=11.66kN			
External damage		Internal damage	
Damage size (mm)	F_T (kN)	Damage size (mm)	F_T (kN)
79	4.90	79	11.61
118	2.85	118	11.43
158	1.44	158	10.92
197	0.61	197	9.88
236	0.18	236	7.99

It can be noticed that for the timber pole with small external damage such as 79mm at the ground location, the tip load is greater than the design wind load; that is, the damaged pole still retains a reasonable load capacity under service condition. However,

the pole with a large damage on the surface at ground level has almost lost its entire load capacity. For the internal damage condition, the pole still retains a higher load capacity even when the large damage appears.

It is surprising that the load capacity of the pole with large internal damage (236mm) is almost twice that of the pole with small external damage (79mm). From the comparison of results, it is obvious that the external damage at ground level influences the load capacity of a utility pole significantly.

For the external and the internal damage at the critical location of ground level, the poles with different damage sizes were studied numerically by ANSYS. From the results of numerical analysis, the same phenomenon was observed. In Table 6-3, R_L and R_W indicate the proportion of the damage part relative to the original dimension. For small external damage, the utility pole still had considerable bending strength under the design wind load. However, the maximum bending stress of the damaged pole was close to the ultimate design strength under design wind load. If the damage size keeps increasing, the maximum stress on the pole under the design wind load will exceed the ultimate bending strength and it will tend to collapse.

Table 6-3 External light damages at ground level influencing the strength of the pole

L=12m D=315mm Ultimate design strength in bending: 38MPa						
Damage size W_D (mm)	L_D (mm)	$R_L=L_D/L_O$	$R_W=W_D/W_O$	Max. load (kN)	Max. stress (MPa)	Safety ratio
79	100	1%	25%	4.57	35	92 %
	200	2%	25%		35	92 %
	300	3%	25%		35	92 %
	400	4%	25%		35	92 %
	500	5%	25%		36	95 %

Note: L_D is the length of damage, L_O is the length of the pole; W_D is the diameter of the damage, W_O is the average diameter of a pole

Table 6-4 gives the corresponding strength parameters of the poles with internal damage appearing at ground level under the design wind load. It can be seen that even when the damage size is reaching 75% of the original diameter, the maximum stress in bending is still smaller than the ultimate design strength. Therefore, the internal damage will not

significantly affect the strength of the pole within a certain range. Another issue which should be noticed is the effect of the damage length. Obviously, neither the Australian standard nor the Ausgrid standard took damage length into account. Actually, the diameter/width of damage is the most important factor to affect the strength of a pole. However, from Table 6-4 it can be seen that with increasing damage diameter, the length of the damage becomes more significant in influencing the bending strength of a pole. For example, the safety ratio is 52% for damage dimension of 236mm by 100mm whereas the ratio is increased to 70% for the dimension of 236mm by 500mm.

Table 6-4 Internal damages at ground level influencing the strength

L=12m D=315mm Ultimate design strength in bending: 38MPa Maximum accepted wind load: 11kN						
Damage size				Max. load (KN)	Max. stress (MPa)	Safety ratio
W_D (mm)	L_D (mm)	$R_L=L_D/L_O$	$R_W=W_D/W_O$			
79	100	1%	25%	4.57	17	44%
	200	2%	25%		17	44%
	300	3%	25%		17	44%
	400	3%	25%		17	44%
	500	4%	25%		17	44%
Damage size				Max. Load (KN)	Max. stress (MPa)	Safety ratio
W_D (mm)	L_D (mm)	$R_L=L_D/L_O$	$R_W=W_D/W_O$			
236	100	1%	37%	4.57	20	52%
	200	2%	37%		22	57%
	300	3%	37%		25	65%
	400	3%	37%		26	68%
	500	4%	37%		27	70%

After comparing the results from these two types of damage, it can be concluded that the dimension of external damage, exceeding 25% of the original diameter of the pole will cause a tendency to collapse, while a utility pole can be still safe even when 75% of the internal cross section has been lost. According to this study, the difference between these two types of damage influencing the strength of the poles is highlighted.

In the next stage the study concentrated on the remaining load capacity when damage appears externally at ground level which is the same concept as the tip load mentioned in Ausgrid NS220. The rate of maximum load capacity (LCR) was used to evaluate the

remaining load capacity by Eq. 6-14. The maximum load capacity was determined from the ultimate design strength in bending which is 38MPa; that is, to reach this maximum strength, the maximum load can be applied on the pole. This study was based on numerical analysis.

$$\text{LCR} = \frac{\text{maximum load capacity of damaged pole}}{\text{maximum load capacity of intact pole}} \qquad \text{Eq. 6-14}$$

Table 6-5 summarises the remaining load capacity for the poles with external damage at ground level. It can be seen that when reaching the maximum bending stress, the intact pole is capable of accepting a maximum wind load of around 11kN. The poles with damage size of 79mm are able to be subjected to a maximum wind load of 4.8kN. Even though this value was still higher than the design wind load of 4.57kN, the load capacity decreases to 44% of the intact one.

From Table 6-5, the poles with the damage diameter of 118mm are not able to carry the design wind load of 4.57kN. As mentioned before, the wind load combines the wind action on the pole as well as on the cable model LVABC. It is obvious that the poles with damage size of 118mm are unsafe to support this cable model under the design wind speed. Another cable model AAC-LV MERCURY 7/4.50 is sometimes used where LVABC is unsuitable especially for long span distribution and is also used for existing mains repairing. According to these practical criteria, if LVABC is replaced by AAC-LV MERCURY 7/4.50, the design wind load on the pole and cable is 2.87kN, which is almost the maximum load capacity of the poles with damage size of 118mm. The load capacity decreases to 25% of the intact pole. From this value, it can be seen that with the damage size reaching around one third of the original diameter of a pole, the load capacity decreases significantly.

For the pole with damage size of 158mm, the maximum load capacity is 1.4kN. This means the pole is not safe under the design wind speed even when there are no cables attached to the pole. However, this is unrealistic. In this case, the poles with this damage size cannot be used in a network distribution application anymore and the remaining load capability is only 13% of the intact pole. For large damage size such as 197mm and 236mm, the poles have lost almost the whole capacity of load bearing.

According to the studies based on numerical models, it can be concluded that for damage sizes greater than 25% of the original diameter of a pole, the damaged pole may not be safe for a distribution application.

Table 6-5 Maximum load capacity for external damage at ground level

L=12m D=315mm Ultimate design strength in bending: 38MPa Maximum accepted wind load: 11kN					
Damage size W_D (mm)	$R_W=W_D/W_O$	Max. load (KN)	Max. stress (MPa)	Safety ratio	LCR
79	25%	4.8	37	97%	44%
118	37%	2.8	37	97%	25%
158	50%	1.4	37	97%	13%
197	63%	0.58	37	97%	5%
236	75%	0.175	37	97%	1.6%

Although, the internal damage in a certain range will not influence the strength of a pole under a design wind load, it is still valuable to find out the maximum load capacity of a damaged pole under the ultimate design bending strength. Table 6-6 indicates the remaining load capacity for the poles with internal damage at ground level. According to the results, it can be seen that the remaining load capacity is not reduced significantly even when half of the cross section of the pole is lost. For the poles with some large damage situations, the remaining load capacity is above 60% of the intact condition.

Table 6-6 Maximum load capacity for internal damage at ground level

L=12m D=315mm Ultimate design strength in bending: 38MPa Maximum accepted wind load: 11kN					
Damage size W_D (mm)	$R_W=W_D/W_O$	Max. load (KN)	Max. stress (MPa)	Safety ratio	LCR
79	25%	10	37	97%	98%
118	37%	9.7	37	97%	95%
158	50%	9.3	37	97%	91%
197	63%	8.2	37	97%	80%
236	75%	6.4	37	97%	63%

However, it should be noticed that the damage length in this study was up to 500mm. For the light damage, such as 79mm, the length of the damage may not affect the strength significantly, but when the damage size increases, the influence of damage length on the load capacity of a pole increases dramatically, such as in the case of the damage with a diameter of 236mm (see Figure 6-9). With a small damage length, the

bending stress is much less than the ultimate design strength value; however, the maximum bending strength of the damaged pole almost reaches the ultimate design strength when the damage length increases to 500mm.

Table 6-7 Strength of the poles with large damage

Damage size W_D (mm)	L_D (mm)	$R_L=L_D/L_O$	$R_W=W_D/W_O$	Max. Load (KN)	Max. stress (MPa)	Safety ratio	LCR
	100	1%	75%		28	80 %	
	200	2%	75%		31	95 %	
236	300	3%	75%	6.4	35	97 %	63%
	400	3%	75%		36	97 %	
	500	4%	75%		37	97 %	

Figure 6-9 summarises the maximum strength for five damage scenarios with different damage length from 100mm to 500mm and indicates the influence of damage length on the maximum strength of the poles under their maximum load capacity. It is clearly demonstrated that the maximum strength of the poles with small damage size (79mm) is almost not affected by damage length. When the damage size increases, the effects of damage length on the maximum strength becomes more obvious.

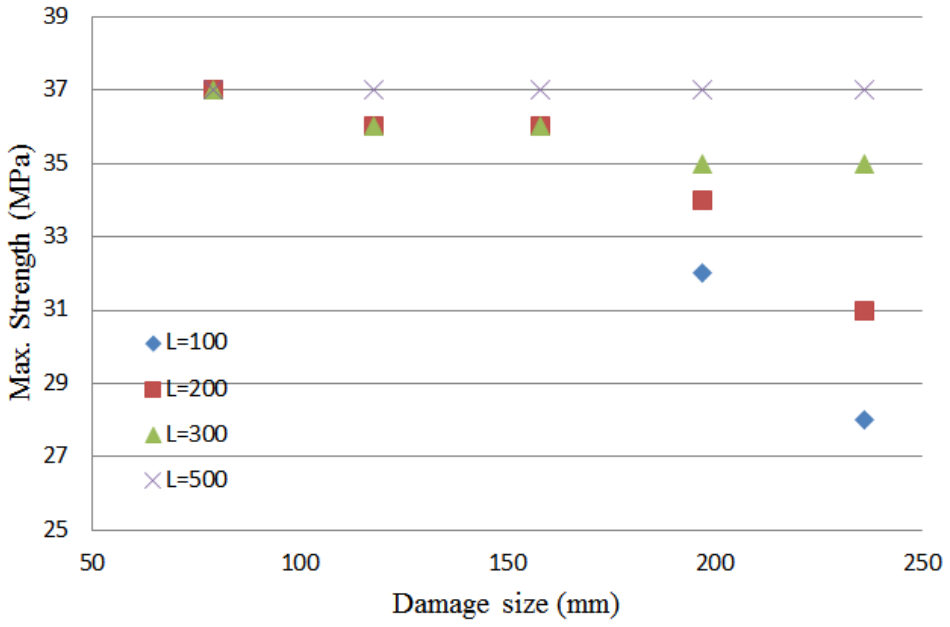

Figure 6-9 Damage length influences on the maximum strength of the poles

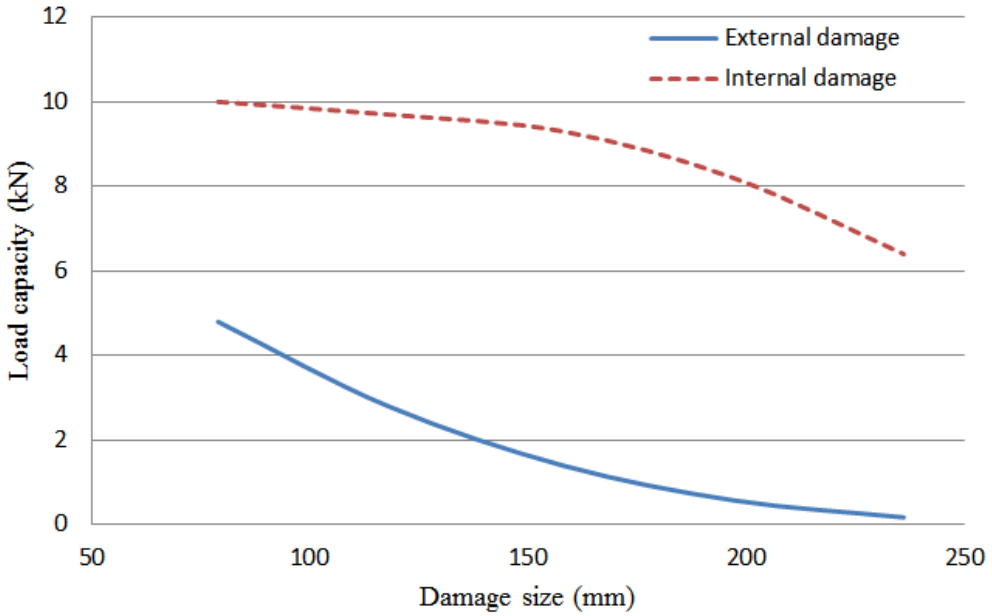

Figure 6-10 Load capacity changes with damage size under different damage types

Figure 6-10 demonstrates the load capacity changing with the damage size under two damage types. The solid curve represents the load capacity change for external damage condition, while the dashed curve indicates the load capacity for the internal damage condition. It can be found that the curve for the internal damage has much lower gradient compared to the curve of the external damage and the maximum load capacity of the utility poles with the internal damage is higher than the external damage condition. For the internal damage situation in the figure, the load capacity does not change much if the damage size is less than 150mm; however, with the damage size increasing, the load capacity decreases significantly. For the external damage condition, the load capacity of the damaged pole drops considerably. The load capacity studies of timber poles in this section considered the transverse wind load. In this situation, the timber pole can be seen as a cantilever beam structure and the maximum stress presents at the bottom of the cantilever beam. The normal bending stress at a distance from the neutral surface is acting on a transverse plane of the structure. Normal bending stresses appear to be of greatest concern for cantilever beams in bending. At any section of a cantilever beam, the fibre stress will be maximum at the surface farthest from the neutral axis. This verifies that the external damage plays a more critical role on affecting the bending strength as well as the remaining load capacity of the utility poles.

6.2.3.2 Damage at middle and top area

After considering the damage at ground level, the damage at the middle and the top areas of the poles has to be taken into account. The same damage scenarios with the previous study, that is, external and internal damage with different damage sizes and lengths were created.

Firstly, the maximum load capacity for the external damage at the middle (4m above ground) of the utility pole was calculated based on numerical analysis and the summarised results are listed in Table 6-8. From the results it can be seen, even with a damage area at the middle of the pole, the external damage still affects the load capacity of poles significantly. For the light damage such as damage size of 79mm, the maximum load capacity is 5.3kN and slightly higher than the load capacity of the pole which has the same damage size at ground level. When the damage size reaches one third of the original diameter of a pole, it can be noticed that the load capacity is smaller than the design wind load. In this case, this damaged pole cannot carry LVABC under the design wind speed. The poles with medium and large damage sizes have almost lost the load capacity. This study indicates that the external damage at the ground level and at the middle of a pole have similar influences on the bending strength of the timber utility poles.

The maximum load capacity for the external damage at the top area (2m below the top) of the pole was investigated by numerical analysis and the summarised results are shown in Table 6-9. It can be seen that the load capacity of the poles with damage size of 79mm and 118mm at the top area is not influenced too much. Although the load capacity decreases dramatically when the damage size increases to 158mm, the damaged pole still has the capacity to take the design wind load. However, for the conditions of large damage size, the damaged poles almost lost the load capacity under the design wind load.

Table 6-8 Maximum load capacity for external damage at the middle of poles

L=12m D=315mm Ultimate design strength in bending: 38MPa Maximum accepted wind load: 11kN					
Damage size W_D (mm)	$R_W=W_D/W_O$	Max. load (KN)	Max. stress (MPa)	Safety ratio	LCR
79	25%	5.3	37	97%	64%
118	37%	3.3	37	97%	39%
158	50%	1.8	37	97%	19.5%
197	63%	0.83	37	97%	8.6%
236	75%	0.23	37	97%	2.6%

Table 6-9 Maximum load capacity for external damage at the top area of poles

L=12m D=315mm Ultimate design strength in bending: 38MPa Maximum accepted wind load: 11kN					
Damage size W_D (mm)	$R_W=W_D/W_O$	Max. load (KN)	Max. stress (MPa)	Safety ratio	LCR
79	25%	8.5	37	97%	91%
118	37%	8.5	37	97%	91%
158	50%	5.4	37	97%	60%
197	63%	2.4	37	97%	25.5%
236	75%	0.78	37	97%	7.8%

Based on the studies above, it can be concluded that, any large external damage always significantly influences the bending strength of the utility poles regardless of the damage location. The poles with light damage in this study were likely to take design wind load under certain conditions even when the maximum load capacity of the pole is influenced. However, whether the pole with medium damage can take the design wind load or not depends on the damage location. The calculation results for different damage length under each damage size are provided in the Appendix.

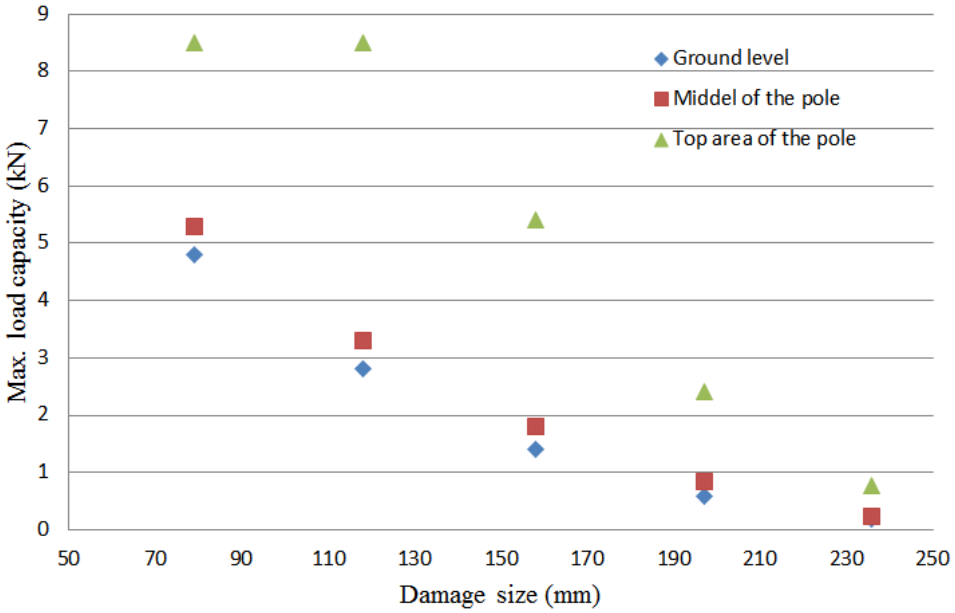

Figure 6-11 Maximum load capacity of utility poles with external damage at different locations

Figure 6-11 provides an intuitive demonstration to indicate that the maximum load capacity is similar if the external damage appears at ground level or the middle of the pole. The maximum load capacity for the poles with light or medium external damage at the top area is much higher than the same damage at the ground level or in the middle. The large external damage such as the damage size of 236mm always leads to the total loss of the load capacity.

The maximum load capacity for the internal damage at the middle and the top area of the utility poles were also analysed by numerical modelling method, and the same damage size was selected for analysis. It was found that the maximum load capacity will not be influenced by whether the internal damage appears at the middle or at the top area. The maximum bending strength of the poles with internal damage at the middle or the top area is almost the same as for the intact pole and, therefore, the internal damage at the middle or the top area of a pole will not affect the maximum bending strength as well as load capacity of a pole according to the numerical results.

6.3 CONCLUSIONS

From the studies in this chapter, it can be concluded that, the damage at ground level will significantly influence the load capacity of a pole. The external damage plays a

more important role in affecting the load capacity of a pole compared with the internal damage condition. Even light external damage can cause a significant reduction in load capacity. However, the pole with large internal damage can still take the design wind load even when the damage is present at ground level. Normally, for industry practice, more than half of the original cross section suffering internal decay will be taken as severe damage for inspection.

In this study, the numerical model provided an ideal situation for examining the effects of strength losses for the damaged poles. The strength analysed by numerical modelling highly depends on the material properties, structural geometry and the boundary conditions. Timber is a product of nature hence the damage condition is different with man-made material such as steel or concrete. The damage of timber is mostly due to insect attack, fungi and ageing. For example, fungal decay can be divided into white rot, brown rot, soft rot and white pocket rot (Ausgrid, 2011). Some fungi will affect the mechanical performance of timber material gradually. In this case, regular inspection is needed if light damage appears regardless of the internal damage or the external damage. Some inspection operators will replace the utility poles if some specific fungi are found since it may totally destroy the mechanical performance of the poles within one week.

7 Conclusions and recommendations

7.1 CONCLUSIONS

This research focused on the exploration of the new condition assessment for the timber utility poles based on numerical simulation using finite element modelling. In order to gain an insight into stress wave propagation in the timber poles, a series of numerical models were developed. Different material characteristics were considered and compared to examine the stress wave behaviour in specific materials. Experimental testing was carried out by another member of the research team to assist in the development of accurate numerical models. A novel wavelet packet energy method was developed to assess the condition of the poles, and the damage condition can be predicted by an optimisation technique. The damage influencing the load capability was studied extensively considering different damage locations and dimensions. Wind load was considered as the main load that was applied on the timber utility poles and the corresponding standards were used as references.

Based on the material properties obtained from relevant literature, numerical modelling using finite element analysis (FEA) of timber utility poles was performed. The FE models comprised material modelling as well as boundary conditions modelling. The material modelling included isotropic, transversely isotropic and orthotropic material characteristics. As it is known, timber is an anisotropic and inhomogeneous material since it is a product of nature. The FE model is not able to fully simulate the timber material, and thus, transversely isotropic and orthotropic materials with homogeneous

properties were used to represent the complexity of the timber material. Experimental testing was conducted to verify the most accurate FE model to represent the wave behaviour in timber poles. The orthotropic material model has the most similar results to the experimental results and accordingly should be used to simulate timber material for the purpose of studying the wave behaviour. Parametric studies including changing of elastic modulus, density as well as Poisson's ratio has been performed for both the isotropic model and orthotropic model to investigate the material properties which influence the wave behaviour. Since only the longitudinal wave was studied in this research, wave behaviour mentioned in this thesis refers to the longitudinal wave. It is found that the elastic modulus (in the longitudinal direction for orthotropic material) affects the wave propagation more significantly than density, while Poisson's ratio has less effects on wave behaviour. Soil modelling was also studied in this research. According to numerical analysis, the perfect bonding contact was the most appropriate way to simulate the interaction between pole and soil comparing with other methods. Linear elastic model and Drucker-Prager model were considered and created to simulate soil material characteristics and the results did not show much difference under a hammer impact.

An inclined impact on a utility pole at approximately 1.5m above ground is an ideal location for field applications. However, the inclined impact will generate three different wave modes and the wave behaviour becomes more complicated when propagating in timber material. Therefore, it causes difficulty in obtaining an effective longitudinal wave signal. In this thesis, the investigation on the impact location and sensing location/orientation was conducted. According to the theory of guided wave propagation in cylindrical structures, for the structures with isotropic or transversely isotropic material, pure longitudinal wave can be obtained at 90 degrees around the circumference from the impact location. The numerical results showed the consistency with the guided wave theory. However, the numerical results of the orthotropic material model indicated that different wave modes are still hardly separated.

This thesis also involved dispersion study of longitudinal wave in isotropic material model. The results of numerical analysis showed consistency with analytical results and gave a guide to choose appropriate excitation frequency for damage detection. Due to the limitation of the finite element analysis, it is hard to obtain the dispersion curve for the transversely isotropic and the orthotropic material models. Dispersion curve for the

transversely isotropic material model in this thesis was obtained through analytical analysis conducted by another PhD student in this research group. It can be found that the waves in the isotropic material model with certain frequencies have fewer modes compared to the waves with the same frequencies in the transversely isotropic material.

Damage detection for timber utility poles was one of the most challenging parts in this research, since little reference has been found in this field. Based on the previous studies, it is noted that wave propagation behaviour in timber is very complicated. Another big challenge in this study is that the sensors cannot be placed to cover the damage area as the damaged part is always below ground. These two issues determined that damage detection for the timber utility poles cannot be based on the reflected wave signal directly. In this situation, wavelet packet energy is imported to obtain the features of the damaged poles based on the wave patterns. As the starting stage in this research field, the intact and the damaged models were considered as isotropic material. The proposed method minimised the interference caused by the incident waves and the reflected waves. The method based on the change of WP energy demonstrates the capability of damage classification as well as damage severity identification. Support vector machine and particle swarm algorithm were used to achieve damage classification while genetic algorithm and artificial fish swarm algorithm were used and compared for damage prediction. Although the prediction results have some errors, the damage can be identified with the error less than 10%.

The study of load capacity influenced by damage formed the last part of this thesis. This part focused on the damage size as well as location affecting the load capacity of the timber utility poles. From industry applications, the damage is divided into external and internal. External damage will influence the load capacity of the timber poles significantly while internal damage will not cause big loss of load capacity within a certain range. Under the design wind load, the external damage has a high potential possibility to cause the collapse of the utility poles while the poles may be safe with internal damage. It should be noticed that the cables attached to the poles also play an important role in determining the load capacity of the poles under the design wind load. The external damage at ground level is the most serious factor to influence the load capacity of the timber poles. The internal damage at ground level in this thesis has less effect on the poles to carry the design wind load comparing with the external damage. The Australian standards and Ausgrid manual were both considered in this study to calculate the design wind load as well as the bending strength and the load capacity of the timber utility poles.

In summary, a novel damage detection method based on reflected wave signal was developed in this thesis. The damage classification and damage prediction demonstrated good accuracy based on numerical results. Although the numerical models only considered an isotropic material, it provided a potential possibility to achieve damage detection when the sensors cannot be placed in the damage area and the reflected wave signals from damaged and intact structures cannot be compared directly.

Timber is a natural product with complicated material characteristics; to obtain an effective condition assessment method for the timber utility poles using stress wave based method, lots of effort is needed in further studies to make it more reliable and applicable.

7.2 RECOMMENDATIONS FOR FUTURE RESEARCH

Further work and some refinements are recommended to make this research work more practical for application. Hence, the purpose of this section is to focus on the issues that should be addressed by future researchers to make a further development as well as application of this novel method for damage detection of timber utility poles.

First of all, soil modelling can be ignored for damage detection of timber utility poles based on stress wave methods, since soil has little effect on wave propagation in structures according to the dispersion study. However, in the future research, embedment length determination of the timber utility poles is also important as the utility poles may collapse if the embedment length reduces significantly. For this specific research purpose, soil modelling has to be employed.

Secondly, as it is the starting stage in condition assessment of the timber utility poles, the proposed method for damage detection is based on the isotropic material model and further studies based on the orthotropic materials should be conducted. Also for selecting the most appropriate excitation frequency, a dispersion study based on numerical analysis on orthotropic material is needed and an effective method to pick the wave number for the orthotropic material has to be developed first. Alternatively, analytical results for the dispersion curve of the orthotropic material can be used directly instead of the numerical analysis.

Thirdly, since the proposed method aims at the longitudinal waves with one mode, combined waves and modes will cause unreliable results. An effective method for

separation of the wave modes is needed to deal with the problem caused by inclined impact at middle of a timber utility pole. The feature of the phase velocity of different modes may provide a possibility to design an effective filter of wave modes to pick up a pure longitudinal wave with single mode.

Finally, further experimental testing as well as field testing is needed. Timber is a complex material with orthotropic mechanical property and complicated microstructure. Behaviour of stress wave propagation in orthotropic material is very challenging and many tangled issues are yet to be solved. This thesis focused on damage detection of the timber utility poles by extracting the wave feature related to defects from complex wave responses. The influence of temperature and moisture will further complicate the study, therefore outside of the scope of the research and it is recommended for the future work.

Bibliography

ABDEL-RAHMAN, K. & ACHMUS, M. 2006. Numerical Modeling of the Combined Axial and Lateral Loading of Vertical Piles. *International Symposium on Frontiers in Offshore Geotechnics.* Perth, Australia.

ADDISON, P. S. & ADDISON, N. 2002. *The Illustrated Wavelet Transform Handbook*, Taylor & Francis.

AGNENI, A. 2000. On the Use of the Gauss Filter in Modal Parameter Estimation. *Mechanical Systems and Signal Processing,* 14**,** 193-204.

AIREY, D. W., CARTER, J. P., ASCE, M. & LIU, M. D. 2011. Sydney Soil Model. *International Journal of Geomechanics,* 11**,** 225-238.

ALVANDI, A. & CREMONA, C. 2006. Assessment of Vibration-based Damage Identification Techniques. *Journal of Sound and Vibration,* 292**,** 179-202.

AMIRI, G. G. & ASADI, A. 2009. Comparison of Different Methods of Wavelet and Wavelet Packet Transform in Processing Ground Motion Records. *International Journal of Civil Engineering,* 7**,** 248-258.

ANSYS, I. 2011. *User's Manual for ANSYS 13.0*. Canonsburg, Pennsylvania, U.S. Patent Application.

ANSYS, I. 2012. ANSYS User Manual. 14 ed. Southpointe, USA: ANSYS, Inc.

AUSGRID 2006. Pole Inspection and Treatment Procedures. Ausgrid.

AUSGRID 2011. Network Standard NS145. *Pole Inspection and Treatment Procedures.*

AUSGRID. 2014. *About Ausgrid* [Online]. http://www.ausgrid.com.au/Common/About-us/Contact-us/About-Ausgrid.aspx.

AUSTRALIAN/NEW ZEALAND STANDARD 1170.2 2011. Structural Design Actions. *Part 2: Wind Actions.* Australia: SAI Global Limited.

AZIZI, R. 2014. Empirical Study of Artificial Fish Swarm Algorithm. *International Journal of Computing, Communications and Networking,* 3**,** 1-7.

BALENDRA, S. 2005. *Numerical Modelling of Dynamic Soil-pile-structure Interaction.* Master of Science Civil Engineering, Washington State University.

BARANEEDARAN, S., GAD, E. F., FLATLEY, I., KAMIRAN, A. & WILSON, J. L. 2009. Review of In-service Assessment of Timber Poles. *18th Annual Conference of the Australian Earthquake Engineering Society.* Newcastle, Australia: Australian Earthquake Engineering Society.

BARTOLI, I., SCALEA, F. L. D., FATEH, M. & VIOLA, E. 2005. Modeling Guided Wave Propagation with Application to the Long-range Defect Detection in Railroad Tracks. *NDT & E International,* 38**,** 325-334.

BISHT, S. S. 2005. *Methods for Structural Health Monitoring and Damage Detection of Civil and Mechanical Systems.* Master, Virginia Polytechnic Institute and State University.

BOOTLE, K. R. 1983. *Wood in Australia,* Australia, McGraw-Hill Australia Pty Ltd.

BOSER, B., GUYON, I. & VAPNIK, V. A Training Algorithm for Optimal Margin Classifiers. *In:* HAUSSLER, D., ed. the Fifth Annual Workshop on Computational Learning Theory, July 27 - 29, 1992 Pittsburgh, USA. ACM New York, 144–152.

BOYABATLI, O. & SABUNCUOGLU, I. 2004. Parameter Selection in Genetic Algorithms. *Journal of Systemics, Cybernetics and Informatitics,* 2**,** 78-83.

BRIAUD, J. L. 1997. The National Geotechnical Experimentation Sites at Texas A&M University: Clay and Sand - A Summary. Texas A&M University, College Station, USA.

BRILLOUIN, L. 1960. *Wave Propagation and Group Velocity*, Academic Press.

BRINKGREVE, R. Selection of Soil Models and Parameters for Geotechnical Engineering Application. *In:* YAMAMURO, J. A. & KALIAKIN, V. N., eds. GeoFrontiers, 2005 US. ASCE, 69-98.

BULLEIT, W. M. & FALK, R. H. 1985. Modeling Stress Wave Passage Times in Wood Utility Poles. *Wood Science and Technology,* 19**,** 183-191.

CARINO, N. J. The Impact-echo Method: An Overview. *In:* CHANG, P. C., ed. the 2001 Structures Congress & Exposition, 2001 Washington D.C., 18.

CERNIGLIA, D., PANTANO, A. & MONTINARO, N. 2010. 3D Simulations and Experiments of Guided Wave Propagation in Adhesively Bonded Multi-layered Structures. *NDT & E International,* 43, 527-535.

CHAO, H. C. 2002. *An Experimental Model for Non-destructive Evaluation on Pile Foundations Using Guided Wave Approach.* PhD, Northwestern University.

CHATTOPADHYAY, A. R. G. 2007. Soil Factors Behind Inground Decay of Timber Poles: Testing and Interpretation of Results *IEEE Transactions on Power Delivery,* 22, 1897-1903.

CHOW, Y. K., PHOON, K. K., CHOW, W. F. & WONG, K. Y. 2003. Low Strain Integrity Testing of Piles: Three-Dimensional Effects. *Journal of Geotechnical and Geoenvironmental Engineering,* 129**,** 1057-1062.

COOK, R. D., MALKUS, D. S. & PLESHA, M. E. 1989. *Concepts and Applications of Finite Element Analysis,* Canada, John Wiley & Sons.

CREMA, L. B. & MASTRODDI, F. 1998. A Direct Approach for Updating and Damage Detection by Using FRF Data. *International Conference on Noise and Vibration Engineering.* Belgium.

CREWS, K. & HORRIGAN, A. 1998. Assessment of Characteristic Properties for Utility Poles in Australia. *5th World Conference on Timber Engineering.* Switzerland.

CUC, A., GIURGIUTIU, V., JOSHI, S. & TIDWELL, Z. 2007. Structural Health Monitoring with Piezoelectric Wafer Active Sensors for Space Applications. *American Institute of Aeronautics and Astronautics Journal,* 45**,** 2838-2850.

DACKERMANN, U., CREWS, K., KASAL, B., LI, J., RIGGIO, M., RINN, F. & TANNERT, T. 2013. In Situ Assessment of Structural Timber Using Stress-wave Measurements. *Materials and Structures,* 47**,** 787-803.

DACKERMANN, U., SKINNER, B. & LI, J. 2014. Guided Wave–based Condition Assessment of In situ Timber Utility Poles Using Machine Learning Algorithms. *Structural Health Monitoring,* 13**,** 374-388.

DACKERMANN, U., YU, Y., LI, J., NIEDERLEITHINGER, E. & WIGGENHAUSER, H. 2015. A New Non-destructive Testing System Based on Narrow-band Frequency Excitation for the Condition Assessment of Pole structures Using Frequency Response Functions and Principle Component Analysis. *International Symposium Non-Destructive Testing in Civil Engineering.* Berlin, Germany.

DATLA, S. V. & PANDEY, M. D. 2006. Estimation of Life Expectancy of Wood Poles in Electrical Distribution Networks. *Structural Safety,* 28**,** 304-319.

DAVENPORT, A. G. Gust Response Factors for Transmission Line Loading. *In:* CERMAK, J. E., ed. 5th International Conference on Wind Engineering, 1979 Fort Collins, Colorado, USA. Permagon Press, 899-909.

DAVIS, A. G. 1998. Nondestructive Test Methods for Evaluation of Concrete in Structures. U. S.: American Concrete Institute.

DAVIS, A. G. & DUNN, C. S. 1974. From Theory to Field Experience with the Non-destructive Vibration Testing of Piles. *Proceedings of Institution of Civil Engineers,* 57.

DAVIS, A. G., LIM, M. K. & PETERSEN, C. G. 2005. Rapid and Economical Evaluation of Concrete Tunnel Linings with Impulse Response and Impulse Radar Non-destructive Methods. *NDT & E International,* 38**,** 5, 181-186.

DESAI, C. S., ZAMAN, M. M., LIGHTNER, J. G. & SIRIWARDANE, H. J. 1984. Thin Layer Elements for Interfaces and Joints. *International Journal for Numerical and Analytic Methods in Geomechanic,* 8**,** 19-43.

DIEULESAINT, E. & ROYER, D. J. 1980. *Elastic Waves in Solids*, Springer.

DODSON, J. C. 2012. *GuidedWave Structural Health Monitoring with Environmental Considerations.* Doctor of Philosophy, Virginia Polytechnic Institute and State University.

DOEBLING, S. W., FARRAR, C. R. & PRIME, M. B. 1998. Summary Review of Vibration-based Damage Identification Methods. *Shock & Vibration Digest,* 30**,** 14, 91-105.

DOEBLING, S. W., FARRAR, C. R., PRIME, M. B. & SHEVITZ, D. W. 1996. Damage Identification and Health Monitoring of Structural and Mechanical Systems from Changes in Their Vibration Characteristics: A Literature Review United States: Los Alamos National Lab., NM (United States).

DONG, C., ZHANG, P. & HUANG, W. F. T. 1994. The Sensitivity Study of the Modal Parameters of A Cracked Beam. *The 12th International Modal Analysis Conference.*

DRUCKER, D. C. & PRAGER, W. 1952. Soil Mechanics and Plastic Analysis or Limit Design. *Applied Math,* 10**,** 157-165.

DRUMM, E., FISHMAN, K. & ZAMAN, M. 2000. Modelling of Interfaces and Joints. *In:* ZAMAN, M., GIODA, G. & BOOKER, J. (eds.) *Modelling in Geomechanics.* England: John Wiley & Sons Ltd.

DUNCAN, J. M. & CHANG, C. Y. 1970. Nonlinear Analysis of Stress and Strain in Soil. *Journal of Soil Mechanics and Foundations Division, ASCE,* 96, 1629-1653.

DUTTA, S. C. & ROY, R. 2002. A Critical Review on Idealization and Modeling for Interaction Among Soil–foundation–structure System. *Computers & Structures,* 80**,** 1579-1594.

EFUNDA. 2014. *Mechanics of Material* [Online]. http://www.efunda.com/formulae/solid_mechanics/mat_mechanics/hooke_orthotropic.cfm.

ELLIS, S. & STEINER, P. 2002. The Behaviour of Five Wood Species in Compression. *International Association of Wood Anatomists Journal,* 23**,** 201-211.

FACCHINI, G., BERNARDINI, L., ATEK, S. & GAUDENZI, P. 2014. Use of The Wavelet Packet Transform for Pattern Recognition in A Structural Health Monitoring Application. *Journal of Intelligent Material Systems and Structures,* 26, 7, 1-17.

FAN, X. & ZUO, M. Z. 2006. Gearbox Fault Detection Using Hilbert and Wavelet Packet Transform. *Mechanical Systems and Signal Processing,* 20**,** 966-982.
FINNO, R. J., CHOU, H. C. & LYNCH, J. 2001. Nondestructive Evaluation of In Situ Concrete Piles at the Advanced Waterfront Technology Test Sites, Port Hueneme, California. Washington D.C.: Naval Facilities Engineering Centre.
FISCHER, J., MISSAL, C., BREUSTEDT, M. & STAHLMANN, J. 2010. Numerical Simulation of Low-strain Integrity Tests on Model Piles. *In:* BENZ, T. & NORDAL, S., eds. the Seventh European Conference on Numerical Methods in Geotechnical Engineering, 2-4 June, 2010, Trondhelm, Norway. Balkems Leiden, The Neitherlands: CRC Press, 655-660.
FRANCIS, L. & NORTON, J. 2006. Australian Timber Pole Resources for Energy Networks A Review. *In:* Department of Primary Industries & Fisheries, Queensland. (ed.).
FRISWELL, M. I. 2008. Inverse Problems in Structural Dynamics. *2nd International Conference on Multidisciplinary Design Optimization and Applications*. Gijon, Spain.
FRISWELL, M. I., PENNY, J. E. T. & GARVEY, S. D. 1998. A Combined Genetic and Eigensensitivity Algorithm for the Location of Damage in Structures. *Computers and Structures,* 69**,** 547-556.
GAO, R. X. & YAN, R. 2011. *Wavelets Theory and Applications for Manufacturing,* United States, Springer.
GHODRATI, A. G., BAGHERI, A. & RAZAGHI, A. 2008. Generation of Multiple Earthquake Accelerograms Compatible with Spectrum Via the Wavelet Packet Transform and Stochastic Neural Networks. *Journal of Earthquake Engineering,* 13**,** 899-915.
GIURGIUTIU, V., BULI, X. & CUC, A. 2005. Dual Use of Traveling and Standing Lamb Waves for Structural Health Monitoring. *Conference & Exposition on Structural Dynamics - Structural Health Monitoring*. Florida, USA.
GOODMAN, R. E., TAYLOR, R. L. & BREKKE, T. L. 1968. A Model for the Mechanics of Jointed Rock. *Journal of the Soil Mechanics and Foundations Division ASCE,* 94**,** 637-659.
GRAFF, K. F. 1975. *Wave Motion in Elastic Solids*, Dover Pubns.
HAN, J. G., REN, W. X. & SUN, Z. S. 2005. Wavelet Packet Based Damage Identification of Beam Structures. *International Journal of Solids and Structures,* 42**,** 17, 6610-6627.
HANIFAH, A. A. 1999. *A Theoretical Evaluation of Guided Waves in Deep Foundations*. PhD, Northwestern University.
HAO, H. & XIA, Y. 2002. Vibration-based Damage Detection of Structures by Genetic Algorithm. *Journal of Computing in Civil Engineering,* 16**,** 222-229.
HIROSE, A. & LONNGREN, K. E. 1985. *Introduction to Wave Phenomena*, Wiley.
HOLLAND, J. 1975. *Adaptation in Natural and Artificial Systems,* U.S., University of Michigan Press.
HOLMES, D. J. 2001. *Wind Loading of Structures,* London, Spon Press.
HUANG, C. L. & DUN, J. F. 2008. A Distributed PSO–SVM Hybrid System with Feature Selection and Parameter Optimization. *Applied Soft Computing,* 8**,** 1381-1391.
HUANG, N. E., SHEN, Z., LONG, S. R., WU, M. C., SHIH, H. H., ZHENG, Q., YEN, N. C., TUNG, C. C. & LIU, H. H. 1998. The Empirical Model Decomposition

and the Hilbert Spectrum for Nonlinear and Non-stationary Time Series Analysis. *Proceedings of the Royal Society A,* 454**,** 903-995.
JALINOOS, F., OLSON, L. & AOUAD, M. 1996. Determination of Unknown Depth of Bridge Foundations Using Two Nondestructive Seismic Methods *Symposium on the Application of Geophysics to Engineering and Environmental Problems*.
JI, Y. & WANG, Y. 2010. Numerical Simulation and Method for a Wharf Pile Integrity Test Based on ANSYS/LS-DYNA. *Journal of Vibration and Shock,* 29**,** 199-205.
JIANG, J., CHEN, H., LI, J., CHEN, W. & ZHANG, L. 2010. Lifting Wavelet Packet Transform Based Damage Detection of Composite Plate Structures. *the 2nd International Conference onSignal Processing Systems.* China.
JUNIOR, C. C. & MOLINA, J. C. 2010. Numerical Modelling Strategy for Analyzing the Behaviour of Shear Connectors in Wood-Concrete Composite Systems. *World Conference on Timber Engineering.* Italy.
KIM, G. H., BARNES, H. M. & LYON, D. E. 1994. Effect of Decay on the Mechanical Properties of Full Sized Lumber. *Holzforschung,* 48**,** 145-149.
KIRKUP, S. 1998. *The Boundary Element Method in Acoustics*, Integrated Sound Software.
KO, J. M., WONG, C. W. & LAM, H. F. Damage Detection in Stell Framed Structures by Vibration Measurement Approach. 12th International Modal Analysis Conference, 1994 Bethel.
KOCIOŁEK, M., MATERKA, A., STRZELECKI, M. & SZCZYPIŃSKI, P. Discrete Wavelet Transform – Derived Features for Digital Image Texture Analysis. Interational Conference on Signals and Electronic Systems, 18-21 September 2001 Lodz, Poland. 163-168.
KWON, S. Y., KIM, M. M., KIM, S. H. & CHOI, J. I. 3D Dynamic Numerical Modeling for Soil-Pile-Structure Interaction in Centrifuge Tests. *In:* PIERRE DELAGE, J. D., ROGER FRANK, ALAIN PUECH, FRANÇOIS SCHLOSSER, ed. the 18th International Conference on Soil Mechanics and Geotechnical Engineering, 2013 Paris. Presses des Ponts, 751-754.
LARRY, M., OLSON, D., JALINOOS, F. & AOUAD, M. F. 1998. Determination of Unknown Subsurface Bridge Foundation. Federal Lands Highway Program Administration.
LAW, S. S., LI, X. Y., ZHU, X. Q. & CHAN, S. L. 2005. Structural Damage Detection from Wavelet Packet Sensitivity. *Engineering Structures,* 27, 1339-1348.
LEE, B. C., MANSON, G. & STASZEWSKI, W. J. 2003. Environmental Effects on Lamb Wave Responses from Piezoceramic Sensors. *Materials Science Forum,* 440**,** 195-202
LEE, B. C. & STASZEWSKI, W. J. 2007. Lamb Wave Propagation Modelling for Damage Detection: I. Two-dimensional Analysis. *Smart Materials and Structures,* 16**,** 249-274.
LEE, Y. Support Vector Machines for Classification: A Statistical Portrait. Spring Conference of the Korean Statistical Society 2011 Korea. Korean Statistical Society, 13-18.
LESLEY, F. & JACK, N. 2006. Australian timber pole resources for Energy Networks. *In:* Department of Primary Industries &Fisheries, Queensland. (ed.). Energy Network Association.
LI, C. & YU, L. 2014. Structural Model Updating and Damage Detection Based on Artificial Fish Swarm Algorithm. *Journal of Vibration and Shock* 33**,** 112-116.

LI, F., MURAYAMA, H., KAGEYAMA, K. & SHIRAI, T. 2009. Guided Wave and Damage Detection in Composite Laminates Using Different Fiber Optic Sensors. *Sensors,* 9, 5, 4005-4021.

LI, H., MANJUNATH, B. S. & MITRA, S. K. 1995. Multisensor Image Fusion Using the Wavelet Transform. *Graphical Models and Image Processing,* 57**,** 235-245.

LI, J., DACKERMANN, U. & SUBHANI, M. M. 2007. R&D of NDTs for Timber Utility Poles in Service – Challenges and Applications.

LI, J., DACKERMANN, U., ZAD, A., SUBHANI, M., SAMALI, B. & CREWS, K. 2011. Recommended Best Practice for Assessment of Timber Structures using Surface Stress Wave Methods. *Internal Report.* University of Technology Sydney.

LI, L. X., SHAO, Z. J. & QIAN, J. X. 2002. An Optimizing Method Based on Autonomous Animate: Fish Swarm Algorithm. *Proceeding of System Engineering Theory and Practice,* 2002**,** 32-38.

LI, M. B. 2007. *Thesis of modelling and Simulation of Wood Mechanical Properties Based on Finite Element Theory.* PhD, Northeast Forest Univeristy, China.

LI, P. Z., LU, X. L., CHEN, B. & CHEN, Y. Q. Computer Simulation on Dynamic Soil-Structure Interaction System. 13th World Conference on Earthquake Engineering Vancouver, 2004 B.C., Canada.

LINJAMA, J. 1992. Estimation of Bending Wave Intensity in Beams Using the Frequency Response Technique. *Journal of Sound and Vibration,* 153**,** 1, 21-36.

LIU, H., SONG, E. & LING, H. I. 2006. Constitutive Modeling of Soil-structure Interface Through the Concept of Critical State Soil Mechanics. *Mechanics Research Communications,* 33**,** 515-531.

LIU, Y., WANG, G., CHEN, H., DONG, H., ZHU, X. & WANG, S. 2011. An Improved Particle Swarm Optimization for Feature Selection. *Journal of Bionic Engineering,* 8**,** 191-200.

LIU, Y. & ZHENG, Y. F. 2005. One-Against-All Multi-Class SVM Classification Using Reliability Measures. *2005 IEEE International Joint Conference on Neural Networks* Montreal, Canada: IEEE.

LIU, Z., ZUO, M. J. & XU, H. 2012. Parameter Selection for Gaussian Radial Basis Function in Support Vector Machine Classification. *2012 International Conference on Quality, Reliability, Risk, Maintenance, and Safety Engineering.* Chengdu, China.

LUNA, R. & JADI, H. 2000. Determination of Dynamic Soil Properties Using Geophysical Methods. *the First International Conference on the Application of Geophysical and NDT Methodologies to Transportation Facilities and Infrastructure.* St. Louis, Missouri.

MADENCI, E. & GUVEN, I. 2006. *The Finite Element Method And Applications in Engineering Using Ansys*, Springer.

MARES, C. & SURACE, C. 1996. An Application of Genetic Algorithms to Identify Damage in Elastic Structures. *Journal of Sound and Vibration,* 195**,** 195-215.

MARWALA, T. 2002. Finite Element Model Updating Using Wavelet Data and Genetic Algorithm. *Journal of Aircraft,* 39**,** 709-711.

MARWALA, T. 2010. *Finite-element-model Updating Using Computional Intelligence Techniques,* London, Springer-Verlag London Limited.

MENDIS, P., NGO, T., HARITOS, N., HIRA, A., SAMALI, B. & CHEUNG, J. 2007. Wind Loading on Tall Buildings. *Electronic Journal of Structural Engineering*.

MIAO, L., GOH, A., WONG, K. & TEH, C. 2007. Three-dimensional Finite Element Analyses of Passive Pile Behaviour. *International Journal for Numerical and Analytical Methods in Geomechanics,* 30**,** 599–613.

MOAVENI, S. 1999. *Finite Element Analysis,* New Jersey, U.S, Prentice Hall.

MOSER, F., JACOBSA, L. J. & QU, J. 1999. Modeling Elastic Wave Propagation in Waveguides with the Finite Element Method. *NDT & E International,* 32**,** 225-234.

MURRAY, Y. D. 2007. Manual for LS-DYNA *Wood Material Model -143.* U.S.: Research, Development, and Technology Turner-Fairbank Highway Research Center.

NESHAT, M., SEPIDNAM, G., SARGOLZAEI, M. & TOOSI, A. N. 2012. Artificial Fish Swarm Algorithm: A Survey of the State-of-the-art, Hybridization, Combinatorial and Indicative applications. *Artificial Intelligence Review* 2012.

NEWCASTLE UNIVERSITY. 2014. *Roulette Wheel Selection* [Online]. http://www.edc.ncl.ac.uk/highlight/rhjanuary2007g02.php: Newcastle Univeristy.

NGUYEN, M., FOLIENTE, G. & WANG, X. 2004. State of the Practice and Challenges in Non-destructive Evaluation of Utility Poles in Service. *Key Engineering Materials-Advances in non-destructive evaluation,* 270-273.

NI, S. H., LEHMANN, L., CHARNG, J. J. & LO, K. F. 2006. Low-strain Integrity Testing of Drilled Piles with High Slenderness Ratio. *Computers and Geotechnics,* 33**,** 11, 283-293.

NINIC, J., STASCHEIT, J. & MESCHKE, G. 2014. Beam–solid Contact Formulation for Finite Element Analysis of Pile–soil Interaction with Arbitrary Discretization. *International Journal for Numerical and Analytical Methods in Geomechanics,* 38**,** 1453–1476.

NOFAL, M. & MORRIS, P. 2003. Criteria for Unacceptable Damage on Wood Systems. *Japan-Canada Conference on Building Envelope.* Vancouver, B.C.

OKAFOR, A. C. & DUTTA, A. 2000. Structural Damage Detection in Beams by Wavelet Transforms. *Smart Materials and Structures,* 9, 906-917.

OLSON, L. D. 2014. *Ultraseismic* [Online]. http://www.olsoninstruments.com/ultraseismic-ndt.php.

OLSON, L. D. & AOUAD, M. F. 2001. Unknown Subsurface Bridge Foundation Testing. NCHRP 21-05

OUIS, D. 1999. Vibrational and Acoustical Experiments on Logs of Spruce. *Wood Science and Technology,* 33**,** 151-184.

PANDEY, A. K. & ANTHONY, R. W. 2005. Inspection and Monitoring Techniques for Bridges and Civil Structures. England: The Institute of Materials, Minerals & Mining.

PANDEY, A. K., KASAL, B. & SAMMAN, M. M. 1991. Damage Detection from Changes in Curvature Mode Shapes. *Journal of Sound and Vibration,* 145**,** 321-332.

PARK, K. C., REICH, G. & ALVIN, K. F. 1998. Structural Damage Detection Using Localized Flexibilities. *Journal of Intelligent Material Systems and Structures,* 9**,** 911-919.

PARKSEISMIC. 2012. *What Are Seismic Waves?* [Online]. http://www.parkseismic.com/Whatisseismicwave.html: Park Seismic. 2012.

PARLOO, E., GUILLAUME, P. & OVERMEIRE, M. V. 2003. Damage Assessment Using Mode Shape Sensitivities. *Mechanical Systems and Signal Processing,* 17**,** 499-518.

PELLICANE, P. J. & FRANCO, N. 1994. Modeling wood pole failure. *Wood Science and Technology,* 28**,** 219-228.

PERCIVAL, D. B. & WALDEN, A. T. 2000. *Wavelet Methods for Time Series Analysis*, Cambridge University Press.

PERERA, R. & RUIZ, A. 2008. A Multistage FE Updating Procedure for Damage Identification in Large-scale Structures Based on Multi-objective Evolutionary Optimization. *Mechanical Systems and Signal Processing,* 22**,** 970-991.

PIAO, C., SHUPE, T. F., TANG, R. C. & HSE, C. Y. 2005. Finite Element Analyses of Wood-Laminated Composite Poles. *Wood Fiber Science,* 37**,** 535–541.

PLUMB, R. A. 2003. Atmospheric and Oceanic Circulations.

POLIKAR, R. 2001. *The Wavelet Tutorial* [Online]. http://person.hst.aau.dk/enk/ST8/wavelet_tutotial.pdf.

POLIKAR, R. 2004. The Wavelet Tutorial. Rowan University web servers: College of Engineering, Rowan University.

PRAKASH, R. 2013. Wavelet Packet Transform Based Damage Identification of GFRP Beam. *Journal of Structural Engineering,* 40**,** 44-47.

PUCKETT, A. D. 2000. Fidelity of a Finite Element Model for Longitudinal Wave Propagation in Thick Cylindrical Wave Guides. Los Alamos National Laboratory.

PUREKAR, A. S. & PINES, D. J. 2010. Damage Detection in Thin Composite Laminates Using Piezoelectric Phased Sensor Arrays and Guided Lamb Wave Interrogation. *Journal of Intelligent Material Systems and Structures,* 21**,** 995-1010.

RAGHAVAN, A. & CESNIK, C. E. S. 2007. Review of Guieded Waves Structural Health Monitoring. *The Shock and Vibration Digest,* 39**,** 2, 91-114.

RAMADAS, C., BALASUBRAMANIAM, K., JOSHI, M. & KRISHNAMURTHY, C. V. 2008. Detection of Transverse Cracks in a Composite Beam Using Combined Features Of Lamb Wave and Vobration Techniques in ANN Environment. *International Journal on Smart Sensing and Intelligent Systems,* 1**,** 970-984.

RAUSCHE, F., LIKINS, G. & KUNG, S. R. 1992. Pile Integrity Testing and Analysis. *In:* BARENDS, F. B. (ed.) *Application of Stress Wave Theory to Piles*. Netherlands: Balkema Rotterdam.

ROBERTSON, A. N., ALVIN, K. F. & PARK, K. C. 1998. Extraction of Impulse Response Data via Wavelet Transform for Structural System Identification. *Journal of Vibration and Acoustics,* 120**,** 9, 252-260.

RYTTER, A. 1994. *Vibration Based Inspection of Civil Engineering Structures*. Doctor, Aalborg University

SAMANTA, B. 2004. Gear Fault Detection Using Artificial Neural Networks and Support Vector Machines with Genetic Algorithms. *Mechanical Systems and Signal Processing,* 18**,** 625–644.

SANDHU, S., KANAPADY, R., TAMMA, K., KAMATH, C. & KUMAR, V. 2001. Damage Prediction and Estimation in Structural Mechanics Based on Data Mining. U.S: Lawrence Livermore National Laboratory, University of California.

SCHANZ, T., VERMEER, P. A. & BONNIER, P. G. The Hardening Soil Model: Formulation and Verification. Internetional Symposium beyond 2000 in Computational Geotechnics, 1999 Netherlands. Rotterdam Balkema.

SCHAUER, M. & LANGER, S. Numerical Simulations of Pile Integrity Tests Using a Coupled FEM SBFEM Approach. *In:* ALBER, H. D., KRAYNYUKOVA, N. & TROPEA, C., eds. 83rd Annual Meeting of the International Association of Applied Mathematics and Mechanics, 2012 Darmstadt, Germany. WILEY-VCH Verlag GmbH & Co. KGaA, Weinheim, 547-548.

SCHOLKOPF, B. 1998. SVMs a Practical Consequence of Learning Theory. *IEEE Intelligent Systems,* 13**,** 18-19.

SERRANO, E. 2000. *Adhesive Joints in Timber Engineering-Modelling and Testing of Fracture Properties.* PhD, Lund University.

SINOU, J. J. 2009. A Review of Damage Detection and Health Monitoring of Mechanical Systems from Changes in the Measurement of Linear and Non-linear Vibrations. *In:* SAPRI, R. C. (ed.) *Mechanical Vibrations: Measurement, Effects and Control.* Nova Science Publishers.

STEINBACH, J. & VEY, E. 1975. Caisson Evaluation by Stress Wave Propagation Method. *Journal of Geotechnical Engineering,* 101, 361-378.

STEPINSKI, T., UHL, T. & STASZEWSKI, W. 2013. *Advanced Structural Damage Detection: From Theory to Engineering Applications,* UK, John Wiley & Sons, Ltd.

SU, Z., YE, L. & LU, Y. 2006. Guided Lamb Waves for Identification of Damage in Composite Structures: A Review. *Journal of Sound and Vibration,* 295**,** 753-780.

SUBHANI, M. 2014. *Study on Behaviour of Guided Wave Propagation in Utility Timber Poles.* PhD, University of Technology Sydney.

SUN, Z. & CHANG, C. 2002. Structural Damage Assessment Based on Wavelet Packet Transform. *Journal of Structural Engineering,* 128**,** 7, 1354-1361.

SUN, Z. & CHANG, C. C. 2004. Statistical Wavelet-based Method for Structural Health Monitoring. *Journal of Structural Engineering, ASCE,* 130**,** 1055-1062.

SURACE, C. & RUOTOLO, R. 1994. Crack Detection of a Beam Using the Wavelet Transform. *the 12th International Modal Analysis Conference.* US.

TABIEI, A. & WU, J. 2000. Three-dimensional Nonlinear Orthotropic Finite Element Material Model for Wood. *Composite Structures,* 50**,** 143-149.

TANASOIU, V., MICLEA, C. & TANASOIU, C. 2002. Non-destructive Testing Techniques and Piezoelectric Ultra-Sonics Transducers for Wood and Built in Wooden Structures. *Journal of Optoelectronics and Advanced Materials,* 4, 949-957.

TANG, J. & YAN, G. 2013. Monitoring and Detection of Structural Damage under Complex Environment Using Guided Waves. *Singapore International NDT Conference & Exhibition.* Singapore.

TI, K. S., HUAT, B. B. K., NOORZAEI, J., JAAFAR, M. S. & SEW, G. S. 2009. A Review of Basic Soil Constitutive Models for Geotechnical Application. 14, 1-18.

UHL, T., STEPINSKI, T. & STASZEWSKI, W. 2013. *Advanced Structural Damage Detection,* United Kingdom, John Wiley & Sons, Ltd.

WANG, C. H., LEICESTER, R. H. & M. NGUYEN 2008. Probabilistic Procedure for Design of Untreated Timber Poles In-ground Under Attack of Decay Fungi. *Reliability Engineering & System Safety,* 93, 3, 476-481.

WANG, H. 2004. Theoretical Evaluation of Embedded Plate-like and Solid Cylindrical Concrete Structures with Guided Waves. Northwestern University.

WANG, H. & CHANG, T. P. 2008. Non-destructive Evaluation of In-service Concrete Piles by Flexural Wave Approach. *In:* SANTOS, J. A. (ed.) *Application of Stress-Wave Theory to Piles.* US: Ios Press.

WANG, H. Y. 2003. *Comparison and Evaluation of Stress Wave Non-Destructive Testing Techniques on Piles.* Master, Chao Yang University of Technology.

WANG, X., ROSS, R. J. & CARTER, P. Acoustic Evaluation of Standing Trees-Recent Research Development. The Fourteenth International Symposium on Nondestructive Testing of Wood, 2005 University of Applied Sciences, Eberswalde, Germany. 455-465.

WANG, Y. 2009. *Damage Identification and Assessment of Civil Infrastructure Using Local and Global Methods.* Doctor, The University of Western Australia.

WOOD, D. M. 1990. *Soil Behaviour and Critical State Soil Mechanics*, Press Syndicate of the University of Cambridge.

WORLTON, D. C. 1961. Experimental Confirmation of Lamb Waves at Megacycle Frequencies. *Journal of Applied Physics,* 32**,** 967-971.

WU, G. 1994. *Dynamic Soil-structure Interaction: Pile Foundations and Retaining Structures.* PhD, University of British Columbia.

WU, X., GHABOUSSI, J. & GARRETT, J. H. 1992. Use of Neural Networks in Detection of Structural Damage. *Computers and Structures,* 42**,** 649-659.

WU, Y., GAO, X. & K.ZENGER 2011. Knowledge-based Artificial Fish-swarm Algorithm. *the 18th IFAC World Congress.* Milano, Italy.

YAM, L. H., YAN, Y. J. & JIANG, J. S. 2003. Vibration-based Damage Detection for Composite Structures Using Wavelet Transform and Neural Network Identification. *Composite Structures,* 60**,** 403-412.

YANG, J. N., LEI, Y., LIN, S. & HUANG, N. 2004. Hilbert-Huang Based Approach for Structural Damage Detection. *Journal of Engineering Mechanics ASCE,* 130**,** 85-95.

YEN, G. G. & LIN, K. C. 2000. Wavelet Packet Feature Extraction for Vibration Monitoring. *IEEE Transactions on Industrial Electronics,* 47**,** 18, 3365-3370.

YU, L. & LI, C. 2014. A Global Artificial Fish Swarm Algorithm for Structural Damage Detection. *Advances in Structural Engineering,* 17**,** 331-348.

ZHAI, Y., LI, H. & ZHOU, Q. 2008. Research on SVM Algorithm with Particle Swarm Optimization. *the 11th Joint Conference on Information Sciences* Shenzhen, China: Atlantis Press.

Appendix

Table A1 Regional wind speed

REGIONAL WIND SPEED m/s				
Speed Probability	Region A	Region B	Region C	Region D
V_{100}	41	48	59	73
V_{200}	43	52	64	79
V_{500}	45	57	69	88
V_{1000}	46	60	74	94
V_{2000}	48	63	77	99

Source: AS/NZS 1170.2 Table 3.1 and Clause 3.4.

Table A2 Terrain/Height multiplier

Building Height (m)	Region A & B (Ultimate limit state) All Regions (Serviceability limit state)				Region C & D (Ultimate limit state)		
	TC1	TC2	TC2.5	TC3	TC 1 & 2	TC2.5	TC 3
<= 3	0.99	0.91	0.87	0.83	0.90	0.85	0.80
5	1.05				0.95	0.88	
10	1.12	1.00	0.92		1.00	0.95	0.89

Source: AS/NZS 1170.2 Table 4.1(A). Linear interpolation may be used for intermediate values of height and terrain category. Building Height is defined in AS/NZS 1170.2 Fig 2.1.

Table A3 Terrain category

TC	Description
1	Exposed open terrain with few or no obstructions
2	Water surfaces, open terrain, grassland with few, well-scattered obstructions having heights generally from 1.5 m to 10 m.
2.5	Terrain with few trees, isolated obstructions such as agricultural land, cane fields or long grass, up to 600 mm high.
3	Terrain with numerous closely spaced obstructions 3 m to 5 m high such as areas of suburban housing.
4	Terrain with numerous large 10 m to 30 m high closely spaced obstructions such as large city centres and well-developed industrial complexes.

Note: Definition and interpolated is in accordance with AS/NZS 1170.2.

Table A4 Typical length of poles used in Ausgrid

Length	Typical Application
10m	Stay poles
11.5m	LV poles
12m	11kv or 22kv poles
14m	Transformer, recloser, regulator, or HV UGOH poles

Source: Ausgrid NS220 Section6.1

Table A5 Internal damages at ground level influence on the strength

L=12m D=315mm Ultimate design strength in bending: 38MPa					
Damage dimension W_D (mm)	L_D (mm)	$R_L=L_D/L_O$	$R_W=W_D/W_O$	Max. stress (MPa)	Safety ratio
79	100	1%	25%	17	44 %
	200	2%	25%	17	44 %
	300	3%	25%	17	44 %
	400	3%	25%	17	44 %
	500	4%	25%	17	52 %
Damage dimension W_D (mm)	L_D (mm)	$R_L=L_D/L_O$	$R_W=W_D/W_O$	Max. stress (MPa)	Safety ratio
118	100	1%	37%	17	44 %
	200	2%	37%	17	44 %
	300	3%	37%	17	44 %
	400	3%	37%	17	44 %
	500	4%	37%	17	44 %
Damage dimension W_D (mm)	L_D (mm)	$R_L=L_D/L_O$	$R_W=W_D/W_O$	Max. stress (MPa)	Safety ratio
158	100	1%	50%	17	44 %
	200	2%	50%	17	44 %
	300	3%	50%	17	44 %
	400	3%	50%	18	47 %
	500	4%	50%	19	49 %
Damage dimension W_D (mm)	L_D (mm)	$R_L=L_D/L_O$	$R_W=W_D/W_O$	Max. stress (MPa)	Safety ratio
197	100	1%	63%	18	47 %
	200	2%	63%	19	49 %
	300	3%	63%	20	52 %
	400	3%	63%	21	55 %
	500	4%	63%	21	55 %
Damage dimension W_D (mm)	L_D (mm)	$R_L=L_D/L_O$	$R_W=W_D/W_O$	Max. stress (MPa)	Safety ratio
236	100	1%	75%	20	52 %
	200	2%	75%	22	57 %
	300	3%	75%	25	65 %
	400	3%	75%	26	68 %
	500	4%	75%	27	70 %

Table A6 Maximum load capacity for external damage at ground level

L=12m D=315mm
Ultimate design strength in bending: 38MPa
Maximum accepted wind load: 11kN

Damage size W_D (mm)	L_D (mm)	$R_L=L_D/L_O$	$R_W=W_D/W_O$	Max. load (kN)	Max. stress (MPa)	Safety ratio	LCR
79	100	1%	25%	4.8	37	97 %	44%
	200	2%	25%		37	97 %	
	300	3%	25%		37	97 %	
	400	4%	25%		38	100 %	
	500	5%	25%		38	100 %	
Damage size W_D (mm)	L_D (mm)	$R_L=L_D/L_O$	$R_W=W_D/W_O$	Max. load (kN)	Max. stress (MPa)	Safety ratio	LCR
118	100	1%	37%	2.8	36	95 %	25%
	200	2%	37%		37	97 %	
	300	3%	37%		37	97 %	
	400	4%	37%		37	97 %	
	500	5%	37%		37	97 %	
Damage size W_D (mm)	L_D (mm)	$R_L=L_D/L_O$	$R_W=W_D/W_O$	Max. load (kN)	Max. stress (MPa)	Safety ratio	LCR
158	100	1%	50%	1.4	36	95 %	13%
	200	2%	50%		37	97 %	
	300	3%	50%		37	97 %	
	400	4%	50%		37	97 %	
	500	5%	50%		37	97 %	
Damage size W_D (mm)	L_D (mm)	$R_L=L_D/L_O$	$R_W=W_D/W_O$	Max. load (kN)	Max. stress (MPa)	Safety ratio	LCR
197	100	1%	63%	0.58	36	95 %	5%
	200	2%	63%		37	97 %	
	300	3%	63%		37	97 %	
	400	4%	63%		37	97 %	
	500	5%	63%		37	97 %	
Damage size W_D (mm)	L_D (mm)	$R_L=L_D/L_O$	$R_W=W_D/W_O$	Max. load (kN)	Max. stress (MPa)	Safety ratio	LCR
236	100	1%	75%	0.175	36	95 %	1.6%
	200	2%	75%		36	95 %	
	300	3%	75%		37	97 %	
	400	4%	75%		37	97 %	
	500	5%	75%		37	97 %	

Table A7 Maximum load capacity for internal damage at ground level

L=12m D=315mm
Ultimate design strength in bending: 38MPa
Maximum accepted wind load: 11kN

Damage size W_D (mm)	Damage size L_D (mm)	$R_L=L_D/L_O$	$R_W=W_D/W_O$	Max. load (KN)	Max. stress (MPa)	Safety ratio	LCR
79	100	1%	25%	10	36	95 %	98%
	200	2%	25%		36	95 %	
	300	3%	25%		37	97 %	
	400	3%	25%		37	97 %	
	500	4%	25%		37	97 %	
Damage size W_D (mm)	Damage size L_D (mm)	$R_L=L_D/L_O$	$R_W=W_D/W_O$	Max. Load (KN)	Max. stress (MPa)	Safety ratio	LCR
118	100	1%	37%	9.7	36	95 %	95%
	200	2%	37%		36	95 %	
	300	3%	37%		37	97 %	
	400	3%	37%		37	97 %	
	500	4%	37%		37	97 %	
Damage size W_D (mm)	Damage size L_D (mm)	$R_L=L_D/L_O$	$R_W=W_D/W_O$	Max. Load (KN)	Max. stress (MPa)	Safety ratio	LCR
158	100	1%	50%	9.3	35	92 %	91%
	200	2%	50%		36	95 %	
	300	3%	50%		37	97 %	
	400	3%	50%		37	97 %	
	500	4%	50%		37	97 %	
Damage size W_D (mm)	Damage size L_D (mm)	$R_L=L_D/L_O$	$R_W=W_D/W_O$	Max. Load (KN)	Max. stress (MPa)	Safety ratio	LCR
197	100	1%	63%	8.2	32	84 %	80%
	200	2%	63%		34	92 %	
	300	3%	63%		35	97 %	
	400	3%	63%		36	97 %	
	500	4%	63%		37	97 %	
Damage size W_D (mm)	Damage size L_D (mm)	$R_L=L_D/L_O$	$R_W=W_D/W_O$	Max. Load (KN)	Max. stress (MPa)	Safety ratio	LCR
236	100	1%	75%	6.4	28	80 %	63%
	200	2%	75%		31	95 %	
	300	3%	75%		35	97 %	
	400	3%	75%		36	97 %	
	500	4%	75%		37	97 %	

Table A8 Maximum load capacity for external damage at the middle of poles

L=12m D=315mm Ultimate design strength in bending: 38MPa Maximum accepted wind load: 11kN							
Damage size		$R_L=L_D/L_O$	$R_W=W_D/W_O$	Max. load (KN)	Max. stress (MPa)	Safety ratio	LCR
W_D (mm)	L_D (mm)						
79	100	1%	25%	5.3	37	97 %	64%
	200	2%	25%		37	97 %	
	300	3%	25%		37	97 %	
	400	3%	25%		37	97 %	
	500	4%	25%		37	97 %	
Damage size		$R_L=L_D/L_O$	$R_W=W_D/W_O$	Max. Load (KN)	Max. stress (MPa)	Safety ratio	LCR
W_D (mm)	L_D (mm)						
118	100	1%	37%	3.3	37	97 %	39%
	200	2%	37%		37	97 %	
	300	3%	37%		37	97 %	
	400	3%	37%		37	97 %	
	500	4%	37%		37	97 %	
Damage size		$R_L=L_D/L_O$	$R_W=W_D/W_O$	Max. Load (KN)	Max. stress (MPa)	Safety ratio	LCR
W_D (mm)	L_D (mm)						
158	100	1%	50%	1.8	34	89 %	19.5%
	200	2%	50%		36	95 %	
	300	3%	50%		37	97 %	
	400	3%	50%		37	97 %	
	500	4%	50%		37	97 %	
Damage size		$R_L=L_D/L_O$	$R_W=W_D/W_O$	Max. Load (KN)	Max. stress (MPa)	Safety ratio	LCR
W_D (mm)	L_D (mm)						
197	100	1%	63%	0.83	34	89 %	8.6%
	200	2%	63%		37	97 %	
	300	3%	63%		37	97 %	
	400	3%	63%		37	97 %	
	500	4%	63%		37	97 %	
Damage size		$R_L=L_D/L_O$	$R_W=W_D/W_O$	Max. Load (KN)	Max. stress (MPa)	Safety ratio	LCR
W_D (mm)	L_D (mm)						
236	100	1%	75%	0.23	32	84 %	2.6%
	200	2%	75%		37	97 %	
	300	3%	75%		37	97 %	
	400	3%	75%		37	97 %	
	500	4%	75%		37	97 %	

Table A9 Maximum load capacity for external damage at the top area of poles

L=12m D=315mm Ultimate design strength in bending: 38MPa Maximum accepted wind load: 11kN							
Damage size				Max. load (KN)	Max. stress (MPa)	Safety ratio	LCR
W_D (mm)	L_D (mm)	$R_L=L_D/L_O$	$R_W=W_D/W_O$				
79	100	1%	25%	8.5	37	97 %	91%
	200	2%	25%		37	97 %	
	300	3%	25%		37	97 %	
	400	3%	25%		37	97 %	
	500	4%	25%		37	97 %	
Damage size				Max. Load (KN)	Max. stress (MPa)	Safety ratio	LCR
W_D (mm)	L_D (mm)	$R_L=L_D/L_O$	$R_W=W_D/W_O$				
118	100	1%	37%	8.5	37	97 %	91%
	200	2%	37%		37	97 %	
	300	3%	37%		37	97 %	
	400	3%	37%		37	97 %	
	500	4%	37%		37	97 %	
Damage size				Max. Load (KN)	Max. stress (MPa)	Safety ratio	LCR
W_D (mm)	L_D (mm)	$R_L=L_D/L_O$	$R_W=W_D/W_O$				
158	100	1%	50%	5.4	35	89 %	60%
	200	2%	50%		36	95 %	
	300	3%	50%		37	97 %	
	400	3%	50%		37	97 %	
	500	4%	50%		37	97 %	
Damage size				Max. Load (KN)	Max. stress (MPa)	Safety ratio	LCR
W_D (mm)	L_D (mm)	$R_L=L_D/L_O$	$R_W=W_D/W_O$				
197	100	1%	63%	2.4	33	87 %	25.5%
	200	2%	63%		36	95 %	
	300	3%	63%		37	97 %	
	400	3%	63%		37	97 %	
	500	4%	63%		37	97 %	
Damage size				Max. Load (KN)	Max. stress (MPa)	Safety ratio	LCR
W_D (mm)	L_D (mm)	$R_L=L_D/L_O$	$R_W=W_D/W_O$				
236	100	1%	75%	0.78	31	84 %	7.8%
	200	2%	75%		37	97 %	
	300	3%	75%		37	97 %	
	400	3%	75%		37	97 %	
	500	4%	75%		37	97 %	